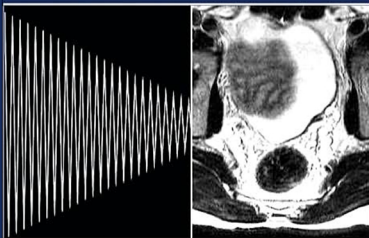


# MRI

*Basic  
Principles  
and  
Applications*

T H I R D   E D I T I O N



MARK A. BROWN, Ph.D.  
RICHARD C. SEMELKA, M.D.

**MRI**

# **MRI BASIC PRINCIPLES AND APPLICATIONS**

**THIRD EDITION**

**MARK A. BROWN, PH.D.**

Senior Technical Instructor  
Siemens Training and Development Center  
Cary, North Carolina

**RICHARD C. SEMELKA, M.D.**

Professor and Director of MR Services  
Department of Radiology  
University of North Carolina School of Medicine  
Chapel Hill, North Carolina



**WILEY-LISS**

A JOHN WILEY & SONS, INC., PUBLICATION

Copyright © 2003 by John Wiley and Sons, Inc. All rights reserved.

Published by John Wiley & Sons, Inc., Hoboken, New Jersey.

Published simultaneously in Canada.

No part of this publication may be reproduced, stored in a retrieval system or transmitted in any form or by any means, electronic, mechanical, photocopying, recording, scanning or otherwise, except as permitted under Section 107 or 108 of the 1976 United States Copyright Act, without either the prior written permission of the Publisher, or authorization through payment of the appropriate per-copy fee to the Copyright Clearance Center, Inc., 222 Rosewood Drive, Danvers, MA 01923, 978-750-8400, fax 978-750-4744, or on the web at [www.copyright.com](http://www.copyright.com). Requests to the Publisher for permission should be addressed to the Permissions Department, John Wiley & Sons, Inc., 111 River Street, Hoboken, NJ 07030, (201) 748-6011, fax (201) 748-6008, e-mail: [permreq@wiley.com](mailto:permreq@wiley.com).

**Limit of Liability/Disclaimer of Warranty:** While the publisher and author have used their best efforts in preparing this book, they make no representation or warranties with respect to the accuracy or completeness of the contents of this book and specifically disclaim any implied warranties of merchantability or fitness for a particular purpose. No warranty may be created or extended by sales representatives or written sales materials. The advice and strategies contained herein may not be suitable for your situation. You should consult with a professional where appropriate. Neither the publisher nor author shall be liable for any loss of profit or any other commercial damages, including but not limited to special, incidental, consequential, or other damages.

For general information on our other products and services please contact our Customer Care Department within the U.S. at 877-762-2974, outside the U.S. at 317-572-3993 or fax 317-572-4002.

Wiley also publishes its books in a variety of electronic formats. Some content that appears in print, however, may not be available in electronic format.

***Library of Congress Cataloging-in-Publication Data:***

Brown, Mark A., 1955–

MRI : basic principles and applications / Mark A. Brown, Richard C.

Semelka. — 3rd ed.

p. cm.

Includes bibliographical reference and index.

ISBN 0-471-43310-1

1. Magnetic resonance imaging. I. Semelka, Richard C. II. Title.

RC78.7.N83B765 2003

616.07'548—dc21

2003004787

Printed in the United States of America.

10 9 8 7 6 5 4 3 2 1



# CONTENTS

---

PREFACE TO THE THIRD EDITION, IX

PREFACE TO THE SECOND EDITION, XI

PREFACE TO THE FIRST EDITION, XIII

<b>1</b>	<b>PRODUCTION OF NET MAGNETIZATION</b>	<b>1</b>
<b>2</b>	<b>CONCEPTS OF MAGNETIC RESONANCE</b>	<b>11</b>
<b>3</b>	<b>RELAXATION</b>	<b>21</b>
3.1	T1 RELAXATION AND SATURATION, 21	
3.2	T2 RELAXATION, T2* RELAXATION AND SPIN ECHOES, 25	
<b>4</b>	<b>PRINCIPLES OF MAGNETIC RESONANCE IMAGING— PART 1</b>	<b>33</b>
4.1	SLICE SELECTION, 34	
4.2	READOUT OR FREQUENCY ENCODING, 37	
4.3	PHASE ENCODING, 40	
4.4	SEQUENCE LOOPING, 43	
<b>5</b>	<b>PRINCIPLES OF MAGNETIC RESONANCE IMAGING— PART 2</b>	<b>49</b>
5.1	FREQUENCY-SELECTIVE EXCITATION, 49	
5.2	RAW DATA AND IMAGE DATA MATRICES, 53	
5.3	RAW DATA AND K SPACE, 55	

---

5.4	REDUCED $K$ SPACE ACQUISITIONS, 62	
5.5	PARALLEL ACQUISITION TECHNIQUES, 64	
<b>6</b>	<b>PULSE SEQUENCES</b>	<b>67</b>
6.1	SPIN ECHO SEQUENCES, 69	
6.2	GRADIENT ECHO SEQUENCES, 73	
6.3	ECHO PLANAR IMAGING SEQUENCES, 80	
6.4	MAGNETIZATION-PREPARED SEQUENCES, 82	
<b>7</b>	<b>MEASUREMENT PARAMETERS AND IMAGE CONTRAST</b>	<b>93</b>
7.1	INTRINSIC PARAMETERS, 94	
7.2	EXTRINSIC PARAMETERS, 97	
7.3	PARAMETER TRADEOFFS, 100	
<b>8</b>	<b>ADDITIONAL SEQUENCE MODIFICATIONS</b>	<b>103</b>
8.1	SPATIAL PRESATURATION, 103	
8.2	FAT SATURATION, 105	
8.3	MAGNETIZATION-TRANSFER SUPPRESSION, 107	
8.4	COMPOSITE PULSES, 110	
<b>9</b>	<b>ARTIFACTS</b>	<b>113</b>
9.1	MOTION ARTIFACTS, 113	
9.2	SEQUENCE/PROTOCOL-RELATED ARTIFACTS, 117	
9.3	EXTERNAL ARTIFACTS, 129	
<b>10</b>	<b>MOTION ARTIFACT REDUCTION TECHNIQUES</b>	<b>141</b>
10.1	ACQUISITION PARAMETER MODIFICATION, 142	
10.2	TRIGGERING/GATING, 144	
10.3	FLOW COMPENSATION, 149	
<b>11</b>	<b>MAGNETIC RESONANCE ANGIOGRAPHY</b>	<b>151</b>
11.1	TIME-OF-FLIGHT MRA, 153	
11.2	PHASE CONTRAST MRA, 157	
11.3	MAXIMUM INTENSITY PROJECTION, 162	

---

<b>12</b>	<b>ADVANCED IMAGING APPLICATIONS</b>	<b>165</b>
12.1	DIFFUSION, 165	
12.2	PERFUSION, 169	
12.3	FUNCTIONAL BRAIN IMAGING, 173	
12.4	ULTRA-HIGH FIELD IMAGING, 176	
12.5	NOBLE GAS IMAGING, 178	
<b>13</b>	<b>MAGNETIC RESONANCE SPECTROSCOPY</b>	<b>181</b>
13.1	ADDITIONAL CONCEPTS, 181	
13.2	LOCALIZATION TECHNIQUES, 186	
13.3	SPECTRAL ANALYSIS AND POSTPROCESSING, 189	
13.4	ULTRAHIGH FIELD SPECTROSCOPY, 194	
<b>14</b>	<b>INSTRUMENTATION</b>	<b>197</b>
14.1	COMPUTER SYSTEMS, 197	
14.2	MAGNET SYSTEM, 201	
14.3	GRADIENT SYSTEM, 204	
14.4	RADIO FREQUENCY SYSTEM, 206	
14.5	DATA ACQUISITION SYSTEM, 208	
14.6	SUMMARY OF SYSTEM COMPONENTS, 210	
<b>15</b>	<b>CONTRAST AGENTS</b>	<b>213</b>
15.1	INTRAVENOUS AGENTS, 214	
15.2	ORAL AGENTS, 221	
<b>16</b>	<b>CLINICAL APPLICATIONS</b>	<b>223</b>
16.1	GENERAL PRINCIPLES OF CLINICAL MR IMAGING, 224	
16.2	EXAMINATION DESIGN CONSIDERATIONS, 225	
16.3	PROTOCOL CONSIDERATIONS FOR ANATOMICAL REGIONS, 226	
16.4	RECOMMENDATIONS FOR SPECIFIC SEQUENCES AND CLINICAL SITUATIONS, 243	
<b>17</b>	<b>REFERENCES AND SUGGESTED READINGS</b>	<b>247</b>
	<b>INDEX</b>	<b>251</b>

# PREFACE TO THE THIRD EDITION

---

Our intention in writing *MRI: Basic Principles and Applications* was to provide a book that would serve as a bridge between the theory and practical usage of magnetic resonance imaging (MRI). We minimized the use of intense mathematical formalism and attempted to show the underlying foundation for MRI as it is currently used. Our attempt was to provide a resource for those medical personnel who needed accurate and detailed information yet could not devote time to study an in-depth theoretical treatise.

In the third edition, we have maintained the organization of the first two editions. We have divided the description of MRI physics into two chapters—the first a more introductory presentation and the second presenting more advanced concepts. We have included a discussion of issues related to ultra-high magnetic field scanning, as these systems are now commercially available. Most of the figures have also been revised and updated.

As in most projects of this type, a number of persons aided us and we are grateful to them. First, we would like to thank the technical staff at the Siemens Training and Development Center and the faculty, fellows, and staff at the University of North Carolina for their interest in this project and their assistance in its completion. In particular, we would like to thank Thomas Beckman, Zeynep Firat, Kathryn Wissink, James R. MacFall, and H.

Cecil Charles for providing images. Finally, we would like to thank our families for their support and patience during the time that this revision was prepared.

MARK A. BROWN

RICHARD C. SEMELKA

*Cary, North Carolina*

*Chapel Hill, North Carolina*

*March, 2003*

# PREFACE TO THE SECOND EDITION

---

Our intention in writing the first edition of *MRI: Basic Principles and Applications* as to provide a book that would serve as a bridge between the theory of magnetic resonance imaging (MRI) and its implementation in commercial scanners. We minimized the use of intense mathematical formalism and attempted to stress the practical aspects of MRI as it is currently used. Our attempt was to provide a resource for those medical personnel who needed accurate and detailed information yet could not devote time to study an in-depth theoretical treatise.

In the second edition, we have maintained the basic organization of the first edition. The first three chapters describe the basic principles behind magnetic resonance as they are applied in the production of image contrast. Chapters 4 through 6 describe the principles used for spatial localization of the MR signal and many of the common techniques that are commercially implemented. The next three chapters describe variations on the resulting basic techniques that increase tissue contrast or ensure the quality of the measurement. Chapters 10 through 12 illustrate some of the major applications of MRI in current use and some areas in which new applications have been developed since the first edition. These include MR spectroscopy and diffusion-weighted imaging. Chapter 13 describes the major hardware components common to all MRI systems. The final chapters describe the use of contrast agents and the principles that should be considered in developing clinical protocols.

We would like to thank many people who aided us in the production of this endeavor. First, we would like to thank the technical staff at the

Siemens Training and Development Center and the faculty, fellows, and staff at the University of North Carolina for their interest in this project and their assistance in its completion. We would also like to thank James R. MacFall for providing Figure 11-5. Finally, we would like to thank our families for their support and patience during the time that this manuscript was prepared.

MARK A. BROWN

RICHARD C. SEMELKA

*Cary, North Carolina*

*Chapel Hill, North Carolina*

*May, 1999*

# PREFACE TO THE FIRST EDITION

---

In the 22 years since the first image of two capillary tubes was produced, the field of magnetic resonance imaging (MRI) has evolved into an indispensable component in the armament of imaging procedures. Much of this evolution has been accomplished through changes in localization techniques and new mechanisms of contrast. Even so, many of the fundamental principles governing image contrast and localization have changed little since they were first determined. Our purpose in writing this book is to present the basic concepts of MRI in a fashion that is comprehensible to a wide range of readers. We include equations in the text for completeness, but the general reader should not be daunted by their presence. Their understanding is not a prerequisite to understanding the accompanying text. We feel that this approach will provide the reader with the tools necessary to assess the various imaging techniques and to understand and apply the contrast mechanisms inherent in each one.

This book is organized into five general sections. The first three chapters describe the source of the magnetic resonance signal and how its manipulation provides the contrast within an image. Chapters 4, 5, and 6 describe the concepts of spatial localization and various imaging techniques that are commonly used. The next four chapters describe several variations on basic imaging techniques for enhancing contrast between tissues and/or for ensuring fidelity of the detected signals. The next



chapter describes the basic hardware components of any MRI system. The final chapters provide an overview of contrast agents in clinical use and clinical applications and concepts to consider in developing imaging protocols.

MARK A. BROWN

RICHARD C. SEMELKA

*Cary, North Carolina*

*Chapel Hill, North Carolina*

*September, 1995*

## PRODUCTION OF NET MAGNETIZATION

---

Magnetic resonance (MR) is based upon the interaction between an applied magnetic field and a nucleus that possesses spin. Nuclear spin or, more precisely, nuclear spin angular momentum, is one of several intrinsic properties of an atom and its value depends on the precise atomic composition. Every element in the Periodic Table except argon and cerium has at least one naturally occurring isotope that possesses spin. Thus, in principle, nearly every element can be examined using MR, and the basic ideas of resonance absorption and relaxation are common to all of these elements. The precise details will vary from nucleus to nucleus and from system to system.

Atoms consist of three fundamental particles: protons, which possess a positive charge; neutrons, which have no charge; and electrons, which have a negative charge. The protons and neutrons are located in the nucleus or core of an atom, whereas the electrons are located in shells or orbitals surrounding the nucleus. The characteristic chemical reactions of elements depend upon the particular number of each of these particles. The properties most commonly used to categorize elements are the atomic number and the atomic weight. The atomic number is the number of protons in the nucleus, and is the primary index used to differentiate between atoms. All atoms of an element have the same atomic number. The atomic weight is the sum of the number of protons and the number of neutrons. Atoms with the same atomic number but different atomic weights are called isotopes.

A third property of the nucleus is spin or intrinsic spin angular momentum. The nucleus can be considered to be constantly rotating about an axis at a constant rate or velocity. This self-rotation axis is perpendicular to the direction of rotation (Figure 1-1). A limited number of values for the spin are found in nature; that is, the spin,  $I$ , is quantized to certain discrete values. These values depend on the atomic number and atomic weight of the particular nucleus. There are three groups of values for  $I$ : zero, half-integral values, and integral values. A nucleus has no spin ( $I = 0$ ) if it has an even number atomic weight and an even atomic number. Such a nucleus does not interact with an external magnetic field and cannot be studied using MR. A nucleus has an integral value for  $I$  (e.g., 1, 2, 3) if it has an even atomic weight and an odd atomic number. A nucleus has a half-integral value for  $I$  (e.g.,  $1/2$ ,  $3/2$ ,  $5/2$ ) if it has an odd atomic weight. Table 1-1 lists the spin and isotopic composition for some elements commonly found in biological systems. The  $^1\text{H}$  nucleus, consisting of a single proton, is a natural choice for probing the body using MR techniques for several reasons. It has a spin of  $1/2$  and is the most abundant isotope for hydrogen. Its response to an applied magnetic field is one of the largest found in nature. Finally, the human body is composed of tissues that contain primarily water and fat, both of which contain hydrogen.

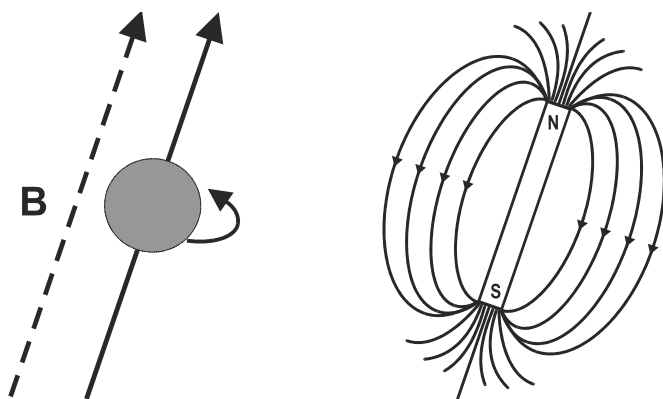


FIGURE 1-1 A rotating nucleus with a positive charge produces a magnetic field known as the magnetic moment oriented parallel to the axis of rotation (left side of figure). This arrangement is analogous to a bar magnet in which the magnetic field is considered to be oriented from the south to the north pole (right side).

TABLE 1-1 Constants for Selected Nuclei of Biological Interest

Element	Nuclear Composition		Nuclear Spin, $I$	Gyromagnetic Ratio $\beta$ (MHz T <sup>-1</sup> )	% Natural Abundance	$\omega$ at 1.5 T (MHz)
	Protons	Neutrons				
<sup>1</sup> H, Protium	1	0	1/2	42.5774	99.985	63.8646
<sup>2</sup> H, Deuterium	1	1	1	6.53896	0.015	9.8036
<sup>3</sup> He	2	1	1/2	32.436	0.000138	48.6540
<sup>6</sup> Li	3	3	1	6.26613	7.5	9.39919
<sup>7</sup> Li	3	4	3/2	16.5483	92.5	24.8224
<sup>12</sup> C	6	6	0	0	98.90	0
<sup>13</sup> C	6	7	1/2	10.7084	1.10	16.0621
<sup>14</sup> N	7	7	1	3.07770	99.634	4.6164
<sup>15</sup> N	7	8	1/2	4.3173	0.366	6.4759
<sup>16</sup> O	8	8	0	0	99.762	0
<sup>17</sup> O	8	9	5/2	5.7743	0.038	8.6614
<sup>19</sup> F	9	10	1/2	40.0776	100	60.1164
<sup>23</sup> Na	11	12	3/2	11.2686	100	16.9029
<sup>31</sup> P	15	16	1/2	17.2514	100	25.8771
<sup>129</sup> Xe	54	75	1/2	11.8604	26.4	17.7906

Source: Adapted from Ian Mills (Ed.) *Quantities, Units, and Symbols in Physical Chemistry*, IUPAC, Physical Chemistry Division, Blackwell, Oxford, UK, 1989.

A rigorous mathematical description of a nucleus with spin and its interactions requires the use of quantum mechanical principles, but most of MR can be described using the concepts of classical mechanics, particularly in describing the actions of a nucleus with spin. The subsequent discussions of MR phenomena in this book use a classical approach. In addition, although the concepts of resonance absorption and relaxation apply to all nuclei with spin, the descriptions in this book are focused on <sup>1</sup>H (commonly referred to as a proton) since most imaging experiments visualize the <sup>1</sup>H nucleus.

In addition to its spin, a positively charged nucleus (the location of the protons) also has a local magnetic field or magnetic moment. This associated magnetic moment is fundamental to MR. A bar magnet provides a useful analogy. A bar magnet has a north and south pole; more precisely, a magnitude and orientation or direction to the magnetic field can be defined. A nucleus with spin has an axis of rotation that can be viewed as a vector with a definite orientation and magnitude (Figure 1-1). The magnetic moment for the nucleus is parallel to the axis of rotation. This orientation of the nuclear

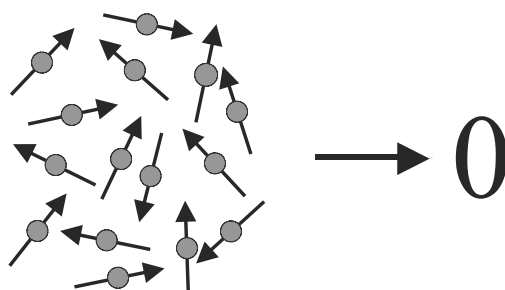


FIGURE 1-2 Microscopic and macroscopic pictures of a collection of protons in the absence of an external magnetic field. In the absence of a field, the protons have their spin vectors oriented randomly (microscopic picture, left side of figure). The vector sum of these spin vectors is zero (macroscopic picture, right side).

spin and the changes induced in it due to the experimental manipulations that the nucleus undergoes provide the basis for the MR signal.

In general, MR measurements are made on collections of similar spins rather than on an individual spin. It is useful to consider such a collection both as individual spins acting independently (a “microscopic” picture) and as a single entity (a “macroscopic” picture). For many concepts, the two pictures provide equivalent results, even though the microscopic picture is more complete. Conversion between the two pictures requires the principles of statistical mechanics. Though necessary for a complete understanding of MR phenomena, the nature of this conversion is beyond the scope of this book. For most concepts presented in this book, the macroscopic picture is sufficient for an adequate description. When necessary, the microscopic picture will be used.

Consider an arbitrary volume of tissue containing hydrogen atoms (protons). Each proton has a spin vector of equal magnitude. However, the spin vectors for the entire collection of protons within the tissue are randomly oriented in all directions. Performing a vector addition of these spin vectors produces a zero sum; that is, no net magnetization is observed in the tissue (Figure 1-2). If the tissue is placed inside a magnetic field  $B_0$ ,\* the individual protons begin to rotate perpendicular to, or precess about,

\*In this book, vector quantities with direction and magnitude are indicated by boldface type, whereas scalar quantities with magnitude only are indicated by regular typeface.

the magnetic field. The protons are tilted slightly away from the axis of the magnetic field, but the axis of rotation is parallel to  $B_0$ . This precession is at a constant rate and occurs because of the interaction of the magnetic field with the spinning positive charge of the nucleus. By convention,  $B_0$  and the axis of precession are defined to be oriented in the z direction of a Cartesian coordinate system. (This convention is not universally followed, but it is the prevailing convention.) The motion of each proton can be described by a unique set of coordinates perpendicular (x and y) and parallel (z) to  $B_0$ . The perpendicular, or transverse, coordinates are nonzero and vary with time as the proton precesses, but the z coordinate is constant with time (Figure 1-3). The rate or frequency of precession is proportional to the strength of the magnetic field and is expressed by Equation 1-1, the Larmor equation:

$$\omega_0 = \gamma B_0 / 2\pi \quad (1-1)$$

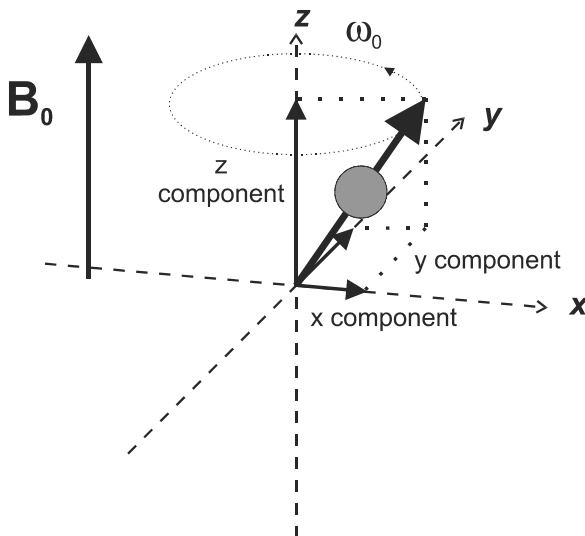


FIGURE 1-3 Inside a magnetic field, a proton precesses or revolves about the magnetic field. The precessional axis is parallel to the main magnetic field  $B_0$ . The z component of the spin vector (projection of the spin onto the z axis) is the component of interest because it does not change in magnitude or direction as the proton precesses. The x and y components vary with time at a frequency  $\omega_0$  proportional to  $B_0$  as expressed by Equation (1-1).

where  $\omega_0$  is the Larmor frequency in megahertz (MHz)<sup>†</sup>,  $B_0$  is the magnetic field strength in Tesla (T) that the proton experiences, and  $\gamma$  is a constant for each nucleus in  $\text{s}^{-1}\text{T}^{-1}$ , known as the gyromagnetic ratio. Values for  $\gamma$  and  $\omega$  at 1.5 T for several nuclei are tabulated in Table 1-1.

If a vector addition is performed, as before, for the spin vectors inside the magnetic field, the results will be slightly different than for the sum outside the field. In the direction perpendicular to  $B_0$ , the spin orientations are still randomly distributed just as they were outside the magnetic field, in spite of the time-varying nature of each transverse component. There is still no net magnetization perpendicular to  $B_0$ . However, in the direction parallel to the magnetic field, there is a different result. Because there is an orientation to the precessional axis of the proton that is constant with time, there is a constant, nonzero interaction or coupling between the proton and  $B_0$ . This is known as the Zeeman interaction. This coupling causes a difference in energy between protons aligned parallel or along  $B_0$  and protons aligned antiparallel or against  $B_0$ . This energy difference  $\Delta E$  is proportional to  $B_0$  (Figure 1-4).

The result of the Zeeman interaction is that spins in the two orientations, parallel (also known as spin up) and antiparallel (spin down), have different energies. The orientation that is parallel to  $B_0$  is of lower energy than the antiparallel orientation. For a collection of protons, more will be oriented parallel to  $B_0$  than will be oriented antiparallel; that is, there is an induced polarization of the spin orientation by the magnetic field (Figure 1-5a). The exact number of protons in each energy level is governed by a distribution known as the Boltzmann distribution:

$$N_{\text{upper}}/N_{\text{lower}} = e^{-\Delta E/kT} \quad (1-2)$$

where  $N_{\text{upper}}$  and  $N_{\text{lower}}$  are the number of protons in the upper and lower energy levels, respectively, and  $k$  is Boltzmann's constant,  $1.381 \times 10^{-23} \text{ J K}^{-1}$ .

<sup>†</sup>The factor of  $2\pi$  in Equation 1-1 is necessary to convert from angular to cyclical frequency. In many discussions of MR,  $\omega$  (Greek letter omega) is used to represent angular frequency, with units of  $\text{s}^{-1}$ , whereas cyclical frequency, in units of Hz, is represented by  $\nu$  (Greek letter nu) or  $f$ . The Larmor equation is more properly written as  $\nu_0 = \gamma B_0 / 2\pi$ . In imaging derivations, the Larmor equation is expressed as Equation 1-1, using  $\omega$  but with units of Hertz. To minimize confusion, we follow the imaging tradition throughout this book.

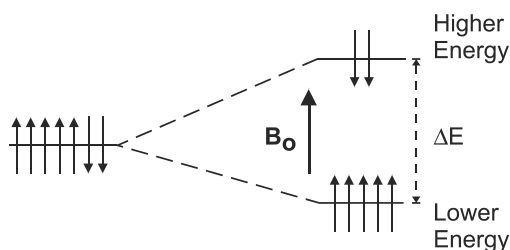


FIGURE 1-4 Zeeman diagram. In the absence of a magnetic field (left side of figure), a collection of protons will have the configurations of  $z$  components equal in energy so that there is no preferential alignment between the spin up and spin down orientations. In the presence of a magnetic field (right side), the spin up orientation (parallel to  $B_0$ ) is of lower energy and its configuration contains more protons than the higher energy, spin down configuration. The difference in energy  $\Delta E$  between the two levels is proportional to  $B_0$ .

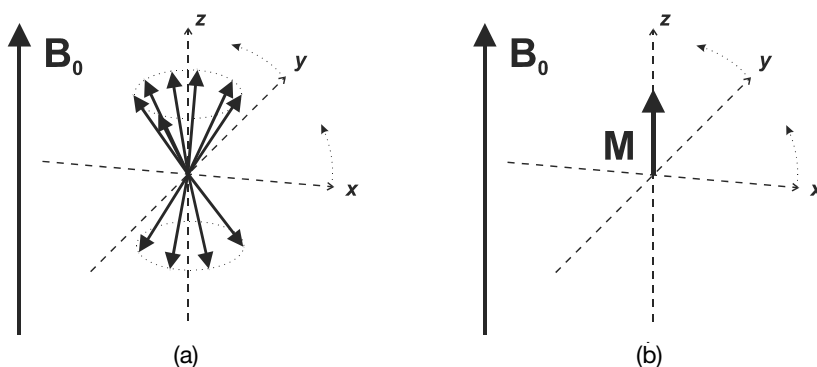


FIGURE 1-5 Microscopic (a) and macroscopic (b) pictures of a collection of protons in the presence of an external magnetic field. Each proton precesses about the magnetic field. If a rotating frame of reference is used with a rotation rate of  $\omega_0$ , then the collection of protons appears stationary. The  $z$  components are one of two values (one positive and one negative), but the  $x$  and  $y$  components can be any value, positive or negative. The protons will appear to track along two “cones,” one with a positive  $z$  component and one with a negative  $z$  component. Because there are more protons in the upper cone, there will be a nonzero vector sum  $M_0$ , the net magnetization. It will be of constant magnitude and parallel to  $B_0$ .



Since the separation between the energy levels  $\Delta E$  depends on the field strength  $B_0$ , the exact number of spins in each level also depends on  $B_0$  and increases with increasing  $B_0$ . For a collection of protons at body temperature (310 K) at 1.5 T, there will typically be an excess of  $\sim 1:10^6$  protons in the lower level out of the approximately  $10^{25}$  protons within the tissue. This unequal number of protons in each energy level means that the vector sum of spins will be nonzero and will point parallel to the magnetic field. In other words, the tissue will become polarized or magnetized in the presence of  $B_0$  with a value  $M_0$ , known as the net magnetization. The orientation of this net magnetization will be in the same direction as  $B_0$  and will be constant with respect to time (Figure 1-5b). For tissues in the body, the magnitude of  $M_0$  is proportional to  $B_0$ :

$$M_0 = \chi B_0 \quad (1-3)$$

where  $\chi$  is known as the bulk magnetic susceptibility or simply the magnetic susceptibility. This arrangement with  $M_0$  aligned along the magnetic field with no transverse component is the normal, or equilibrium, configuration for the protons. This configuration of spins has the lowest energy and is the arrangement to which the protons will naturally try to return following any perturbations such as energy absorption. This induced magnetization,  $M_0$ , is the source of signal for all of the MR experiments. Consequently, all other things being equal, the greater the field strength, the greater the value of  $M_0$  and the greater the potential MR signal.

Another way to visualize this net magnetization is to recall that the individual spins are precessing about the magnetic field. When the spins absorb energy, this precessional motion continues but becomes more complicated to describe. A useful technique to simplify the description is called a rotating frame of reference, or rotating coordinate system. In a rotating frame, the coordinate system rotates about one axis while the other two axes vary with time. By choosing a suitable axis and rate of rotation for the coordinate system, the moving object appears stationary.

For MR experiments, a convenient rotating frame uses the z axis, parallel to  $B_0$ , as the axis of rotation while the x and y axes rotate at the Larmor frequency,  $\omega_0$ . When viewed in this fashion, the precessing spin appears stationary in space with a fixed set of x, y, and z coordinates. If the entire col-

lection of protons in the tissue volume is examined, a complete range of  $x$  and  $y$  values will be found, both positive and negative, but only two  $z$  values. There will be an equal number of positive and negative  $x$  and  $y$  values, but a slight excess of positive  $z$  values, as just described. If a vector sum is performed on this collection of protons, the  $x$  and  $y$  components sum to zero but a nonzero, positive  $z$  component will be left, the net magnetization,  $M_0$ . In addition, since the  $z$  axis is the axis of rotation,  $M_0$  does not vary with time. Regardless of whether a stationary or fixed coordinate system is used,  $M_0$  is of fixed amplitude and is parallel to the main magnetic field. For all subsequent discussions in this book, a rotating frame of reference with the rotation axis parallel to  $B_0$  is used when describing the motion of the protons.

## CONCEPTS OF MAGNETIC RESONANCE

---

The MR experiment, in its most basic form, can be analyzed in terms of energy transfer. During the measurement, the patient or sample is exposed to energy at the correct frequency that will be absorbed. A short time later, this energy is reemitted, at which time it can be detected and processed. A detailed presentation of the processes involved in this absorption and reemission are beyond the scope of this text. However, a general description of the nature of the molecular interactions is useful. In particular, the relationship between the molecular picture and the macroscopic picture provides an avenue for explanation of the principles of MR.

Chapter 1 described the formation of the net magnetization,  $M_0$ , by the protons within a sample. The entire field of MR is based on the manipulation of  $M_0$ . The simplest manipulation involves the application of a short burst, or pulse, of radiofrequency (rf) energy. This pulse, also known as an excitation pulse, contains many frequencies spread over a narrow range or bandwidth. During the pulse, the protons absorb the portion of this energy at a particular frequency. Following the pulse, the protons reemit the energy at the same frequency. The particular frequency absorbed is proportional to the magnetic field  $B_0$ ; the equation relating the two is the Larmor equation, Equation 1-1.

The frequency of energy absorbed by an individual proton is defined very precisely by the magnetic field that the proton experiences due to the quantized nature of the spin. When a proton is irradiated with energy of the correct frequency ( $\omega_0$ ), it will be excited from the lower energy (spin up) ori-

entation to the higher energy (spin down) orientation (Figure 2-1). At the same time, a proton at the higher energy level will be stimulated to release its energy and will go to the lower energy level. The energy difference ( $\Delta E$ ) between the two levels is exactly proportional to the frequency  $\omega_0$  and thus the magnetic field  $B_0$ :

$$\Delta E = \hbar \omega_0 = \hbar \gamma B_0 / 2\pi \quad (2-1)$$

where  $\hbar$  is Planck's constant,  $6.626 \times 10^{-34}$  J s, and  $\hbar$  is  $h$  divided by  $2\pi$ . Only energy at this frequency stimulates transitions between the spin up and spin down energy levels. This quantized energy absorption is known as resonance absorption and the frequency of energy is known as the resonant frequency.

Although an individual proton absorbs the radiofrequency energy, it is more useful to discuss the resonance condition by examining the effect of the energy absorption on the net magnetization  $M_0$ . For a large number of protons such as in a volume of tissue, there is a significant amount of both absorption and emission occurring during the rf pulse. However, because there are more protons at the lower energy level (Figure 2-1), there will be a net absorption of energy by the tissue. The energy is applied as an rf pulse

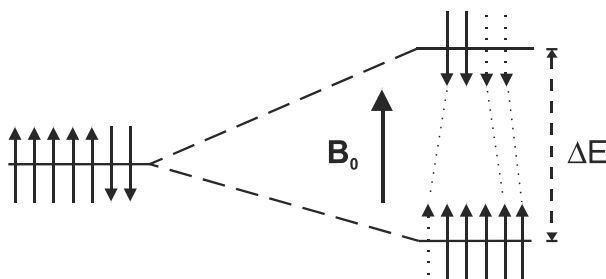


**FIGURE 2-1** Energy absorption (microscopic). The difference in energy  $\Delta E$  between the two configurations (spin up and spin down) is proportional to the magnetic field strength  $B_0$  and the corresponding precessional frequency  $\omega_0$  as expressed in Equation 2-1. When energy at this frequency is applied, a spin from the lower energy state is excited to the upper energy state. Also, a spin from the upper energy state is stimulated to give up its energy and relax to the lower energy state. Because there are more spins in the lower energy state, there is a net absorption of energy by the spins in the sample.

with a central frequency  $\omega_0$  and an orientation perpendicular to  $B_0$ , as indicated by an effective field  $B_1$  (Figure 2-2). This orientation difference allows a coupling between the rf pulse and  $M_0$  so that energy can be transferred to the protons. Absorption of the rf energy of frequency  $\omega_0$  causes  $M_0$  to rotate away from its equilibrium orientation. The direction of rotation of  $M_0$  is perpendicular to both  $B_0$  and  $B_1$ . If the transmitter is left on long enough and at a high enough amplitude, the absorbed energy causes  $M_0$  to rotate entirely into the transverse plane, a result known as a  $90^\circ$  pulse. When viewed in the rotating frame, the motion of  $M_0$  is a simple vector rotation; however, the end result is the same whether a rotating or stationary frame of reference is used.

When the transmitter is turned off, the protons immediately begin to realign themselves and return to their original equilibrium orientation. They emit energy at frequency  $\omega_0$  as they do so. In addition, the net magnetization will begin to precess about  $B_0$ , similar to the behavior of a gyroscope when tilted away from a vertical axis. If a loop of wire (a receiver coil) is placed perpendicular to the transverse plane, the protons induce a voltage in the wire during their precession. This induced voltage, the MR signal, is known as the FID or free induction decay (Figure 2-3a). The initial magnitude of the FID signal depends on the value of  $M_0$  immediately prior to the  $90^\circ$  pulse. The FID decays with time as more of the protons give up their ab-

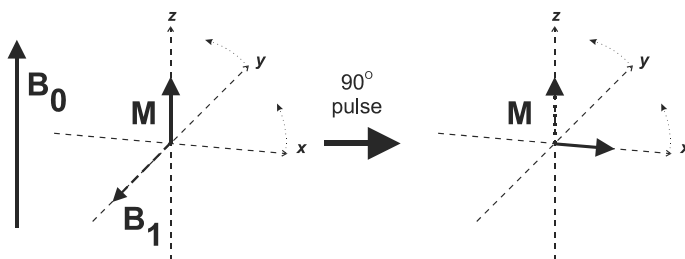
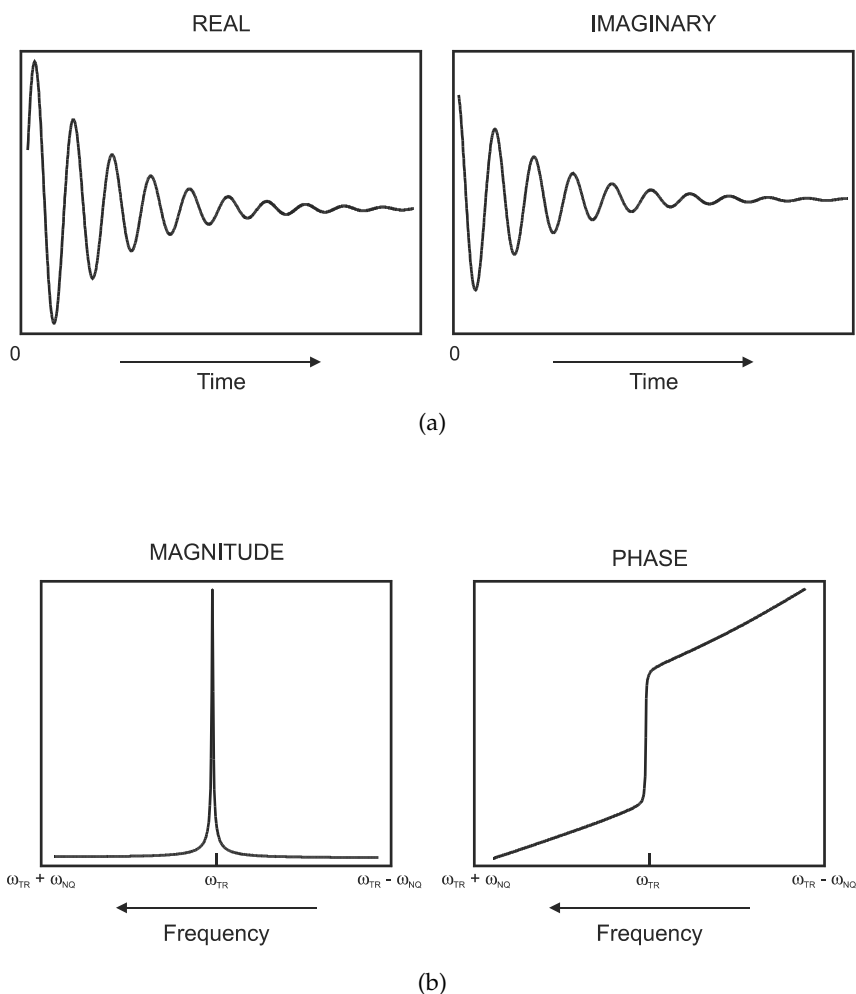


FIGURE 2-2 Energy absorption (macroscopic). In a rotating frame of reference, the rf pulse broadcast at the resonant frequency  $\omega_0$  can be treated as an additional magnetic field  $B_1$  oriented perpendicular to  $B_0$ . When energy is applied at the appropriate frequency, the protons absorb it and  $M$  rotates into the transverse plane. The direction of rotation is perpendicular to both  $B_0$  and  $B_1$ . The amount of resulting rotation of  $M$  is known as the pulse flip angle.



**FIGURE 2-3** (a) Free induction decay, real and imaginary. The response of the net magnetization  $M$  to an rf pulse as a function of time is known as the free induction decay or FID. It is proportional to the amount of transverse magnetization generated by the pulse. The FID is maximized when using a  $90^\circ$  excitation pulse. (b) Fourier transformation of (a), magnitude and phase. The Fourier transformation is used to convert the digital version of the MR signal (FID) from a function of time to a function of frequency. Signals measured with a quadrature detector are displayed with the transmitter (reference) frequency  $\omega_{TR}$  in the middle of the display. The Nyquist frequency  $\omega_{NQ}$  below and above  $\omega_{TR}$  are the minimum and maximum frequencies of the frequency display, respectively. For historical reasons, frequencies are plotted with lower frequencies on the right side and higher frequencies on the left side of the display.

sorbed energy through a process known as relaxation (see Chapter 3) and the coherence or uniformity of the proton motion is lost.

In general, three aspects of an MR signal are of interest: its magnitude or amplitude, its frequency, and its phase relative to the rf transmitter phase (Figure 2-4). As mentioned previously, the signal magnitude is related to the value of  $M_0$  immediately prior to the rf pulse. The signal frequency is related to the magnetic field influencing the protons. If all the protons experience the same magnetic field  $B_0$ , then only one frequency would be present within the FID. In reality, there are many magnetic fields throughout the magnet, and thus many MR signals at many frequencies following the rf pulse. These signals are superimposed so that the FID contains many frequencies varying as a function of time. It is easier to examine such a multi-component signal in terms of frequency rather than of time. The conversion of the signal amplitudes from a function of time to a function of frequency is accomplished using a mathematical operation called the Fourier transformation. In the frequency presentation or frequency domain spectrum, the

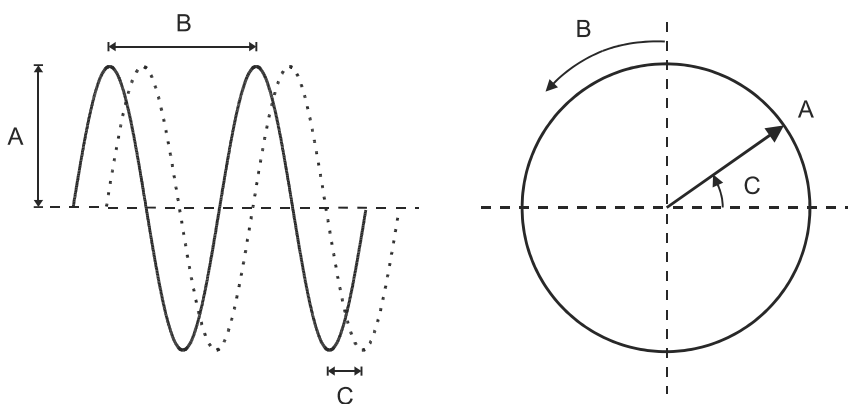


FIGURE 2-4 Planar and circular representations of a time-varying wave. The amplitude (A) is the maximum deviation of the wave from its mean value. The period (B) is the time required for completion of one complete cycle of the wave. The frequency of the wave is the reciprocal of the period. The phase or phase angle of the wave (C) describes the shift in the wave relative to a reference (a second wave for the planar representation, horizontal axis for circular representation). The two plane waves displayed have the same amplitude and period (frequency), but have a phase difference of  $\pi/4$  or  $90^\circ$ .

MR signal is mapped according to its frequency relative to a reference frequency, typically the transmitter frequency  $\omega_{TR}$ . For systems using quadrature detectors (see Chapter 14),  $\omega_{TR}$  is centered in the display with frequencies higher and lower than  $\omega_{TR}$  located to the left and right, respectively (Figure 2-3b). The frequency domain thus provides a simple way to examine the magnetic environment that a proton experiences. This simplification is not without a penalty. Use of the Fourier transformation loses the ability to directly relate signal intensities to the number of protons producing the signal. However, the signal intensity can be related from one frequency to another within the same measurement; that is, only relative signal intensities can be compared. Absolute signal intensities cannot be obtained without using an external reference standard.

Since the proton precession is continuous, the MR signal is continuous or analog in nature. However, postprocessing techniques such as Fourier transformation require a digital representation of the signal. To produce a digital version, the FID signal is measured or sampled using an analog-to-digital converter (ADC). In most instances, the resonant frequencies of protons are greater than many ADCs can process. For this reason, a phase-coherent difference signal is generated based on the frequency and phase of the input rf pulse; that is, the signal actually digitized is the measured signal relative to  $\omega_{TR}$ . Under normal conditions, this so-called demodulated signal is digitized for a predetermined time known as the sampling time and with a user-selectable number of data points. In such a situation, there will be a maximum frequency, known as the Nyquist frequency  $\omega_{NQ}$ , that can be accurately measured:

$$\omega_{NQ} = (\text{Total number of data points})/2 * (\text{Sampling time}) \quad (2-2)$$

In MR, the Nyquist frequency can be 500–500,000 Hz, depending on the combination of sampling time and number of data points. To exclude frequencies greater than the Nyquist limit from the signal, a filter known as a low-pass filter is used prior to digitization. Frequencies excluded by the low-pass filter are usually noise, so that filtering provides a method for improving the signal-to-noise ratio (S/N) for the measurement. The optimum S/N is usually obtained by increasing the sampling time to match the Nyquist frequency and low-pass filter width for the particular measure-



ment conditions. For quadrature detection systems typically used in MR, the total receiver bandwidth is  $2 * \omega_{NQ}$  centered about  $\omega_{TR}$  (Figure 2-3b).

The specific frequency that a proton absorbs is dependent on magnetic fields arising from two sources. One is the applied magnetic field  $B_0$ . The other one is molecular in origin and produces the chemical shift. In patients, the bulk of the hydrogen MR signals arise from two sources: water and fat. Water has two hydrogen atoms bonded to one oxygen atom, whereas fat has many hydrogen atoms bonded to a long-chain carbon framework (typically 10–18 carbon atoms in length). Because of its different molecular environment, a water proton has a different local magnetic field than a fat proton. This local field difference is known as chemical shielding and is proportional to the main magnetic field  $B_0$ :

$$B_i = B_0(1 - \sigma_i) \quad (2-3)$$

where  $\sigma_i$  is the shielding term for proton  $i$ . Chemical shielding produces different resonant frequencies for fat and water protons under the influence of the same main magnetic field. Because the shielding term is typically small ( $\sim 10^{-4}$ – $10^{-6}$ ), these frequency differences are small. It is more practical to

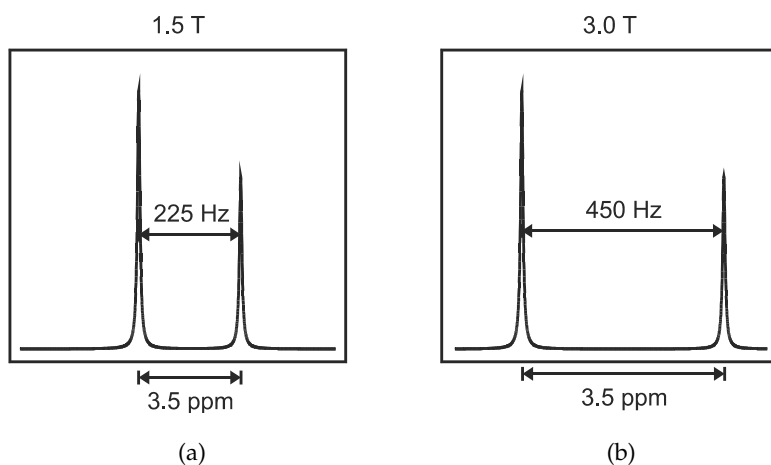
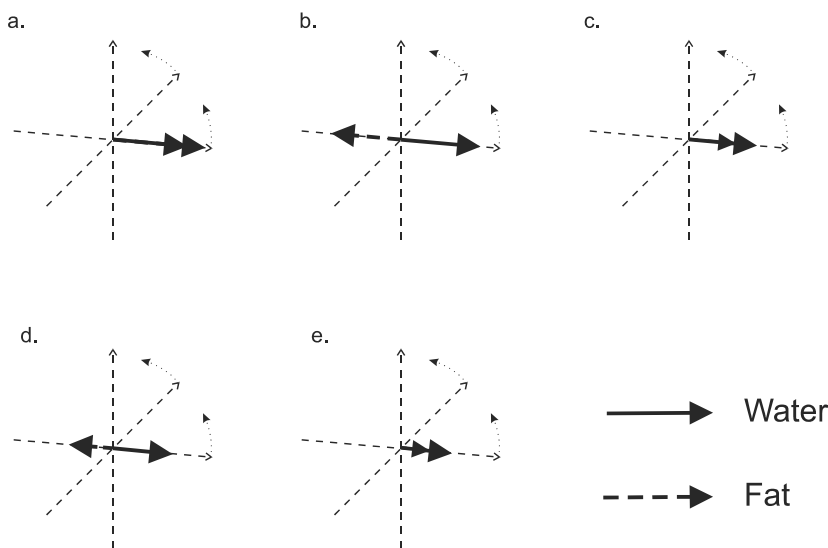


FIGURE 2-5 Spectrum of water and fat at 1.5 T (a) and 3.0 T (b). The resonant frequencies for water and fat are separated by approximately 3.5 ppm, which corresponds to an absolute frequency difference of 220 Hz for a 1.5 T magnetic field (63 MHz) or 450 Hz at a magnetic field of 3.0 T (126 MHz).

analyze the frequencies using these differences rather than using absolute terms. A convenient scale to express frequency differences is the ppm scale, which is the resonant frequency of the proton of interest relative to a reference frequency:

$$\omega_{i(\text{ppm})} = (\omega_{i(\text{Hz})} - \omega_{\text{ref}}) / \omega_{\text{ref}} \quad (2-4)$$

Frequency differences expressed in this form are known as chemical shifts. The choice of  $\omega_{\text{ref}}$  is arbitrary, but it is convenient to use  $\omega_{\text{TR}}$  as  $\omega_{\text{ref}}$ . The primary advantage of the ppm scale is that frequency differences are independent of  $B_0$ . For fat and water, the difference in chemical shifts at all field



**FIGURE 2-6** Precession of fat and water protons. Because of the 3.5 ppm frequency difference, a fat proton precesses at a slower frequency than a water proton. In a rotating frame at the water resonance frequency, the fat proton cycles in and out of phase with the water proton. Following the excitation pulse, the two protons are in phase (a). After a short time, they will be 180° out of phase (b), then in phase (c), then 180° out of phase (d), then in phase (e). The contribution of fat to the total signal fluctuates and depends on when the signal is detected. At 1.5 T, the in-phase times are 0 (a), 4.5 (c), and 9 (e) ms, whereas the out-of-phase times are 2.25 (b) and 6.7 (d) ms. At 3.0 T, the in-phase times are 0, 2.25 and 4.5 ms, whereas the out-of-phase times are 1.12 and 3.4 ms, respectively.

strengths is approximately 3.5 ppm, with fat at a lower frequency. At 1.5 T, this difference is 220 Hz, whereas at 3.0 T, it is 450 Hz (Figure 2-5).

The chemical shift difference between fat and water can be visualized in the rotating frame. A 150 Hz difference in frequency means that the fat resonance precesses slower than the water resonance by 6.7 ms per cycle ( $1/150$  Hz). The fat resonance will align with or be in phase with the water resonance every 6.7 ms at 1.0 T. For a 1.5 T MR system, the same cycling will occur every 4.5 ms ( $1/220$  Hz) and every 2.25 ms for a 3.0 T system (Figure 2-6). The 3.5 ppm chemical shift difference mentioned previously is an approximate difference. The fat resonance signal is a composite from all the protons within the fat molecule. The particular chemical composition (e.g., saturated versus unsaturated hydrocarbon chain, length of hydrocarbon chain) determines the exact resonant frequency for this composite signal. The 3.5 ppm difference applies to the majority of fatty tissues found in the body. Chemical shift differences between protons in different molecular environments provide the basis for MR spectroscopy, which is described in more detail in Chapter 13.

## RELAXATION

---

As mentioned in Chapter 2, the MR measurement can be analyzed in terms of energy transfer. Relaxation is the process by which protons release the energy that they absorbed from the rf pulse. Relaxation is a fundamental process in MR, as essential as energy absorption, and provides the primary mechanism for image contrast, as discussed in Chapter 7. In resonance absorption, rf energy is absorbed by the protons only when it is broadcast at the correct frequency. The additional energy disturbs the equilibrium arrangement of spins parallel and antiparallel to  $\mathbf{B}$ . Following excitation, relaxation occurs in which the protons release this added energy and return to their original configuration through naturally occurring processes. Although an individual proton absorbs the energy, relaxation times are measured for an entire sample and are statistical or average measurements. Relaxation times are measured for gray matter or cerebrospinal fluid as bulk samples rather than for the individual water or fat molecules within the organs. Two relaxation times can be measured, known as  $T_1$  and  $T_2$ . Both times measure the spontaneous energy transfer by an excited proton, but they differ in the final disposition of the energy.

### 3.1 $T_1$ RELAXATION AND SATURATION

The relaxation time  $T_1$  is the time required for the  $z$  component of  $\mathbf{M}$  to return to 63% of its original value following an excitation pulse. It is also known as the spin-lattice relaxation time or longitudinal relaxation time. Recall from Chapter 2 that  $\mathbf{M}_0$  is parallel to  $\mathbf{B}_0$  at equilibrium and that energy absorption will rotate  $\mathbf{M}_0$  into the transverse plane.  $T_1$  relaxation pro-

vides the mechanism by which the protons give up their energy to return to their original orientation. If a  $90^\circ$  pulse is applied to a sample,  $M_0$  will rotate as illustrated in Figure 2-2, and there will be no longitudinal magnetization present following the pulse. As time goes on, a return of the longitudinal magnetization will be observed as the protons release their energy (Figure 3-1). This return of magnetization follows an exponential growth process, with  $T_1$  being the time constant describing the rate of growth:

$$M(\tau) = M_0(1 - e^{(-\tau/T_1)}) \quad (3-1)$$

where  $\tau$  is the time following the rf pulse. After three  $T_1$  time periods,  $M$  will have returned to 95% of its value prior to the excitation pulse,  $M_0$ . The term spin lattice refers to the fact that the excited proton ("spin") transfers its energy to its surroundings ("lattice") rather than to another spin. The energy no longer contributes to spin excitation.

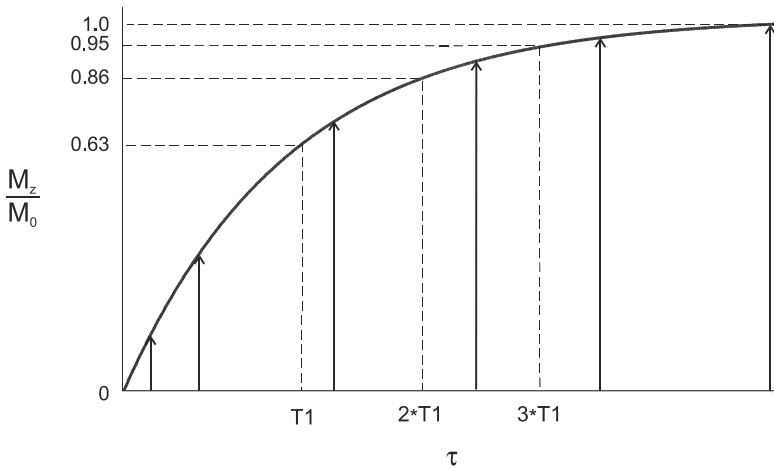


**FIGURE 3-1**  $T_1$  relaxation curve. Following a  $90^\circ$  rf pulse, there is no longitudinal magnetization. A short time later, longitudinal magnetization will be observed as the protons release their energy through  $T_1$  relaxation. Gradually, as more protons release their energy, a larger fraction of  $M_z$  is reestablished. Eventually,  $M_0$  will be restored completely. The change of  $M_z/M_0$  with time  $\tau$  follows an exponential growth process, as described by Equation 3-1. The time constant for this process is  $T_1$ , the spin-lattice relaxation time, and is the time when  $M_z$  has returned to 63% of its original value.

This energy transfer to the surroundings has some very important consequences. Suppose the rf energy is continuously applied at the resonant frequency so that no relaxation occurs. A comparison of the microscopic and macroscopic pictures is useful at this point. In the microscopic picture, the protons in the lower energy level absorb the rf energy, and the protons in the upper energy level are stimulated to emit their energy. Since energy is continuously transmitted, the proton populations of the two levels will gradually equalize. When this equalization occurs, no further net absorption of energy is possible, a condition known as saturation. In the macroscopic picture,  $\mathbf{M}$  will rotate continuously but gradually get smaller in magnitude until it disappears as the net population difference approaches zero. Since there is no net magnetization, there will be no coherence of proton motion in the transverse plane and thus no signal will be produced. This condition is known as saturation. There is a limited amount of energy that a collection of protons can absorb before they become saturated.

In a modern MR experiment, pulsed rf energy is applied to the protons repeatedly with a delay time between the pulses. This time between pulses allows the excited protons to give up the absorbed energy ( $T_1$  relaxation). As the protons give up this energy to their surroundings, the population difference (spin up versus spin down) is reestablished so that net absorption can reoccur after the next pulse. In the macroscopic picture,  $\mathbf{M}$  returns toward its initial value  $\mathbf{M}_0$  as more energy is dissipated. Since  $\mathbf{M}$  is the ultimate source of the MR signal, the more energy that is dissipated, the more signal that will be generated following the next rf pulse.

For practical reasons, the time between successive rf pulses is usually insufficient for complete  $T_1$  relaxation so that  $\mathbf{M}$  will not be completely restored to  $\mathbf{M}_0$ . Application of a second rf pulse prior to complete relaxation will rotate  $\mathbf{M}$  into the transverse plane, but with a smaller magnitude than following the first rf pulse. The following experiment describes the situation (Figure 3-2):

1. A  $90^\circ$  rf pulse is applied.  $\mathbf{M}$  is rotated into the transverse plane.
2. A time  $\tau$  elapses, insufficient for complete  $T_1$  relaxation. The longitudinal magnetization at the end of  $\tau$ ,  $\mathbf{M}'$ , is less than in step 1.

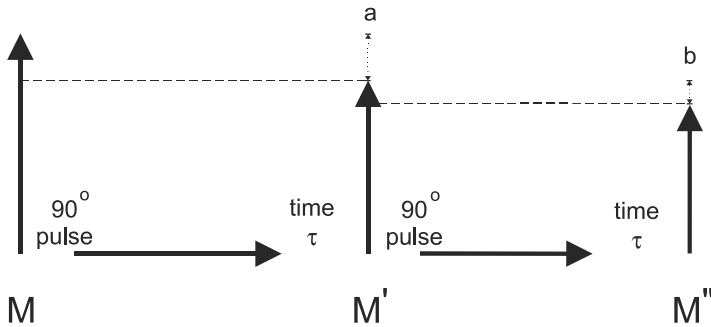


FIGURE 3-2 Following a  $90^\circ$  rf pulse, longitudinal magnetization is regenerated via  $T_1$  relaxation. If the time between successive rf pulses  $\tau$  is insufficient for complete recovery of  $M$ , then only  $M'$  will be present at the time of the next rf pulse (a). If time  $\tau$  elapses again, then only  $M''$  will be present (b).  $M''$  will be smaller than  $M'$ , but the difference will be less than the difference between  $M$  and  $M'$ .

3. A second  $90^\circ$  rf pulse is applied.  $M'$  is rotated into the transverse plane.
4. After a second time  $\tau$  elapses,  $M''$  is produced. It is smaller in magnitude than  $M'$ , but the difference is less than the difference between  $M$  and  $M'$ .

Following a few repetitions,  $M$  returns to the same magnitude prior to each rf pulse; i.e.,  $M$  achieves a steady-state value. In general, this steady-state value depends on five parameters:

1. The main magnetic field  $B_0$ . The larger the value for  $B_0$ , the larger  $M$ .
2. The number of protons producing  $M$  (per unit volume of tissue, known as the proton density).
3. The amount of energy absorbed by the protons (the pulse angle or flip angle).
4. The rate of rf pulse application (time  $\tau$ ).
5. The efficiency of the protons in giving up their energy ( $T_1$  relaxation time).

For many MRI experiments such as standard spin-echo and gradient-echo imaging, a steady state of  $M$  is present because multiple rf pulses are applied and the repetition time  $TR$  between the pulses is nearly always less than sufficient for complete relaxation. To produce this steady state prior to data collection, additional rf pulses are applied to the tissue immediately prior to the main imaging pulses. These extra rf pulses are known as preparatory pulses or dummy pulses because the generated signals are usually ignored. These preparatory pulses ensure that  $M$  has the same magnitude prior to every measurement during the scan.

As mentioned earlier, spin-lattice relaxation measures energy transfer from an excited proton to its surroundings. The key to this energy transfer is the presence of some type of molecular motion (e.g., vibration, rotation) in the vicinity of the excited proton with an intrinsic frequency,  $\omega_L$ , that matches the resonant frequency,  $\omega_0$ . The closer  $\omega_0$  is to  $\omega_L$ , the more readily the motion absorbs the energy and the more frequently this energy transfer occurs, allowing the collection of protons to return to its equilibrium configuration sooner. In tissues, the nature of the protein molecular structure and any metal ions that may be present have a pronounced effect on the particular  $\omega_L$ . Metals ions such as iron or manganese can have significant magnetic moments that may influence the local environment. Although the particular protein structures are different for many tissues, the molecular rotation or tumbling of most proteins typically have  $\omega_L$  approximately 1 MHz. Therefore, at lower resonant frequencies (lower  $B_0$ ), there is a better match between  $\omega_L$  and  $\omega_0$ . This enables a more efficient energy transfer to occur and thus  $T1$  is shorter. This is the basis for the frequency dependence of  $T1$ ; namely, that  $T1$  decreases with decreasing strength of the magnetic field. This is also the reason that a larger  $B_0$  does not necessarily translate to a greater signal, as saturation is more prevalent due to the longer  $T1$  times.

### **3.2 $T2$ RELAXATION, $T2^*$ RELAXATION, AND SPIN ECHOES**

The relaxation time  $T2$  is the time required for the transverse component of  $M$  to decay to 37% of its initial value via irreversible processes. It is also known as the spin-spin relaxation time or transverse relaxation time. Recall



from Chapter 1 that  $M_0$  is oriented only along the  $z$  ( $B_0$ ) axis at equilibrium and that no portion of  $M_0$  is in the  $xy$  plane. The coherence is entirely longitudinal. Absorption of energy from a  $90^\circ$  rf pulse, as in Figure 2-2, causes  $M_0$  to rotate entirely into the  $xy$  plane, so that the coherence is in the transverse plane at the end of the pulse. As time elapses, this coherence disappears, while at the same time the protons release their energy and reorient themselves along  $B_0$ . This disappearing coherence produces the FID described in Chapter 2. As this coherence disappears, the value of  $M$  in the  $xy$  plane decreases toward 0.  $T_2$  or  $T_2^*$  relaxation is the process by which this transverse magnetization is lost.

A comparison of the microscopic and macroscopic pictures provides additional insight. At the end of the  $90^\circ$  rf pulse, when the protons have absorbed energy and are oriented in the transverse plane, each proton precesses at the same frequency  $\omega_0$  and is synchronized at the same point or phase of its precessional cycle. Since a nearby proton of the same type will have the same molecular environment and the same  $\omega_0$ , it can readily absorb the energy that is being released by its neighbor. Spin-spin relaxation refers to this energy transfer from an excited proton to another nearby proton (Figure 3-3). The absorbed energy remains as spin excitation rather than being transferred to the surroundings as in  $T_1$  relaxation. This proton-proton energy transfer can occur many times as long as the protons are in close proximity and remain at the same  $\omega_0$ . Intermolecular and intramolecu-

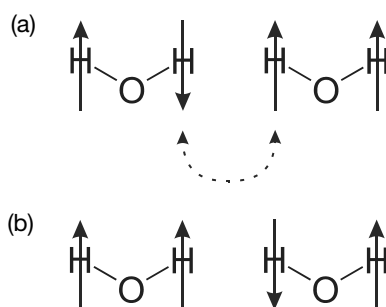


FIGURE 3-3 Spin-spin relaxation. (a) Two water molecules; one spin on one molecule has absorbed rf energy and is excited (spin down). (b) If the spins are in close proximity, the energy can be transferred from the first molecule to a spin on the second molecule.

lar interactions such as vibrations or rotations cause  $\omega_0$  to fluctuate. This fluctuation produces a gradual, irreversible loss of phase coherence to the spins as they exchange energy and reduce the magnitude of the transverse magnetization and the generated signal (Figure 3-4).  $T_2$  is the time when the transverse magnetization is 37% of its value immediately after the  $90^\circ$  pulse when this irreversible process is the only cause for the loss of coherence. As more time elapses, this transverse coherence completely disappears, only to reform in the longitudinal direction as  $T_1$  relaxation occurs. This dephasing time  $T_2$  is always less than or equal to  $T_1$ .

There are several potential causes for a loss of transverse coherence to  $M$ . One is the movement of the adjacent spins due to molecular vibrations or rotations. This movement is responsible for spin-spin relaxation or the true  $T_2$ . Another cause arises from the fact that a proton never experiences a magnetic field that is 100% uniform or homogeneous. As the proton precesses, it experiences a fluctuating local magnetic field, causing a change in  $\omega_0$  and a loss in transverse phase coherence. This nonuniformity in  $B_0$  comes from three sources:

1. Main field inhomogeneity. There is always some degree of nonuniformity to  $B_0$  due to imperfections in magnet manufacturing, composition of nearby building walls, or other sources of metal. This field distortion is constant during the measurement time.
2. Sample-induced inhomogeneity. Differences in the magnetic susceptibility or degree of magnetic polarization of adjacent tissues (e.g., bone, air) will distort the local magnetic field near the interface between the different tissues. This inhomogeneity is of constant magnitude and is present as long as the patient is present within the magnet.
3. Imaging gradients. As discussed in Chapter 4, the technique used for spatial localization generates a magnetic field inhomogeneity that induces proton dephasing. This inhomogeneity is transient during the measurement.

Proper design of the pulse sequence eliminates the imaging gradients as a source of dephasing. The other sources contribute to the total transverse relaxation time,  $T_2^*$ :

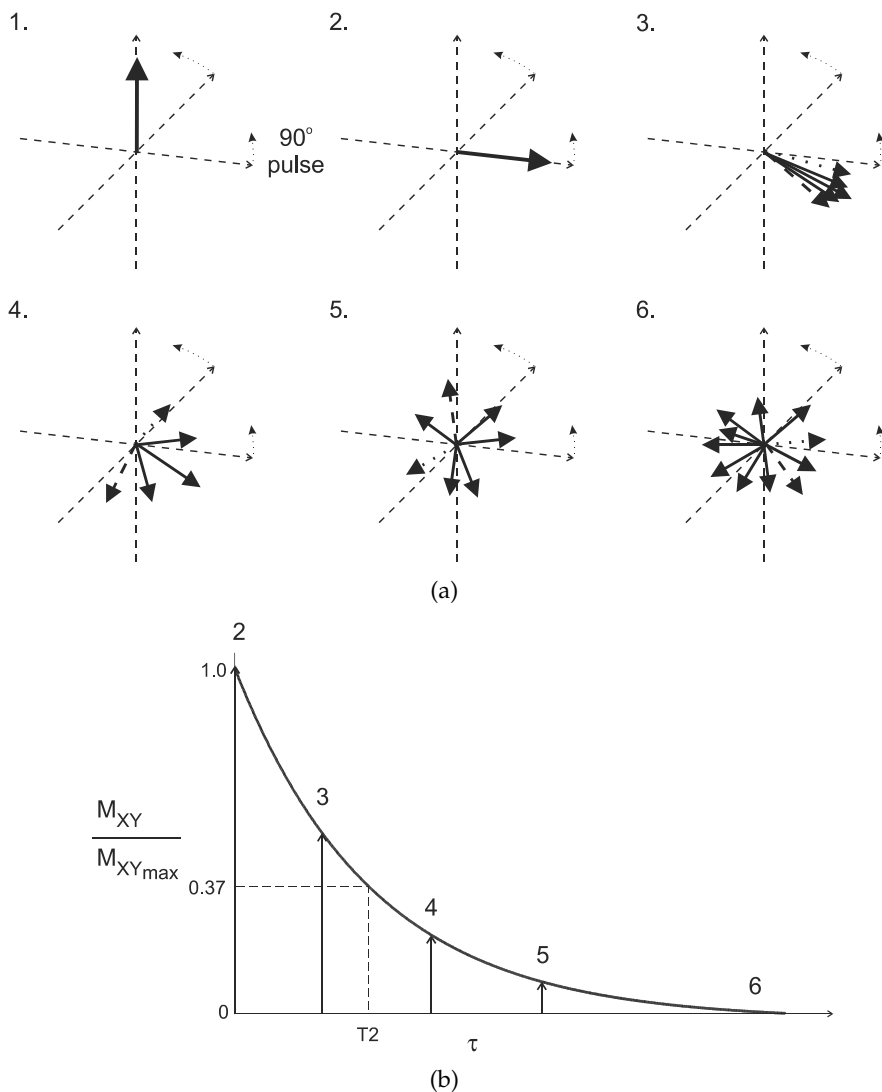


**FIGURE 3-4** (a) A rotating frame slower than  $\omega_0$  is assumed for this figure. Net magnetization  $M$  (arrow) is oriented parallel to  $B_0$  (not shown) prior to pulse (1). Following a 90° rf pulse, the protons initially precess in phase in the transverse plane (2). Due to inter- and intramolecular interactions, the protons begin to precess at different frequencies (dashed arrow—faster; dotted arrow—slower) and become asynchronous with each other (3). As more time elapses (4, 5), the transverse coherence becomes smaller until there is complete randomness of the transverse components and no coherence (6). (b) Plot of the relative  $M_{XY}$  component as a function of time. The numbers correspond to the expected  $M_{XY}$  component from Figure 3-3a. The change in  $M_{XY}/M_{XYmax}$  with time follows an exponential decay process as described by Equation 3-3. The time constant for this process is the spin-spin relaxation time  $T_2$  and is the time when  $M_{XY}$  has decayed to 37% of its original value.

$$1/T2^* = 1/T2 + 1/T2_M + 1/T2_{MS} \quad (3-2)$$

where  $T2_M$  is the dephasing time due to the main field inhomogeneity and  $T2_{MS}$  is the dephasing time due to the magnetic susceptibility differences. The decay of the transverse magnetization following a  $90^\circ$  rf pulse, the FID, follows an exponential process with the time constant of  $T2^*$  rather than just  $T2$ :

$$M_{XY}(t) = M_{XY\max} e^{(-t/T2^*)} \quad (3-3)$$

where  $M_{XY\max}$  is the transverse magnetization  $M_{XY}$  immediately following the excitation pulse. For most tissues or liquids,  $T2_M$  is the major factor in determining  $T2^*$ , whereas for tissue with significant iron deposits or air-filled cavities,  $T2_{MS}$  predominates  $T2^*$ .

Some sources of proton dephasing can be reversed by the application of a  $180^\circ$  rf pulse, which is described by the following sequence of events (Figure 3-5):

1. A  $90^\circ$  rf pulse
2. A short delay of time  $t$
3. A  $180^\circ$  rf pulse
4. A second time delay  $t$

The initial  $90^\circ$  rf pulse rotates  $M_0$  into the transverse plane. During the time  $t$ , proton dephasing will occur through  $T2^*$  relaxation processes and the transverse coherence will diminish. Application of the  $180^\circ$  rf pulse causes the protons to reverse their phases relative to the resonant frequency. The rates and directions of precession for the protons do not change, only their relative phase. If time  $t$  elapses again, then the protons will regain their transverse coherence. This reformation of phase coherence induces another signal in the receiver coil, known as a spin echo. Sources of dephasing that do not change during the two time periods—the main field inhomogeneity and magnetic susceptibility differences—are eliminated because the protons experience exactly the same interactions prior to and following the  $180^\circ$  pulse. This means that the contributions to  $T2^*$  relaxation from these static sources will disappear. Only the irreversible spin-spin relaxation is

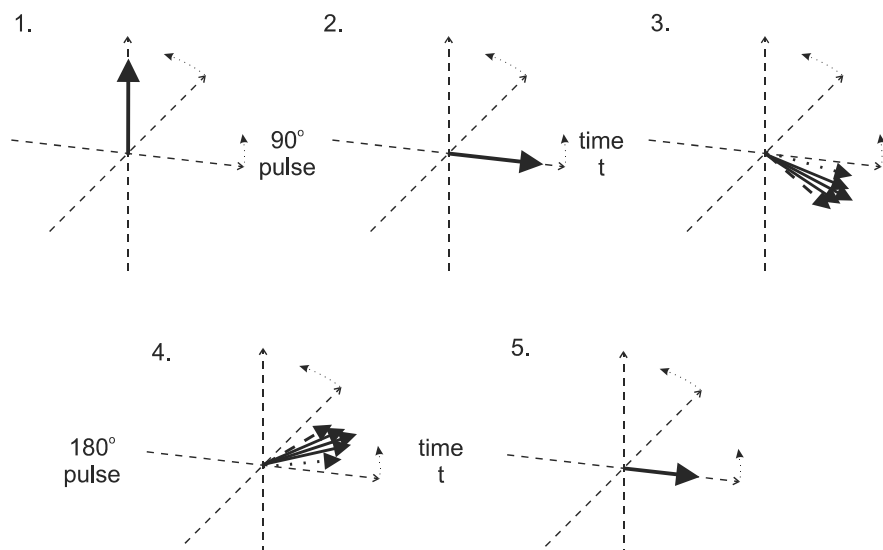


**FIGURE 3-5** A rotation frame slower than  $\omega_0$  is assumed for this figure. Net magnetization  $M$  (arrow) is oriented parallel to  $B_0$  (not shown) prior to pulse (1). Application of a  $90^\circ$  rf pulse rotates  $M$  into the transverse plane (2). Due to  $T2^*$  relaxation processes, the protons become asynchronous with each other during time  $t$  (3). Application of a  $180^\circ$  rf pulse causes the protons to reverse their phase relative to the transmitter phase. The protons that precessed most rapidly are farthest behind (dashed arrow), whereas the slowest protons are in front (dotted arrow) (4). Allowing time  $t$  to elapse again allows the protons to regain their phase coherence in the transverse plane (5), generating a signal in the receiver coil known as a spin echo. The loss in magnitude of the reformed coherence relative to the original coherence (2) is due to irreversible processes (i.e., true spin-spin or  $T2$  relaxation).

unaffected by the  $180^\circ$  rf pulse so that the loss of phase coherence and signal amplitude for a spin echo is due only to true  $T2$  relaxation.

Following the echo formation, the protons continue to precess and dephase a second time as the sources of dephasing continue to affect them. Application of a second  $180^\circ$  rf pulse again reverses the proton phases and generates another coherence to the protons, producing another spin echo. This second echo differs from the first echo by the increased amount of  $T2$  relaxation contributing to the signal loss. This process of spin echo formation by  $180^\circ$  rf pulses can be repeated as many times as desired, until  $T2$  relaxation completely dephases the protons. The use of multiple  $180^\circ$  pulses

maintains phase coherence to the protons longer than the use of a single  $180^\circ$  rf pulse because of the significant dephasing that the field inhomogeneity induces over very short time periods.

One important difference between  $T1$  and  $T2$  relaxation is in the influence of  $B_0$ . As mentioned earlier,  $T1$  is very sensitive to  $B_0$ , with longer  $T1$  times measured for a tissue at higher  $B_0$ .  $T2$  is relatively insensitive to  $B_0$  at the relatively large field strengths currently used in MRI. Only at very low  $B_0$  (less than 0.05 T) will there be significant changes in  $T2$ . The other components of  $T2^*$ — $T2_M$  and  $T2_{MS}$ —become more prominent at higher  $B_0$ . Good magnetic field uniformity is more difficult to generate at high magnetic fields, so that  $T2_M$  will be shorter. Greater  $B_0$  will also cause greater differences in  $M_0$  between two tissues with different magnetic susceptibilities, producing shorter  $T2_{MS}$ . The result is that  $T2$ -weighted techniques will see little sensitivity to  $B_0$ , whereas  $T2^*$ -weighted techniques will show greater signal differences at higher  $B_0$ .

# PRINCIPLES OF MAGNETIC RESONANCE IMAGING—PART 1

---

Chapter 2 described the relationship between the frequency of energy that a proton absorbs and the magnetic field strength that it experiences. MRI uses this field dependence to localize these proton frequencies to different regions of space. In MRI, the magnetic field is made spatially dependent through the application of magnetic field gradients. These gradients are small perturbations superimposed on the main magnetic field  $B_0$ , with a typical imaging gradient producing a total field variation of less than 1%. They are also linear perturbations to  $B_0$ , so that the exact magnetic field is linearly dependent on the location inside the magnet:

$$B_i = B_0 + G_T \otimes r_i \quad (4-1)$$

where  $B_i$  is the magnetic field at location  $r_i$  and  $G_T$  is the total gradient amplitude, mathematically represented as a tensor. Gradients are also applied for short periods of time during a scan and are referred to as gradient pulses.

In clinical MRI, the magnetic field gradients produce linear variations primarily in one direction only, so that the tensor product in Equation 4-1 can be reduced to a vector representation. Three physical gradients are used, one in each of the x, y, and z directions. Each one is assigned, through the operating software, to one or more of the three “logical” or functional

gradients required to obtain an image: slice selection, readout or frequency encoding, and phase encoding. The particular pairing of physical and logical gradients is somewhat arbitrary and depends on the acquisition parameters and patient positioning as well as the particular manufacturer's choice of physical directions. The combination of gradient pulses, rf pulses, data sampling periods, and the timing between each of them that are used to acquire an image is known as a pulse sequence.

The presence of magnetic field gradients requires an expanded version of the Larmor equation given in Equation 1-1:

$$\omega_i = \gamma(B_0 + \mathbf{G} \cdot \mathbf{r}_i) \quad (4-2)$$

where  $\omega_i$  is the frequency of the proton at position  $\mathbf{r}_i$  and  $\mathbf{G}$  is a vector representing the total gradient amplitude and direction. The dimensions of  $\mathbf{G}$  are usually expressed in millitesla per meter ( $\text{mT m}^{-1}$ ) or gauss per centimeter ( $\text{G cm}^{-1}$ ), where  $1 \text{ G cm}^{-1} = 10 \text{ mT m}^{-1}$ . Equation 4-2 states that, in the presence of a gradient field, each proton will resonate at a unique frequency that depends on its exact position within the gradient field. The MR image is simply a frequency and phase map of the protons generated by unique magnetic fields at each point throughout the image. The displayed image consists of digital picture elements (pixels) that represent volume elements (voxels) of tissue. The pixel intensity is proportional to the number of protons contained within the voxel weighted by the  $T_1$  and  $T_2$  relaxation times for the tissues within the voxel.

## 4.1 SLICE SELECTION

The initial step in MRI is the localization of the rf excitation to a region of space, which is accomplished through the use of frequency-selective excitation in conjunction with a gradient known as the slice selection gradient,  $G_{ss}$ . The gradient direction (x, y, or z) determines the slice orientation, whereas the gradient amplitude together with certain rf pulse characteristics determine both the slice thickness and slice position. A frequency-selective rf pulse has two parts associated with it: a central frequency and a nar-



row range or bandwidth of frequencies (typically 1–2 kHz) (see Chapter 5 for a more detailed description of selective pulses). When such a pulse is broadcast in the presence of the slice selection gradient, a narrow region of tissue achieves the resonance condition (Equation 4-2) and absorbs the rf energy. The duration of the rf pulse and its amplitude determines the amount of resulting proton rotation (e.g.,  $90^\circ$ ,  $180^\circ$ ). The central frequency of the pulse determines the particular location excited by the pulse when the slice selection gradient is present. Different slice positions are achieved by changing the central frequency. The slice thickness is determined by the gradient amplitude  $G_{SS}$  and the bandwidth of frequencies  $\Delta\omega_{SS}$  incorporated into the rf pulse:

$$\Delta\omega = \gamma\Delta(G_{SS} * \text{Thickness}) \quad [4-3]$$

Typically,  $\Delta\omega$  is fixed so that the slice thickness is changed by modifying the amplitude of  $G_{SS}$  (Figure 4-1). Thinner slices require larger  $G_{SS}$ . Once  $G_{SS}$  is determined by the slice thickness, the central frequency is calculated using

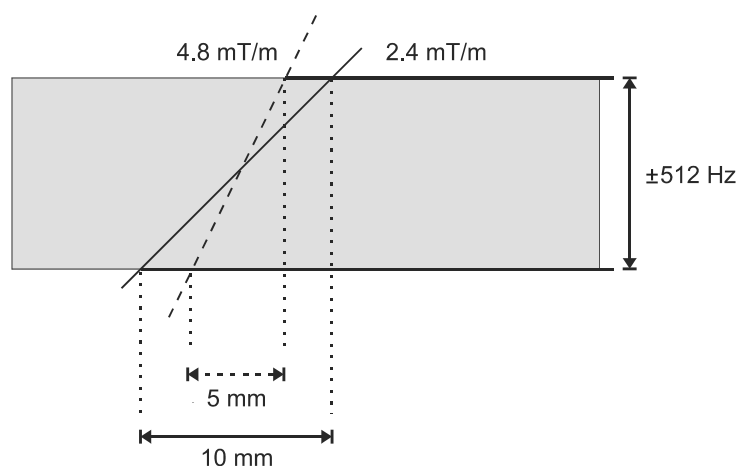


**FIGURE 4-1** For a given range (bandwidth) of frequencies included in the rf pulse, the desired slice thickness is determined by the slice selection gradient amplitude. The user interface typically allows variation of slice thickness, which is achieved by increasing or decreasing the slice selection gradient amplitude, as appropriate.

Equation 4-2 to bring the desired location into resonance. Multislice imaging, the most commonly used approach for MRI, uses the same  $G_{SS}$  but a unique rf pulse during excitation for each slice. Each rf pulse has the same bandwidth but a different central frequency, thereby exciting a different region of tissue (Figure 4-2).

The slice orientation is determined by the particular physical gradient or gradients defined as the logical slice selection gradient. The slice orientation is defined so that the gradient orientation is perpendicular or normal to the surface of the slice, so that every proton within the slice experiences the same total magnetic field regardless of its position within the slice. Orthogonal slices are those in which only the x, y, or z gradient is used as the slice selection gradient. Oblique slices, those not in one of the principal directions, are obtained by applying more than one physical gradient when the rf pulse is broadcast. The total gradient amplitude, whether from one, two, or three physical gradients, determines the slice thickness, as shown in Equation 4-3. When images are viewed on the monitor or film, the slice selection direction is always perpendicular to the surface, that is, hidden from the viewer (Figure 4-3).

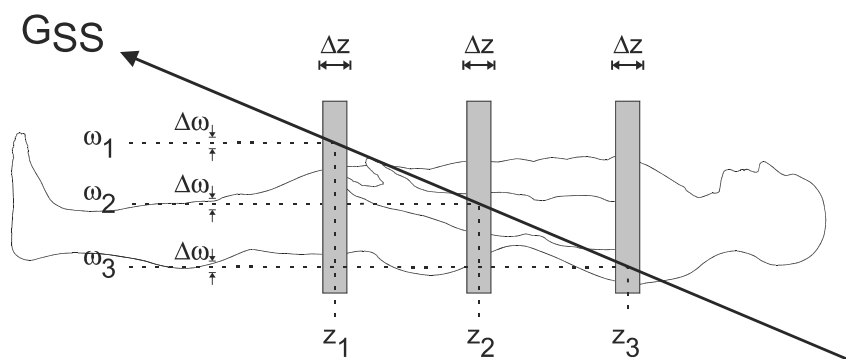


**FIGURE 4-2** Slice selection process. In the presence of a gradient ( $G_{SS}$ ), the total magnetic field that a proton experiences and its resulting resonant frequency depend on its position, according to Equation 4-2. Tissue located at position  $z_i$  will absorb rf energy broadcast with a center frequency  $\omega_i$ . Each position will have a unique resonant frequency. The slice thickness  $\Delta z$  is determined by the amplitude of  $G_{SS}$  and by the bandwidth of transmitted frequencies  $\Delta\omega$ .

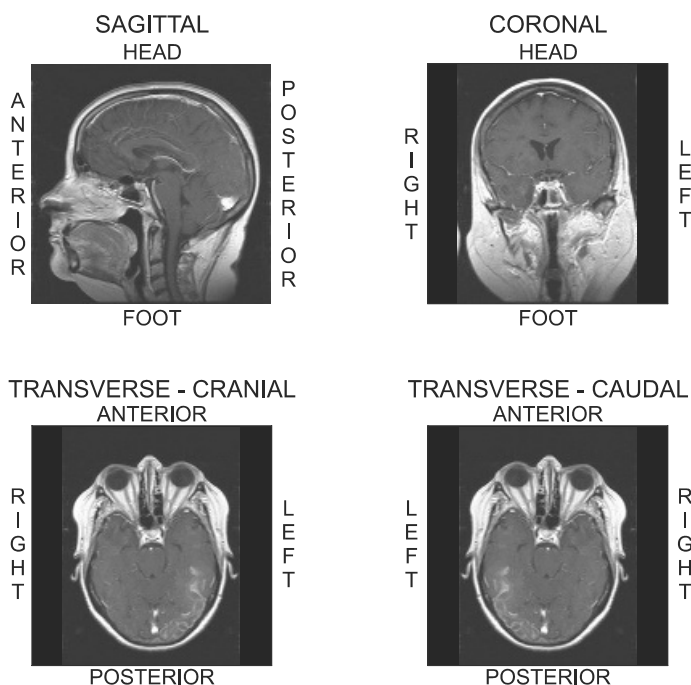


FIGURE 4-3 Images in standard slice directions: sagittal, coronal, and transverse or axial. For transverse images, two view directions are possible: cranial and caudal. Annotations are based on patient axes.

## 4.2 READOUT OR FREQUENCY ENCODING

The signal detection portion of the MRI measurement is known as the readout or frequency encoding. The readout process differentiates MRI from MR spectroscopy, the other type of MR process (see Chapter 13). In an imaging pulse sequence, the MR signal is always detected in the presence of a gradient known as the readout gradient  $G_{RO}$ , which produces one of the two visual dimensions of the image on the film. A typical pulse sequence uses some form of excitation, such as a  $90^\circ$  slice-selective pulse, to excite a particular region of tissue. Following excitation, the net magnetization within the slice is oriented transverse to  $B_0$  and will precess with frequency  $\omega_0$ .  $T2^*$  processes induce dephasing of this transverse magnetization (see Chapter 3). This dephasing can be partially reversed to form an echo by the application of a  $180^\circ$  rf pulse, a

gradient pulse, or both. As the echo is forming, the readout gradient is applied perpendicular to the slice direction. Under the influence of this new gradient field, the protons begin to precess at different frequencies depending on their position within it, in accordance with Equation 4-2. Each of these frequencies is superimposed into the echo. At the desired time, the echo signal is measured by the receiver coil and digitized for later Fourier transformation. The magnitude of  $G_{RO}$  ( $G_{RO}$ ) and the frequency that is detected enable the corresponding position of the proton to be determined (Figure 4-4).

The magnitude of  $G_{RO}$  is determined by two user-definable parameters: the field of view in the readout direction,  $FOV_{RO}$ , and the Nyquist frequency,  $\omega_{NQ}$ , for the image, often referred to as the receiver bandwidth (Equation 2-2). This relationship is expressed in Equation 4-4:

$$\Delta\omega_{RO} = 2 * \omega_{NQ} = \gamma\Delta(G_{RO} * FOV_{RO}) \quad (4-4)$$

where  $\Delta\omega_{RO}$  is the total range of frequencies in the image.  $G_{RO}$  is chosen so that protons located at the edge of  $FOV_{RO}$  precess at the Nyquist frequency for the image (Figure 4-5). Smaller  $FOV_{RO}$ s are achieved by increasing  $G_{RO}$ ,

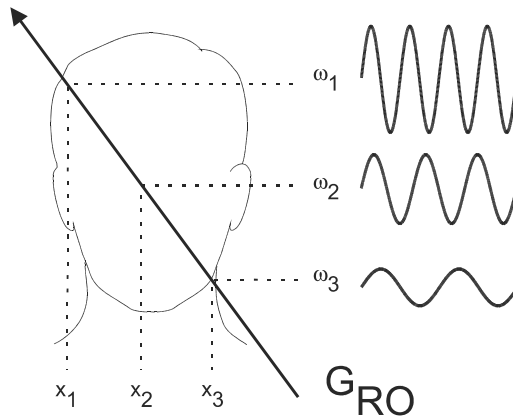


FIGURE 4-4 Readout process. Following excitation, each proton within the excited volume (slice) precesses at the same frequency. During detection of the echo, a gradient ( $G_{RO}$ ) is applied, causing a variation in the frequencies for the protons generating the echo signal. The frequency of precession  $\omega_i$  for each proton depends upon its position  $x_i$ , according to Equation 4-2. Frequencies measured from the echo are mapped to the corresponding position.

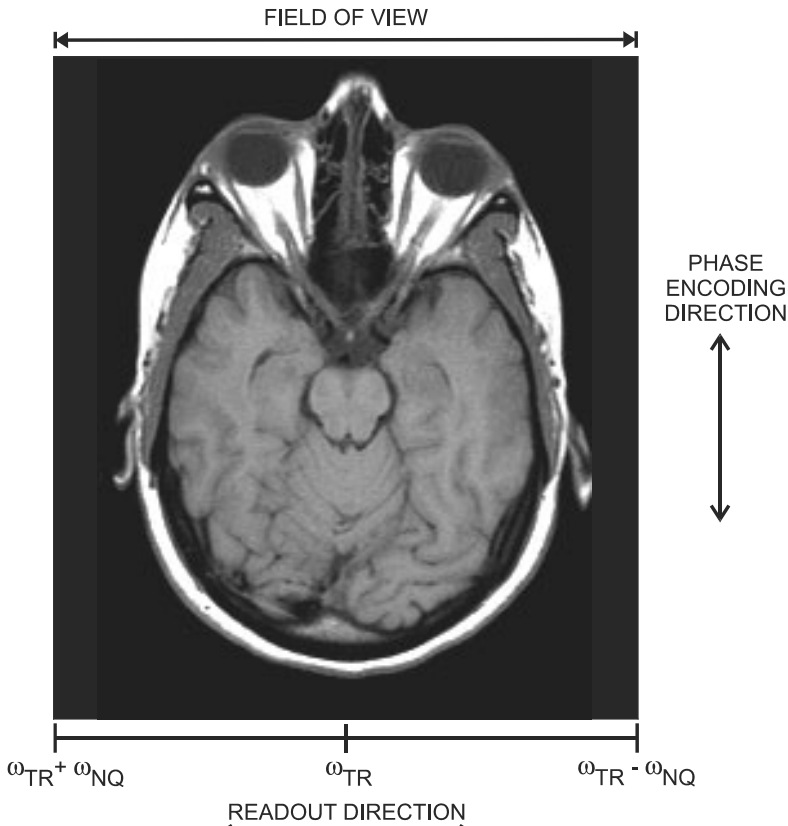


FIGURE 4-5 In any image, one of the visualized directions is the readout direction and the other is the phase-encoding direction. A proton located at the edge of the FOV in the readout direction precesses at the Nyquist frequency  $\omega_{NQ}$  above or below the transmitter frequency  $\omega_{TR}$ . Changing the FOV of the image changes the spatial resolution (mm per pixel) but not the frequency resolution (Hz per pixel).

keeping the Nyquist frequency and thus the total frequency bandwidth constant (Figure 4-6).

In an MR image, the resolution may be expressed in one of two ways: spatial resolution or frequency resolution. The spatial resolution, expressed as the voxel size with units of mm/pixel, is derived from two user parameters:  $FOV_{RO}$  and the number of readout sample points in the acquisition matrix,  $N_{RO}$ :

$$VOX_{RO} = FOV_{RO}/N_{RO} \quad (4-5)$$

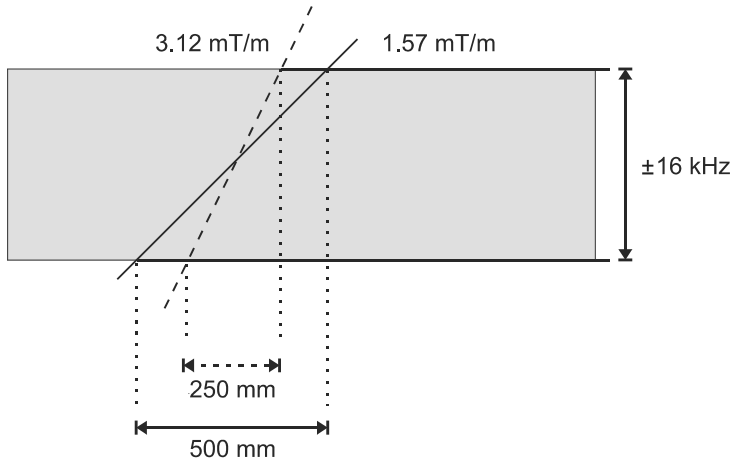


FIGURE 4-6 For a given range (bandwidth) of frequencies that are measured in the signal, the desired *FOV* is determined by the readout gradient amplitude. The user interface typically allows variation of the *FOV*, which is achieved by increasing or decreasing the readout gradient amplitude, as appropriate.

The frequency resolution, with units of Hz/pixel, is based on  $N_{RO}$  and the total bandwidth  $\Delta\omega_{RO}$  for the image:

$$\text{Pixel bandwidth} = \Delta\omega_{RO}/N_{RO} = 2 * \omega_{NQ}/N_{RO} \quad (4-6)$$

It is possible to improve the frequency resolution for the measurement independent of the spatial resolution by increasing the total sampling time used to measure the signal. This reduces the Nyquist frequency for the image and the background noise contributing to the measurement. In order to maintain the correct spatial resolution within the image,  $G_{RO}$  is reduced, in accordance with Equation 4-4.

### 4.3 PHASE ENCODING

The third direction in an MR image is the phase encoding direction. It is visualized along with the readout direction in an image (see Figure 4-5). The phase encoding gradient,  $G_{PE}$ , is perpendicular to both  $G_{SS}$  and  $G_{RO}$  and is the only gradient that changes amplitude during the data acquisition loop

of a standard two-dimensional (2D) imaging sequence. Any signal amplitude variation detected from one acquisition to the next is assumed to be caused by the influence of  $G_{PE}$  during the measurement.

The principle of phase encoding is based on the fact that the proton precession is periodic in nature. Prior to the application of  $G_{PE}$ , a proton within a slice precesses at the base frequency  $\omega_0$ . In the presence of  $G_{PE}$ , its precessional frequency increases or decreases according to Equation 4-2. Once  $G_{PE}$  is turned off, the proton precession returns to its original frequency, but is ahead or behind in phase relative to its previous state. The amount of induced phase shift depends on the magnitude and duration of  $G_{PE}$  that the proton experienced and the proton location. Protons located at different positions in the phase encoding direction experience different amounts of phase shift for the same  $G_{PE}$  pulse (Figure 4-7). A proton located at the edge of the chosen  $FOV$  experiences the maximum amount of phase shift from each phase encoding step. The MR image information is obtained by repeating the slice excitation and signal detection multiple times, each with a different amplitude of  $G_{PE}$ . The second Fourier transformation in the image converts signal amplitude at each readout frequency from a function of  $G_{PE}$  to a function of phase.

The spatial resolution in the phase-encoding direction depends on two user-selectable parameters: the field of view in the phase encoding direction  $FOV_{PE}$ , and the number of phase encoding steps in the acquisition matrix,  $N_{PE}$ . The  $FOV_{PE}$  is determined by the change in  $G_{PE}$  from one step to the next. For a proton located at the chosen  $FOV_{PE}$ , each phase-encoding step induces one-half cycle ( $180^\circ$ ) of phase change relative to the previous phase encoding step, assuming a constant pulse duration (Figure 4-8).  $N_{PE}$  determines the total number of cycles of phase change ( $N_{PE}/2$ ) produced at the edge of the  $FOV$  and thus the maximum frequency ( $\omega_{NQ}$ ) in the phase encoding direction for the given pulse duration. The spatial resolution in the phase-encoding direction is expressed as the voxel size and is measured in mm/pixel:

$$VOX_{PE} = FOV_{PE}/N_{PE} \quad (4-7)$$

Increased resolution is obtained by reducing the  $FOV_{PE}$  or by increasing  $N_{PE}$ . The  $FOV$  reduction is accomplished by increasing the gradient amplitude change from one  $G_{PE}$  to the next.

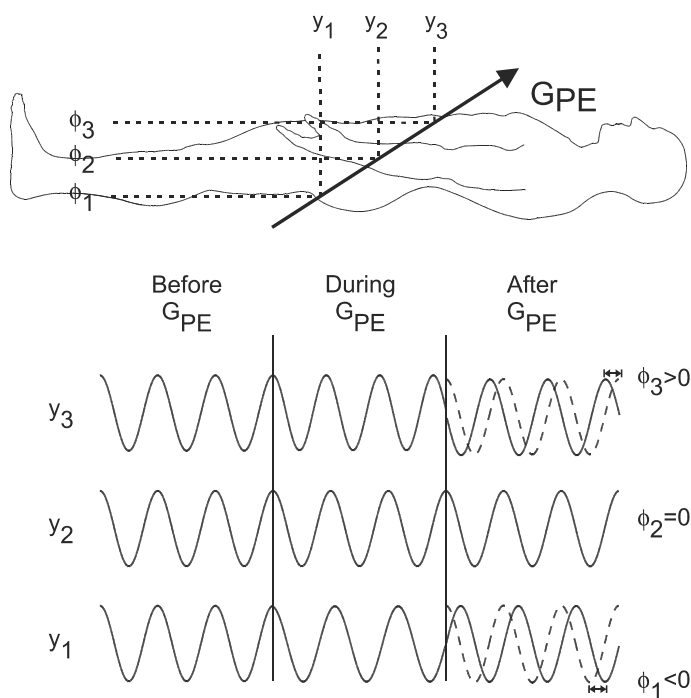


**FIGURE 4-7** Concept of phase encoding. Prior to application of  $G_{PE}$ , all protons precess at the same frequency. When  $G_{PE}$  is applied, a proton increases or decreases its precessional frequency, depending on its position,  $y_i$ . A proton located at  $y_i = 0$  ( $y_2$ ) experiences no effect from  $G_{PE}$  and no change in frequency or phase ( $\phi_2 = 0$ ). A proton located at  $y_3$  precesses faster while  $G_{PE}$  is applied. Once  $G_{PE}$  is turned off, the proton precesses at its original frequency, but is ahead of the reference frequency (dashed curve); that is, a phase shift  $\phi_3$  has been induced in the proton by  $G_{PE}$ . A proton located at  $y_1$  decreases its frequency while  $G_{PE}$  is applied. Once  $G_{PE}$  is turned off, it precesses at its original frequency but is behind the reference by a phase shift of  $\phi_1$ .

Because of the two different physical processes involved, the *FOV* in the phase-encoding direction is not required to be the same as the *FOV* in the readout direction, nor is the voxel size. The ratio of  $VOX_{RO}$  to  $VOX_{PE}$  is known as the aspect ratio between the two dimensions. An aspect ratio of 1.0 (100%) means that the voxel size is the same in both directions, a situation referred to as isotropic resolution. An aspect ratio less than 1.0 (<100%) is referred to as anisotropic resolution, with  $VOX_{PE}$  typically larger than  $VOX_{RO}$ .



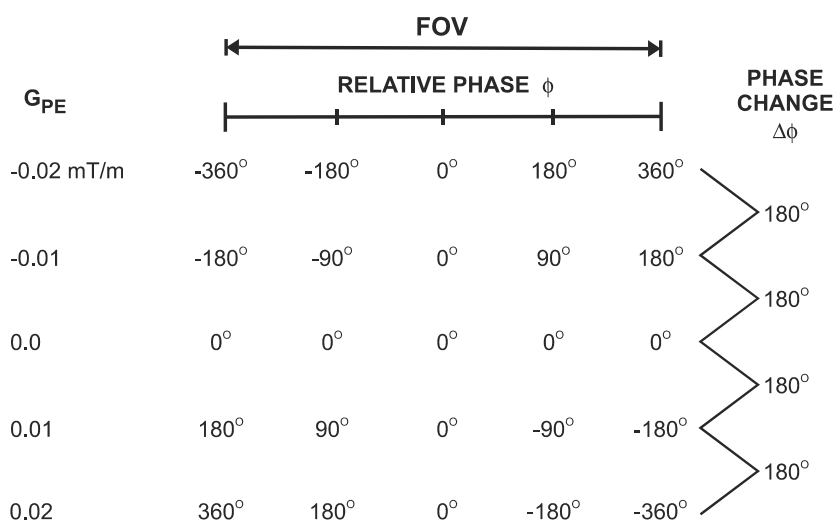


FIGURE 4-8 Phase-encoding process. A proton at the edge of the *FOV* in the phase-encoding direction undergoes 90° of phase change  $\Delta\phi$  from one phase encoding step to the next. Each point within the *FOV* undergoes progressively less phase change for the same gradient amplitude. A proton at the isocenter never experiences any phase change. The change in gradient amplitude (0.01 mT/m in this example) from one phase-encoding step to the next depends on the particular *FOV* chosen.

## 4.4 SEQUENCE LOOPING

The previous section described the individual steps used for spatial localization of the MR signal to a point within a slice. For most MR applications, information from many slices is measured during the scan in order to acquire images from large volumes of tissue. Several approaches are used for data acquisition that balance the desire for good spatial resolution and contrast-to-noise ratio (signal difference relative to background noise) while maintaining reasonable scan times.

In order to accomplish efficient data collection with minimal computer processing, most MRI techniques use some form of repetitive execution, which is achieved using computer instructions known as loops. This allows common instructions such as fixed amplitude gradient pulses (e.g., readout or slice selection gradient pulses) to be programmed one time yet provide a

convenient method for modifying variable quantities such as phase-encoding gradient amplitudes or rf pulse center frequencies.

Measurement techniques can be divided into 2D and 3D categories based on the volume of excited tissue that is used to generate the signal. The most common technique is 2D-multislice imaging, in which a narrow volume of tissue (typically < 10 mm) is excited by a slice-selective rf pulse and generates the echo signal. The  $TR$  specified by the user is the time between successive excitation pulses for a given slice. The total number of lines of data collected for each slice depends on the number of phase encoding steps,  $N_{PE}$ , and the number of signals added together for signal averaging,  $N_{SA}$ . The sequence kernel time or minimum  $TR$  per slice is the actual time required for the measurement hardware to perform all the steps necessary to acquire a line of raw data from a slice. In general, the sequence kernel time is much shorter than  $TR$ , allowing excitation and detection of many slices to be performed within one  $TR$  time period.

Traditionally, multislice scanning acquires one line of data from each slice during each  $TR$  time period (Figure 4-9a). This approach sets lower limits for  $TR$ . By subdividing the slice loop into subloops so that a subset of slices is acquired, shorter  $TR$  and greater contrast control are allowed. The total scan time is  $TR$  times the total number of lines times the number of subloops:

$$\text{Scan time}_{\text{multislice}} = TR * N_{SA} * N_{PE} * N_{\text{SUBLOOP}} \quad (4-8)$$

Two multislice loop structures are commonly used. Traditional multislice looping uses  $N_{\text{SUBLOOP}} = 1$  (Figure 4-9a), so that one line of data is acquired for each slice prior to measurement of a second line of data from any slice. The maximum number of slices is limited by  $TR$ . This provides the most efficient data collection process for a given  $TR$  and is useful when  $TR$  is relatively long. At the midpoint of a scan using this looping scheme, each image has  $N_{PE}$  lines of raw data, each with the requested number of acquisitions.

The other approach uses  $N_{\text{SUBLOOP}}$  equal to the number of slices (Figure 4-9b), a so-called sequential slice technique. In this technique, all information for a slice is acquired before acquiring any information for another slice. Only one line of data is measured during each  $TR$  time period. This al-

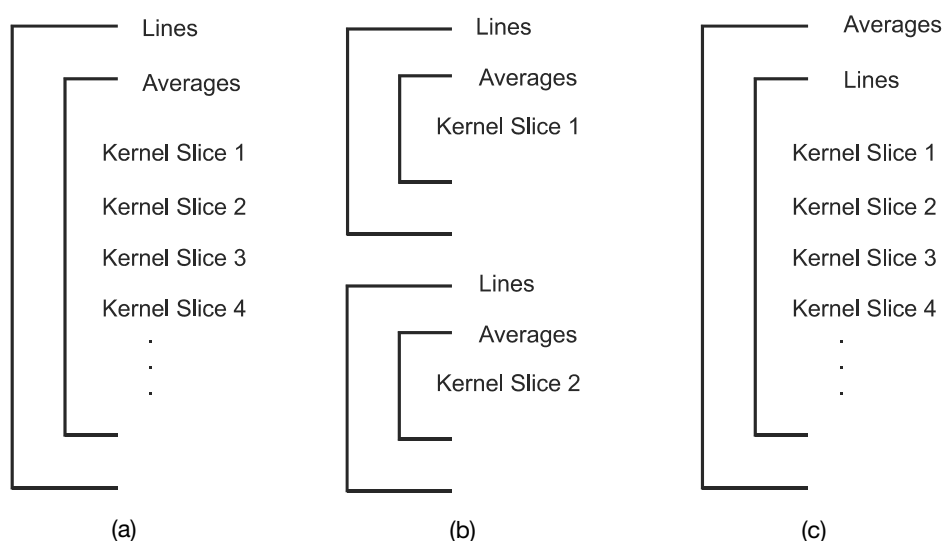


**FIGURE 4-9** Two-dimensional slice loop structures. Three slice loop structures are commonly used: (a) Traditional multislice looping. The slice loop is the inner-most loop ( $N_{\text{SUBLOOP}} = 1$  not indicated). Each slice is excited and the signal is detected prior to any slice being excited a second time for purposes of signal averaging or phase encoding (lines). This loop structure is the most common. (b) Sequential slice looping. All information for a given slice is acquired prior to any excitation for a different slice. In this figure,  $N_{\text{SUBLOOP}} = 2$ . (c) Long-term averaging. All lines for all slices are acquired before performing signal averaging.

lows the use of very short  $TR$  times when acquiring large numbers of slices. At the midpoint of a scan using this looping scheme, all the data for one-half the requested number of slices has been acquired.

There is also variability in the order of the main loops for a 2D multislice. Traditional looping as in Figure 4-9a acquires all signals for a specified phase-encoding step (all slices, all averages) before acquiring a signal for a different phase-encoding step. This allows all signal averaging for a given raw data line to be done within a short period of time and allows initial steps of image reconstruction to be performed. The other variation acquires a complete raw data set for a slice before beginning any signal averaging (Figure 4-9c). This increases the elapsed time between successive signals being averaged together, reducing any possible contamination between the signals, but renders the image more susceptible to gross patient motion.

The other category of measurement technique is 3D-volume acquisition, which is, in essence, a double phase-encoding technique. For 3D-volume imaging, tissue volumes of 30–150 mm are excited as compared to 3–10 mm in 2D imaging. In addition, a second phase-encoding table is applied in the slice selection direction to “partition” or subdivide the volume into individual slices. Each echo is acquired following application of encoding gradients in both the phase-encoding and slice-selection directions, one amplitude from each. For each excitation volume, the number of slices is determined by the number of partitions,  $N_{\text{PART}}$ . The total scan time is

$$\text{Scan time}_{3\text{D}} = TR * N_{\text{SA}} * N_{\text{PE}} * N_{\text{PART}} * N_{\text{SUBLOOP}} \quad (4-9)$$

The advantages of 3D-volume acquisition techniques are that the slices within a volume are contiguous and that the detected signal is based on the total volume excited rather than the effective slice thickness. 3D-volume acquisitions have two primary disadvantages. Because of the potentially long

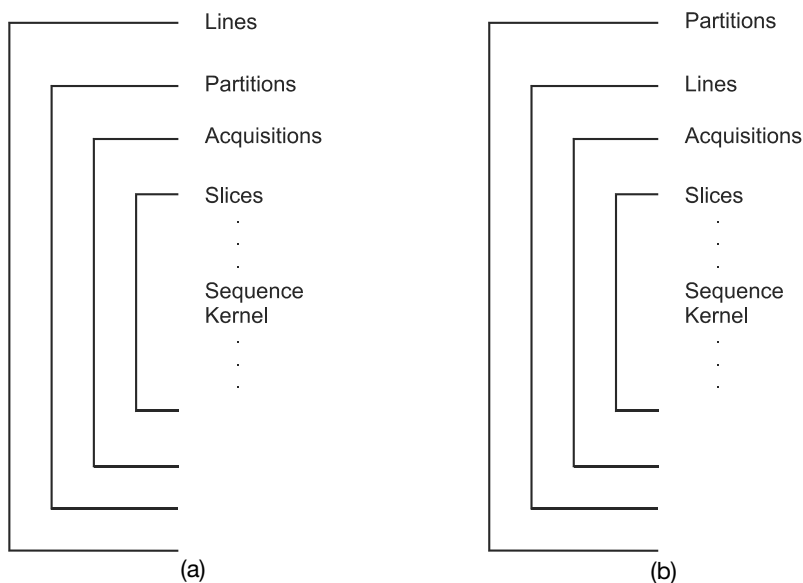


FIGURE 4-10 Three-dimensional slice loop structures. A fourth loop, the partitions loop, is added. Two slice loop structures are commonly used. (a) Partitions-in-lines: The partition gradient amplitudes are varied most frequently. (b) Lines-in-partitions. The line gradient amplitudes are varied most frequently.

scan times, they are usually gradient echo or echo train spin echo sequences and are limited to one or two volumes. Image processing is also longer since there are three Fourier transformations that must be performed in order to produce an image.

There are two possibilities for the order of the encoding loops. Traditional looping has the partitions loop inside the phase-encoding loop (Figure 4-10a), typical of 3D gradient echo techniques. Since the partitions loop normally has fewer entries, this enables initial image processing to be performed while data collection continues. The other order has the phase encoding loop inside the partitions loop (Figure 4-10b). This is more typical for 3D echo train spin echo, where the phase-encoding loop is segmented in nature (see Chapter 5).

## PRINCIPLES OF MAGNETIC RESONANCE IMAGING—PART 2

---

The basic steps for spatial localization of the MR signal were described in Chapter 4. These steps (slice selection, frequency and phase encoding, looping) are common features of nearly all MRI measurements. Although the descriptions in Chapter 4 are generally correct as presented, there are additional concepts that are integral to the process and must be considered in order to obtain an accurate understanding of MRI.

### 5.1 FREQUENCY-SELECTIVE EXCITATION

Chapter 2 presented the concepts of rf excitation and resonance absorption by protons. In MR, the rf energy is applied as pulsed excitation, with several features characterizing the pulse. When a pulse is applied, there will be a center frequency, duration, shape, phase, and amplitude defined. The center frequency of the pulse is normally chosen as the resonant frequency for the particular collection of protons under observation. The duration and shape of the pulse determine the bandwidth or range of frequencies on either side of the center frequency that are excited by the pulse. The phase of the pulse defines the effective orientation of the rf energy (see Figure 2-2) and determines the axis of rotation for the net magnetization under the influence of the pulse. The pulse amplitude or, more precisely, the pulse amplitude integral, determines the amount of rotation that the protons under-

go (flip angle). In addition, the pulse amplitude is related to the amount of energy that the protons absorb and therefore must dissipate through  $T_1$  relaxation. Pulses may be applied using amplitude modulation, in which the energy is distributed to all frequencies at the same time during the pulse, or using frequency modulation, in which frequencies are sequentially excited during application of the pulse. Regardless of the type of modulation, most MRI applications require uniform excitation of the frequencies encompassed by the rf pulse; that is, the rf pulse excites all frequencies equally within its selected range. This ensures that all protons within the excitation volume will have a common starting point in the detection process.

A common means of classification of rf pulses is by the pulse shape, referred to as the pulse envelope, that is broadcast, and the resulting bandwidth of frequencies that are excited by the pulse. The rf envelope consists of a time-varying set of complex data points, typically several hundred in number. These digital points are converted to an analog signal prior to mixing with the carrier frequency and broadcasting. Nonselective pulses, also known as rectangular or “hard” pulses, are of short duration and constant amplitude and excite a broad frequency range with a uniform amplitude. They are usually used to determine the resonant frequency of the patient. Nonselective pulses may also be used in a series of pulses applied in a very short time period, known as a composite pulse (see Chapter 8). Strictly speaking, “nonselective” pulses are frequency selective since the pulsed nature of the excitation limits the frequency bandwidth that can be incorporated into the pulse.

The other class of rf envelopes are frequency-selective or “soft” pulses. Frequency-selective pulses do not have constant amplitude at all times or at all frequencies during broadcast. The transmitter duration is longer than for a nonselective pulse, allowing for a narrower frequency bandwidth. In MRI, most rf pulses used are frequency-selective pulses because it is desirable to focus the excitation on narrow regions of tissue for most applications. The frequency bandwidth of the pulse determines the slice thickness, according to Equation 4-2, and the slice profile.

For standard slice-selective excitation pulses, uniform amplitude and phase excitation throughout the slice is necessary; that is, all the protons within the slice should be rotated the same amount and in the same direc-

tion. This is easiest to accomplish using an amplitude-modulated pulse of short duration. For a pulse to excite a particular frequency, that frequency must be included within its bandwidth. As more frequencies at the same phase are included in a pulse, the amplitude variations as a function of time (the pulse shape) approach a function known as a sinc function, an infinite function that contains all possible frequencies (Figure 5-1). Due to the short duration of the pulse and its limited bandwidth (the pulse bandwidth is inversely related to its duration), the actual pulse shape used for slice selective pulses is a truncated sinc function. This truncation causes the frequency cutoff to be less than ideal and has two important consequences: frequencies outside the desired bandwidth are excited as well as those within the bandwidth, and the dropoff of the excitation, known as the pulse profile, is not rectangular but has sloped sides. The extraneous excitation can be mini-

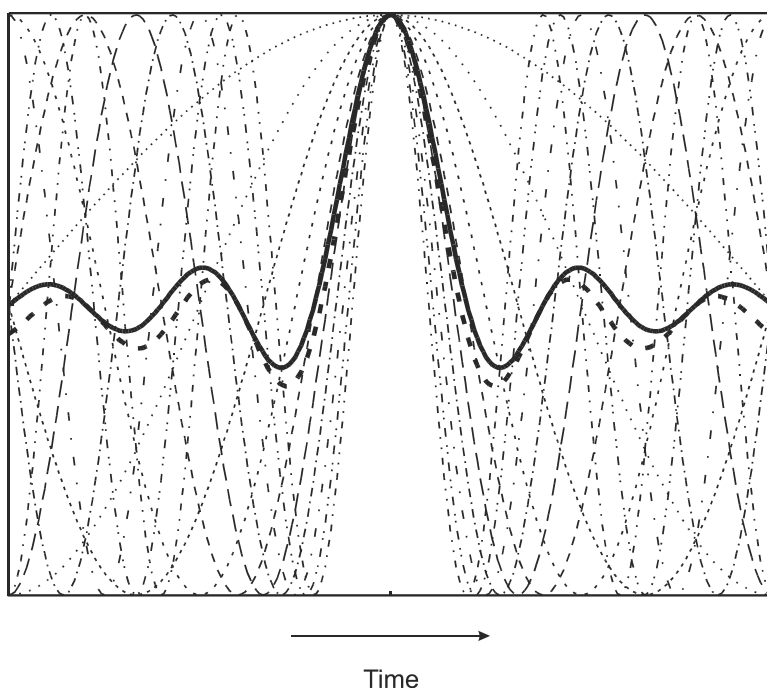


**FIGURE 5-1** A series of sine waves of different frequencies, all in phase at one point in time, sum to give an approximation (broken dark line) to an infinite sinc function (solid dark line).



mized by filtering the sinc function or mathematically forcing it to zero at the edges. This reduces the total power contained within the pulse, but accentuates the sloped nature of the pulse profile (Figure 5-2).

The response of the protons to pulsed excitation is complicated and requires the use of linear response theory for a complete description, which is beyond the scope of this book. However, in general, amplitude-modulated rf excitation pulses are subject to two competing criteria:

1. Short duration pulses require high peak pulse amplitudes to achieve the same pulse area (flip angle). Depending on the particular rf amplifier and transmitter coil, the maximum power that can be broadcast is limited.
2. Sinc functions produce rectangular, phase-coherent excitation profiles only with low flip angles ( $<30^\circ$ ). High amplitude pulses such as  $90^\circ$  or  $180^\circ$  pulses have excitation profiles that are significantly nonrectangular. Manufacturers strive to provide uniform excitation profiles, subject to criterion 1. Specific questions about particular rf pulse profiles should be addressed to the individual manufacturer.

Two additional rf profiles are used for specific applications. Gaussian pulses are often used for frequency-selective saturation pulses such as fat suppression or magnetization transfer suppression due to a narrower exci-

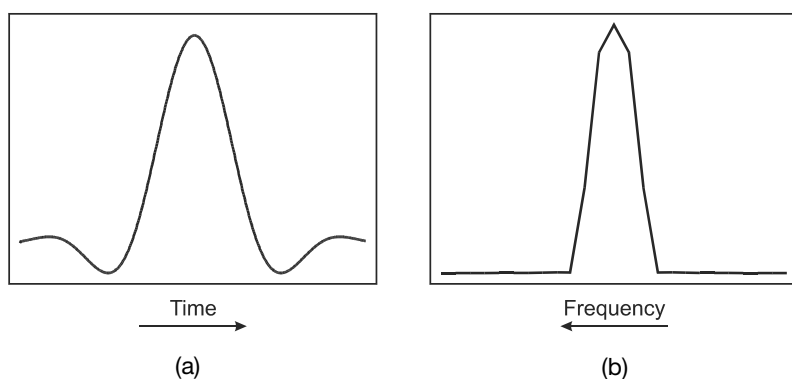


FIGURE 5-2 A truncated sinc excitation pulse and the corresponding excitation profile.

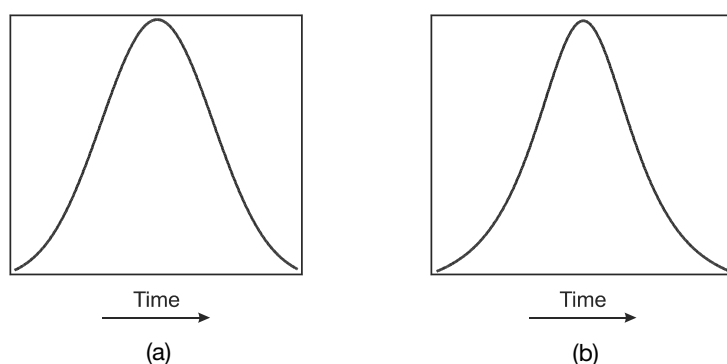


FIGURE 5-3 Other common rf pulse shapes. The horizontal and vertical scales are equal in both graphs. (a) Gaussian function, typically used for frequency-selective saturation pulses (fat saturation, magnetization transfer suppression). (b) Hyperbolic secant, often used for inversion pulses.

tation bandwidth (see Chapter 7). These pulses have excitation profiles that follow a Gaussian shape, which is narrower than the sinc function. Another pulse shape is known as the hyperbolic secant. This pulse is usually applied as a frequency- or phase-modulated adiabatic pulse and produces  $180^\circ$  inversion pulses with very uniform frequency profiles at low transmitter amplitude levels. Hyperbolic secant pulses are often used in inversion recovery sequences (see Chapter 6), but they have phase variations that make them unsuitable for use as a refocusing pulse. Figure 5-3 illustrates these pulse shapes.

## 5.2 RAW DATA AND IMAGE DATA MATRICES

In analyzing measured MRI data, two formats for the data may be used: raw data and image data. Both data sets contain the same information from the slice or slices and both formats are used for different purposes. They are stored and manipulated as a grid or matrix of points representing the slice. The two formats are related by the Fourier transformation, with the raw data being the format used in the data collection process and the image data being the format normally used for viewing and interpretation.

In MRI, the raw data consists of the digitized data measured for a given echo from a given slice or volume of tissue. Whether an analog or digital re-

ceiver is used (see Chapter 14), each echo signal amplitude measured by the receiver coil is digitized as a function of time and converted into a complex format. The digital form of the signal is stored as a complex data array with each signal point represented by real and imaginary values. For the raw data matrix, the detected signal amplitudes for a given echo correspond to a row and each row differs by the value of  $G_{PE}$  applied prior to detection. The rows are typically displayed in order of increasing phase-encoding amplitudes from top to bottom, corresponding to maximum negative to maximum positive amplitudes. The raw data matrix is thus a grid of points with the readout direction displayed in the horizontal direction and the phase-encoding direction displayed in the vertical direction. Its dimensions depend on the number of readout data points  $N_{RO}$  and the number of phase-encoding steps  $N_{PE}$  for the scan (Figure 5-4).

The image data or display matrix is obtained via the 2D Fourier transformation (rows and columns) of the complex raw data matrix. The image matrix is a complex frequency and phase map of the proton signal intensity from a volume element weighted by the  $T_1$  and  $T_2$  values of the tissues con-

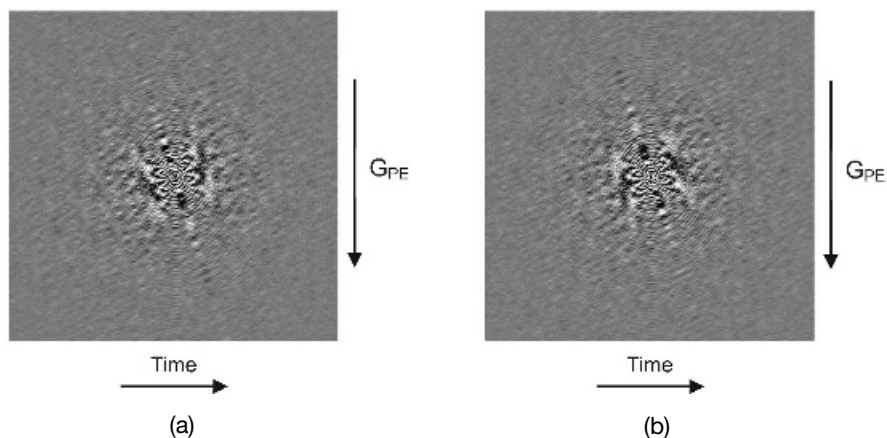


FIGURE 5-4 Raw data, real (a) and imaginary (b). The raw data matrix has dimensions of  $N_{PE} * N_{RO}$ . Each row is a measured signal at a particular  $G_{PE}$ . The number of rows corresponds to  $N_{PE}$ . Signals acquired with high negative amplitude  $G_{PE}$  are displayed at the top, low amplitude  $G_{PE}$  in the middle, and high positive amplitude  $G_{PE}$  at the bottom of the matrix. Each column corresponds to a data point sampled at a different time following the excitation pulse.

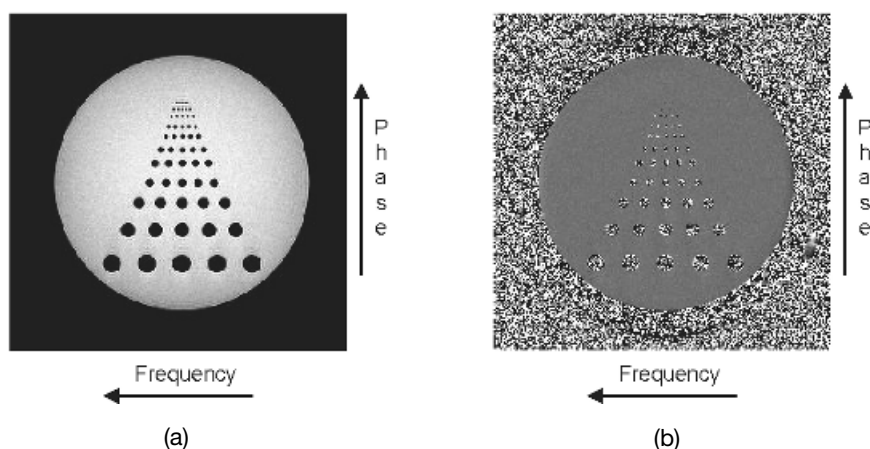


FIGURE 5-5 Image data, magnitude (a) and phase (b). The image data is obtained by performing a 2D Fourier transformation on the data set displayed in Figure 5-4a. The rows and columns correspond to the phase-encoding and readout directions. The specification of rows and columns as readout and phase-encoding directions up to the operator.

tained within the volume. The specific frequencies and phases are unique to the location of the volume element and are measured relative to the base transmitter frequency. Rather than viewing images as complex arrays, the displayed image matrix is normally an array of real or integer values, consisting either of the signal magnitudes or the relative phases at each point. Although they must be the same dimension as the raw data matrix, image matrices are usually displayed as square arrays with readout as one direction and phase encoding as the other direction in the image (Figure 5-5). The choice of rows and columns for readout and phase encoding is at the operator's discretion and is normally made to minimize artifacts in the area of interest. The maximum dimensions in the displayed image matrix normally correspond to the chosen *FOV* in each direction.

### 5.3 RAW DATA AND *K* SPACE

All the information necessary to reconstruct an image is contained within the raw data matrix. Although each data point contributes to all aspects (frequency, phase, and amplitude) of every location within the slice, some data

points emphasize different features in the final image. The maximum signal content is located in the central portion of the raw data matrix. These lines are acquired with low-amplitude  $G_{PE}$  and the measured signal amplitude variations are predominantly due to differences in the inherent tissue signals. These lines are primarily responsible for the contrast in the image. The outer portions of the raw data matrix have relatively low signal amplitude and are acquired with either high positive amplitude or high negative amplitude  $G_{PE}$ . These gradients produce high frequencies (by the Larmor equation) and provide mainly edge definition to the resultant image (Figure 5-6).

An alternate way to describe the raw data matrix is called the  $k$  space formalism. In this approach, the complex array of raw data points is treated as a two-dimensional grid of points  $(k_x, k_y)$ , where each  $k_x$  value corresponds to a different complex time point in the readout direction and each  $k_y$  value corresponds to a different phase-encoding gradient amplitude. Each  $(k_x, k_y)$  data point corresponds to the echo signal amplitude influenced by the combination of readout and phase encoding gradient areas (gradient pulse duration \* gradient amplitude):

$$\begin{aligned} k_x &= \gamma G_{RO} t_{RO} \\ k_y &= \gamma G_{PE} t_{PE} \end{aligned} \quad (5-1)$$

where  $t_{RO}$ ,  $t_{PE}$  corresponds to the cumulative time in which the respective gradient is active. The total gradient influence at each  $(k_x, k_y)$  point in the matrix is different and unique. The point  $(0, 0)$ , referred to as the origin of  $k$  space, has the maximum amplitude in the raw data matrix ( $G_{PE} = 0$ , maximum data point of the echo signal). The  $k$  values are measured in units of  $\text{mm}^{-1}$  and are often referred to as spatial frequencies, in analogy with cyclical frequencies measured in units of  $\text{s}^{-1}$ . The change in  $k$  in each direction from point to point ( $\Delta k_x$  or  $\Delta k_y$ ) is inversely related to the  $FOV$  in that direction. Using  $k$  space terminology, contrast in the image is primarily determined by data in the center, whereas edge definition is primarily determined by data at the edges of  $k$  space. The  $k$  space formalism provides a convenient way to describe ordering methods to acquire raw data.

Two requirements for producing artifact-free images are that the raw data space be sampled continuously (no gaps in lines or columns) and with

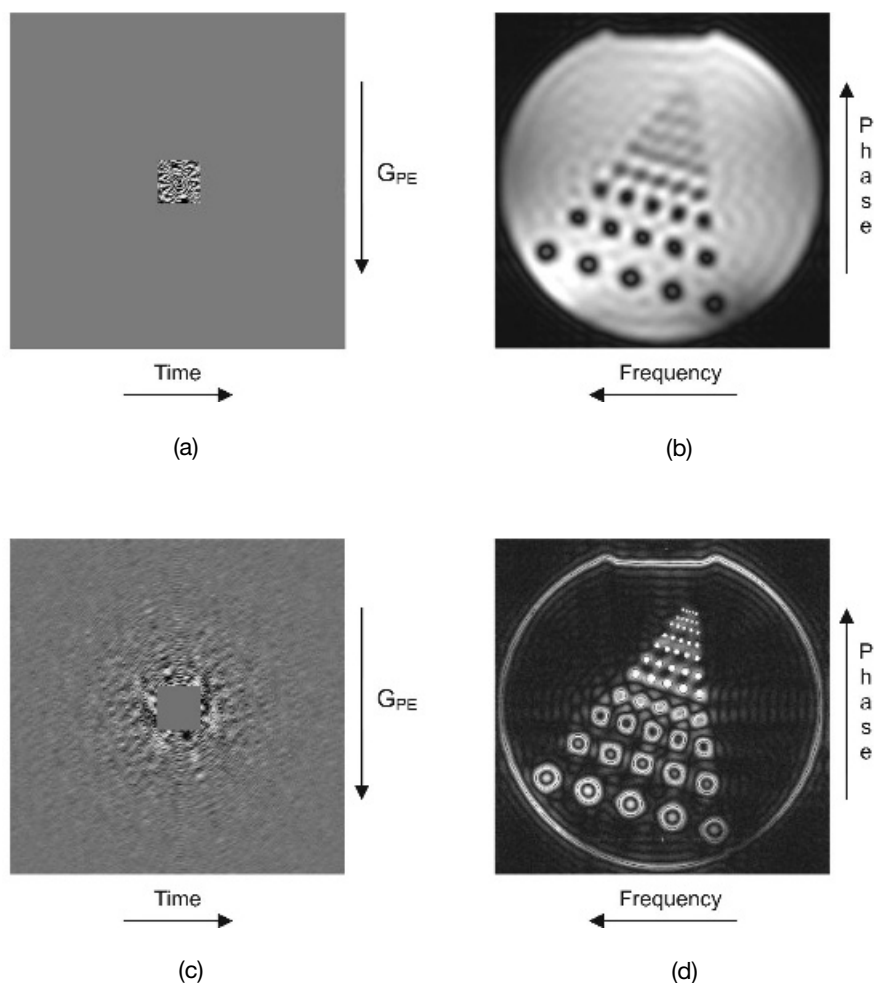
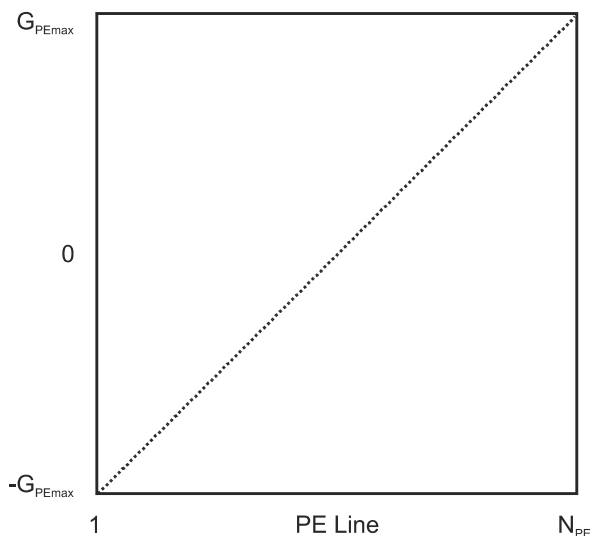


FIGURE 5-6 Raw data and corresponding images. (a) Same raw data set as in Figure 5-4, except that only the central  $32 \times 32$  data points are kept and zero values are defined for the remaining data. Imaginary portion not shown. (b) Magnitude image data of (a). The image intensity is approximately the same as in Figure 5-5a, but there is a loss of edge definition, exhibited as blurring in the phantom. (c) Same raw data set as Figure 5-5a, except the central  $32 \times 32$  data points are eliminated, corresponding to 1.56% of the total data set. Imaginary portion not shown. (d) Magnitude image data of (c). The image intensity (central portion of the phantom) is virtually absent, whereas the edges of the phantom are present.

a uniform density ( $\Delta k_x$  and  $\Delta k_y$  must be constant). This provides equal weight to both contrast and edge definition in the final image. These requirements may be accomplished in one of two ways. One approach, used in traditional scanning, involves rectilinear data collection. Each MR signal is measured in the presence of a constant amplitude  $G_{RO}$  with the same number of sample points measured at a constant rate (constant dwell time) and with the phase-encoding gradient  $G_{PE}$  changed by a constant increment ( $\Delta G_{PE}$ ) from line to line (Figure 5-7). When used with a complete set of  $G_{PE}$  lines, a raw data set is produced that fulfills both criteria. The other approach measures the raw data in a nonrectilinear fashion, then converts the raw data to a rectilinear form prior to Fourier transformation using a process known as regridding. Failure to obtain a gap-free raw data set or to regrid a nonrectilinear data set will produce images with potentially severe phase artifacts. Two important examples of nonrectilinear sampling are



**FIGURE 5-7** Sequential  $k$  space filling. Each line of  $k$  space (phase encoding line) corresponds to a measured MR signal. Lines of  $k$  space are acquired serially in time with the data from the maximum negative  $G_{PE}$  acquired first and the data from the maximum positive  $G_{PE}$  acquired last. The center of  $k$  space ( $G_{PE} = 0$  mT/m step) is acquired halfway through the data collection period. This is the traditional data collection method.

ramped and spiral sampling. Ramped sampling is a simple variation from the traditional rectilinear sampling. A normal gradient pulse consists of two amplitude-varying parts known as the ramps and a constant amplitude portion known as the plateau (see Chapter 6). If sampling of the echo occurs while the readout gradient amplitude is changing (ramped sampling), the effect of the gradient will not be uniform for each sample point of the echo ( $\Delta k_x$  will not be constant). Ramped sampling may be desired in order to obtain specific measurement parameters. Spiral  $k$  space sampling is a technique in which the  $k_x$  and  $k_y$  gradient amplitudes are both varied in a sinusoidal fashion during the echo sampling. This has the result of generating a raw data set that has data points forming a spiral.

A continuous raw data set must be acquired prior to Fourier transformation, but the order in which the individual lines are acquired is somewhat arbitrary. This filling order is also known as the  $k$  space trajectory. The traditional method for data collection is sequential filling or a linear trajectory. The raw data matrix is filled, one line at a time, with adjacent  $k_y$  lines acquired serially in time, beginning with the most negative  $G_{PE}$  and ending with the most positive  $G_{PE}$ . This method varies  $G_{PE}$  in a linear fashion and acquires the  $k_y = 0$  signal halfway through the data collection. Other methods for filling  $k$  space are used for special applications or when additional contrast control is required. Reordered  $k$  space refers to methods of data collection where the raw data are acquired in a nonsequential fashion. Centric ordering acquires the low-amplitude  $G_{PE}$  steps earliest in the scan and acquires the higher-amplitude  $G_{PE}$  steps later (Figure 5-8). Variations on sequential and centric ordering are possible, in which the center of the  $k$  space is acquired at other times of the scan. Another useful approach for data collection is the segmented method, in which successive echoes in the scan measure lines from different regions or segments of  $k$  space. Data are collected in a segment-serial fashion, one phase-encoding step from each segment. The number of segments, the number of lines per segment, and the order of segment acquisition may be independently varied (Figure 5-9), though the total number of measured lines will be the product of the number of lines per segment times the number of segments.

For 3D-volume scanning, the  $k$  space description requires the addition of a third dimension,  $k_z$ , corresponding to the partitions gradient mentioned



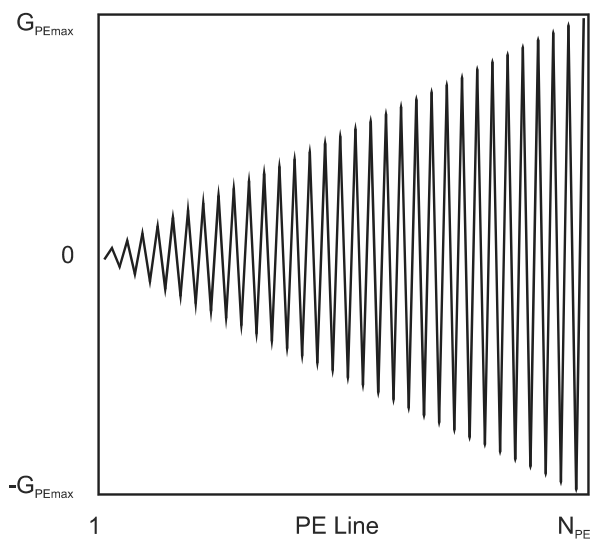


FIGURE 5-8 Centric  $k$  space filling. Lines of  $k$  space are acquired serially, beginning at the center of the  $k$  space, then in increasing  $G_{PE}$  amplitudes of alternating polarity.

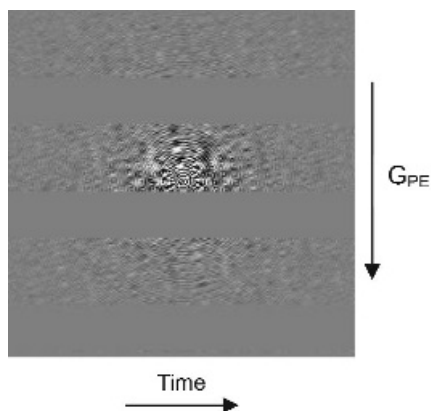


FIGURE 5-9 Raw data from segmented data collection. Lines of  $k$  space are acquired in groups or segments. The example here shows three segments. One line of data is acquired from each segment before a second line is acquired from any segment. The center of  $k$  space is acquired at a time dependent on the number of lines per segment, number of segments, and the order of acquisition within a segment and between segments.

in Chapter 4. In general, the principles discussed above for  $k$  space of 2D images are also true for 3D-volume scanning. The raw data space is a 3D volume defined with three coordinates ( $k_x$ ,  $k_y$ ,  $k_z$ ), analogous to the 2D volume defined by ( $k_x$ ,  $k_y$ ) described earlier. The change in  $k_z$  from step to step ( $\Delta k_z$ ) controls the distance of accurate measurement in the slice direction (typically matching the volume of rf excitation). The origin of the volume (0, 0, 0) contributes most to the contrast and the edges of the  $k$  volume contribute edge definition in the resulting images. The 3D looping structures illustrated in Figure 4-10 can be identified as the two ordering schemes for varying the  $k_y$  and  $k_z$  gradient amplitudes, either fixed  $k_z$ -varying  $k_y$  or fixed  $k_y$ -varying  $k_z$ , respectively. The continuity and uniform sampling density of the  $k$  volume are also necessary for artifact-free imaging. The two gradient tables ( $k_y$  and  $k_z$ ) are independent of each other and need not be varied in the same fashion. For example, one table may use sequential stepping while the other may use centric or segmented. Spiral scanning in 3D refers to the stepping order of the  $k_y$ - $k_z$  gradients, in which the two amplitude variations form a

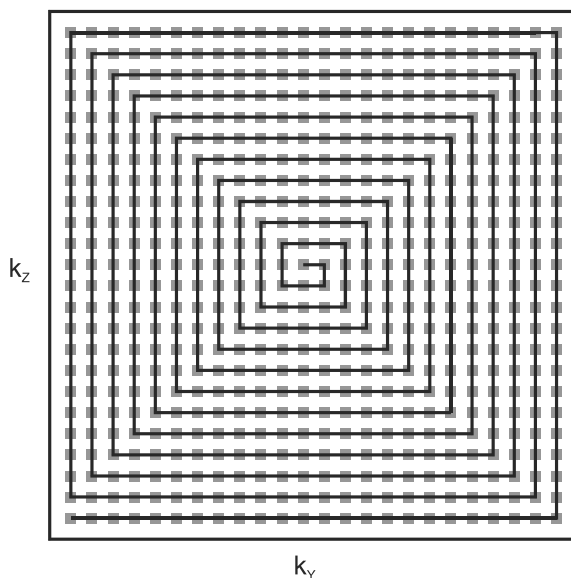


FIGURE 5-10 Spiral filling of 3D  $k$  space.  $k_y$  and  $k_z$  amplitudes are varied in an increasing spiral pattern. The lowest amplitude values are used to acquire the earliest echoes in the scan.

spiral (Figure 5-10). This approach is useful in acquiring the contrast-determining echoes early in the measurement, allowing control of tissue contrast or minimizing motion artifacts.

## 5.4 REDUCED $k$ SPACE ACQUISITIONS

The requirements for continuity and uniform density of the raw data matrix do not require that a complete raw data set be measured in order to produce artifact-free images. In fact, it is possible to acquire fewer echoes than necessary if they are properly distributed, which will reduce the total scan time. Several methods incorporate this concept. Two approaches reduce the total number of  $G_{PE}$  amplitudes symmetrically around  $G_{PE} = 0$ . The missing lines are replaced by zeros prior to Fourier transformation so that the final image matrix will be square. If the change in amplitude  $\Delta G_{PE}$  between successive steps is the same as for the “complete” raw data matrix, the  $FOV$  in the phase encoding direction will be the same in both images. This results in a loss of spatial resolution in the final image due to pixel interpolation from the Fourier transformation (Figure 5-11). If the  $\Delta G_{PE}$  is increased, the  $FOV$  in the phase-encoding direction will be reduced. This process regains the loss in spatial resolution due to the reduced number of lines, but reduces the area of accurate phase measurement, potentially causing aliasing artifacts.

A second method for reducing the number of measured raw data lines is known as partial Fourier imaging. Due to the usage of positive and negative polarity  $G_{PE}$  gradients, a symmetry to the raw data matrix is generated. This symmetry is known as Hermitian symmetry, with the negative amplitude  $G_{PE}$  gradients producing real signals with the same value as the imaginary signals generated by the positive amplitude  $G_{PE}$  gradients (Figure 5-12). The partial Fourier technique reduce the total number of  $G_{PE}$  amplitudes acquired for the raw data matrix but in an asymmetric fashion about the  $G_{PE} = 0$  line. The maximum amplitude  $G_{PE}$  and  $\Delta G_{PE}$  between each acquisition are the same as for a “full” acquisition; they maintain the spatial resolution and  $FOV$ , respectively. The missing raw data (high positive amplitude  $G_{PE}$ ) are extrapolated from the measured data through the Hermitian symmetry prior to Fourier transformation. The resulting image has the same  $FOV$  and resolution as that from a full raw data matrix, but the

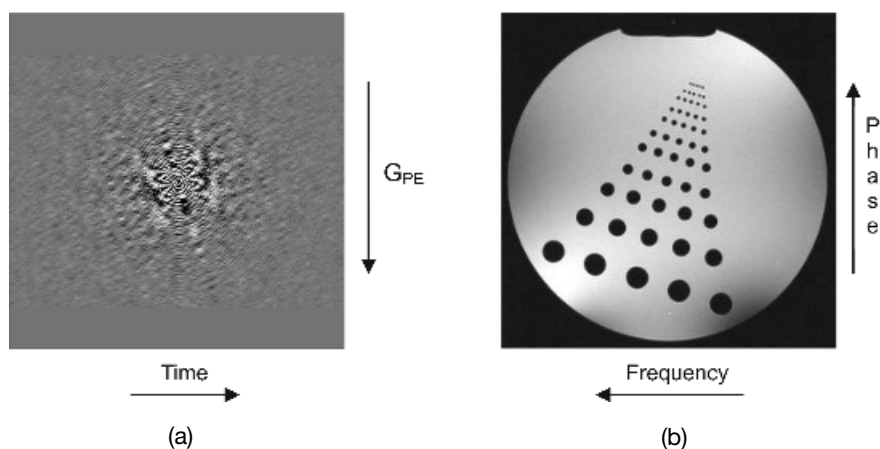


FIGURE 5-11 Raw data and corresponding image. (a) Same raw data set as in Figure 5-4, except that only the central 192 lines are kept and zero values are defined for the remaining data. Imaginary portion not shown. (b) Magnitude image data of (a). The image intensity is almost identical to that of Figure 5-5a, but there is a slight loss of edge definition, exhibited as blurring in the phantom.

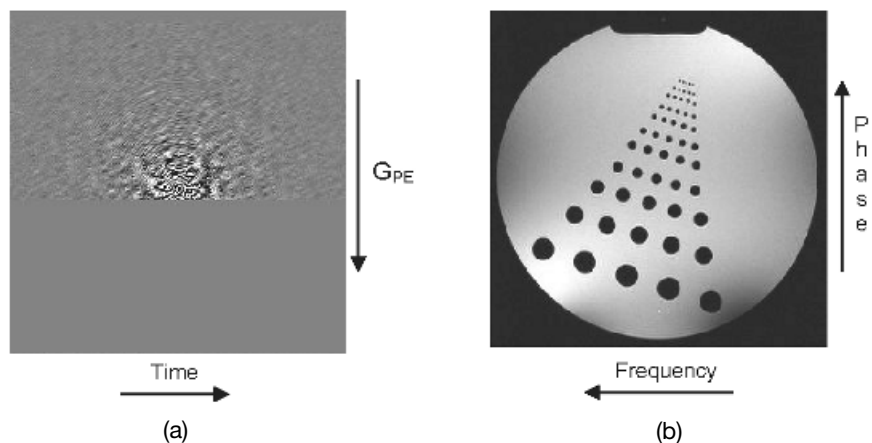


FIGURE 5-12 Raw data and corresponding image. (a) Same raw data set as in Figure 5-4, except that only the upper 136 lines are kept and zero values are defined for the remaining data. Imaginary portion not shown. (b) Magnitude image data of (a). The spatial resolution and signal intensity is identical to that of Figure 5-5a, but there is a slight increase in noise.

scan time is reduced. The problems with partial Fourier techniques are a loss in S/N due to the reduced number of detected lines and an enhanced sensitivity to artifacts due to the replication of the information.

## 5.5 PARALLEL ACQUISITION TECHNIQUES

A recent development in scanning methodology that reduces measurement times is a class of techniques known as parallel acquisition techniques. These methods take advantage of the multiple receiver coils constituting so-called phased-array coils (see Chapter 14). Traditional phased array coils individually measure and process the signals from a slice, then combine them to form an image covering a larger area of anatomy. Each element of the phased-array coil scans its own  $k$  space completely and produces a complete image. Parallel acquisition technique acquires a subset of  $k$  space with each coil element, then combines them to form the final image. The scan time is reduced due to the reduced number of lines acquired for each element. The number of elements used in the measurement is proportional to the scan time reduction. These techniques produce images with fewest artifacts when the line between the element centers (coil geometry) and the  $k_y$  axis is the same. This means that there will be certain coil geometries for which parallel acquisitions will not be suitable. Calibration scans are also necessary to compensate for differences in individual coil sensitivities.

SMASH (simultaneous acquisition of spatial harmonics) is a technique performed on the time-domain data measured from the phased-array coils. A subset of lines in  $k$  space is acquired using  $\Delta k_y$  such that there are frequencies in the detected signal with higher spatial harmonics (phase wraps) than can be accurately measured. In normal imaging, these higher harmonics would produce aliasing artifacts (see Chapter 9). In SMASH, the signals measured by the coils are not processed individually but are used to extract the correct (unaliased) signal from the combination signal. Each element of the array will detect different amplitudes of the spatial harmonics that are produced by a particular  $k_y$  line due to its different location. The coil geometry is such that multiple sinusoidal patterns can be generated mathemati-

cally using linear combinations of the coil sensitivities, enabling the missing signals to be determined.

SENSE (sensitivity encoding) is another parallel acquisition technique that uses image-domain data measured from the phased-array coils. With SENSE, the number of  $k_y$  lines is reduced but  $\Delta k$  is increased so that the total coverage of  $k$  space is maintained, effectively reducing the  $FOV_{PH}$  for the image. An image is produced from the  $k$  space sampled from each element containing both the correct image and the aliased portion due to the higher harmonics, but the correct and aliased signal amplitudes are different for each element. By comparing the different images and knowing the position and sensitivity of the element, a “true” image can be extracted from the different partial images.

## PULSE SEQUENCES

---

A pulse sequence is the measurement technique by which an MR image is obtained. It contains the hardware instructions (rf pulses, gradient pulses, and timings) necessary to acquire the data in the desired manner. As implemented by most manufacturers, the pulse sequence actually executed during the measurement is defined from parameters directly selected by the operator (e.g., *TR*, *FOV*) and variables defined in template files (e.g., relationships between rf pulses and slice selection gradients). This allows the operator to create a large number of pulse sequences using a limited number of template files. It also enables the manufacturer to limit parameter combinations to those suitable for execution. Some parameter limits of a pulse sequence (e.g., minimum *TR*, *FOV*) depend on how the manufacturer has implemented the technique (e.g., gradient pulse duration), whereas other parameters (e.g., maximum gradient amplitude, gradient rise time) are determined by limitations of the scanner hardware. The effect of common operator-selectable parameters on the signal intensity produced from a volume element of tissue is discussed in more detail in Chapter 7.

One of the more confusing aspects of MRI is the variety of pulse sequences available from the different equipment manufacturers. In addition, similar sequences may be known by a variety of names by the same manufacturer. As a result, comparison of techniques and protocols between manufacturers is often difficult due to differences in sequence implementation. An accurate description and detailed comparison of techniques between manufacturers would require knowledge of proprietary information. This chapter describes several pulse sequences commonly used in imaging by all manufacturers and some of the general characteristics of each one. In addi-

tion, where appropriate, the common acronyms used by some of the major manufacturers for the sequences are included.

Comparison of pulse sequences is facilitated by the use of timing diagrams. Timing diagrams are schematic representations of the basic steps performed by the different hardware components during sequence execution. Although there may be stylistic differences in the diagrams prepared by different authors, the general features are the same for all diagrams (Figure 6-1). Elapsed time during sequence execution is indicated from left to right along the horizontal axis. The vertical separation between lines is employed only for visualization. Each horizontal line corresponds to a different hardware component. At a minimum, four lines are used to describe any pulse sequence: one representing the radio frequency (rf) transmitter and one representing each gradient (labeled as  $G_{\text{SLICE}}$ ,  $G_{\text{READ}}$ , and  $G_{\text{PHASE}}$ , or  $G_X$ ,  $G_Y$ , and  $G_Z$ ). Additional lines may be added to indicate other activity

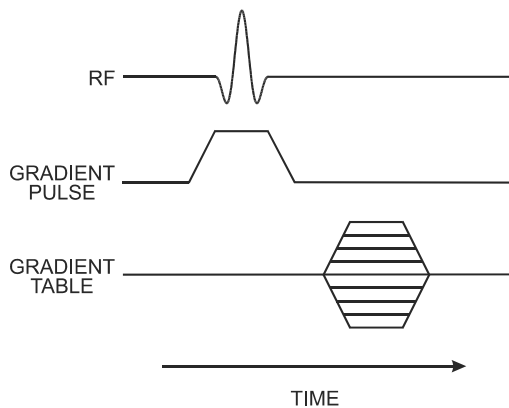


**FIGURE 6-1** Simple timing diagram. The horizontal axis is time during sequence execution. Each line corresponds to a different hardware component (rf transmitter, gradient amplifier, or ADC sampling period). Activity for a component is shown as a deviation from the baseline. Times during sequence execution when more than one hardware component is active (e.g., rf transmitter and gradient) are illustrated as activity in both lines. Gradient activity that does not change from measurement to measurement (e.g., slice selection amplitude) is shown as a constant deviation from baseline. Gradient activity that changes from measurement to measurement (e.g., phase encoding amplitude) is shown as a hashed region to illustrate multiple values.



such as analog-to-digital converter (ADC) sampling. Activity for a particular component such as a gradient pulse is shown as a deviation above or below the horizontal line (zero). Simultaneous activity from more than one component such as the rf transmitter and slice selection gradient is indicated by nonzero activity from both lines at the same vertical position. Constant-amplitude gradient pulses are shown as simple deviations from zero. Gradient tables such as for phase encoding are represented as hashed regions. Timing diagrams typically represent the hardware activity for the fundamental repeating unit of the pulse sequence, often called the kernel of the sequence. Specific details regarding exact timings, individual gradient amplitudes, or looping structures are not included as much of this information is determined by the specific measurement parameters or is proprietary to the various manufacturers. The generic nature of the representations makes timing diagrams suitable for representing classes of pulse sequences when making comparisons between the various measurement techniques.

## 6.1 SPIN ECHO SEQUENCES

A commonly used pulse sequence in MR imaging is a spin echo sequence. It has at least two rf pulses, an excitation pulse [often called the alpha ( $\alpha$ ) pulse] and one or more  $180^\circ$  refocusing pulses that generate the spin echo(es). A refocusing pulse is required for every echo produced. Spin echo sequences also utilize gradient pulses of opposite polarity in the readout and slice selection directions to refocus the protons at the same time as the spin echo. Spoiler gradients are used following signal detection to dephase any residual transverse magnetization and minimize spurious echoes. In a spin echo sequence, the repetition time,  $TR$ , is the time between successive excitation pulses for a given slice. The echo time,  $TE$ , is the time from the excitation pulse to the echo maximum. A multislice loop structure is used to acquire signals from multiple slices within one  $TR$  time period. Table 6-1 lists some of the common names for spin echo sequences.

Three types of spin echo sequences are commonly used: standard single echo, standard multiecho, and echo-train spin echo. Standard single echo sequences are generally used to produce  $T_1$ -weighted images when acquired with relatively short  $TR$  and  $TE$  (less than 700 ms and 30 ms, respec-

TABLE 6-1 Spin Echo Pulse Sequence Acronyms

Siemens	GE	Philips
Single spin echo	Spin echo	Spin echo
Double echo	Multiecho multiplanar (MEMP)	Modified spin echo
	Variable echo multiplanar (VEMP)	Multiple spin echo (MSE)
Turbo spin echo (TSE)	Fast spin echo (FSE)	Turbo spin echo (TSE)
Half Fourier acquisition turbo spin echo (HASTE)	Single shot FSE (SS-FSE)	Ultrafast spin echo (UFSE)

tively). A multislice loop structure is used with a single pair of excitation and refocusing pulses applied per slice loop. A single phase-encoding amplitude is applied per excitation pulse. Each echo within the scan is measured at the selected  $TE$  but with a different amplitude for  $G_{PE}$  (Figure 6-2). A rectilinear, sequential filling of the  $k$  space is used. Any raw data signal amplitude variations from echo to echo during the scan are due to changes in  $G_{PE}$  only. Following reconstruction, amplitude variations between tissues in the image are the result of differences between tissue-specific properties (proton density,  $T1$ , or  $T2$ ).

Standard multiecho sequences apply multiple  $180^\circ$  refocusing rf pulses following a single excitation pulse. Each refocusing pulse produces a spin echo, each one at a different  $TE$  defined by the user. A single  $G_{PE}$  is used per rf excitation pulse (Figure 6-3). Differences in raw data signal intensity at each  $TE$  are still due to differences in  $G_{PE}$  only. Raw data signal intensity variations from echo to echo ( $TE_1$  to  $TE_2$ ) are due to  $T2$  relaxation. Multiecho sequences are used to produce proton-density-weighted images using short  $TE$  (less than 30 ms) and  $T2$ -weighted images using long  $TE$  (greater than 80 ms) when  $TR$  is long enough to allow relatively complete  $T1$  relaxation for most tissues (2000 ms or longer).

The third type of spin echo sequence is known as echo-train spin echo (ETSE). It is based on the RARE (rapid acquisition with relaxation enhancement) technique for imaging. The ETSE sequences are similar to standard multiecho sequences in that multiple  $180^\circ$  pulses are applied to produce multiple echoes following a single excitation pulse. However,

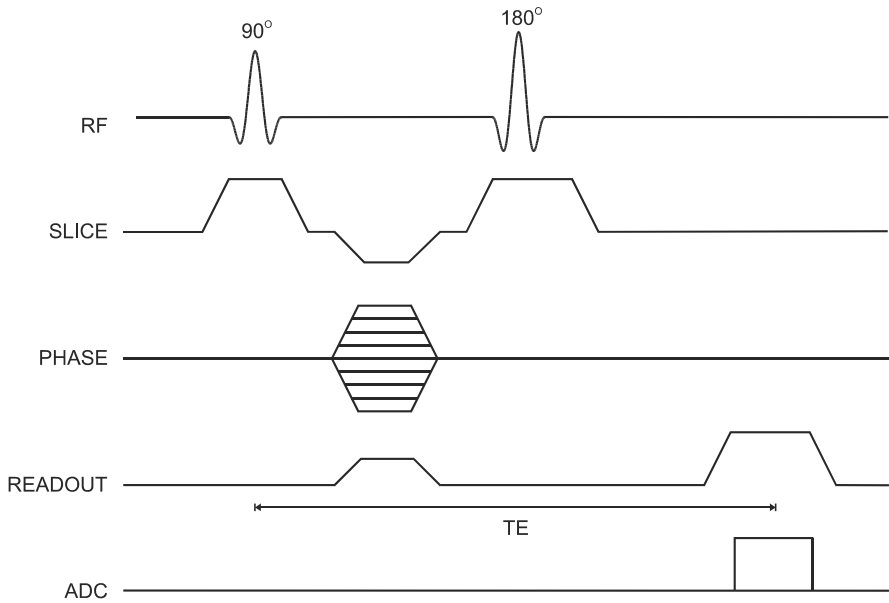
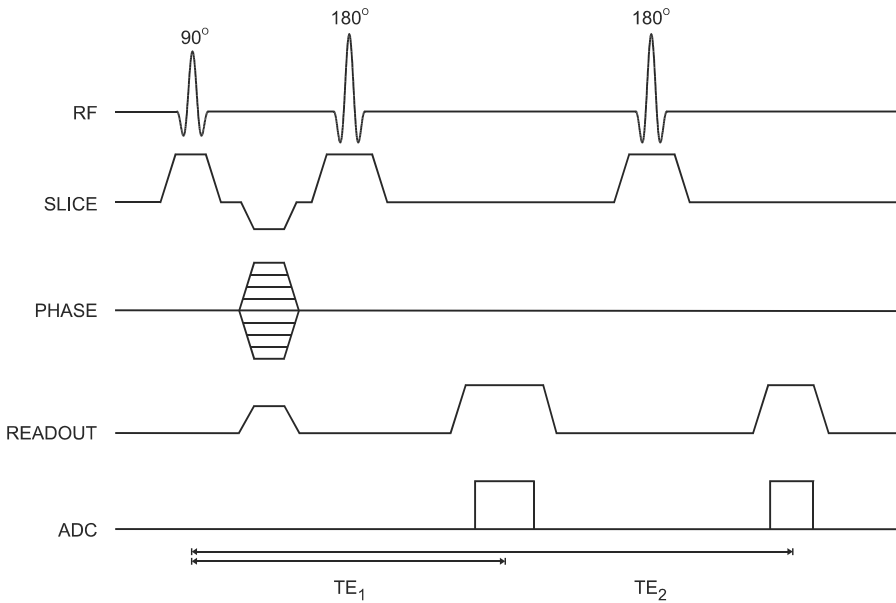


FIGURE 6-2 Standard single echo spin echo sequence timing diagram. These sequences are characterized by a single  $180^\circ$  refocusing pulse, a single detected echo, and a single phase-encoding table. The TE time is measured from the middle of the excitation pulse to the center of the echo.

each echo signal is acquired with a different  $G_{PE}$  as well as a different TE (Figure 6-4). The image is produced using some or all of the measured echoes as determined by the sequence design. The echo-train length or turbo factor corresponds to the number of echoes used to create the image. A segmented filling of  $k$  space is used with one echo from each segment acquired as part of the echo train for each rf pulse. The primary advantage of the ETSE technique is that the data collection process is more efficient and the scan time is reduced:

$$\text{Scan time}_{\text{echo-train spin echo}} = TR * N_{SA} * N_{PE} / \text{Echo train length} \quad (6-1)$$

The contrast in ETSE sequences is determined primarily by the echoes detected at or near  $G_{PE} = 0$  and the TEs for these echoes. The TE assigned to the image is referred to as an effective TE since there are echoes with different TEs contributing to the final image. This use of multiple TEs in the cre-



**FIGURE 6-3** Standard multiecho spin echo sequence timing diagram. Two echoes are illustrated. Additional echoes may be generated by adding additional 180° rf pulses, slice selection gradient pulses, readout gradient pulses, and ADC sampling times. Note the single phase-encoding gradient table. Both TE times are measured from the middle of the excitation pulse to the center of the respective echo.

ation of the image makes ETSE sequences unsuitable for use when subtle differences in  $T_2$  between tissues are responsible for the image contrast. Fat will also contribute increased signal compared to standard spin echo or multiecho images acquired with the same  $TE$ .

Although ETSE sequences can be used to produce  $T_1$ -weighted images, their most common application has been to produce  $T_2$ -weighted images. This is due to the significant reduction in scan time that can be achieved for long  $TR$  scans when modest echo-train lengths are used. Echo-train lengths less than 10 are typically used for brain and spine imaging, but very long echo trains (100 or more) can be used in abdominal imaging to acquire  $T_2$ -weighted images in less than one second. Termed snapshot or ultrafast ETSE, the scan times are sufficiently short to freeze bowel motion, yet provide good  $T_2$  contrast between tissues.

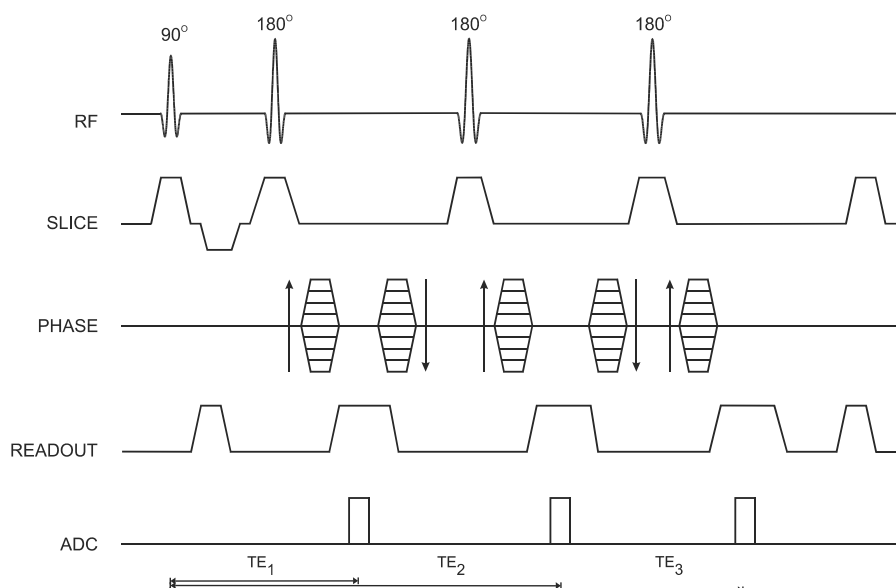


FIGURE 6-4 Echo-train spin echo sequence timing diagram. A three-segment (echo-train length of 3) version is illustrated, each with  $N_{PE}/3$  values of  $G_{PE}$  per segment to acquire  $N_{PE}$  total lines of raw data. The arrows beside the  $G_{PE}$  tables indicate the direction in which the phase-encoding values change from one excitation pulse to the next. Gradient tables on opposite sides of the ADC sampling time have equal amplitudes but opposite polarity. The effective TE is the TE time (1, 2, or 3) during which the  $G_{PE} = 0$  lines of data are acquired.

## 6.2 GRADIENT ECHO SEQUENCES

Gradient echo sequences are a class of imaging techniques that do not use a 180° pulse to refocus the protons. The echo signal is generated only through gradient reversal. As mentioned in Chapter 3, application of imaging gradients induce proton dephasing. Application of a second gradient pulse of the same duration and magnitude but opposite polarity reverses this dephasing and produces an echo known as a gradient echo. All gradient echo sequences use gradient reversal pulses in at least two directions—the slice selection and the readout directions—to generate the echo signal. Excitation angles less than 90° are normally used.

The absence of the 180° rf pulse in gradient echo sequences has sever-

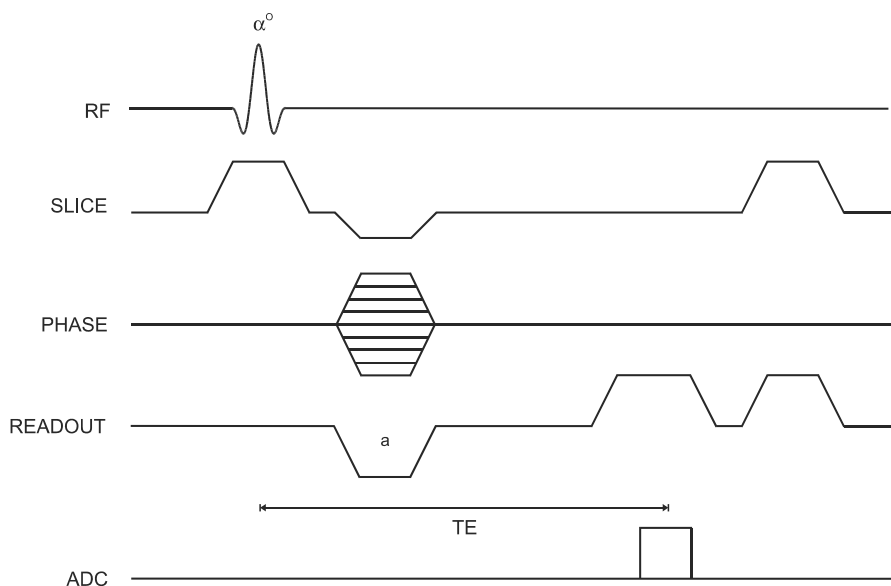
al important consequences. The sequence kernel time may be shorter than for an analogous spin echo sequence, enabling more slices to be acquired for the same  $TR$  if a multislice loop is used. Less total rf power is applied to the patient, so that the total rf energy deposition is lower. Additional contrast mechanisms are also possible. The static sources for proton dephasing— $B_0$  inhomogeneity and magnetic susceptibility differences—contribute to the signal decay, so the  $TE$  determines the amount of  $T2^*$  weighting in a gradient echo image rather than only  $T2$  weighting as in a spin echo image (Equation 3-2). For this reason, the overall signal level in gradient echo images will be less than for spin echo images with comparable acquisition parameters. The image quality of gradient echo sequences is also more sensitive to metal implants and to the region of anatomy under investigation. In addition, fat and water protons within a voxel also contribute different amounts of signal depending upon the chosen  $TE$ , a process known as phase cycling (see Chapter 9, Section 9.2.3). Table 6-2 lists some of the common gradient echo sequences currently in use.

TABLE 6-2 Gradient Echo Pulse Sequence Acronyms

Siemens	GE	Philips
Fast low-angle shot (FLASH)	Spoiled GRASS (SPGR), Fast spoiled GRASS (FSPGR), Multiplanar spoiled GRASS (MPSPGR), Fast multiplanar spoiled GRASS (FMPSPGR)	T1 contrast-enhanced FFE (T1 CE-FFE)
Fast imaging with steady state precession (FISP), True FISP	Gradient acquisition in the steady state (GRASS), Fast GRASS, Multiplanar GRASS (MPGR), Fast multiplanar GRASS (FMPGR), Fast imaging employing steady-state acquisition (FIESTA)	Fast field echo (FFE), Balanced FFE
Reversed FISP (PSIF)	Steady state free precession (SSFP)	T2 contrast-enhanced FFE (T2 CE-FFE)
TurboFLASH, Magnetization-prepared rapid acquisition gradient echo (MP-RAGE)	IR-prepared fast GRASS, Driven-equilibrium (DE)-prepared fast GRASS	Turbo field echo (TFE)

The simplest gradient echo sequence is a spoiled gradient echo sequence. This sequence uses a spoiling scheme to dephase the transverse magnetization following signal detection. As a result, only longitudinal magnetization contributes to  $M$  at the time of the next excitation pulse (e.g.,  $TR$ ). Spoiling may be done either by applying high-amplitude gradient pulses known as “spoiler” or “crusher” pulses to dephase the magnetization or by varying the phase of the rf excitation pulse in a pseudorandom fashion following each application. This approach, known as rf spoiling, produces an incoherent addition of any residual transverse magnetization so that the only remaining coherence at the time of the next excitation pulse is in the longitudinal direction (Figure 6-5).

In many respects, spoiled gradient echo sequences are the gradient echo counterpart of spin echo sequences. However, the contrast behavior of



**FIGURE 6-5** Spoiled gradient-echo sequence timing diagram, 2D method. Because there is no  $180^\circ$  rf pulse, the polarity of the  $G_{RO}$  dephasing gradient pulse (a) is opposite that of the readout gradient pulse applied during signal detection. Gradient spoiling is illustrated at the end of the loop. The TE time is measured from the middle of the excitation pulse to the center of the echo.

spoiled gradient echo techniques is slightly more complicated. The  $TE$  determines the amount of  $T2^*$  rather than  $T2$  weighting. The combination of excitation angle and  $TR$  determines the amount of  $T1$  weighting. Low excitation angle pulses impart minimal rf energy and leave most of  $M$  in the longitudinal direction. This allows a shorter  $TR$  to be used without producing saturation of the protons. Proton-density-weighted images are produced for small excitation angles ( $15\text{--}20^\circ$ ), relatively long  $TR$  (500 ms), and short  $TE$  (less than 10 ms).  $T2^*$  weighted images can be obtained using the same excitation angle and  $TR$  but a long  $TE$  (25–30 ms). Substantial  $T1$  weighting is obtained using large excitation angles ( $80^\circ$  or greater), short  $TR$  (100–150 ms), and short  $TE$  (less than 10 ms). Spoiled gradient echo images may be acquired using any of the sequence looping techniques discussed in Chapter 4. Routine spoiled gradient-echo imaging for spinal or abdominal studies uses a 2D multislice mode. A 2D sequential mode is used for MR angiography (see Chapter 11), whereas a 3D volume acquisition can produce very thin slices useful for multiplanar reconstruction of images in arbitrary orientations.

A second group of gradient sequences belongs to a class of techniques known as refocused or steady-state gradient echo sequences. Refocused gradient echo sequences use a single excitation pulse with a  $TR$  shorter than the  $T2$  relaxation time. Once  $M$  has reached a steady-state value (following a few rf pulses), both longitudinal and transverse components are present at the time of the next excitation pulse. Unlike spoiled gradient-echo sequences, refocused sequences apply rephasing gradient pulses in one, two, or all three directions to maintain the transverse magnetization as much as possible. In addition, the excitation pulses are applied rapidly enough (short  $TR$ ) so that spin echoes are generated that occur simultaneously with the subsequent excitation pulses. These spin echoes refocus the transverse magnetization as in spin echo imaging so that the signal amplitude in refocused pulse sequences depends strongly upon the  $T1$  and  $T2$  relaxation times of the tissues under observation. Optimal contrast can only be achieved in tissues with long  $T1$  and  $T2$  relaxation times.

Two signals can be measured from a refocused pulse scheme, one before and one after the excitation pulse (Figure 6-6). This scenario is analogous to examining a normal spin echo and using the protons as they rephase prior to  $TE$  to produce one signal and as they dephase following  $TE$



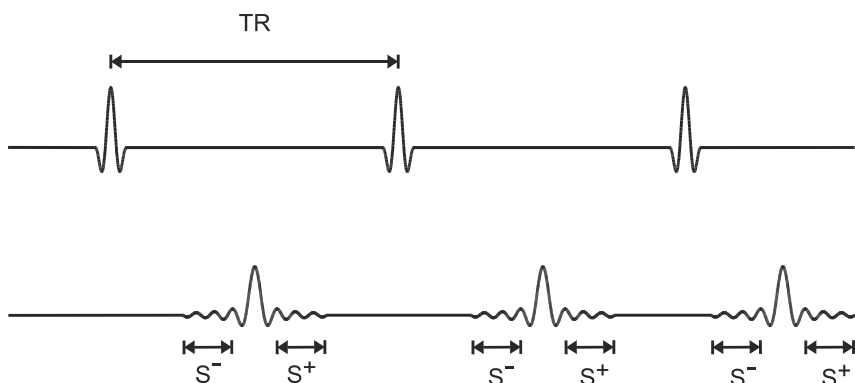
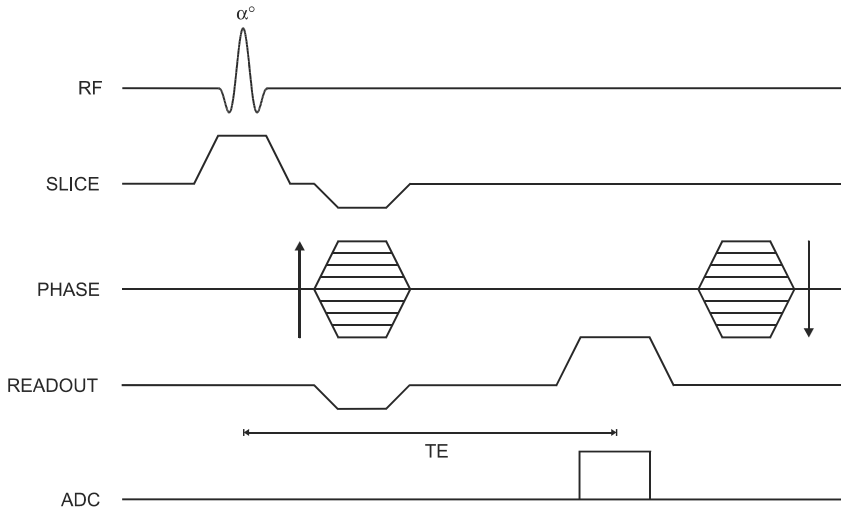


FIGURE 6-6 A series of equally spaced rf pulses produces spin echoes that form at the time of the subsequent rf excitation pulses. Once a steady state is reached (following several  $TR$  time periods), signal is induced prior to and following the excitation pulse. The preexcitation pulse signal  $S^-$  is strictly echo reformation. The postexcitation pulse signal ( $S^+$ ) is a combination of echo and free induction decay. Images can be produced from either signal or from both.

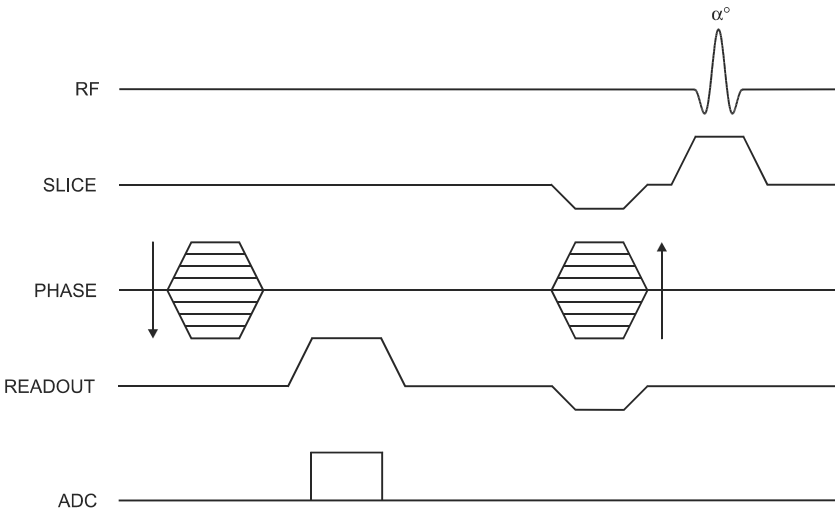
to produce the other signal. In spin echo imaging, both halves of the echo are detected and are processed together. In gradient echo imaging, each half of the echo can produce an image. The two pulse sequences are complementary in their sequence timing (Figure 6-7a,b). The technique using the postexcitation pulse signal is conceptually similar to the spoiled gradient echo technique except for the unspoiled transverse magnetization.

Bright signals are produced by both pre- and postexcitation techniques for tissues such as cerebrospinal fluid and blood with relatively long  $T_2$  and when  $TR$  is short so that the transverse coherence is maintained. A difference between the two techniques is observed when using a long  $TR$  or for tissues with  $T_2$  that is much shorter than  $T_1$ . In general, the postexcitation  $S^+$  signal in Figure 6-6 is based on net magnetization derived from two sources present at the time of the rf excitation pulse: the transverse magnetization  $M_T$  produced by previous excitation pulses, which generates a spin echo and decays based on  $T_2$  relaxation, and the longitudinal magnetization  $M_L$  resulting from  $T_1$  relaxation, which generates an FID and decays based on  $T_2^*$ .

Elimination of this  $M_T$ -based component is accomplished in two ways. The use of spoiling, either gradient-based or rf-based, explicitly removes



(a)



(b)

**FIGURE 6-7** Refocused gradient echo sequence-timing diagrams. Instead of spoiling the transverse magnetization, rephasing gradients are used to maintain the transverse magnetization as much as possible. (a) Postexcitation imaging sequence. (b) Preexcitation imaging sequence.

this component. Use of a long  $TR$  (e.g., 500 ms) with a small excitation pulse angle ( $10^\circ$ – $15^\circ$ ) allows this component to decay naturally. In both approaches, only the  $M_L$ -generated component is present, so that the decay of  $S^+$  is based on  $T2^*$ . This means that equivalent contrast results are obtained for spoiled and refocused gradient echo techniques if a long  $TR$  and low excitation pulse angle are used. For the preexcitation technique, the signal is derived from the  $M_T$ -based component only so that with spoiling or using long  $TR$ , no image is produced.

For refocused gradient-echo sequences using short  $TR$  and a large excitation pulse angle, the presence of the  $M_T$ -based component in  $S^+$  increases the signal from tissues with long  $T2$  such as fluids. These two resulting transverse magnetizations can decay at different rates, particularly if the magnet homogeneity is not uniform. There may also be variations in resonant frequency across the slice. These can cause phase differences to develop and can result in an interference banding artifact appearing in the postexcitation images if there is significant signal from the  $M_T$ -generated component (Figure 6-8). The use of refocusing gradients retains this compo-

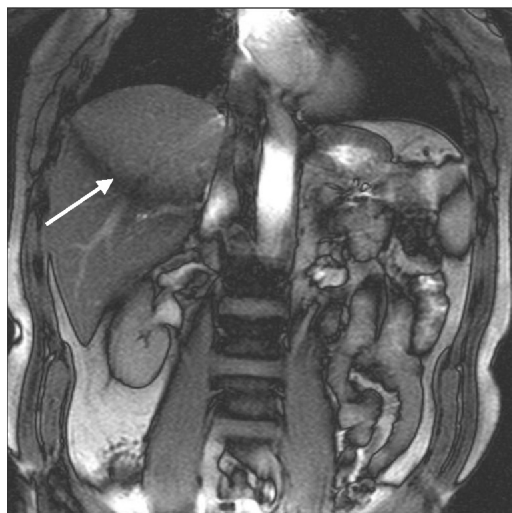


**FIGURE 6-8** Coronal image acquired with fully refocused gradient echo technique. The arrow indicates a signal cancellation artifact due to interference between the preexcitation and postexcitation signals. (Image courtesy of H. Cecil Charles, Duke University.)

ment as much as possible, but the extent of banding increases with increased refocusing. Use of complete gradient refocusing (so-called steady-state free precession sequences) should be preceded by adjustment of the magnet homogeneity. This will increase the  $T2^*$  for the  $M_L$ -based signal and will reduce frequency variations and the extent of banding.

### 6.3 ECHO PLANAR IMAGING SEQUENCES

A third type of pulse sequence, echo planar imaging (EPI), uses a very different method for data collection. EPI sequences are characterized by a series of gradient reversals in the readout direction. Each reversal produces a gradient echo, with the second half of one readout period being rephased by the first half of the subsequent readout period. The gradient reversals are performed very rapidly, allowing echo planar images to be acquired in 100–200 ms. Two types of schemes are used to phase encode each gradient echo. The continuous phase-encoding method applies the phase-encoding gradient continuously throughout the readout period. A preparatory phase-encoding pulse is applied, then each echo is acquired with a different amount of total phase accumulation; that is, the  $k$  space is sampled in a continuous and sinusoidal fashion (Figure 6-9a). Alternately, a “blipped” phase-encoding technique applies a small-amplitude  $G_{PE}$  pulse (equal to  $\Delta k_y$ ) prior to each sampling period. No phase-encoding gradient is applied during signal detection so that the phase encoding for each echo is constant (Figure 6-9b). The raw data matrix is acquired in a rectilinear, zigzag fashion. Because of the use of gradient echoes, EPI sequences are very sensitive to  $T2^*$  effects. In particular, magnetic susceptibility differences will cause image distortions at tissue–bone or tissue–air interfaces, making their use problematic in some anatomical regions.

Two data collection schemes are used in EPI sequences: single-shot and segmented or multishot. Single-shot techniques acquire all phase-encoding steps following a single excitation pulse. Since only one rf pulse is applied per slice position, each image can be acquired with an “infinite”  $TR$ . Special gradient amplifiers may be required for single-shot EPI imaging because of the rapid switching necessary to acquire all the echoes. Segmented techniques acquire a subset of phase-encoding steps following each excitation pulse. A segmented loop structure with multiple excitation pulses is used to

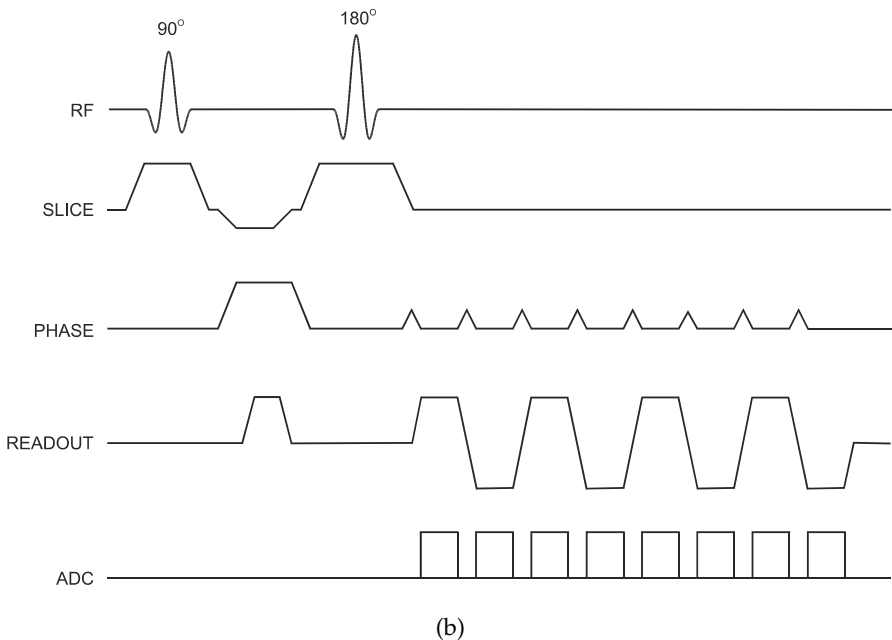
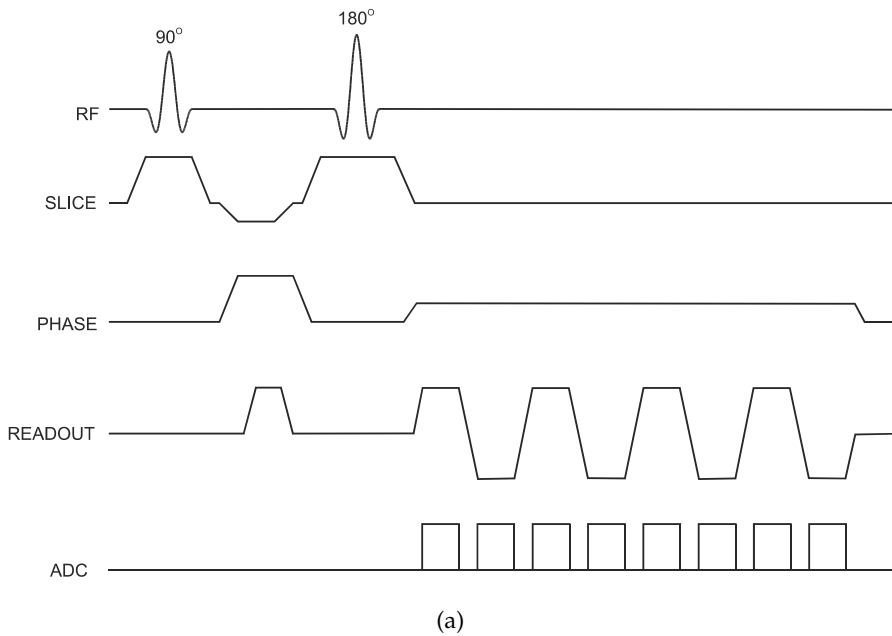


**FIGURE 6-9** Echo planar imaging sequence timing diagrams. A spin echo excitation scheme and an echo-train length of 8 are illustrated. (a) Constant phase encoding. The phase-encoding gradient is on for the entire data collection period. Each data point of each echo has a unique amount of  $G_{PE}$  influence. (b) Blipped phase encoding. The phase-encoding gradient is incrementally applied prior to detection of each echo. Each echo is influenced by a different amount of  $G_{PE}$ , but each data point within the echo has the same amount of  $G_{PE}$  influence.

acquire all phase-encoding steps. Segmented EPI can often be performed with standard imaging gradient systems.

The contrast in EPI images is determined by the  $TE$  for the echo acquired when  $k_y = 0$ . Each echo is acquired at a different  $TE$ , similar to echo-train spin echo sequences, so the  $TE$  of the image is referred to as an effective  $TE$ . Variations in contrast for EPI sequences are achieved using magnetization-preparation pulses (see below) applied prior to the readout period.  $T1$ -weighted images are produced using a  $180^\circ$  inversion rf pulse prior to the excitation pulse.  $T2$ -weighted images can be obtained using a  $90^\circ$ – $180^\circ$  pair of pulses to produce a spin echo. Spoiled gradient echo EPI sequences use no preparatory pulse and produce  $T2^*$ -weighted images.

## 6.4 MAGNETIZATION-PREPARED SEQUENCES

The pulse sequences described above provide the fundamental methods used for spatial localization in MRI today. For some combinations of measurement parameters, the images that result from these techniques may have a lack of tissue contrast or poor spatial resolution. In order to overcome these limitations, the basic techniques may be modified using rf pulses to preset the net magnetization to a given state prior to execution of the spatial localization steps. These extra pulses are known as magnetization-preparation pulses and the sequences that incorporate them are collectively known as magnetization-prepared (MP) sequences.

One example of an MP sequence is known as inversion recovery (IR). The traditional IR sequence is a variation of the spin echo sequence. It is a spin echo sequence with an additional  $180^\circ$  pulse, usually slice-selective, applied prior to the initial excitation pulse. The  $180^\circ$  pulse inverts  $M$  for the protons within the slice, producing enhanced  $T1$  sensitivity at the time of the excitation pulse. The inversion time,  $TI$ , is a user-selectable delay time between the  $180^\circ$  pulse and the excitation pulse and determines the amount of  $T1$  relaxation that occurs between the two pulses. A standard phase-encoding gradient table is used, and  $TE$  is defined as for spin echo sequences (Figure 6-10). Table 6-3 lists common names and features for inversion recovery sequences. Inversion recovery sequences require long  $TR$  times to allow maximal  $T1$  relaxation between successive excitation rf pulses.

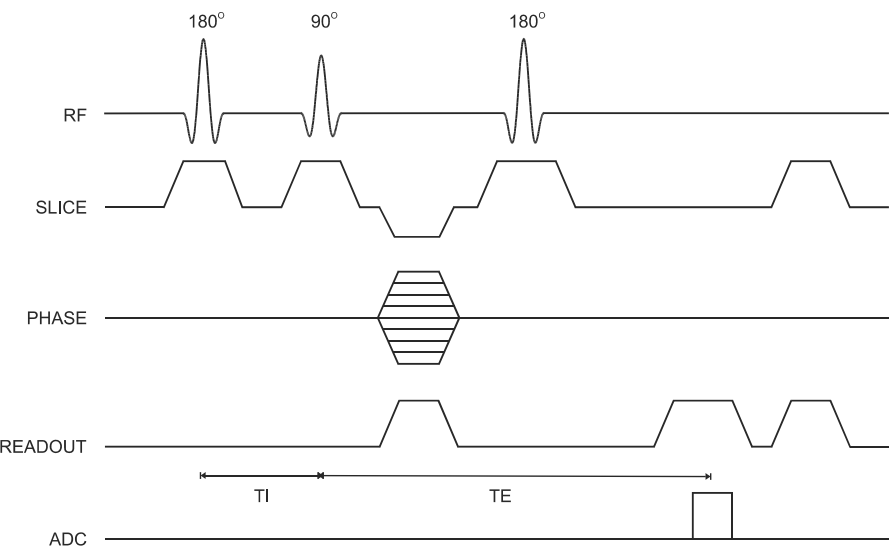


**FIGURE 6-10** Standard inversion recovery sequence timing diagram. The *TI* time is measured from the middle of the inversion (initial 180°) pulse to the excitation pulse. The *TE* time is measured from the middle of the excitation pulse to the center of the echo.

es. Insufficient *TR* causes loss of signal due to saturation for tissues with long *T1* relaxation times such as fluids.

There are three sequence variations used for IR sequences. The echo-train inversion recovery sequence combines features of the normal IR and the ETSE sequences. The 180° inversion pulse is applied prior to an ETSE acquisition sequence rather than a normal spin echo sequence. The contrast obtained in an echo-train IR sequence is based on the *TI* and the tissue *T1*

TABLE 6-3 Inversion Recovery Pulse Sequence Acronyms		
Siemens	GE	Philips
Standard Inversion Recovery	Multiplanar IR (MPIR)	IR
Echo-Train Inversion Recovery	Fast multiplanar IR (FMPIR)	IR-turbo spin
Interleaved Excitation	Nonsequential (standard)	echo (IR-TSE)
Magnitude Reconstruction	Absolute value, Magnitude	Modulus
Phase Sensitive Reconstruction		Real

times as in the IR sequence, whereas the echo-train length and effective  $TE$  have equivalent effects to these parameters in the ETSE sequence (Figure 6-11). The second modification is the looping mode for multislice imaging. If the  $TI$  time is relatively short, all rf pulses are applied and a signal is detected from a slice before progressing to another slice. If the  $TI$  time is relatively long, all inversion rf pulses are applied in order, followed by the excitation and refocusing pulses and signal detection. This allows for more efficient data collection during one  $TR$  time period (Figure 6-12).

The third type of sequence modification is determined by the image reconstruction process. The inversion of  $M$  by the  $180^\circ$  rf pulse allows for the generation of negative amplitude signals. Short  $TI$  times allow minimal  $T1$  relaxation between the inversion and excitation rf pulses. Most tissues will have  $M$  inverted at the time of the excitation pulse. Long  $TI$  times allow more complete relaxation of tissues between the two pulses to occur, pro-

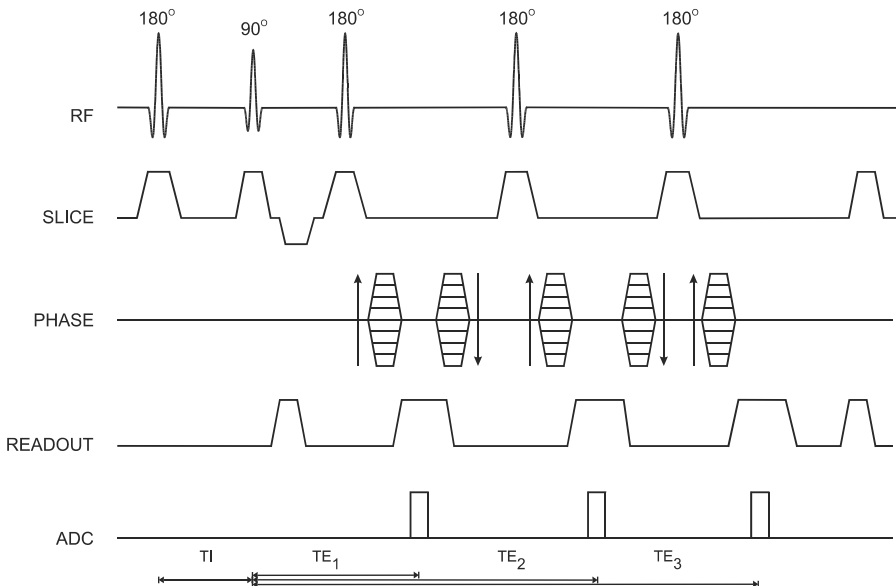


**FIGURE 6-11** Echo-train inversion recovery sequence timing diagram. A three-segment (echo train length of 3) version is illustrated, each segment with  $N_{PE}/3$  values for  $G_{PE}$ . The  $TI$  time is measured from the middle of the inversion (initial  $180^\circ$ ) pulse to the excitation pulse. The effective  $TE$  is the  $TE$  time (1, 2, or 3) during which the  $G_{PE} = 0$  lines of data are acquired.



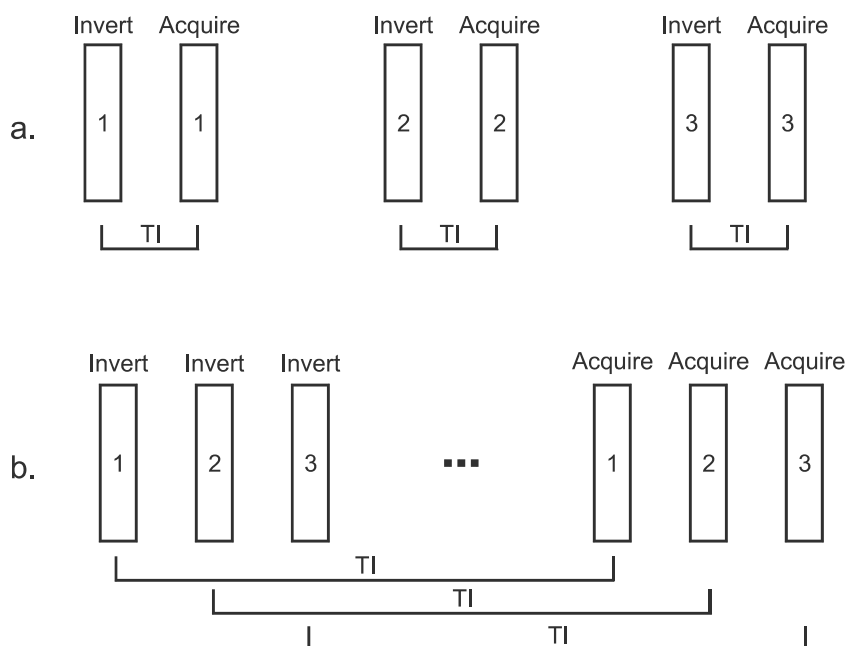
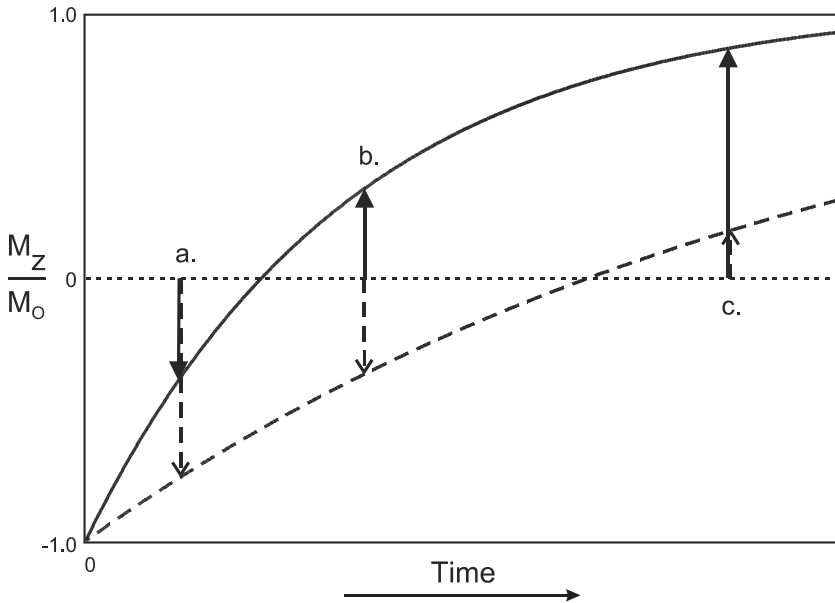


FIGURE 6-12 Inversion recovery looping modes. (a) Inversion for a given slice is immediately followed by echo acquisition. This is typically used when the  $TI$  time is relatively short. (b) All inversion pulses for all slices are performed followed by echo acquisition. This is typically used when  $TI$  is relatively long.

ducing positive values for  $M$ . Intermediate  $TI$  gives a mixture of positive and negative  $M$ , depending on  $TI$  and the specific tissue  $T1$  values (Figure 6-13). During image reconstruction, the phase of  $M$  can be incorporated into the pixel intensity. Termed phase-sensitive IR, these images have negative pixel values for tissues with inverted  $M$ . These are produced by tissues with long  $T1$  values at short  $TI$  times. Background air is assigned a midrange pixel value. Alternately, the phase of  $M$  can be ignored in the final image. Termed absolute value or magnitude IR, these images have pixel values based only on the signal magnitude. Tissues with very short or very long  $T1$  relaxation times have high pixel values, and background air has a low pixel value (Figure 6-14).

The inversion pulse also allows for the suppression of signals through the proper choice of  $TI$ . If the  $TI$  time is chosen so that the tissue of interest



**FIGURE 6-13**  $T_1$  recovery curves for inversion recovery sequences. The  $180^\circ$  inversion pulse inverts the net magnetization for all tissues. Tissue with a short  $T_1$  time (solid curve) recovers faster than tissue with a long  $T_1$  (dashed curve) time. For  $TI$  time (a), both tissues contribute significant negative amplitude signal. For  $TI$  time (b), the short  $T_1$  tissue contributes a positive amplitude signal and the long  $T_1$  tissue contributes a negative amplitude signal. For  $TI$  time (c), the short  $T_1$  tissue contributes a significant positive amplitude signal and the long  $T_1$  tissue contributes a minimal signal. If the signal polarity is considered (phase-sensitive IR sequences), signal difference will be seen at all three  $TI$  times. If the signal polarity is ignored (absolute value or magnitude IR sequences), no difference in signal between the two tissues will be seen at time (b).

has no longitudinal component at the time of the excitation pulse, then that tissue contributes no signal to the final image. This time, known as the null time for the tissue, is determined by the  $T_1$  relaxation time for the tissue:

$$TI_{\text{NULL}} = 0.693 * T_1 \quad (6-2)$$

assuming the  $TR$  time is sufficiently long. The two most common applications of IR sequences are for the suppression of cerebrospinal fluid (CSF) and fat. Normal CSF has a  $T_1$  relaxation time of approximately 3000 ms at

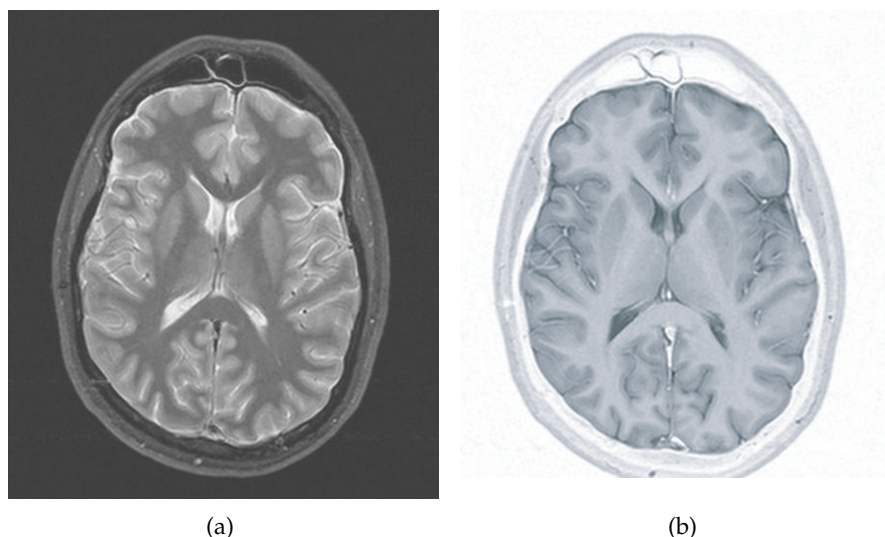


**FIGURE 6-14** Magnitude (a) and phase-sensitive (b) inversion recovery images. All other measurement parameters are equal: pulse sequence, echo-train spin echo, 5 echoes;  $TR$ , 7000 ms;  $TE$ , 14 ms;  $TI$ , 140 ms; acquisition matrix:  $N_{PE}$ , 224;  $N_{RO}$ , 256;  $FOV$ , 201 mm PE  $\times$  230 mm RO;  $N_{SA}$ , 1; slice thickness, 5 mm.

1.5 T. A  $TI$  time of 2080 ms will apply the excitation pulse when the CSF magnetization has no longitudinal component and produces an image with no CSF signal. This technique, known as fluid-attenuated IR (FLAIR), allows easy visualization of gray- and white-matter inflammation.

Fat has a  $T_1$  relaxation time of approximately 200–250 ms at 1.5 T. If a  $TI$  value of 140–160 ms is selected, the excitation pulse occurs when the fat magnetization has no longitudinal component and produces an image with no fat signal. This technique is known as STIR or short  $TI$  inversion recovery. Virtually complete and uniform fat suppression throughout the imaging volume can be achieved using STIR imaging. However, it suffers from two major limitations. One is that a limited number of slices can be acquired for typical  $TR$ . Because of this, complete coverage of the imaging volume may require the use of multiple scans or the ETSE variation. The second problem occurs when using a  $T_1$  contrast agent. As described in Chapter 15, a contrast agent such as Gd-DTPA shortens the  $T_1$  relaxation time for the water in tissues that absorb the agent. Tissues with long  $T_1$  values that

would normally be bright in a STIR image will lose signal when the contrast agent is present as the tissue  $T_1$  approaches that of the fat tissue. Visualization of these tissues thus becomes difficult. For this reason, STIR imaging is usually not performed when contrast agents are administered.

Magnetization preparation pulses can also be incorporated into gradient echo sequences. These pulses are often used to improve tissue contrast for scans in which short measurement times are desired. For example, a  $TR$  of 7 ms with  $N_{PE} = 128$  will require 900 ms of scan time. The excitation angle must be between  $5^\circ$  and  $10^\circ$  to minimize saturation effects yet produce sufficient transverse magnetization to generate a signal. Added contrast may be obtained by manipulating the longitudinal magnetization through the application of additional rf pulses prior to the data collection period. These preparation pulses generate enhanced amplitude variations to  $M$  that can be measured during the rapid data collection time. This is the concept of MP gradient echo sequences.

One major difference between the usage of MP pulses in gradient echo sequences compared to spin-echo-based sequences is in the frequency of application of the MP pulse. Spin-echo-based sequences apply one MP pulse per excitation pulse so that the MP-modified net magnetization has a steady-state value for the scan. Gradient echo sequences typically apply multiple excitation pulses for a single MP pulse. As a result, gradient echo MP techniques are non-steady-state techniques since  $M$  does not have the same value prior to each phase-encoding step. Each phase-encoding step is acquired at a different point in time following the preparation pulses. The resulting image contrast depends on when the  $G_{PE} = 0$  step is acquired during the data collection period. The  $G_{PE} = 0$  time is determined by the particular gradient-table-ordering scheme used. Linear  $k$  space ordering has the  $k_y = 0$  line in the middle of the phase-encoding table so that the contrast-controlling echoes are acquired at a time  $TR * N_{PE} * N_{SA}/2$  into the data collection period (see Figure 5-7). The contrast in this case depends on the matrix size and acquisitions. Centric ordering acquires the  $G_{PE} = 0$  step at the beginning of the data collection period so that the  $G_{PE} = 0$  step occurs at a time  $TR$  into the data collection period (see Figure 5-8). The contrast for a centric-ordered magnetization-prepared sequence does not vary as dramatically with the extrinsic variables and has more predictable contrast behavior.

Magnetization-prepared gradient echo sequences can employ either 2D or 3D techniques. Two-dimensional magnetization-prepared techniques are acquired as sequential slice techniques in that all data collection is acquired for a slice following a single set of preparation pulses. The rapid measurement times make them very insensitive to patient motion. These sequences may also be acquired using a segmented  $k$  space in order to increase spatial resolution. Three-dimensional magnetization-prepared techniques typically apply one preparation pulse per phase encoding entry so that the non-steady-state behavior of  $M$  is only present during the loop through the partitions gradient table (Figure 6-15). This enables the image contrast to be unaffected by the acquisition matrix.

Two types of preparatory schemes are used in MP gradient-echo sequences. For  $T_1$ -weighted images, a single  $180^\circ$  inversion rf pulse is applied (Figure 6-16a). This pulse may be nonselective to invert all protons within

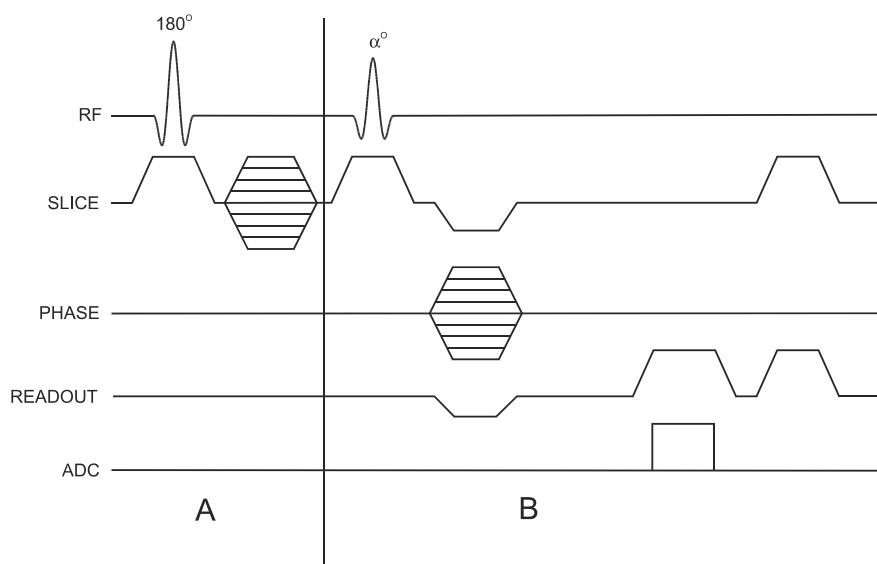


**FIGURE 6-15** 3D-MP sequence timing diagram,  $T_1$ -weighted. A  $180^\circ$  inversion rf pulse is applied followed by encoding in the slice ( $k_z$ ) direction (section A). This inversion provides significant  $T_1$  weighting to  $M$ . The portion of the sequence indicated by B is repeated for the desired  $N_{PE}$ . The entire process (A and B) is repeated for the desired  $N_{SA}$  and  $N_{PAR}$ .

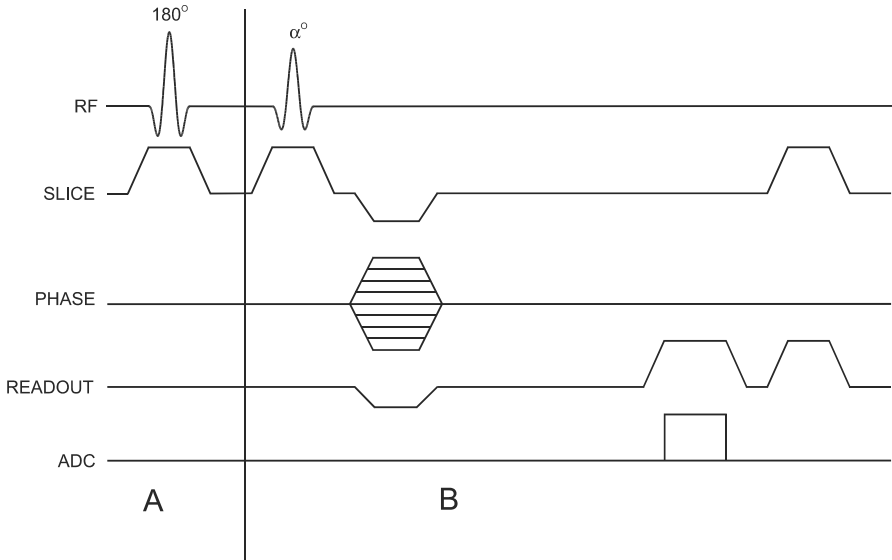


**FIGURE 6-16** 2D-MP sequence timing diagrams. (a)  $T1$ -weighted. A single  $180^\circ$  inversion rf pulse is applied once per scan (section A). This inversion provides significant  $T1$  weighting to  $M$ . The portion of the sequence indicated by B is repeated for the desired  $N_{AV}$  and  $N_{PE}$ ; (b)  $T2$ -weighted. A  $90^\circ$ – $180^\circ$ – $90^\circ$  rf pulse train is applied once prior to the data collection scheme (section A). The first two pulses produce  $T2$  weighting to  $M$ , which is restored to the longitudinal direction by the final pulse prior to the data collection. The portion of the sequence indicated by B is repeated for the desired  $N_{AV}$  and  $N_{PE}$ .

the transmitter coil or slice selective to invert only the protons in the slice of interest. A delay time  $TI$  between the inversion pulse and the data collection period produces variation in longitudinal magnetization of the tissues.  $T1$  MP sequences differ from the IR sequences described previously in that only one inversion pulse is applied for the entire data collection period. The contrast is determined by the effective  $TI$ , which is the user-selected  $TI$  plus the time to the  $k_y = 0$  line:

$$TI_{\text{effective}} = TI + TR * N_{SA} * N_{PE} / 2 \quad (6-2)$$

For  $T2$  MP gradient-echo sequences, a series of rf pulses known as a driven equilibrium pulse train is used. Three rf pulses are used and applied

in the scheme  $90^\circ - \tau - 180^\circ - \tau - 90^\circ$  (Figure 6-16b). The first two pulses generate a spin echo and produce  $T_2$  weighting to the transverse magnetization. The third pulse rotates this magnetization into the longitudinal direction, producing changes in  $M$  based on the  $T_2$  relaxation times and the interpulse spacing  $\tau$ . Use of a centric-ordered data collection produces  $T_2$ -weighted images with good contrast.

## MEASUREMENT PARAMETERS AND IMAGE CONTRAST

---

As mentioned in Chapter 6, many of the measurement parameters of a pulse sequence may be modified through the user-interface software. The particular parameters will be determined by the scanner manufacturer, based on the template pulse sequence (which parameters are appropriate) and the desired interface design (which parameters should the operator be allowed to modify). There are three general criteria that should be considered when modifying measurement parameters: acceptable scan time, adequate spatial resolution, and sufficient contrast between tissues relative to the background noise (contrast-to-noise ratio). These criteria are often in conflict in clinical imaging. For example, obtaining images with high spatial resolution (pixel sizes  $< 0.7$  mm) and high contrast-to-noise ratio between tissues will require long scan times due to signal averaging. For each scan, the important criterion must be identified so that appropriate parameter variations can be made. One complication is that, although the scan time and spatial resolution for the final image can be calculated before the scan begins, the contrast-to-noise ratio cannot be determined prior to the measurement. This is because the measured signal amplitude depends on the specific tissue(s) within the imaging volume and their relaxation times.

As mentioned above, the specific parameters that are variable within the user interface will be determined by the manufacturer. However, many parameters are commonly available in most pulse sequences. One approach to categorizing them is by their effect on the final image. Intrinsic param-



ters modify the inherent signal produced by a volume element of tissue (voxel). These parameters probe the characteristic tissue properties that are the response to the measurement procedure. Intrinsic parameters affect only the signal-producing portion of the image, which is normally patient anatomy and not background air. Extrinsic parameters influence the mechanics of data collection (e.g., voxel size) or other factors external to the tissue. They typically affect the spatial resolution or general background noise levels in the final image. Many of these parameters are specific to the particular choice of pulse sequence used for the measurement and may not be available in all instances.

## 7.1 INTRINSIC PARAMETERS

Repetition time,  $TR$ , measured in ms, is the time between successive rf excitation pulses applied to a given volume of tissue. In conjunction with the excitation angle (see below),  $TR$  determines the amount of  $T1$  weighting contributing to the image contrast. If all other factors are equal, longer  $TR$  allows more time for the rf excitation energy to be dissipated by the protons through spin-lattice relaxation, producing images with less  $T1$  weighting (Figure 7-1). For a multislice loop,  $TR$  limits the number of slices that can be acquired during the measurement.

Echo time,  $TE$ , measured in ms, is the time between the excitation pulse and the echo (signal) maximum. It determines the amount of  $T2$  weighting for spin echo images (Figure 7-2). For gradient echo images,  $TE$  determines the amount of  $T2^*$  weighting and the ratio of fat and water signal contributions (see Figure 2-6). Longer  $TE$  allows more time for proton dephasing and produces lower signal amplitudes. In echo-train spin echo and echo planar sequences,  $TE$  is considered to be an effective  $TE$  since all echoes used in image reconstruction are not acquired at the same echo time.

Inversion time,  $TI$ , measured in ms, is the time between the  $180^\circ$  inversion pulse and the imaging excitation pulse.  $TI$  is used in inversion recovery (IR), echo-train IR, and magnetization-prepared gradient echo sequences, and determines the amount of time allowed for  $T1$  relaxation following the inversion pulse. Short  $TI$  times allow minimum  $T1$  relaxation, whereas long  $TI$  times allow significant  $T1$  relaxation prior to the imaging excitation

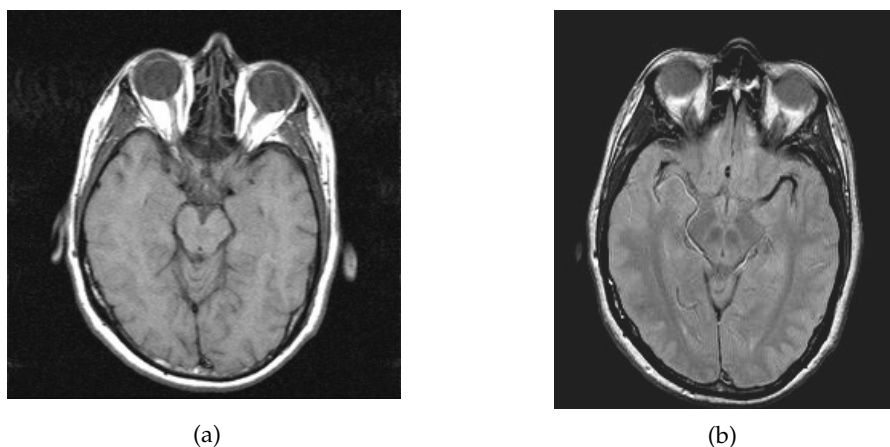


**FIGURE 7-1** *TR* effects on image contrast. Longer *TR* allows more time for *T1* relaxation and produces more signal from tissues with long *T1* values. Other measurement parameters are: pulse sequence, spin echo; *TE*, 30 ms; acquisition matrix:  $N_{PE}$ , 224;  $N_{RO}$ , 256; *FOV*, 201 mm PE  $\times$  230 mm RO;  $N_{SA}$ , 1; slice thickness, 5 mm. (a) *TR* of 500 ms; (b) *TR* of 2000 ms. Note reversal of contrast between gray matter and white matter in (b) compared to (a).

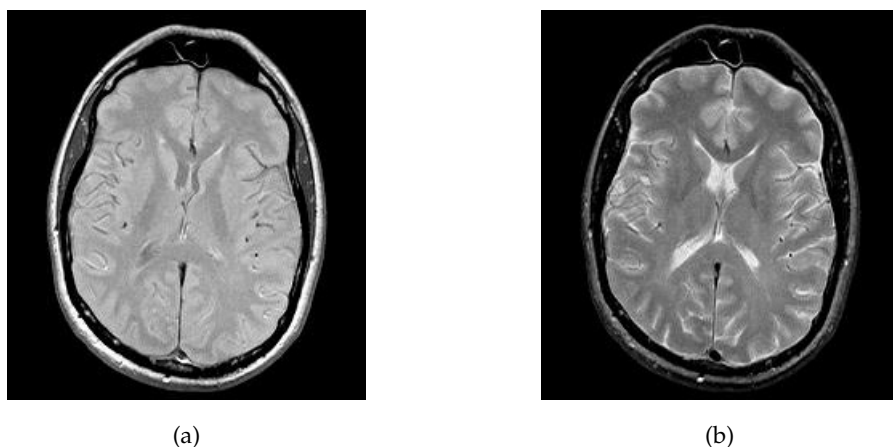


**FIGURE 7-2** *TE* effects on image contrast. Longer *TE* allows more time for *T2* relaxation and produces more signal from tissues with long *T2* values. Other measurement parameters are: pulse sequence, spin echo; *TR*, 2000 ms; acquisition matrix:  $N_{PE}$ , 224;  $N_{RO}$ , 256; *FOV*, 201 mm PE  $\times$  230 mm RO;  $N_{SA}$ , 1; slice thickness, 5 mm. (a) *TE* of 30 ms; (b) *TE* of 80 ms. Note bright signal from cerebrospinal fluid (CSF) in (b) compared to (a).

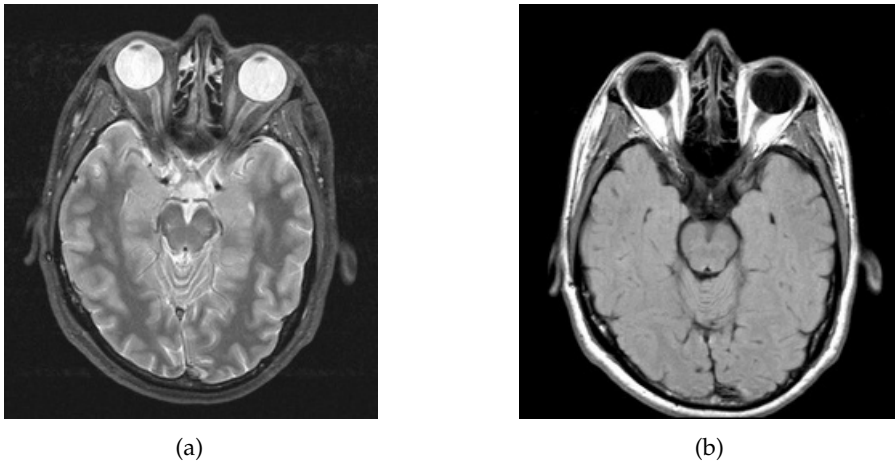


**FIGURE 7-3** *TI* effects on image contrast. Longer *TI* allows more time for *T1* relaxation following the inversion pulse. The choice of *TI* can cause signal suppression of different tissues. Other measurement parameters are: pulse sequence, echo-train spin echo, 5 echoes; *TR*, 7000 ms; *TE*, 14 ms; acquisition matrix:  $N_{PE}$ , 224;  $N_{RO}$ , 256; *FOV*, 201 mm PE  $\times$  230 mm RO;  $N_{SA}$ , 1; slice thickness, 5 mm. (a) *TI* of 140 ms (fat suppression); (b) *TI* of 2100 ms (CSF suppression).

pulse. Proper choice of *TI* enables signal suppression of tissues based on their *T1* relaxation times (Figure 7-3).

Echo train length (also known as the turbo factor) is the number of echoes (number of phase-encoding steps) measured following an excitation pulse that are used to create an image. The echo-train length is used in echo-train spin echo and echo-train IR sequences. Longer echo-train lengths allow shorter scan times through more efficient data collection. The sequence kernel time (minimum *TR* per slice) is longer with longer echo-train lengths, producing greater signal attenuation through *T2* relaxation as well as requiring longer *TR* to obtain an equal number of slices. The number of phase-encoding steps for the measurement is a multiple of the echo-train length.

Echo spacing, measured in ms, is the time between each echo of an echo train. The echo spacing is used in echo-train spin echo, echo-train IR, and echo planar sequences. Longer echo spacing allows more time for *T2* relaxation between each echo. Shorter echo spacing reduces the sequence kernel time.

Excitation angle (also known as the flip angle), measured in degrees, is the amount of rotation away from the equilibrium axis that  $M$  undergoes through rf absorption. If not variable under the operating software, the excitation angle is usually  $90^\circ$  in order to generate the maximum transverse magnetization. The excitation angle is also proportional to the amount of signal produced by the protons and is related to the amount of energy absorbed. The excitation angle, together with  $TR$  and the  $T1$  values for the individual tissues, determines the amount of  $T1$  weighting present in an image. The Ernst angle  $\alpha_E$  is the excitation angle that produces the maximum signal from a tissue for a particular  $TR$ :

$$\cos(\alpha_E) = \exp(-TR/T1) \quad (7-1)$$

## 7.2 EXTRINSIC PARAMETERS

Slice thickness,  $TH$ , measured in mm, is the volume of tissue in the slice selection direction that absorbs the rf energy during irradiation and generates the signal. Variation in slice thickness is usually accomplished through changing the magnitude of  $G_{SS}$ . Thicker slices provide more signal per voxel, whereas thinner slices produce less partial volume averaging.

Slice gap, measured in mm, is the space between adjacent slices. The slice gap may also be expressed as a fraction of the slice thickness, depending on the operating software. The slice gap allows the user to control the size of the total imaging volume by increasing or decreasing space between slices. The slice gap also provides a method to compensate for the imperfect rf excitation pulses. If the slices are closely spaced, excitation pulses applied to adjacent slice position partially overlap and excite the same region of tissue because the slice excitation profiles are not uniform. This situation is known as crosstalk (Figure 7-4). Due to the rapid rf pulse application, these regions of overlap become saturated and contribute little to the detected signal. The slice gap allows space between adjacent slice positions and reduces the extent of crosstalk for the measurement.

Excitation order refers to the temporal order in which slices are excited during the measurement. Two ordering schemes are typically used (see Figure 7-4). Sequential ordering excites adjacent slice positions in successive time periods. This approach is preferred when relative timing of adjacent slices is crit-

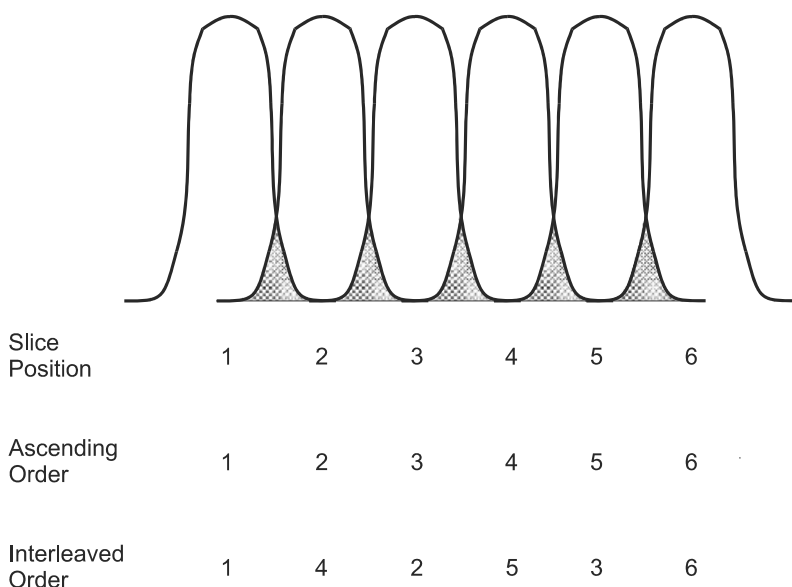


**FIGURE 7-4** Excitation order and crosstalk. If the slices are closely spaced, then the bases of adjacent slices overlap (shaded regions). Tissues located in this overlap region experience rf pulses from both slices and become saturated. This double excitation is called crosstalk and causes reduced signal from these regions. The order of slice excitation also determines the contribution of crosstalk to the image intensity. Ascending order of excitation (second row) acquires data from adjacent slice positions in successive time periods. Interleaved ordering (third row) acquires data from every other slice position first, then acquires data from the intermediate positions. This will minimize the effects of crosstalk between all slices.

ical, such as for electrocardiogram-triggered studies of the heart (see Chapter 10). Interleaved ordering excites alternate slices in successive time periods. Interleaved ordering allows the maximum amount of time for  $T_1$  relaxation of the overlap region prior to the subsequent excitation pulse. The effects of crosstalk are also reduced for all slices as much as possible. Arbitrary ordering may also be performed if permitted by the operating software.

Number of partitions,  $N_{\text{PART}}$ , is used in 3D volume studies and corresponds to the number of slices into which the excited volume is divided. The slices have signals derived from the total excited volume and are contiguous. The effective slice thickness is the volume excited (thickness) divided by  $N_{\text{PART}}$ . The scan time for a 3D sequence is linearly proportional to  $N_{\text{PART}}$  (see Equation 4-9).

Field of view,  $FOV$ , measured in  $\text{mm}^2$ , specifies the area from which the MR signals are accurately sampled. The  $FOV$  may be specified separately for the readout and phase-encoding directions (permitting anisotropic or rectangular  $FOV$ ), or it may be listed as a single number (isotropic or square  $FOV$ ). Decreasing the  $FOV$  is accomplished by increasing the corresponding gradient amplitude. Increasing spatial resolution is achieved by decreasing the  $FOV$ , which decreases the voxel size at the expense of the signal-to-noise ratio ( $S/N$ ).

Acquisition matrix ( $N_{PE}$ ,  $N_{RO}$ ) defines the raw data sampling grid used for the measurement of the base image. It consists of two numbers: One specifies the number of phase-encoding steps ( $N_{PE}$ ) and the other specifies the number of readout sampling data points ( $N_{RO}$ ). Different manufacturers have conventions regarding which number is specified first. The acquisition matrix divides the  $FOV$  into individual areas that, together with the slice thickness, define the voxel size. Increased spatial resolution may be obtained by using larger acquisition matrices to produce smaller voxels. Data acquired beyond that necessary for defining the image  $FOV$  is referred to as oversampling and is used to reduce the presence of high-frequency aliasing artifacts (see Chapter 9).

The image matrix,  $a$ , consists of the number of rows and columns of the image. Image matrices are usually square with equal numbers of rows and columns. Identification of row and column to readout and phase-encoding directions is controlled through the operating software.

Number of signal averages,  $N_{SA}$ , (also known as  $N_{EX}$ , the number of excitation pulses) is the number of times the signal from a given slice for a given phase-encoding amplitude is measured and added together for signal averaging. Depending on the operating software, all acquisitions may be performed at each phase-encoding amplitude for a slice, or the entire set of phase-encoding amplitudes may be measured for each slice before performing the second acquisition for any slice. The  $S/N$  ratio is proportional to the square root of  $N_{SA}$ , whereas the measurement time is proportional to  $N_{SA}$ .

Receiver bandwidth,  $BW_{REC}$ , measured in Hz, is the maximum frequency (Nyquist frequency) that can be accurately digitized. The Nyquist frequency depends on the sampling time and  $N_{RO}$ . The receiver bandwidth may also be expressed as the total bandwidth over the entire  $FOV$  or as the bandwidth per pixel (frequency resolution), depending on the particular

convention. Lower  $BW_{REC}$  improves the S/N at the expense of potentially larger chemical shift artifacts (see Chapter 9).

### 7.3 PARAMETER TRADEOFFS

As mentioned above, the three criteria used for determining a “good” measurement protocol are sufficient spatial resolution to resolve the underlying anatomy, reasonable signal-difference-to-noise (termed contrast-to-noise) ratio between tissues, and an acceptable measurement time. In general, these three criteria conflict with one another, and the difficulty in protocol optimization is to obtain the proper balance between them. In addition, optimal parameters for one set of tissues may or may not be optimal for another set of tissues. Finally, while each parameter can be specified separately, they are not completely independent. For example,  $TE$  must be less than  $TR$ . The following formulas can provide guidance on the trade-off of one parameter versus another for S/N or image intensity. Tables 7-1 and 7-2 also summarize the parameter changes and their effects on spatial resolution, S/N, and measurement time.

#### 7.3.1 INTRINSIC VARIABLES

Standard Single Spin Echo Signal Intensity

$$I_{SE} = N * K * \exp(-TE/T2) * \{1 - 2 \exp[-(TR - TE/2)/T1] + \exp(-TR/T1)\} \quad (7-2)$$

Standard Inversion Recovery Signal Intensity

$$I_{IR} = N * K * \exp(-TE/T2) * \{1 - 2 \exp(-TI/T1) + 2 \exp[-(TR - TE/2)/T1] - \exp(-TR/T1)\} \quad (7-3)$$

Standard Spoiled Gradient Echo Signal Intensity

$$I_{SGE} = N * K * \exp(-TE/T2^*) * \sin \alpha * [1 - \exp(-TR/T1)] / [1 - \cos \alpha * \exp(-TR/T1)] \quad (7-4)$$

TABLE 7-1 Measurement Effects—Extrinsic Parameters

Parameter	Direction of Change	Effect on Voxel Size	Effect on S/N Ratio	Effect on Scan Time
$TH$	Increase	Linear Increase	Linear Increase	None
$N_{PART}$	Increase	Linear Decrease	Square Root Increase	Linear Increase
$FOV_{RO}$	Increase	Linear Increase	Linear Increase	None
$FOV_{PE}$	Increase	Linear Increase	Linear Increase	None
$N_{RO}$	Increase	Linear Decrease	Square Root Increase	None
$N_{PE}$	Increase	Linear Decrease	Square Root Increase	Linear Increase
$N_{SA}$	Increase	None	Square Root Increase	Linear Increase
$BW_{REC}$	Increase	None	Square Root Decrease	None

TABLE 7-2 Measurement Effects—Intrinsic Parameters

Parameter	Direction of Change	Effect on Voxel Size	Effect on S/N Ratio	Effect on Scan Time
$TR$	Increase	None	Increase	Linear Increase
$TE$	Increase	None	Decrease	None
Excitation angle, $\alpha$	Increase	None	Increase for Long TR Decrease for Short TR	None

Equations 7-2, 7-3, and 7-4 assume exact rf pulses of the desired excitation angle. For the spin echo and inversion recovery equations, the excitation angle is assumed to be  $90^\circ$  and the refocusing and inversion pulses are assumed to be  $180^\circ$ . For the spoiled gradient echo equation, the excitation angle is  $\alpha$ .  $K$  contains constants and terms based on the extrinsic parameters and  $N$  is the number of protons per unit volume being excited.

### 7.3.2 EXTRINSIC VARIABLES

Standard 2D Imaging Acquisition

$$S/N_{2D} = K' (TH)(FOV_{RO}/N_{RO})(FOV_{PE}/N_{PE}) (N_{SA}N_{RO}N_{PE}/BW_{REC})^{1/2} \quad (7-5)$$



## Standard 3D Imaging Acquisition

$$\frac{S}{N_{3D}} = K' (TH/N_{PART})(FOV_{RO}/N_{RO})(FOV_{PE}/N_{PE}) \\ (N_{SA}N_{RO}N_{PE}N_{PART}/BW_{REC})^{1/2} \quad (7-6)$$

Equations 7-5 and 7-6 assume uniform tissue content and relaxation behavior throughout the excited volume.  $K'$  contains constants and terms based on the intrinsic parameters. The terms in parentheses represent voxel dimensions and the square root term relates to noise contributions to the final measured signal. These equations may be used to estimate S/N changes for combinations of parameter changes. For example, the S/N changes in a linear manner with variation in slice thickness, but changes linearly with the square root of  $N_{SA}$ . A twofold reduction in slice thickness may be offset by a fourfold increase in  $N_{SA}$ .

## ADDITIONAL SEQUENCE MODIFICATIONS

---

Chapter 6 presented the concept of a pulse sequence and described several classes of pulse sequences. The rf and gradient pulses were applied in very precisely defined ways to uniformly affect the signal intensity from all the protons within the volume of measured tissue. Additional rf excitation pulses may be added to any of these sequences to manipulate the net magnetization  $M$  of some of the tissue within the imaging volume and differentially affect its contribution to the detected signal. Three basic types of rf pulses may be added: frequency-selective pulses applied in conjunction with a gradient (spatial presaturation), frequency-selective pulses applied in the absence of a gradient (magnetization transfer suppression, fat saturation), and a series of closely spaced pulses acting as a unit (composite pulses). In all of these cases, additional time within the sequence kernel time is required to implement the pulses. This reduces the maximum number of slices possible for a given  $TR$  when a multislice loop structure is used. In addition, the additional rf pulse(s) increases the total rf power deposition to the patient. Limitations due to the specific rate of rf energy absorption (SAR) (see Chapter 14) may be required, particularly for spin-echo-based sequences using short  $TR$ .

### 8.1 SPATIAL PRESATURATION

Spatially localized presaturation pulses are frequency-selective rf pulses applied in conjunction with a gradient pulse. They are used to suppress unde-

sired signals from tissues within the imaging volume. They are often employed to suppress artifactual signals from peristaltic and respiratory motion in lumbar spine imaging. Spatial presaturation pulses are also used to reduce blood flow artifacts from the aorta or inferior vena cava in abdominal imaging by saturating the blood before it enters the imaging volume. These types of pulses are also used to produce a saturation tag for analyzing the direction of blood flow or cardiac motion.

Spatial presaturation pulses are usually applied prior to the imaging slice pulses during sequence execution. They may be applied once per slice loop or once per  $TR$  time period. Due to their rapid occurrence, the presaturation pulses saturate the selected tissue so that its steady-state net magnetization is much smaller than the net magnetization for the remaining tissue of the slice. In addition, spoiler gradients are applied to dephase any resid-

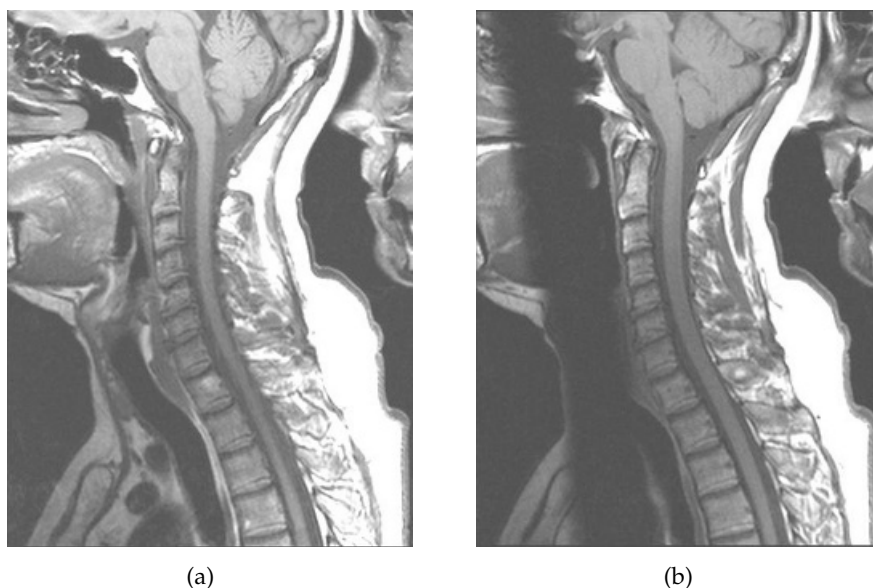


**FIGURE 8-1** Application of a spatial presaturation pulse to moving tissue will suppress signals from that tissue. Measurement parameters are: pulse sequence, spin echo;  $TR$ , 500 ms;  $TE$ , 16 ms; excitation angle,  $90^\circ$ ; acquisition matrix:  $N_{PE}$ , 192,  $N_{RO}$ , 256;  $FOV$ , 210 mm  $PE \times 280$  mm  $RO$ ;  $N_{SA}$ , 3; slice thickness, 4 mm. (a) No presaturation pulse. (b) Oblique coronal spatial presaturation pulse, suppressing artifact from swallowing.

ual transverse magnetization following the presaturation pulse. The result is that the signal from the presaturated region is significantly less than the signal from the nonpresaturated tissue (Figure 8-1). In addition to the problems regarding sequence kernel times and rf power deposition previously mentioned, spatial presaturation pulses will not remove all signals from the selected tissue. The saturated tissue experiences  $T_1$  relaxation during the time between the presaturation pulse and the imaging excitation pulse so that longitudinal magnetization is present within the presaturated region at the time the slice excitation pulse is applied. This generates signals from the saturated region that may have significant amplitude, depending on the particular  $TR$  for the measurement and the tissue  $T_1$  values. The amount of apparent signal suppression depends on the amount of signal produced in the saturated region relative to the signal produced in the unsaturated region.

## 8.2 FAT SATURATION

Normal MR imaging methods visualize protons from both water and fat molecules within the tissue. In Chapter 6, the STIR technique that visualizes only the tissue water was described. Another method for visualizing only the tissue water is fat saturation. As mentioned in Chapter 2, fat and water have a chemical shift difference of approximately 3.5 ppm in their resonant frequencies. Fat saturation uses a narrow-bandwidth rf pulse centered at the fat resonant frequency applied in the absence of a gradient (Figure 8-2). The resulting transverse magnetization is then dephased by spoiler gradients. A standard imaging sequence may then be performed that produces images from the water protons within the slice (Figure 8-3a). The number of fat saturation pulses applied during the sequence loop is variable, ranging from once per  $TR$  time period to once per slice excitation pulse. The signal suppression mechanism is similar to that of spatial presaturation described previously in that minimal net magnetization from the fat protons is present at the time of the excitation pulse for the slice.

Fat saturation has two main advantages over STIR imaging for fat suppression. First, it may be incorporated into any type of imaging sequence.

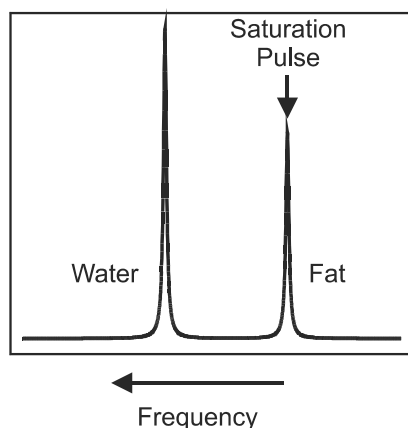
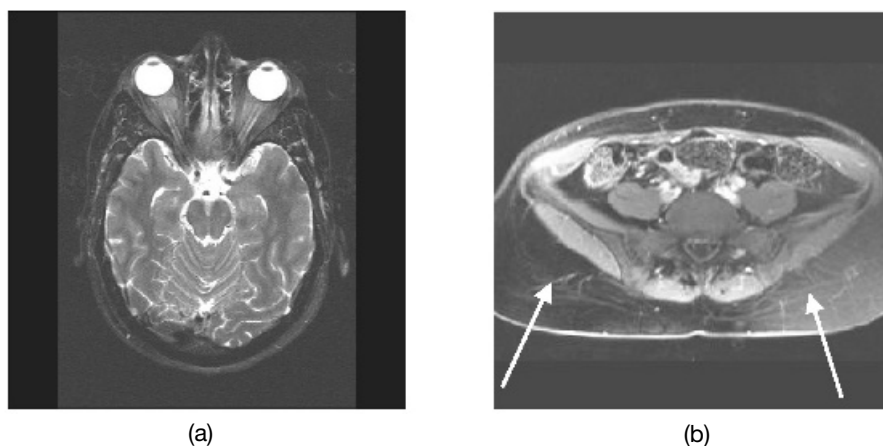


FIGURE 8-2 Frequency spectrum of fat and water. Fat saturation applies an additional rf excitation pulse centered at the fat resonant frequency. This pulse is applied prior to the primary slice excitation pulse, so that the signal from the slice is produced primarily from the water.

Second,  $T_1$  fat saturation sequences may also be used with gadolinium-based  $T_1$  contrast agents since the contrast agent shortens the  $T_1$  relaxation times of only the water protons (see Chapter 15). The  $T_1$  reduction enables the enhanced tissues to generate significant signals while the fat signal remains minimal in the presence or absence of the contrast agent. However, three potential problems are inherent with fat saturation, in addition to the problems of increased slice loop time and rf power deposition. One is that there will be magnetization-transfer suppression (see below) of the water protons by the saturation pulse. The second problem is that the fat protons undergo significant  $T_1$  relaxation during the time between the saturation pulse and the imaging pulses due to their short  $T_1$  times and will contribute to the detected signal. As the fat signal approaches the water signal in amplitude, the contrast between the fat and water tissues is reduced. Multiple fat saturation pulses within a slice loop may be required to achieve the desired signal suppression. Finally, fat saturation is particularly sensitive to the magnetic-field homogeneity. The exact resonant frequency for a fat proton depends upon the magnetic field that a voxel experiences. If the homogeneity is not uniform throughout the imaging volume, the center frequency of the saturation pulse will be off-resonance for some of the fat and will



**FIGURE 8-3** Frequency-selective saturation (fatsat) pulses are applied to suppress signals from fat protons. (a) With a homogeneous magnetic field, the suppression of fat is uniform throughout the slice. (b) With a nonhomogeneous magnetic field, the saturation pulse suppresses fat well in one region of the image and poorly in another region (arrows).

not be effective in suppression (Figure 8-3b). In some cases, the water protons may be saturated rather than the fat protons. For this reason, optimization of the field homogeneity to the specific patient prior to applying a fat saturation pulse is advisable.

### **8.3 MAGNETIZATION-TRANSFER SUPPRESSION**

Another signal suppression technique similar in hardware implementation to fat saturation is magnetization-transfer suppression, which is used to selectively irradiate water protons that have very short  $T_2$  values. Water within a tissue is either mobile (freely moving) or bound (adsorbed to macromolecules). The bound fraction water protons have a very short  $T_2$  due to the rapid dephasing they undergo. The resonance peak for these spins is very broad and normally does not contribute significantly to the measured signal. The mobile water molecules have a much longer  $T_2$  and a narrow resonance peak. These two resonances are superimposed at the same center frequency (Figure 8-4).

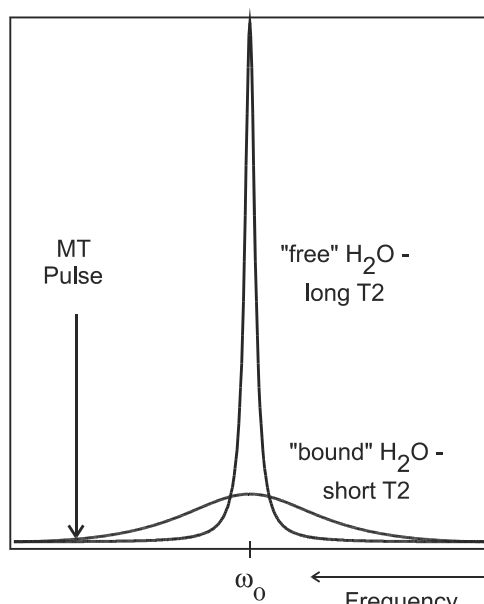
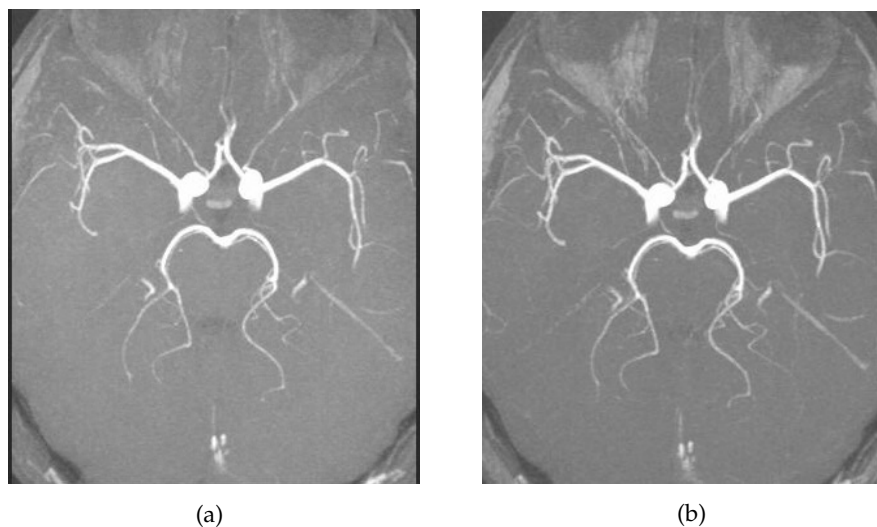


FIGURE 8-4 Magnetization-transfer suppression. Mobile or “free” tissue water has protons with long  $T_2$  values and produces a narrow resonance peak. Water adsorbed or “bound” to macromolecules has protons with short  $T_2$  values and produces a wide resonance peak normally not visualized in an image. Both types of water protons have the same resonant frequency. The magnetization transfer rf pulse is applied at a frequency different (off-resonance) from the water to saturate the bound water protons. Exchange between the bound and free water transfers the saturation to the free water protons, reducing signal intensity from the free water.

Magnetization-transfer suppression is accomplished using a narrow bandwidth saturation pulse known as a magnetization-transfer (MT) pulse centered 1–10 kHz away from the central water frequency applied in the absence of a gradient. Only the bound water protons are irradiated by the rf pulse and become saturated. An exchange occurs between the bound water protons and the unsaturated mobile water protons that transfer the saturation to the mobile fraction protons, causing a loss of steady-state magnetization and reducing the signal from the mobile fraction protons. This process is called magnetization-transfer suppression. Contrast is enhanced between tissues that undergo magnetization transfer (water-containing tissues) and those that do not (fat-containing tissues). Magnetization-transfer pulses are

used in spin echo or gradient echo sequences to produce additional signal suppression of tissue water.

Magnetization-transfer suppression is most often used to reduce signal from normal tissue water in studies where this tissue is of little interest. Two examples illustrate this. Time-of-flight MR angiography (see Chapter 11) is a technique for visualizing blood flow within the vascular network. Suppression of the normal brain tissue water using magnetization-transfer pulses enables smaller vessels to be distinguished (Figure 8-5). The other application of magnetization transfer is  $T_1$  studies following the administration of a contrast agent.  $T_1$  contrast agents shorten the  $T_1$  relaxation time for tissues in which the agent is located (see Chapter 14). Comparison of images acquired before and after contrast administration enable determination of the agent dispersal within a tissue. Use of a magnetization



**FIGURE 8-5** Effects of magnetization transfer in 3-D MR angiography. Application of MT pulse suppresses background signals from gray and white matter, enabling better visualization of blood vessels. An apparent increase in signal from suborbital fat is observed (arrows). Measurement parameters are: pulse sequence, 3D refocused gradient echo, postexcitation;  $TR$ , 42 ms;  $TE$ , 7 ms; excitation angle,  $25^\circ$ ; acquisition matrix:  $N_{PE}$ , 192;  $N_{RO}$ , 512 with twofold readout oversampling;  $FOV$ , 201 mm PE  $\times$  230 mm RO;  $N_{SA}$ , 1; effective slice thickness, 0.78 mm. (a) No MT pulse. (b) MT pulse.



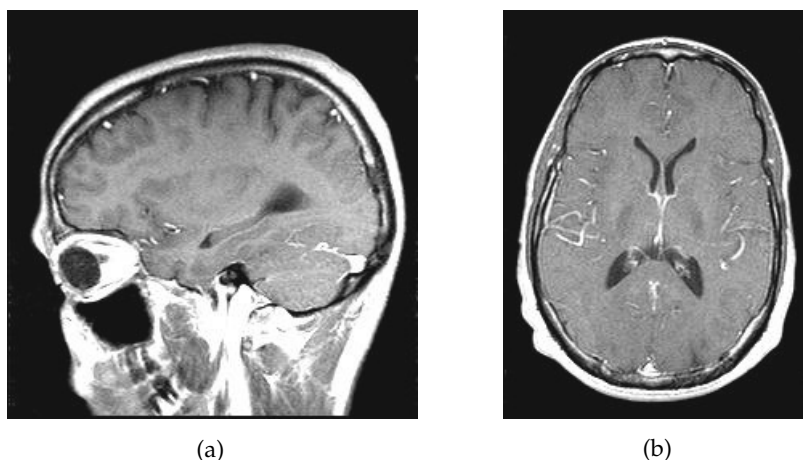


**FIGURE 8-6** Effects of magnetization transfer in T1-weighted imaging following contrast administration. Application of MT pulse suppresses background signals from normal matter, enabling better visualization of contrast-enhanced tissues such as tumors or vascular structures. (a) No MT pulse. (b) MT pulse.

transfer pulse during the postcontrast measurement reduces the signal from the unenhanced tissues, increasing their contrast with the enhanced tissue (Figure 8-6).

## 8.4 COMPOSITE PULSES

A composite rf pulse is a series of closely spaced rf pulses applied over a short time period that affect the protons like a single pulse. The pulse amplitudes for each rf pulse typically form a binomial progression (e.g., 11, 121, 1331), with the effective flip angle being the sum of the individual flip angles. The timing between the pulses allows protons with different resonant frequencies to cycle in phase and undergo different effects from each pulse (Figure 8-7). The individual pulses may be nonselective (rectangular) or frequency selective, resulting in a composite pulse of the same character. In general, composite pulses require less transmitter power than single rf pulses for the same flip angle because of the short duration of the individual pulses.

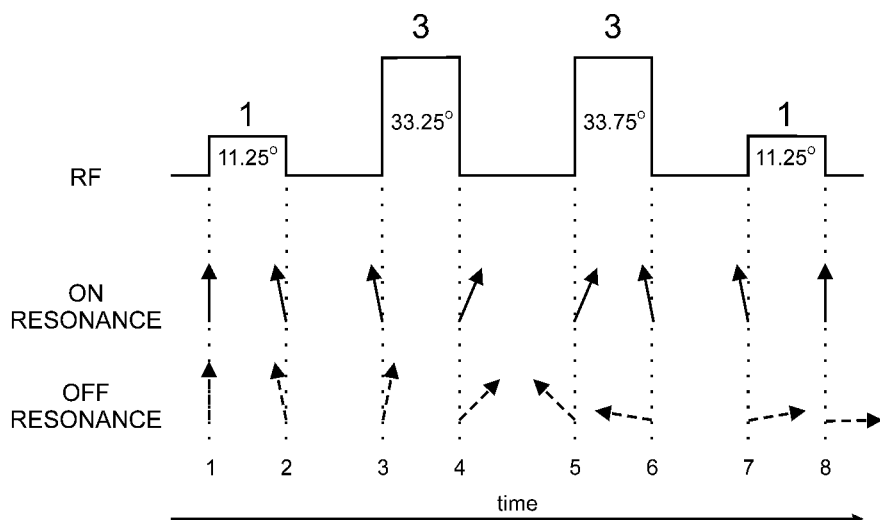


FIGURE 8-7 Composite pulse. A 1331 composite pulse is shown with a total excitation angle of  $90^\circ$ . A rotating frame corresponding to the on-resonant frequency is assumed. Prior to the first rf pulse (1), both on-resonance (solid arrow) and off-resonance (dashed arrow) protons are unexcited. At the end of the first rf pulse (2), both will be excited to  $11.25^\circ$ . Because of the difference in resonant frequencies, the off-resonant protons become out of phase. The time for the second rf pulse (3) is chosen so that the off-resonance protons are exactly  $180^\circ$  out of phase. At the end of the second rf pulse (4), the off-resonance protons are excited to  $-45^\circ$ , whereas the on-resonance protons are excited to  $-22.5^\circ$ . The delay between the second and third rf pulses is chosen so that the off-resonance protons are  $180^\circ$  out of phase with the on-resonance protons (5). A similar delay is chosen between the third and fourth rf pulses (6, 7). At the end of the fourth rf pulse (8), the on-resonance protons are at  $0^\circ$  (unexcited), whereas the off-resonance protons are rotated  $90^\circ$ .

Composite pulses can be used for general slice excitation, but the most common application is for signal suppression. Fat suppression using a composite pulse excites the fat protons and leaves the water protons unexcited. Spoiler gradients may be applied to dephase the fat transverse magnetization. Application of a standard imaging pulse or pulses produce signals from only the tissue water. Alternately, a composite pulse can be used to selectively excite the water protons by changing the relative polarity of the individual pulses. Known as water excitation, gradient spoiling is not necessary for elimination of the fat signal (Figure 8-8). Composite pulses are very



**FIGURE 8-8** Water excitation image acquired using composite rf pulse. Measurement parameters: pulse sequence, 3D gradient echo, combination pre- and postexcitation;  $TR$ , 25.4 ms;  $TE$ , 9 ms; excitation angle;  $35^\circ$  cumulative; acquisition matrix:  $N_{PE}$ , 256;  $N_{RO}$ , 256;  $FOV$ , 160 mm PE  $\times$  160 mm RO;  $N_{SA}$ , 1; effective slice thickness, 1.56 mm.

sensitive to field homogeneity since differences in the resonant frequency change the cycling time for fat relative to water. Poor homogeneity causes undesired excitation and/or incomplete suppression. For this reason, optimization of the field homogeneity to each patient is advisable.

## ARTIFACTS

---

Artifacts in MR images refer to pixels that do not faithfully represent the anatomy being studied. The general appearance of the images is that the underlying anatomy is visualized but spurious signals are present that do not correspond to actual tissue at that location. The artifacts may or may not be easily discernible from normal anatomy, particularly if they are of low intensity, and may or may not be reproducible. Artifacts can be categorized in many ways; one approach divides them into three groups, according to the cause of the signal misregistration. The first group is a consequence of motion of patient tissue during the measurement. This includes both gross physical motion by the patient and internal physiological motion such as blood flow. The second group is produced primarily as a result of the particular measurement technique and/or specific measurement parameters. The final group of artifacts are independent of the patient or measurement technique, being generated either through a malfunction of the MR scanner during data collection or from a source external to the patient or scanner.

### 9.1 MOTION ARTIFACTS

Motion artifacts occur as a result of movement of tissue during the data acquisition period. They are manifested as signal misregistrations in the phase-encoding direction, though the specific appearance of the artifact depends on the nature of the motion and the particular measurement technique. The artifacts are caused by tissue that is excited at one location and produces signals that are mapped to a different location during detection. As mentioned

in Chapter 4, the typical MRI scan excites and detects signals from a tissue volume multiple times with the phase-encoding gradient  $G_{PE}$  changing amplitude following each rf excitation pulse. The assumption is made that any measured signal intensity variations from one measurement to the next are as a result of  $G_{PE}$  only. When tissue moves, the protons are at a different location at the time of detection and experience a different  $G_{RO}$  amplitude, contributing a different frequency and phase for that measurement. The Fourier transformation mismaps these protons to an incorrect location along the phase-encoding direction in the image. The misregistered signals occur along the phase-encoding direction rather than the readout direction because the encoding of phase by  $G_{PE}$  occurs prior to signal detection, whereas it occurs concurrently with signal detection for  $G_{RO}$ . In general, many measurements are made in the production of an image, each with a different amount of motion contamination. The Fourier transformation of the entire set of measurements does not result in a unique set of frequencies and phases, but in multiple signals in the phase-encoding direction throughout the entire *FOV*.

The sensitivity of a measurement to motion depends on the amount of frequency and phase variation that occurs between successive echoes due to the tissue movement. If the motion occurs during measurements with high positive or negative  $G_{PE}$  (at the edges of the  $k$  space), then the misregistered signal will have very little amplitude and will generate minimal artifacts regardless of the nature of the motion. If the motion occurs during measurements with low amplitude  $G_{PE}$  (low  $k_y$ ), the nature of the motion and the measurement technique will affect the artifact appearance. If the echo timing is relatively slow or the motion is at a moderate rate, significant artifacts will be generated. If the time between successive echoes (echo spacing in echo-train sequences, TR for traditional sequences) is rapid and the motion is relatively slow, the echoes near the center of the  $k$  space may be acquired with the tissue in the same location, so that there are minimal artifactual signals generated. This is the principle behind visualizing the small bowel using single-shot ETSE.

The sequence looping may affect which images of the scan will show motion artifacts, subject to the  $G_{PE}$  discussion above. For scans with one subloop, all images will generally exhibit artifacts. For scans with multiple subloops, artifacts will be present for all images within a subloop. When in-

interleaved acquisition ordering is used, images at adjacent slice positions may show different amounts of artifact contamination.

Probably the most common motion artifact in MRI is due to blood flow. The artifact from blood flow is dependent on the nature of the flow and the flow direction relative to the slice orientation. Through-plane flow (flow that is perpendicular to the slice plane) typically produces a localized artifact in the image with a width equal to the vessel diameter and in line with the source of the flow. Flow that is relatively fast compared to  $TR$  will produce a relatively continuous artifact throughout the  $FOV$ , such as in spin echo images (Figure 9-1a). If the flow is relatively periodic, such as pulsatile flow, then the artifact appears as “ghost” vessels at discrete points, based on the frequency difference between the flow periodicity and  $TR$ . This is often seen from blood flow in the aorta or inferior vena cava (IVC) in transverse slices of the abdomen acquired with gradient echo images (Figure 9-1b). In-

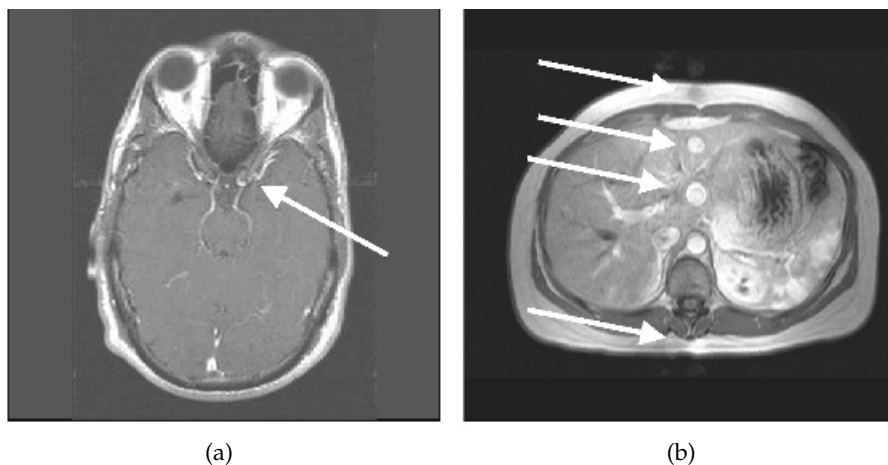


**FIGURE 9-1** Flow misregistration artifact, through-plane. (a) Flow that is fast compared to measurement technique produces a zipper-like artifact (arrow). Measurement parameters are: pulse sequence, spin echo;  $TR$ , 479 ms;  $TE$ , 17 ms; acquisition matrix  $N_{PE}$ , 192;  $N_{RO}$ , 256;  $FOV$ , 172 mm  $PE \times 230$  mm  $RO$ ;  $N_{SA}$ , 1; slice thickness, 5 mm.  $PE$  direction: R–L;  $RO$  direction: A–P. (b) Periodic flow from the aorta will be misregistered as multiple ghosts (arrows). Measurement parameters are: pulse sequence, spoiled gradient echo;  $TR$ : 164 ms;  $TE$ : 4 ms, excitation angle;  $70^\circ$ , acquisition matrix:  $N_{PE}$ , 134,  $N_{RO}$  256;  $FOV$ , 262 mm  $PE \times 350$  mm  $RO$ ;  $N_{SA}$ , 1; slice thickness, 5 mm;  $PE$  direction, A–P;  $RO$  direction, L–R.

plane flow (flow that is parallel to the slice plane) produces a more diffuse artifact, which can be observed from the aorta and IVC in coronal images. The vessel extends through the entire image field and thus the artifact affects all regions of the image (Figure 9-2a). Flow of the cerebrospinal fluid in the brain and spinal canal are also problematic, and can produce analogous artifacts on *T2*-weighted images (Figure 9-2b).

In abdominal or lumbar spine imaging, respiratory motion and peristalsis are the most common causes of severe artifactual signals. The movement of the abdomen during the data collection process produces multiple mis-

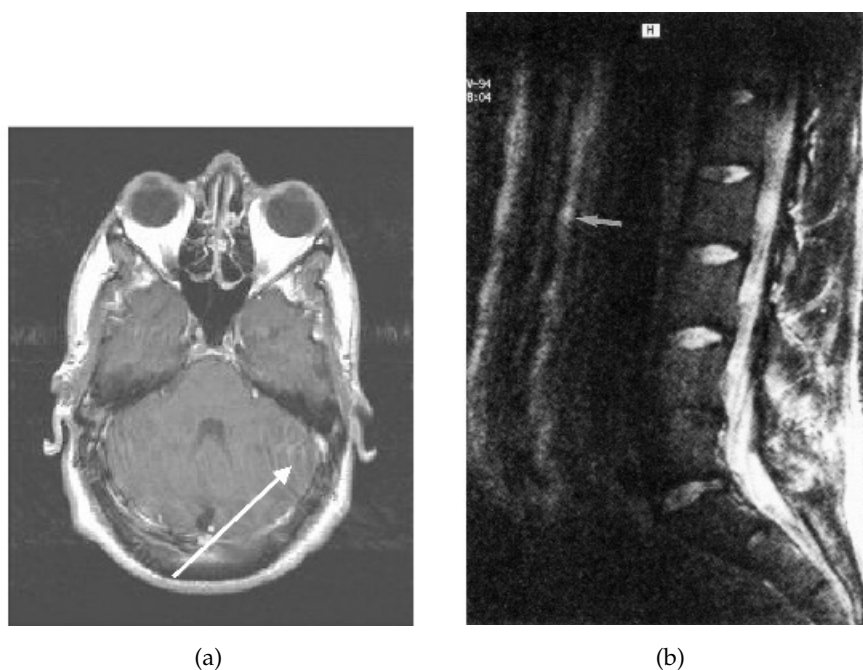


**FIGURE 9-2** Flow misregistration artifact, in-plane. (a) In-plane blood flow will produce severe signal misregistration (arrow). Measurement parameters are: spin echo, *TR*, 479 ms; *TE*, 17 ms; acquisition matrix:  $N_{PE}$ , 192;  $N_{RO}$ , 256; *FOV*, 172 mm *PE*  $\times$  230 mm *RO*;  $N_{SA}$ , 1; slice thickness, 5 mm; *PE* direction: R–L; *RO* direction: A–P. (b) Flow misregistration artifact. Flowing CSF will be misregistered as a “ghost” canal (arrow). Measurement parameters are: pulse sequence, spin echo; *TR*, 2500 ms; *TE*, 90 ms; excitation angle, 90°; acquisition matrix:  $N_{PE}$ , 192,  $N_{RO}$ , 256 with 2 $\times$  frequency oversampling; *FOV*, 210 mm *PE*  $\times$  280 mm *RO*;  $N_{SA}$ , 1; slice thickness, 5 mm; *PE* direction, A–P; *RO* direction, H–R.

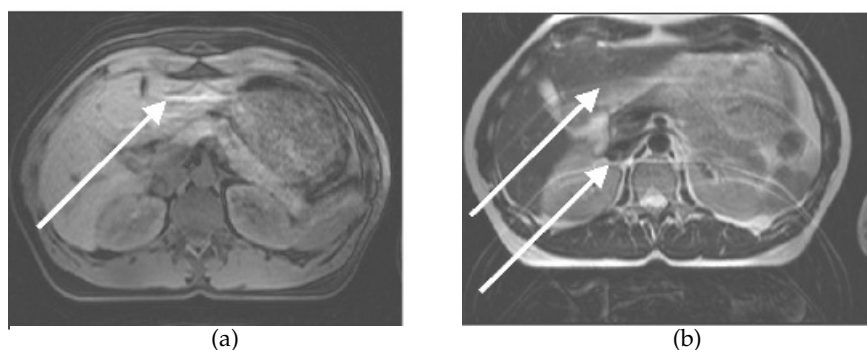


**FIGURE 9-3** Respiratory motion artifact. Extraneous “ghost” images are generated due to motion of the abdominal wall during data acquisition (arrows). The number and severity of the ghosts depends on the  $TR$ , respiration rate, and the particular measurement technique. (a) Pulse sequence, spoiled gradient echo;  $TR$ , 159 ms. (b) Pulse sequence, echo-train spin echo;  $TR$ , 4000 ms.

registration artifacts. If the respiration rate is constant, the “ghost” images are either few in number or discrete and offset in the phase-encoding direction from the true image by an amount proportional to the respiration rate. If the respiration rate is variable, the “ghost” images are numerous and appear as a smearing of the signal throughout the entire image (Figure 9-3a). For segmented techniques such as echo-train spin echo techniques, respiratory motion may appear as multiple lines or so-called “venetian blinds” superimposed throughout the entire  $FOV$  in the phase-encoding direction. The number and spacing of the lines is based on the number of segments for the scan (Figure 9-3b). Peristalsis produces motion artifacts that are less distinct than those from respiratory motion. In most instances, a general blurring of the large and small bowel occurs and a layer of noise is superimposed over the entire image.

## 9.2 SEQUENCE/PROTOCOL-RELATED ARTIFACTS

A second class of artifacts results from the specific measurement process used to acquire the image. Although the appearance of motion artifacts also depends on the particular measurement protocol, this group of artifacts is



more sensitive to technical aspects of the particular pulse sequence and method of data collection used. The origin of these artifacts is relatively constant over the course of the measurement and the resulting signal misregistrations are easily recognized when present.

### 9.2.1 ALIASING

The techniques used for spatial localization assign a unique frequency and phase to each location within the image. These are determined by the acquisition matrix and the desired  $FOV$  in the phase-encoding and readout directions. Aliasing in the readout direction occurs when tissue outside the chosen  $FOV_{RO}$  is excited. This can occur if an  $FOV_{RO}$  smaller than the anatomical slice is selected. The frequencies for this tissue exceed the Nyquist limit for the sampling conditions and are mapped to a lower frequency, a situation known as high-frequency aliasing or frequency wrap-around (Figure 9-4a). The technique used to overcome this is known as frequency oversampling, in which the number of readout data points is increased while maintaining the same sampling time and the same readout gradient amplitude. This is equivalent to increasing the span of  $k_x$  using the same  $\Delta k$ . The oversampled data results in an increase of the Nyquist frequency for the measurement, according to Equation 2-2. Because  $G_{RO}$  is constant, the frequencies at the chosen  $FOV_{RO}$  are unchanged, so that extraction of the central range of frequencies produces an image of the desired size and number of data points. For example, for a  $256 \times 256$  matrix with twofold frequency oversampling, 512 data points are measured but only the central 256 data points are used to create the image (Figure 9-4b).

Aliasing can also occur in the phase-encoding direction when tissue outside the  $FOV_{PE}$  is excited. The protons within this region undergo phase changes corresponding to frequencies greater than can be accurately measured for the  $G_{PE}$  pulse duration (Nyquist limit). They are mapped via the Fourier transformation to a lower phase, in a manner analogous to the aliasing in the readout direction described above. Phase-encoding aliasing can only be eliminated by increasing the effective  $FOV_{PE}$  for the scan. This may be accomplished either by reducing the change in gradient amplitude  $\Delta k_y$  from one phase-encoding step to the next (increasing the  $FOV_{PE}$ ) or by in-

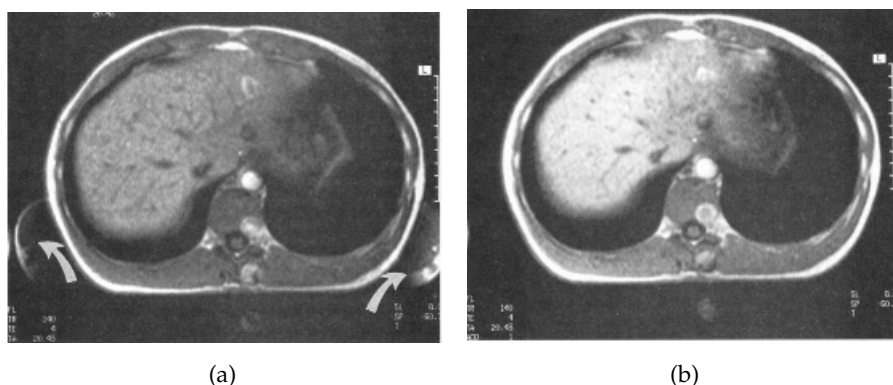


**FIGURE 9-4** Effects of oversampling. (a) Without frequency oversampling, frequencies for the protons within the arms exceed the Nyquist limit and are aliased or incorrectly mapped into the image (arrows). Measurement parameters are: pulse sequence, spoiled gradient echo;  $TR$ , 140 ms;  $TE$ , 4 ms; excitation angle,  $80^\circ$ ; acquisition matrix:  $N_{PE}$ , 128,  $N_{RO}$ , 256;  $FOV$ , 263 mm  $PE \times 350$  mm  $RO$ ;  $N_{SA}$ , 1; slice thickness, 8 mm. (b) Same as Figure 8-4a except with frequency oversampling. The frequencies for the protons within the arms are accurately measured by increasing the number of readout data points measured during the same sampling time while maintaining the same  $G_{RO}$ . Only frequencies corresponding to the selected  $FOV$  are stored so that the arms are excluded from the final image. Measurement parameters are same as (a) except  $N_{RO} = 512$ .

creasing the number of phase changes (i.e., Nyquist frequency) while maintaining the same  $\Delta k_y$ , a technique known as phase-encoding oversampling. Because more echoes are acquired, phase-encoding oversampling will increase the total measurement time while also improving the S/N ratio.

### 9.2.2 CHEMICAL SHIFT ARTIFACTS

Chemical-shift-based artifacts arise from the inherent 3.5 ppm frequency difference between fat and water protons under the influence of an external magnetic field, as described in Chapter 2. Two constant artifacts may be generated by this frequency difference. One is known as the chemical shift artifact, which is a misregistration of fat and water protons from a voxel that are mapped to different pixels. As described in Chapter 4, the detected signal from a voxel is mapped to a position based on its frequency accord-

ing to Equation 4-1, under the assumption that all protons within a voxel resonate at the same frequency. Due to the difference in molecular structure, fat protons have an intrinsically lower resonant frequency than water protons when exposed to the same external magnetic field. Fat protons within a voxel are affected by the same  $G_{RO}$  as the water protons but will be mapped to a lower-frequency pixel in the readout direction. This misregistration is not noticeable in tissues with uniform fat–water content, but can be seen at the borders between tissues with significantly different fat–water content; for example, between disk and vertebrae in the spine or between kidney and retroperitoneal fat. Parallel areas of bright and dark pixels can be visualized where the fat and water signals superimpose and where they do not, respectively (Figure 9-5a). The number of pixels corresponding to the chemical shift artifact (CSA) depends upon the frequency difference in Hz between fat and water, the total receiver bandwidth, and the number of readout data points spanning the  $FOV_{RO}$ :

$$CSA = \Delta\omega * N_{RO} / BW_{REC} \quad (9-1)$$

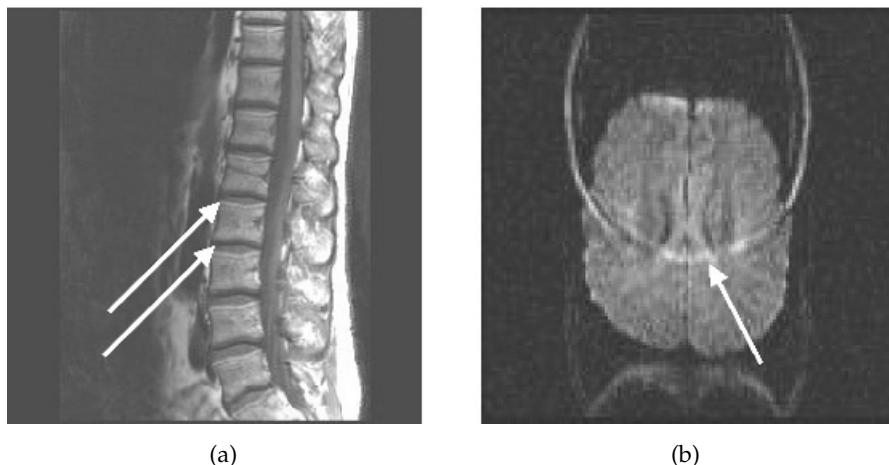


**FIGURE 9-5** Chemical shift artifact. (a) Note alternate bands of light and dark at the interface between the vertebrae and disk (arrows). Measurement parameters: pulse sequence, spin echo; receiver bandwidth 20 kHz; readout direction, L – R. (b) A complete misregistration of fat from the bone marrow of the skull (arrow). Measurement parameters are: pulse sequence, spin echo EPI; phase-encoding direction, A–P.

At 1.5 T, the frequency difference is 225 Hz so that, for a scan with a total receiver bandwidth of 20 kHz and  $N_{RO} = 256$ , the CSA will be 2.8 pixels. The severity of the artifact in the final image will depend on the  $FOV_{RO}$ . If an  $FOV_{RO}$  of 350 mm is used, this translates into a fat/water misregistration of 3.6 mm. For an  $FOV$  of 175 mm, the artifact is only 1.8 mm. For a scan with a receiver bandwidth of 33 kHz, the CSA will be 1.7 pixels with a misregistration of 2.2 mm. Chemical shift artifacts are most prominent at magnetic field strengths greater than 1.5 T, using low or narrow receiver bandwidths and large  $FOV$ , and at fat–water tissue interfaces.

In theory, chemical shift artifacts are possible in all three directions (slice selection, phase encoding, and readout), since magnetic field variations (gradient pulses) are used for localization in all cases. In the slice selection direction, the rf pulse bandwidth and gradient amplitude are chosen to keep this at a minimum. In addition, because the slice selection direction is not directly visualized, any misregistration in this direction is difficult to discern. This may not be the case in MR spectroscopic scans, where there may be observable variations in signal amplitude (see Chapter 13).

The appearance of the chemical shift artifact in the readout and phase-encoding directions depends on the particular pulse sequence. For routine imaging techniques such as spin echo, echo-train spin echo, or gradient echo, the phase-encoding process is reinitiated following each excitation pulse. Since  $\Delta k_y$  is constant, fat and water protons located at the same position undergo equal amounts of phase change. They are mapped to the same location in the image and no artifact results. For these techniques, chemical shift artifacts may be observed in the readout direction, based on the specific criteria described previously. For echo planar imaging, the receiver bandwidth is normally very large (in excess of 100 kHz) so that fat and water frequencies are mapped to the same pixel. However, the phase-encoding process for the entire image occurs in a continuous fashion following one or two excitation pulses. Chemical shift artifacts will be observed in the phase-encoding direction and are very significant. Because the  $G_{PE}$  amplitude is very low, the misregistration may be as much as 12–15 pixels (Figure 9-5b). Use of fat suppression techniques is necessary to minimize the artifact.

### 9.2.3 PHASE CANCELLATION ARTIFACT

The second artifact induced by the chemical shift difference is known as the phase cancellation artifact, observed in out-of-phase gradient echo images. As shown in Figure 2-6, the fat protons cycle in phase relative to the water proton precession. For normal spin echo and fast spin echo sequences, this phase cycling is exactly reversed by the  $180^\circ$  rf pulse(s) so that the fat and water protons always contribute to the signal at the echo time,  $TE$ , with the same polarity; that is, the fat and water protons are described as “in phase” when the signal is detected regardless of the choice of  $TE$ . In gradient echo sequences, the phase cycling is not reversed and this causes fat and water protons to contribute differently to the detected signal, depending on the particular  $TE$ . Voxels containing both fat and water have additional signal intensity variations in addition to those due to relaxation. For certain choices of  $TE$ , known as “out-of-phase”  $TE$ , very little signal will be detected if the voxel has equal water and fat content such as those voxels located at interfaces between fat- and water-based tissues. This signal cancellation appears as a dark ring surrounding the tissue (Figure 9-6).

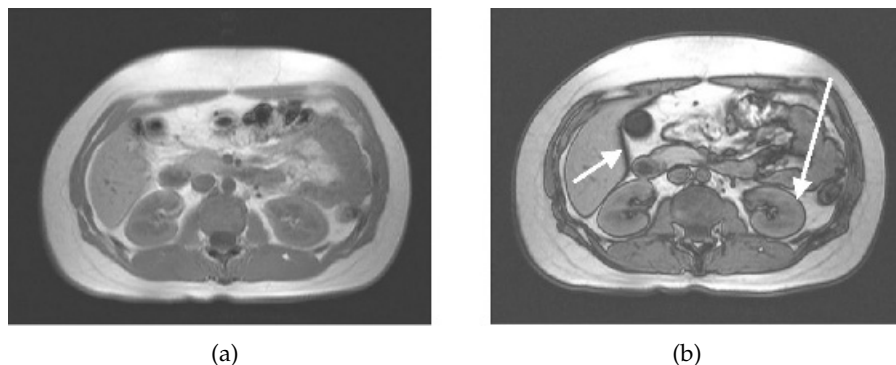


**FIGURE 9-6** Phase cancellation artifact. Other measurement parameters are: pulse sequence, 2D spoiled gradient echo;  $TR$ , 164 ms; excitation angle,  $70^\circ$ ; acquisition matrix:  $N_{PE}$ , 134,  $N_{RO}$ , 256;  $FOV$ , 263 mm  $PE \times 350$  mm  $RO$ ;  $N_{SA}$ , 1; slice thickness, 9 mm. (a) In-phase image ( $TE$  4.5 ms). Fat and water protons have the same phase and contribute in the same fashion to the image contrast. (b) Out-of-phase image ( $TE$  2.2 ms). Fat and water protons have opposite phases and contribute in opposite fashion to the image contrast. For voxels with equal amounts of fat and water, such as at the interface between liver or kidney and retroperitoneal fat, cancellation of signal occurs, producing a dark band (arrows).

The  $TE$  values that generate this phase cancellation depend on the magnetic field strength, since the time for the phase cycling depends upon the resonant frequency difference  $\Delta\omega$  in Hz between fat and water:

$$TE_{\text{inphase}} = 1/\Delta\omega \quad (9-2)$$

The out-of-phase  $TE$  times occur midway between the in-phase times (Table 9-1). Out-of-phase images are often used to assess the amount of fat contribution to a voxel. The phase cancellation artifact observed using out-of-phase  $TE$  makes it difficult to assess the interface of tissues with different fat and water contents. The phase cycling also affects the signal content of all tissues throughout the image. Unless there is a specific reason for using an out-of-phase  $TE$ , such as for the assessment of fatty infiltration in the liver or adrenal masses or to use very short  $TR$ , a  $TE$  corresponding to an in-phase relationship is preferable.

#### 9.2.4 TRUNCATION ARTIFACTS

Truncation artifacts are produced by insufficient digital sampling of the echo. The most common instance of this condition occurs when data collection is terminated while significant signal is still being emitted by the protons, which can happen in  $T1$ -weighted imaging when there is a high signal amplitude from fat at the edge of the region still present at the end of data collection. The Fourier transformation of this truncated data set produces a “ringing” type of signal oscillation that emanates from the edge of the anatomy (Figure 9-7). Truncation artifacts can also occur if the echo is sampled in an asymmetrical fashion; that is, the echo is not sampled equally on both sides of the echo maximum (Figure 9-8). This type of data sampling is often used in very short  $TE$  sequences (<3 ms) to minimize the receiver bandwidth.

TABLE 9-1 Phase Cycling  $TE$  Times

Field Strength, T	In-Phase $TE$ , ms	Out-of-Phase $TE$ , ms
0.5	13.3, 26.67	6.67, 20
1.0	6.67, 13.3, 20	3.3, 10, 16.67
1.5	4.5, 9.0, 13.5, 18.0	2.25, 6.75, 11.25, 15.75
3.0	2.25, 4.5, 6.75, 9.0	1.12, 3.38, 5.63, 7.88



**FIGURE 9-7** Truncation artifact. Image acquisition with asymmetric sampling produces a banding artifact (arrow) originating from the high signal of subcutaneous fat. Measurement parameters: pulse sequence, spoiled gradient echo;  $TR$ , 170 ms;  $TE$ , 4 ms; excitation angle,  $80^\circ$ ; acquisition matrix,  $N_{PE}$ , 144,  $N_{RO}$  256 with twofold oversampling;  $FOV$ , 262 mm  $PE \times 350$  mm  $RO$ ;  $N_{SA}$ , 1.

Reduction of truncation artifacts involves reducing the signal amplitude so that it is minimal at the beginning or end of the data collection period. This reduction can be achieved in two ways. One is to reduce the fat signal through fat suppression (since fat typically has the largest signal in  $T1$ -weighted images), either using a fat-saturation pulse or using an inversion recovery technique. This approach changes the intrinsic image contrast and may be unacceptable for the particular clinical application. The other method is to apply an apodization filter to the raw data prior to Fourier transformation. This numerical process forces the signal amplitude to zero at the end of the data collection period. Several types of apodization filters are available (e.g., Fermi, Gaussian, Hanning), each with different characteristics regarding the filter shape. Use of apodization filters improves the signal-to-noise ratio by removing high-frequency noise from the signal. However, excessive filtering eliminates high frequencies responsible for

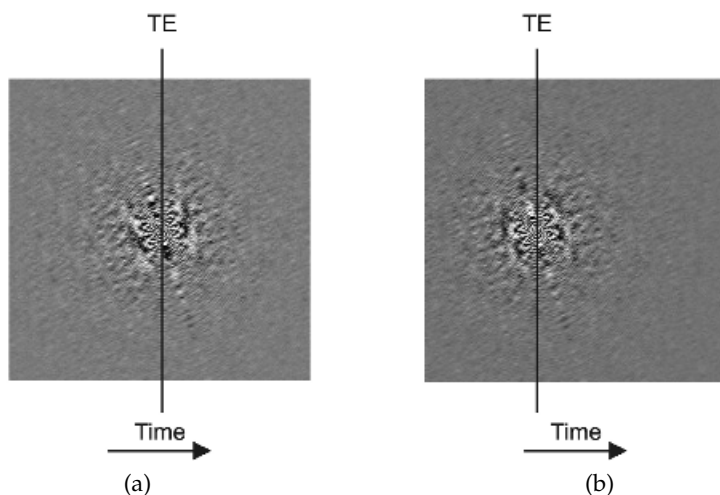


**FIGURE 9-8** Symmetric versus asymmetric echo sampling. (a) In symmetric sampling, the echo is maximum ( $TE$ ) midway through the sampling period so that both sides of the echo signal are measured equally. Filtering of the data can be performed in a symmetrical fashion. (b) In asymmetric sampling, the echo maximum is in the early portion of the sampling period. Significant signals are present when the sampling begins and filtering of the signals is difficult.

fine spatial resolution or edge definition so that blurring is possible. Asymmetric echo sampling may require more extensive filtering to reduce truncation artifacts. Acquiring the echo in a symmetric fashion reduces the amount of filtering necessary.

### 9.2.5 COHERENCE ARTIFACTS

Coherence artifacts are a class of artifacts that can have a variable appearance, based on the particular measurement technique used and how it is implemented on the scanner. They are produced by the rf pulses generating unwanted transverse magnetization that contributes to the detected signal. One coherence artifact is known as an FID artifact. As mentioned in Chapter 5, the rf excitation pulses are not uniform in profile. For instance, while most of the protons in a slice would experience a  $180^\circ$  excitation pulse, those located at the edges of the slice would experience a range of excitation



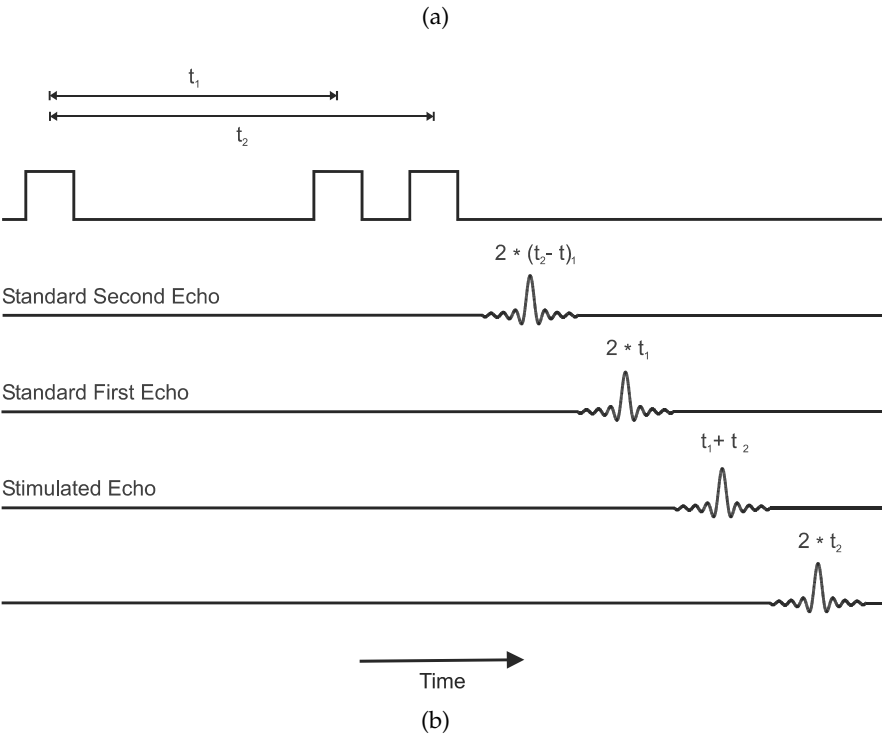
angles, all less than  $180^\circ$ . The FID from these protons may still be producing significant signals when the desired echo signal is measured. Because the  $180^\circ$  rf pulse normally occurs after the phase-encoding gradient during sequence execution, the induced signal will contribute identically during each ADC sampling period. The resulting artifact is a line of constant phase in the final image.

Another coherence artifact may be produced by the effects of the multiple rf excitation pulses on the protons. The spin echoes used to produce  $T_1$ - and  $T_2$ -weighted images are but two of several echoes generated by rf excitation pulses within an imaging sequence. For example, a series of three rf pulses such as a presaturation pulse and a  $90^\circ$ – $180^\circ$  pulse pair or a  $90^\circ$ – $180^\circ$ – $180^\circ$  pulse trio may generate four or five echoes. The timing and number of echoes depends on the exact spacing of the pulses (Figure 9-9). The amplitude of each echo depends on the excitation angle of the individual pulses and the particular tissues being measured. These “secondary” echoes contain all the frequency information of the so-called primary echoes normally used, but the signals have different  $T_1$  and  $T_2$  weightings. Should these other echoes occur while the ADC is sampling the primary echoes, they will contribute to the final image. They may produce either line artifacts if not phase encoded, or an additional image if phase encoded (Figure 9-10). One of these echoes, the stimulated echo, is incorporated into the design of fast spin echo imaging techniques and the volume selection in MR spectroscopy (Chapter 13).

Pulse sequences are usually designed with great care to minimize the contamination of the desired echo signals by the undesired echoes. When these undesired echoes form during the ADC sampling period due to the particular rf pulse timing, some form of coherence spoiling is used. Two approaches are used to dephase the transverse magnetization so that there is

---

**FIGURE 9-9** Echo timing plots. (a) Time  $t_1$  is less than  $t_2$ , typical of a standard short  $TE$ /long  $TE$  spin echo pulse sequence. Five echoes are formed. Two are used in routine imaging (echoes 1 and 3). The stimulated echo occurs at time  $t_1 + t_2$  (echo 2); (b) Time  $t_1$  is greater than  $t_2$ , typical of a spin echo pulse sequence with a short  $TE$  and a spatial presaturation pulse. Four echoes are formed. Two are used in routine imaging (echoes 1 and 2). The stimulated echo occurs at time  $t_1 + t_2$  (echo 3).



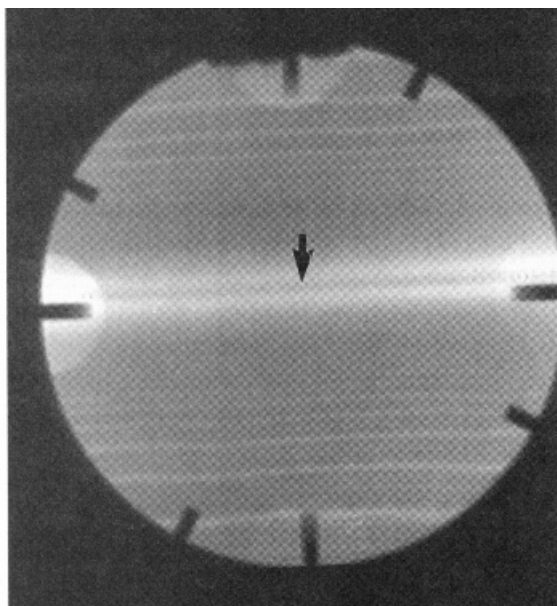


FIGURE 9-10 Signal contributions from undesired echoes produce banding artifacts (arrow). These echoes can be minimized through the use of coherence spoiling.

minimal coherence present from these secondary echoes. The most common method is to include additional gradient pulses applied at appropriate times during the pulse sequence, an approach known as gradient spoiling. These gradient pulses are usually of high amplitude and/or long duration. The time at which these pulses are applied depends on which coherence is to be spoiled and what  $TE$  is chosen. Spoiler gradients applied following the  $180^\circ$  refocusing pulse reduce the FID artifact resulting from nonuniform rf excitation. Spoiler gradients following the data collection, such as those used in spin echo sequences (see Figure 6-2), minimize coherence contamination of the subsequent echoes. For many sequences, the duration of the spoiler gradient pulse may be 30–50% of the slice loop. Gradient spoiling may also use a series of amplitudes rather than a constant amplitude pulse in order to improve spoiling if the rf interpulse time is short.

The other approach for spoiling unwanted transverse coherence is known as rf spoiling. Normal data acquisition techniques apply rf pulses of constant phase or with a  $180^\circ$  phase alternation of the excitation pulse (i.e.,

$+90^\circ$ ,  $-90^\circ$ ,  $+90^\circ$ , ...). The receiver is also phase alternated to match the transmitter phase so that signal averaging can be performed. Rf spoiling applies a phase variation other than  $\pm 90^\circ$  or  $\pm 180^\circ$  to the excitation pulse and receiver. The desired echo signals add in a coherent fashion, whereas the other echoes add in an incoherent manner. If a sufficiently large number of phase variations is used, the net result is that the undesired signals average to zero. Rf spoiling does not require additional time during the slice loop, but does require sophisticated phase modulation of the transmitter.

### 9.2.6 MAGNETIC-SUSCEPTIBILITY DIFFERENCE ARTIFACTS

A third artifact whose appearance is sensitive to the measurement sequence is caused by differences in magnetic susceptibility  $\chi$  between adjacent regions of tissue. As mentioned in Chapter 1, the magnetic susceptibility is a measure of the spin polarization induced by the external magnetic field. The degree of polarization depends on the electronic and atomic structure of the sample. Tissues such as cortical bone or air-filled organs such as lungs or bowel contain little polarizable material and have very small  $\chi$  values. Soft tissue has a greater degree of polarization and a larger  $\chi$ . At the interface between soft tissues and the area of different susceptibility, a significant change in the local magnetic field is present over a short distance, causing an enhanced dephasing of the protons located there. As  $TE$  increases, there is more time for proton dephasing to occur, which results in signal loss. This dephasing is reversed by the  $180^\circ$  refocusing pulse in spin echo imaging since it is constant over time, but contributes to the contrast in gradient echo imaging (Figure 9-11). Magnetic susceptibility dephasing is also observed following administration of a paramagnetic contrast agent as the agent accumulates in the kidney and bladder. A significant signal loss occurs as the agent concentration in these organs increases (Figure 9-12).

## 9.3 EXTERNAL ARTIFACTS

External artifacts are generated from sources other than patient tissue. Their appearance in the final images depends on the nature of the source and the

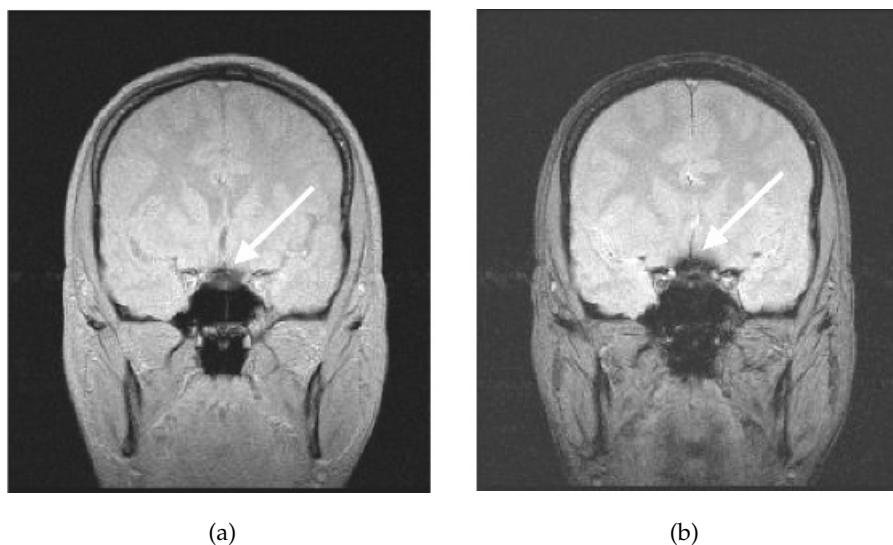


**FIGURE 9-11** Magnetic susceptibility difference artifact. Increase in  $TE$  causes increased sensitivity to  $T2^*$  in gradient echo pulse sequences. Increased distortions occur in areas where there are significant differences in magnetic susceptibility such as in the posterior fossa (arrows). Other measurement parameters: pulse sequence, spoiled gradient echo;  $TR$ , 170 ms; excitation angle,  $30^\circ$ ; acquisition matrix:  $N_{PE}$ , 224,  $N_{RO}$ , 256;  $FOV$ , 201 mm  $PE \times 230$  mm  $RO$ ;  $N_{SA}$ , 1. (a)  $TE$ , 4 ms; (b)  $TE$ , 15 ms.

measurement conditions. The sources may be classified into two general categories: those originating from a malfunction or miscalibration of the MRI hardware and those that are not. Excluded from this group are hardware problems that cause complete failure of data collection or image reconstruction. Manufacturers exert great effort to ensure that the acquired images faithfully represent the MR signals from the defined area of interest. The artifacts described here are not specific to any particular manufacturer, but can occur on any MR system.

### 9.3.1 MAGNETIC FIELD DISTORTIONS

One of the most common system-related problems is produced by static distortions of the main magnetic field. During system installation, manufac-



**FIGURE 9-12** Magnetic susceptibility difference artifact. As paramagnetic contrast agents accumulate in the kidneys, the local magnetic field is distorted, causing enhanced dephasing of the protons in the vicinity and producing signal voids (arrows). Measurement parameters are: pulse sequence, spoiled gradient echo;  $TR$ , 140 ms;  $TE$ , 4 ms; acquisition matrix:  $N_{PE}$ , 128,  $N_{RO}$  256 with twofold oversampling;  $FOV$ , 263 mm  $PE \times 350$  mm  $RO$ ;  $N_{SA}$ , 1.

turers perform a field-optimization procedure known as shimming to eliminate coarse distortions of the central magnetic field caused by metal in the immediate vicinity of the magnet. However, patients also produce field distortions due to their nonuniform shape and tissue content. These distortions can cause contrast variations within the image, particularly when fat saturation is used.

Metal implants will deform the local magnetic field homogeneity surrounding it, producing significant artifacts. These artifacts frequently appear as an expansive rounded signal void with peripheral areas of high signal intensity distorting the surrounding regions, termed a “blooming” artifact. The size and shape of the artifact depends on the size, shape, orientation, and nature of the metal and the pulse sequence used for the scan

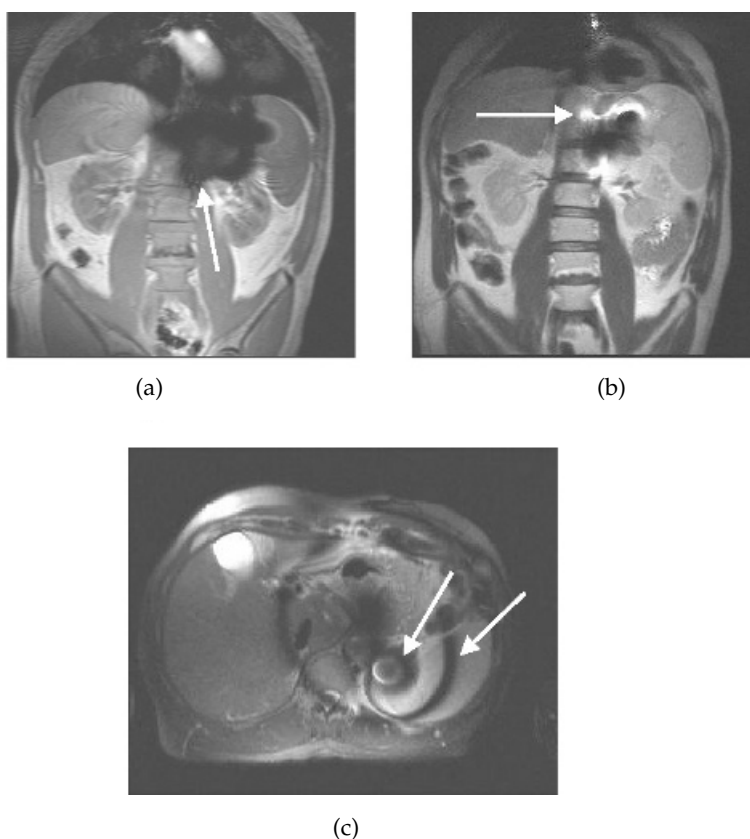


**FIGURE 9-13** Magnetic susceptibility difference artifact. Surgical clips produce a void of signals caused by the significant magnetic field distortion. (a) Spoiled gradient echo sequence shows significant signal distortion (arrow). (b) Single-shot echo-train spin echo at the same level shows less signal loss (arrow). (c) Single-shot echo-train spin echo with fat saturation shows incomplete saturation due to field distortions (arrows).

(Figure 9-13). Titanium or tantalum produce very localized distortions, whereas stainless steel can produce severe distortions that may compromise the images (Figure 9-14). All echoes are affected by the presence of the metal. Gradient echo sequences are much more sensitive to metal distortions. In some instances, only spin echo sequences may produce acceptable images. Echo-train spin echo techniques with very long echo trains are least sensitive to these distortions, and should be used when metal is

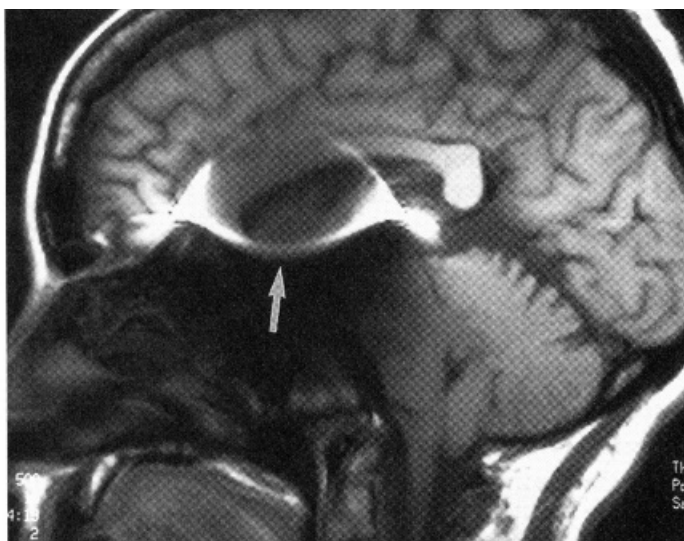


FIGURE 9-14 Stainless steel aneurysm clip produces severe field distortion. Pulse sequence, spin echo.

known to be in the imaging field. In addition, common metal objects within the bore, such as paper clips or staples, can cause severe image distortion.

The amount of image distortion observed from static field inhomogeneities depends on the specific measurement technique. If the field homogeneity disruption is severe, the signal loss will be enough to preclude any image whatsoever. In general, gradient echo sequences are most sensitive to field distortions. This is due to the echo signal amplitude being a function of  $T2^*$ , in which proton dephasing from magnetic field inhomogeneities is a significant factor affecting the image contrast. As in the case of magnetic-susceptibility differences discussed earlier, very short  $TE$  values allow little time for such dephasing and result in smaller signal voids. Longer  $TE$  values allow more time for dephasing and can produce significant artifacts. Spin echo sequences, which include a  $180^\circ$  refocusing rf pulse, can also be used to minimize the intensity variations.

Another instance of magnetic field distortion occurs when fat saturation



is used. As mentioned in Chapter 9, fat saturation pulses are rf pulses centered at the fat resonant frequency that saturate the fat protons, leaving only the water protons to contribute to the image. If the field homogeneity is not uniform, the fat-suppression pulse may not uniformly suppress the fat and may even suppress the water within the tissue. This condition results in regions of nonuniform fat suppression within the image (see Figure 8-3b) and is most commonly observed at the edges of the optimized portion of the field, as can occur in images with large *FOV* or with extreme superior or inferior positions. It is advisable to try to center the anatomy within the magnet as much as possible and to perform field homogeneity correction with the patient inside the scanner prior to fat saturation.

### 9.3.2 MEASUREMENT HARDWARE

Hardware-induced artifacts are those produced by malfunctioning of one or more of the scanner components during the data collection. Most MR techniques perform multiple measurements on the volume of tissue, varying only a single gradient amplitude (the phase-encoding gradient) from one measurement to the next. The assumption is that any amplitude variation in the detected signal is caused by the phase-encoding gradient, providing the basis for localization in that direction. One of the primary requirements for success of the measurement hardware used in this approach is that the gradient and rf transmitter systems act in a reliable and reproducible fashion. A lack of stability in the performance of either system causes amplitude or phase modulations that distort the detected signal in addition to those intrinsic to the measurement. These distortions result in smearing or ghosting artifacts in the phase-encoding direction throughout the entire image field. The magnitude and nature of the instability determines the amount of smearing. In many instances, the instability artifacts are indistinguishable from motion artifacts. Manufacturers perform tests during system calibration to assess the stability of the various systems to ensure that their performance is reproducible and stable.

Proper calibration of the measurement hardware is another important contribution to high-quality MR imaging. The gradient, rf transmitter, and receiver systems are calibrated to ensure their proper performance.

Improper calibration produces variable distortions, depending on which component is considered. Nonlinear gradient pulses or incorrect amplitude calibration cause incorrect spatial localization and/or image distortion (Figure 9-15). Improper rf calibration causes incorrect or nonuniform excitation power, which may or may not be noticeable in the resulting images. The rf power deposition as measured by the specific absorption rate (SAR) will also be inaccurate. Receiver miscalibration causes incorrect amplification of the echo signal, which may result in insufficient gain so that the signal does not exceed the background noise or in excessive gain, which may cause the echo signal to exceed the digitization limits of the scanner (Figure 9-16).

### 9.3.3 NOISE

A final artifact often present in MR images is noise. Noise can have a variety of appearances, depending on the origin and nature of the source. It may



**FIGURE 9-15** Gradient miscalibration. The phase-encoding gradient is two times the correct amplitude. Note the incorrect aspect ratio.

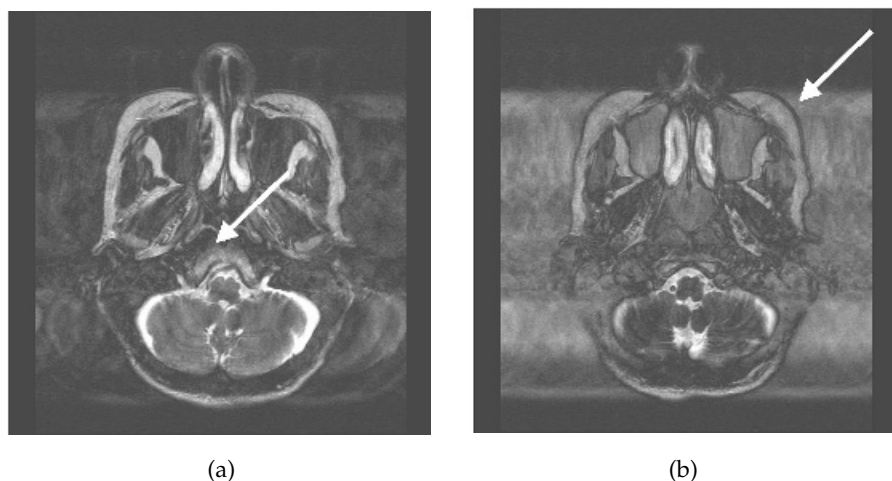
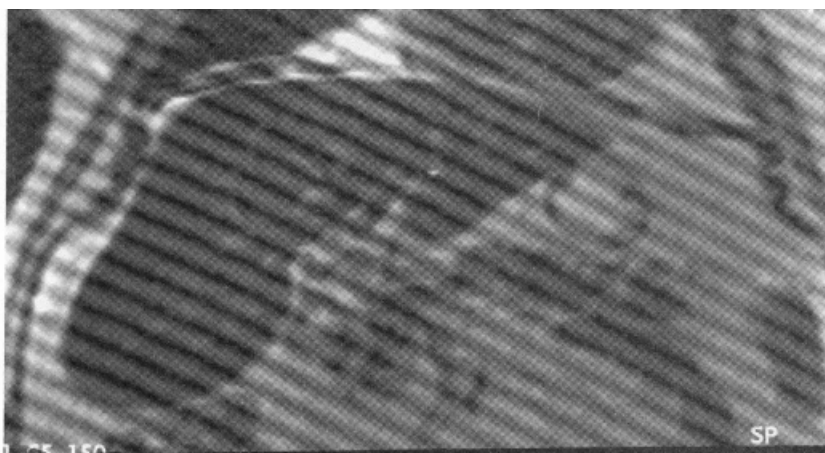


**FIGURE 9-16** Receiver miscalibration. (a) Normal image. (b) Image from same scan with signal amplified in excess of the maximum input voltage for the ADC. Note the enhanced background signal (arrow) and changes in contrast.

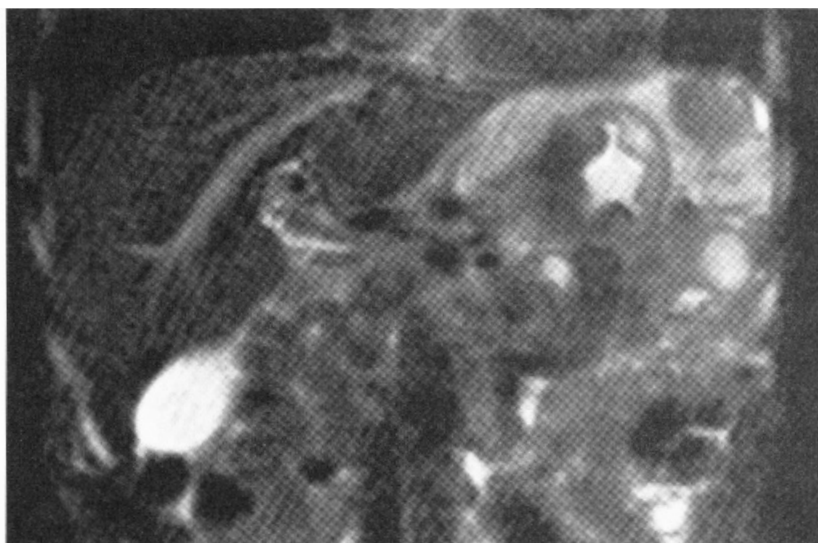
appear as a film superimposed over the normal anatomy, with or without discernible patterns, or it may have a discrete pattern or patterns. The two most common examples of coherent noise are spikes and those arising from external sources.

Spikes are noise bursts of short duration that occur randomly during the data collection. They are normally caused by static electricity discharges or arcing of electrical components, but may be generated by many different sources. Their appearance in an image depends on the severity, number, and location of the spikes in relation to the signal maximum but tend to appear as waves superimposed on the normal image data (Figure 9-17). They may or may not occur in all images of the scan. Spikes are particularly problematic to isolate because they are often irreproducible, particularly if the source is static discharge.

External interference artifacts occur when there is a source of time-varying signals detected by the receiver. They appear as lines of constant frequency within the image. Their positions depend on the receiver bandwidth of the sequence and the frequency difference from the transmitter. The most common example of this is from the alternating nature of stan-



(a)

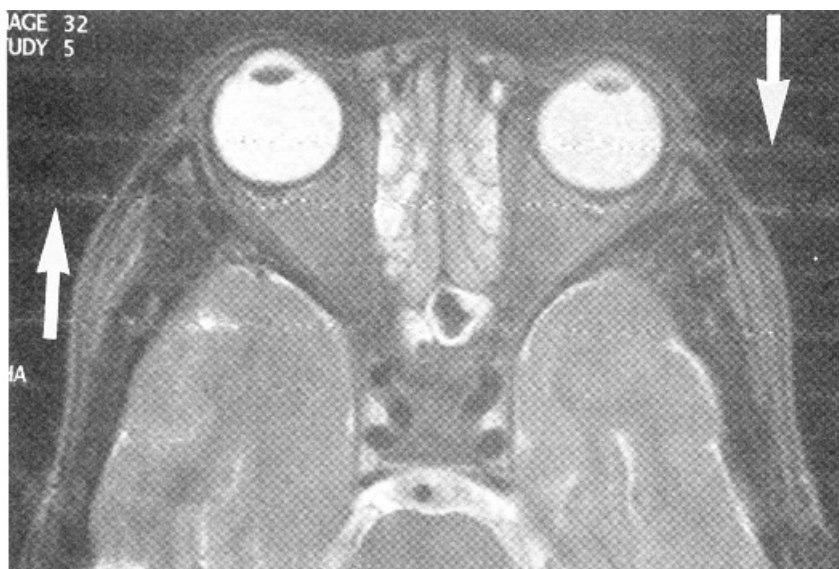


(b)

**FIGURE 9-17** (a and b). Spikes. Transient electrical discharges (spikes) during the data collection period produce a banding pattern that is superimposed across the entire imaging field. The direction and spacing of the bands depends on the timing of the discharge relative to the collection of the central phase encoding steps.



(a)



(b)

**FIGURE 9-18** External interference. (a). Artifact due to electrical source outside the scanner room. (b) Interference from portable patient medication unit operating in scanner room during the measurement (arrows).

dard electrical current (AC; 60 Hz in the United States, 50 Hz in Europe and Asia) (Figure 9-18). Electrical connections for any equipment such as external patient monitoring devices used in the scanner room should be filtered before being allowed to penetrate the Faraday shield, or the use of nonalternating (DC) current should be considered. Manufacturers should be consulted before incorporating any electrical equipment into the scanner room to ensure compatibility with the MR scanner.

## MOTION ARTIFACT REDUCTION TECHNIQUES

---

As discussed in Chapter 9, motion in an MR image can produce severe image artifacts in the phase-encoding direction. The severity of the artifact depends on the nature of the motion, the time during data collection when the motion occurs, and the particular pulse sequence and measurement parameters. The most critical portion of the data collection period for artifact generation is during the collection of echoes following low-amplitude phase-encoding steps (center of  $k$  space). Motion during the high-amplitude phase-encoding steps (edges of  $k$  space) can cause blurring but not severe signal misregistration in the image.

Four methods are commonly used to reduce the severity of the motion artifact in the final image. If signals from the moving tissue are not of interest, use of a spatial presaturation pulse, as described in Chapter 8, can significantly reduce artifactual signals. This is useful to suppress abdominal or cardiac motion artifacts in spine examinations. The other techniques are useful when signals from the moving tissue are desired. Two of these, acquisition parameter modification and physiological triggering, affect the mechanics of the data collection process, and the third method, flow compensation, alters the intrinsic signal from the moving tissue. Although none of these approaches completely removes motion artifacts from the image, use of one or more of these techniques substantially reduces the impact of motion on the final images.

## 10.1 ACQUISITION PARAMETER MODIFICATION

Proper choice of the acquisition parameters can alter the appearance of motion artifacts. One example of this is to define the phase encoding direction so that the motion artifact does not obscure the area of interest. This may be referred to as motion artifact rotation or switching the frequency and phase-encoding directions. This approach does not eliminate or minimize the artifact, but only changes its position within the image. For example, motion artifacts due to eye movement or blood flow from the sagittal sinus vein may obscure lesions in the cerebrum if the phase-encoding direction for a transverse slice is in the anterior–posterior direction. If the phase-encoding direction is in the left–right direction, the eye motion artifacts are superimposed and lie outside the brain. The blood flow artifact also appears in an area outside the brain (Figure 10-1).

Another example of parameter modification is to increase the number of signal averages. This approach is of particular benefit in abdominal imaging, in which respiratory motion can produce severe ghosting. With multi-

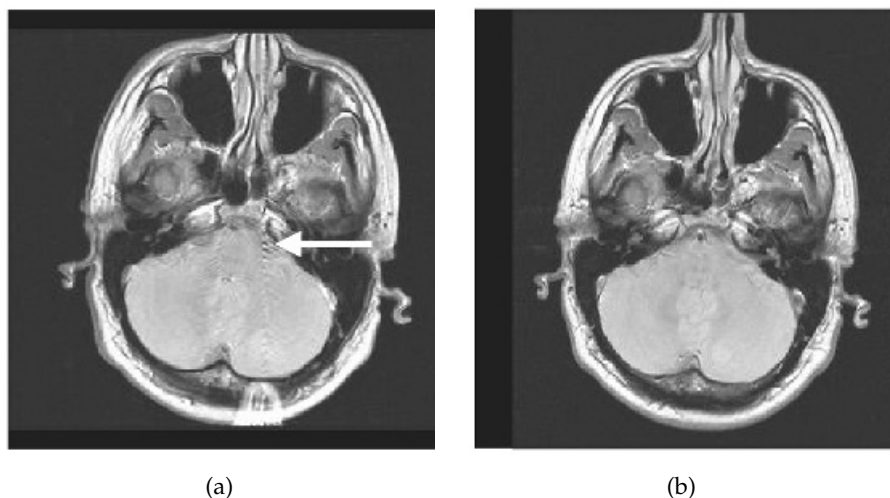


**FIGURE 10-1** The direction of motion artifacts is determined by the phase-encoding gradient. Blood flow during the scan produces motion artifacts (arrows). (a) *PE*: left–right. *RO*: anterior–posterior; (b) *PE*: anterior–posterior. *RO*: left–right.



ple averages, the signal from the tissue is based on its average position throughout the scan. Since the tissue is in the same location most of the time, the signals add coherently. The motion artifact signal will be reduced in amplitude relative to the tissue signal.

Alternately, removal of respiratory artifacts in abdominal or cardiac imaging can be accomplished by measuring all the scan data within one breath-hold. For example, a  $TR = 140$  ms,  $N_{PE} = 128$ , and  $N_{SA} = 1$  can produce a complete scan in 18 seconds. The spatial resolution may be compromised in the phase-encoding direction, depending on the  $FOV$ , but respiratory motion and its artifacts will not be present if the patient suspends respiration. Extreme examples of this approach are single-shot echo-train spin echo and EPI techniques, in which images can be acquired in less than one second, producing heart and bowel images that are virtually motion-artifact free (Figure 10-2).



FIGURE 10-2 Single-shot echo-train spin echo image of abdomen. Note lack of motion artifact from heart and bowel.

## 10.2 TRIGGERING/GATING

Another method for visualizing moving tissue allows the tissue to move but synchronizes the data collection with a periodic signal produced by the patient, such as a pulse or heartbeat. The data-collection-timing-signal relationship can be exploited in two ways. Prospective methods initiate the data collection following detection of the timing signal. The signal detection for a particular slice always occurs at the same time following the timing signal. Since the moving tissue is in the same relative position at this time, there is minimal misregistration of signal and a significant reduction of the resulting motion artifact. Retrospective methods measure the timing signal together with the echo signal, but the timing signal is not analyzed nor are the measured data adjusted until the scan is completed. The data collection process can also be triggered by or gated to the timing signal.

Triggering examinations are commonly prospective in nature and begin the data collection following detection of a signal. The noise produced by the scanner during sequence execution is also synchronized to the signal source. The  $TR$  controlling the contrast is based on the repetition time for the trigger signal  $T_{REP}$  rather than the  $TR$  entered in the user interface. Several external methods for detection of the timing signal can be used. For cardiac imaging, data collection is synchronized to the electrocardiogram (ECG) signal measured from the patient using lead wires. Pulse triggering uses a pulse sensor to detect the pulse, usually measured on an extremity. Respiratory triggering uses a pressure transducer attached to the patient to measure either chest or abdominal motion. An internal method for a timing reference uses a so-called “navigator echo” that, when properly positioned, can measure an MR signal from the diaphragm or other tissue and indicate that motion has occurred.

There are several potential problems with triggered studies. One is that the scan time is longer for a triggered study than for the corresponding untriggered study. Time must be allowed from the end of data collection (traditionally  $TR$ ) to the next trigger signal to ensure that the trigger signal is properly detected by the measurement hardware. This extra time is usually 150–200 ms to allow for variation of the rate of the trigger signal for the patient. The total scan time will be extended by approximately 1–2 minutes.

Another problem occurs if the rate of the trigger signal is irregular. The  $T_{REP}$  for a particular phase encoding step depends on the R-R time interval immediately prior to the step under consideration. Variation in the heart rate causes variation in the amount of  $T_1$  relaxation from measurement to measurement for each phase-encoding step. This variation produces amplitude changes in the detected signal, producing misregistration artifacts in the final images even if the triggering is perfect. Stability of the heart rate is most critical during collection of the echoes around the  $k$  space center ( $k_y = 0$ ).

Cardiac examinations are one example of an examination that typically uses prospective triggering. The peak R wave is normally used as the timing reference point. Each phase-encoding step is acquired at the same point in time following the R wave so that the heart is in the same relative position (Figure 10-3). Since the kernel time per slice is shorter than the duration

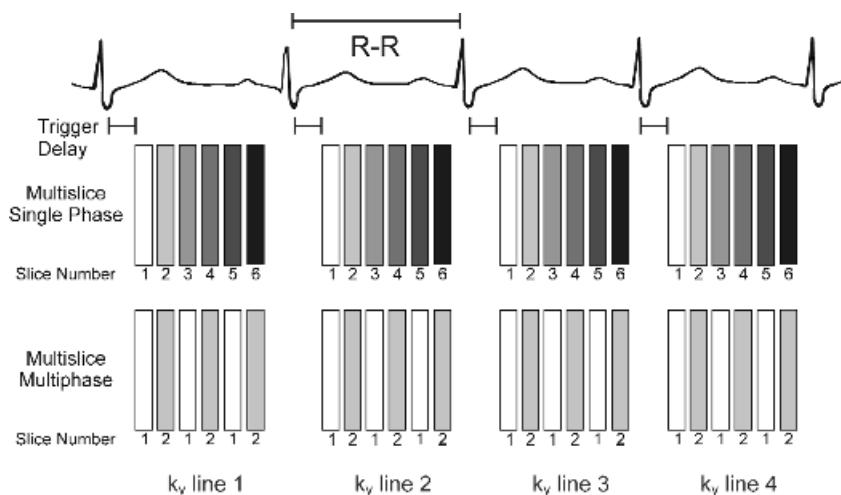


FIGURE 10-3 Principle of ECG triggering. Triggering the data collection to the ECG signal from the patient decreases the severity of the motion artifact. The R wave is used as an initiation signal. For multislice, single-phase imaging, one phase-encoding step for each slice is acquired per heartbeat. Information for a particular slice is acquired at the same time following the R wave. The  $T_1$  contrast is based on the R-R time interval rather than the user-defined  $TR$ . Alternately, a multislice, multiphase acquisition may be performed in which slices are acquired at different times during the cardiac cycle at the same position. A trigger delay (TD) can be used to initiate data collection at any desired time during the cardiac cycle.

of the R–R interval ( $T_{REP}$ ), several signals can be acquired within one heartbeat. Proper detection of the ECG signal from the patient is critical. Improper electrode placement may detect significant signals from the blood during its flow through the aortic arch. In addition, the transmitted rf energy and the gradient pulses may also interact with the lead wires, inducing significant noise to the detected ECG signal. High-resistance lead wires may even burn the patient through this coupling.

Two types of examinations are commonly used in cardiac studies. Spin echo imaging acquires one signal from a slice acquired at a different slice position per heartbeat. Each image within the scan is acquired at a different position and a different time point in the cardiac cycle. These images are typically  $T_1$ -weighted (depending on the R–R time interval) with minimal blood signal, and are used for morphological studies of the heart (Figure 10-4). Another approach produces significant blood signals and is known as cine heart imaging. In this method, multiple images are acquired at a slice position during the R–R time interval. Rapid display of these images allows a dynamic visualization of the heart and cardiac hemodynamics during the different phases of the cardiac cycle (Figure 10-5).

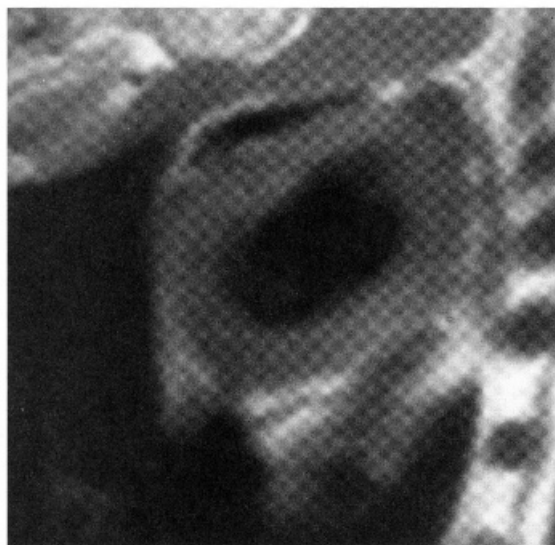


FIGURE 10-4 Short-axis,  $T_1$ -weighted image acquired using a triggered multi-slice mode.

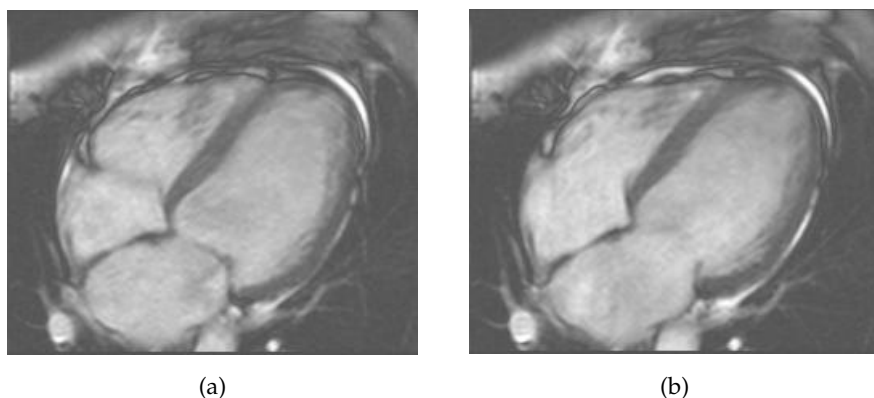


FIGURE 10-5 Cine heart images acquired at different phases of cardiac cycle. Measurement parameters: pulse sequence, 2D spoiled gradient echo;  $TR$ , 35.4 ms;  $TE$ , 1.5 ms, excitation angle,  $65^\circ$ ; acquisition matrix,  $N_{PE}$ , 108,  $N_{RO}$  128;  $FOV$ , 169 mm  $PE \times 200$  mm  $RO$ ;  $N_{SA}$ , 1. (a) 92 ms following R wave. (b) 552 ms following R wave.

Traditional cine heart examinations use gradient echo sequences with standard  $k$  space filling, acquiring one echo per slice per heartbeat. However, more advanced cine examinations use a segmented filling of  $k$  space, allowing multiple echoes per slice to be acquired per heartbeat. Unlike the echo-train spin echo sequence in which multiple  $k_y$  lines are measured following a single excitation pulse, segmented gradient echo techniques repeat the gradient echo kernel multiple times, each repetition with a different  $G_{PE}$  amplitude (Figure 10-6). This allows a complete raw data set to be acquired in fewer heartbeats, which reduces the scan sensitivity to a variable heart rate. In many cases, the scan times are short enough for patients to suspend respiration, which reduces artifacts from respiratory motion. Prospective cine examinations are problematical because the initial image in the dataset, representing the first phase of the cardiac cycle for the scan, will often be brighter than the subsequent images in the scan. This is due to the greater amount of  $T1$  relaxation that the net magnetization undergoes for this time point compared to the other images, due to the “dead” time waiting for the trigger pulse.

Gating methods typically have the sequence continuously executing rf and gradient pulses but not measuring signals, and use the timing signal to control when echoes are actually measured. The continuous execution

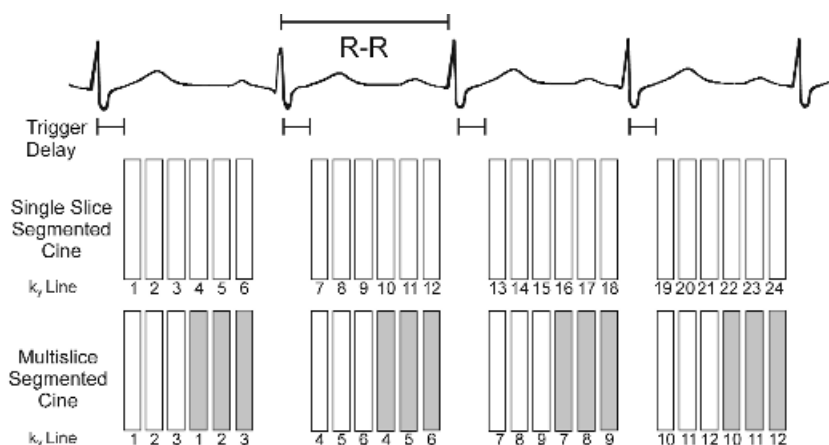


FIGURE 10-6 Segmented Cine Data Collection. Data collection can be performed acquiring either one slice position per heartbeat (top row) or multiple slice positions per heartbeat (bottom row).

maintains a relatively constant net magnetization so that all images will have comparable contrast. Prospective gating has been used in cardiac imaging and in abdominal imaging to reduce artifacts from respiratory motion. Two approaches are used, both of which synchronize the data collection to the respiratory cycle of the patient. Simple respiratory gating acquires the data when there is minimal motion. It suffers from significantly longer scan times since the time during respiratory motion is not used for data collection. An alternative technique used for  $T_1$ -weighted imaging—respiratory compensation—rearranges the order of phase encoding so that adjacent  $G_{PE}$  echoes are acquired when the abdomen is in the same relative position. Typically, the low-amplitude  $G_{PE}$  echoes are acquired at or near end expiration so that the echoes contributing the most signals are measured when there is the least motion. Higher-amplitude  $G_{PE}$  echoes are acquired during inspiration. Significant improvement of respiratory-induced ghosts can be achieved by either technique as long as there is a uniform respiration rate during the scan. Nonuniform respiration may produce artifacts as severe as those produced from a nongated scan.

An alternative to prospective triggering for cine heart imaging is known as retrospective gating. In this approach, the ECG signal is measured but the data collection is not controlled by the timing signal. Instead,

the data are measured in an untriggered fashion and the time following the R wave when each phase-encoding step was measured is stored with it. Following completion of the data collection, images are reconstructed corresponding to various time points within the cardiac cycle. The data for any phase-encoding step not directly measured are interpolated from the measured values.

### 10.3 FLOW COMPENSATION

A final method for reducing motion artifacts adds additional gradient pulses to the pulse sequence to correct for phase shifts experienced by the moving protons. It is known as flow compensation, gradient motion rephasing (GMR), or the motion artifact suppression technique (MAST). As described in Chapter 6, gradient pulses of equal area but opposite polarity are used to generate a gradient echo. Proper dephasing and rephasing of the protons and correct frequency and phase mapping occur as long as there is no motion during the gradient pulses. Movement during either gradient pulse results in incomplete phase cancellation or a net phase accumulation at the end of the second gradient pulse time. The amount of phase accumulation is related to the velocity of the motion. This phase accumulation produces signal intensity variations that are manifest as motion artifacts in the phase-encoding direction (Figure 10-7a), regardless of the direction of the motion or the gradient pulses.

If the motion of the protons is relatively simple with respect to time, then it may be modeled mathematically using a limited Taylor series expansion. The motion-induced phase changes can be predicted and may be corrected by applying additional gradient pulses. These pulses will be applied in the direction for which compensation is desired. The number, duration, amplitude, and timing of the pulses can be defined so that protons moving with constant velocity (first-order motion), acceleration (second-order motion), and pulsatility (third-order motion) can be properly mapped within the image (Pipe, 1991). For gradient echo sequences, first-order compensation is normally sufficient for proper registration of cerebrospinal fluid, whereas for spin echo sequences, higher-order compensation can often be achieved with minimal complications (Figure 10-7b).

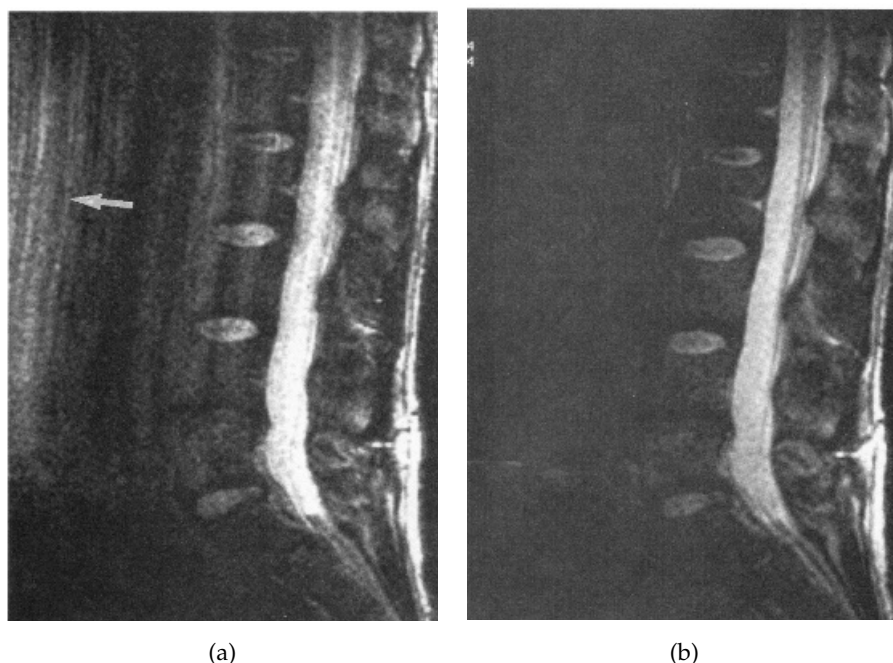


**FIGURE 10-7** Flow compensation. Use of flow compensation gradient pulses will map moving protons such as cerebrospinal fluid to their proper location. Measurement parameters are: pulse sequence, spin echo;  $TR$ , 2500 ms;  $TE$ , 90 ms; excitation angle,  $90^\circ$ ; acquisition matrix:  $N_{PE}$ , 192,  $N_{RO}$ , 256 with twofold readout oversampling;  $FOV$ , 210 mm  $PE \times 280$  mm  $RO$ ;  $N_{SA}$ , 1; slice thickness, 5 mm. (a) No flow compensation. Misregistration artifact from CSF flow appears anterior to the spinal canal (arrow). (b) First-order flow compensation in readout and slice selection directions. CSF is properly mapped into the spinal canal.

Flow compensation requires that certain limitations be placed on the pulse sequence. Since additional gradient pulses are applied during the slice loop, the minimum  $TE$  for the sequence must be extended to allow time for their application. In pulse sequences in which short  $TE$ s are desired, higher-amplitude gradient pulses of shorter duration may be used. This will limit the minimum  $FOV$  available for the sequence. In practice, only modest increases in  $TE$  and the minimum  $FOV$  are normally required.



## MAGNETIC RESONANCE ANGIOGRAPHY

---

One of the strengths of MRI for imaging patient tissue is its ability to acquire information regarding its function as well as its structure. The most common example is the examination of flowing blood within the vascular network using MR angiography (MRA). In Chapter 9, moving tissue was shown to produce severe image artifacts. MRA uses flowing tissue such as blood to provide the primary source of signal intensity in the image. It provides visualization of the normal, laminar flow of blood within the vascular system and its disruptions due to pathologic conditions such as stenoses or occlusions. MRA can be of particular benefit in evaluating vessel patency. MRA techniques have the advantage over conventional X-ray-based angiographic techniques in that use of a contrast agent is not always required. Consequently, multiple scans may be performed if desired (e.g., visualizing arterial then venous flow).

The most common MRA approach is known as a “bright-blood” method. Signals from the moving protons are accentuated relative to the stationary protons through the pulse sequence and measurement parameters. Whether the vessels are displayed as white pixels on a dark background or dark pixels on a bright background, bright-blood MRA techniques assign high pixel amplitudes to the laminar-flowing blood. Bright-blood MRA techniques can be divided into two approaches: time-of-flight and phase contrast methods. In their simplest implementation, both methods visualize arterial and venous flow simultaneously through the volume of interest. This can lead to ambiguous identification if the vessels are

in close proximity to each other. One way to select either arterial or venous flow is to apply spatial presaturation pulses to saturate the undesired blood signal prior to its entry into the imaging volume (Figure 11-1). Presaturation pulses may also be used in “black-blood” MRA techniques, in which the blood signal is saturated and the vessels appear dark relative to the surrounding tissue. These techniques are seldom used and will not be discussed further in this book.

MRA techniques use gradient echo sequences as the measurement technique for data collection and may use 2D-sequential slice (number of slices equal to the number of subloops) or 3D-volume acquisition modes. Gradient echo sequences allow the use of short  $TE$  times (usually less than 10 ms), which minimize  $T2^*$  dephasing of the blood signal. The choice of 2D versus 3D is usually dictated based on the total volume of tissue to be examined and by the total scan time. Three-dimensional techniques provide the best in-plane resolution and minimize vessel misregistration artifacts. However, saturation of blood at the distal side of the volume limits the slab thickness to approximately 70 mm unless a  $T1$  relaxation agent is used. 3D methods require significantly longer scan times. The 2D method is preferable for imaging vessels with slow flow velocity such as veins or

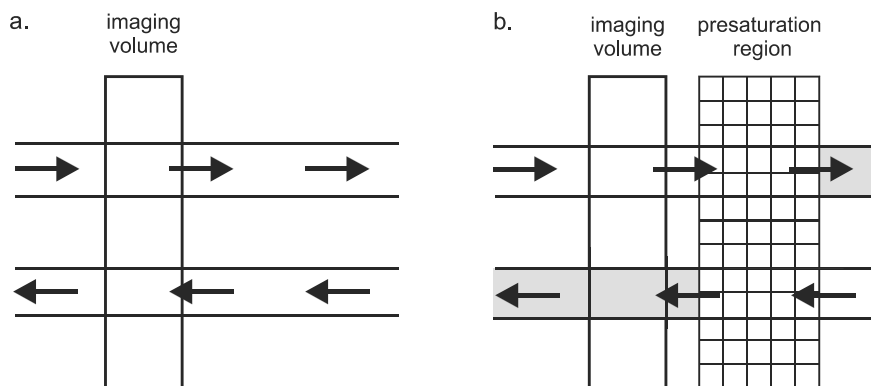


FIGURE 11-1 Flow selection in MR angiography. (a) In the absence of a presaturation pulse, flowing blood entering the imaging volume is visualized regardless of the direction of the flow. (b) A presaturation pulse that saturates flowing blood prior to its entry into the imaging volume suppresses signals from that volume.

to limit saturation effects from in-plane flow. Coverage of large areas of anatomy is possible in one scan since the volume of excitation is typically 3–4 mm per slice.

There are two additional problems associated with MRA. One is that the saturation pulse becomes less effective as more time elapses between the presaturation and the excitation pulses. This problem occurs both due to increased  $T_1$  relaxation of the blood as well as time-of-flight effects (see Section 11.1). This loss of effectiveness can be minimized by proper positioning of the presaturation pulse near the volume of excitation. Care must be taken in positioning if there is pulsatile flow in the vessel of interest, as too close a position to the imaging volume could cause a reduction in signal if the flow is retrograde. A second problem is an exaggerated sensitivity to vessel stenosis. The stenotic region disrupts the laminar flow in the area of and distal to the stenosis, causing a loss of vessel signal to a greater extent than from the stenotic region alone. As the laminar flow is reestablished within the vessel, bright signal from blood can again be measured.

## **11.1 TIME-OF-FLIGHT MRA**

Time-of-flight techniques are the most time-efficient methods for obtaining MRA images. A single measurement is performed, with the stationary tissue signal suppressed relative to the flowing-tissue signal. A moderate excitation pulse angle and a  $TR$  much shorter than the tissue  $T_1$  values are used to accomplish this. The stationary tissue experiences every rf excitation pulse but the flowing tissue does not. A volume of blood will be at a different location at the time of each excitation pulse due to its motion during  $TR$  (Figure 11-2). The signal from the blood volume is largest at the entry point of the slice because it has not undergone any excitation pulses. As the blood volume travels through the slice, it becomes saturated as it undergoes more excitation pulses and loses signal. If the flow direction is perpendicular to the slice (through-plane flow) and the volume of excitation is small, then the volume of blood exits the slice before it is completely saturated and significant blood signal can be measured throughout the entire slice. The degree of blood saturation depends on the slice thickness,  $TR$ , excitation angle, and flow velocity.

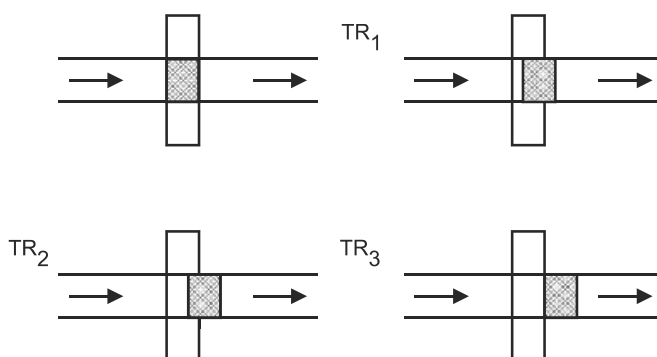
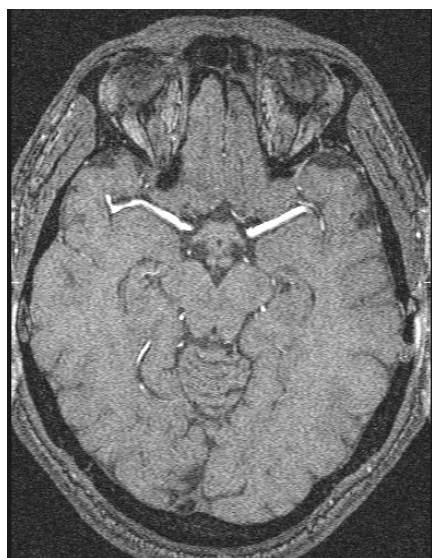


**FIGURE 11-2** Time-of-flight effect. During data collection, the imaging volume experiences multiple rf pulses. Flowing blood (hashed box) experiences the first rf pulse (upper left). During the first  $TR$  period, the excited blood volume moves (upper right) and only a portion experiences the second rf pulse. During the second  $TR$  time period, the initial volume of blood continues to move (lower left). By the end of a third  $TR$  time period, the initial volume of blood is entirely outside the volume of excitation and does not contribute to the detected signal (lower right).

Time-of-flight techniques suffer from incomplete suppression of the stationary tissue due to the faster  $T_1$  relaxation times of the stationary tissues, particularly fat, relative to the blood. Magnetization transfer (MT) pulses are often incorporated for additional suppression of the stationary tissue water to enhance the ability for small vessel detection at the expense of increased  $TR$  and relative fat signal (Figure 11-3). Three-dimensional time-of-flight techniques also result in increased saturation of the blood due to the large number of excitation pulses of the imaging volume. For this reason, they are suitable only for visualizing vessels with fast flow velocities, such as moderate-sized arteries.

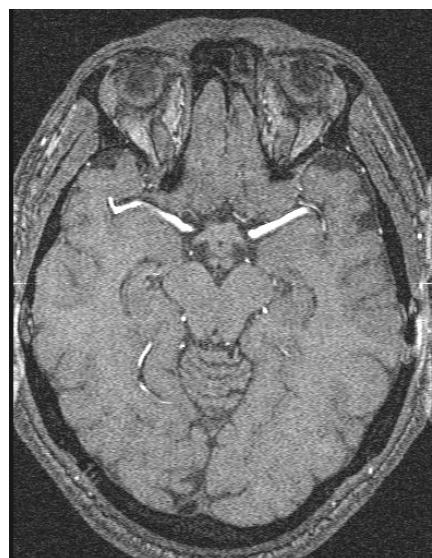
Two approaches have been developed to overcome this saturation. For 3D examinations with through-plane flow, the excitation pulse can be modified to produce a ramped or nonuniform range of excitation angles across the imaging volume (Figure 11-4). The effective excitation ramp is oriented so that increased energy is applied to protons at the distal side of the imaging volume. This induces more transverse magnetization and more signal from the more saturated protons (Figure 11-5). A second approach is analogous to traditional X-ray angiography and is used for examinations with in-



(a)



(b)



(c)



(d)

**FIGURE 11-3** Time-of-flight MRA showing effects of magnetization-transfer pulse. Other measurement parameters are: pulse sequence, 3D refocused gradient echo, postexcitation;  $TR$ , 42 ms;  $TE$ , 7 ms; excitation angle,  $25^\circ$ ; acquisition matrix:  $N_{PE}$ , 192;  $N_{RO}$ , 512 with twofold readout oversampling;  $FOV$ , 201 mm  $PE \times 230$  mm  $RO$ ;  $N_{SA}$ , 1; effective slice thickness, 0.78 mm. (a) Source image, one from data set acquired without MT pulse. (b) Transverse postprocessed image of (a). (c) Source image, one from data set acquired with MT pulse. (d) Transverse postprocessed image of (c). Note reduction of background gray and white matter in (c) compared to (a) and improved visualization of vessels in (d) compared to (b) (arrow).

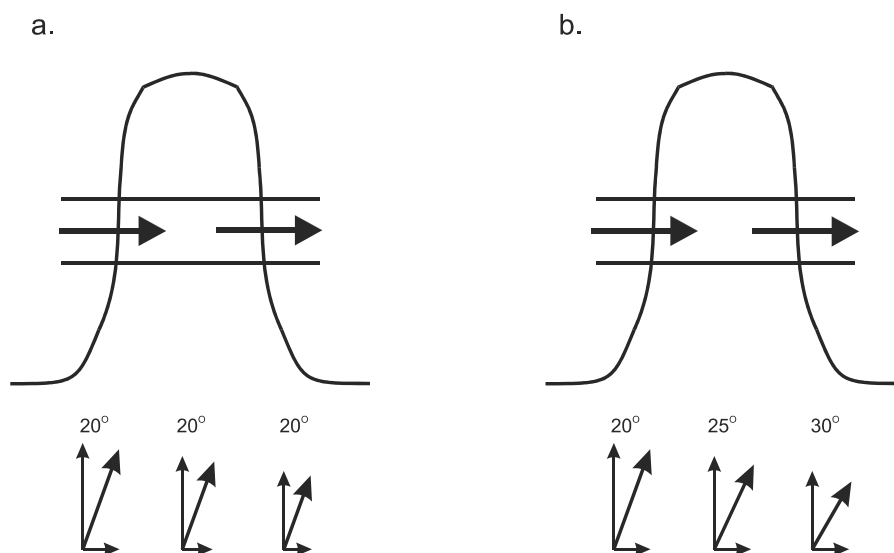


**FIGURE 11-4** TONE rf pulse. (a) Standard excitation pulses provide uniform energy deposition across the slice, which gradually increases saturation of and reduces the transverse magnetization from blood located at the exit side of the slice, causing a loss of signal. (b) Nonuniform excitation pulses known as ramped or tilted optimized nonuniform excitation (TONE) rf pulses increase the excitation across the slice. As the amount of saturation increases, the resulting transverse magnetization remains constant so that the blood signal remains uniform throughout the imaging volume.

plane flow such as the visualization of pulmonary or abdominal arteries.  $T_1$  contrast agents can be administered to shorten the  $T_1$  relaxation time of blood and obtain more blood signal (Figure 11-6). Measurement times can be reduced to a few seconds through the use of interpolation in the slice selection, enabling serial scan volumes to be acquired coupled with suspension of respiration during the scan. Subtraction of pre- and postcontrast volumes eliminates residual signals from stationary tissue. Use of contrast agents for abdominal MRA has enabled rapid, reliable, and high-quality studies to be obtained with minimal contamination from patient motion. Studies of peripheral vessels by MRA can also be performed following contrast administration. Multilevel acquisitions together with rapid movement of the patient table allows for run-off studies of extremities within a single short imaging session (Figure 11-7).

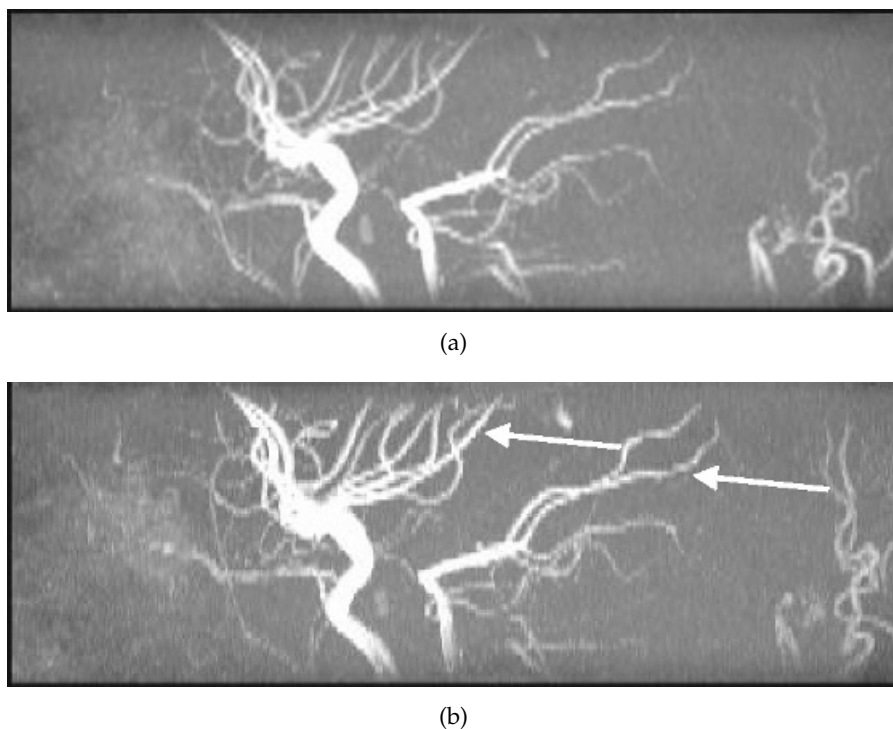


**FIGURE 11-5** Time-of-flight MRA showing effects of TONE rf pulse. Measurement parameters are: pulse sequence, 3D refocused gradient echo, postexcitation;  $TR$ , 42 ms;  $TE$ , 7 ms; excitation angle,  $25^\circ$ ; acquisition matrix:  $N_{PE}$ , 192;  $N_{RO}$ , 512 with twofold readout oversampling;  $FOV$ , 201 mm  $PE \times 230$  mm  $RO$ ;  $N_{SA}$ , 1; effective slice thickness, 0.78 mm. (a) Sagittal projection of volume using normal uniform excitation pulse. (b) Sagittal projection of volume using TONE excitation pulse. Note improved signal from vessels (arrow).

## 11.2 PHASE CONTRAST MRA

Phase contrast MRA is a technique in which the background tissue signal is subtracted from a flow-enhanced image to produce flow-only images, analogous to digital-subtraction X-ray angiography. The acquisition sequence may produce a one-dimensional profile, or standard 2D or 3D images. A minimum of two images are measured at each slice position. One image, known as the reference image, is acquired with flow compensation (see Chapter 10). Subsequent images are acquired following application of addi-

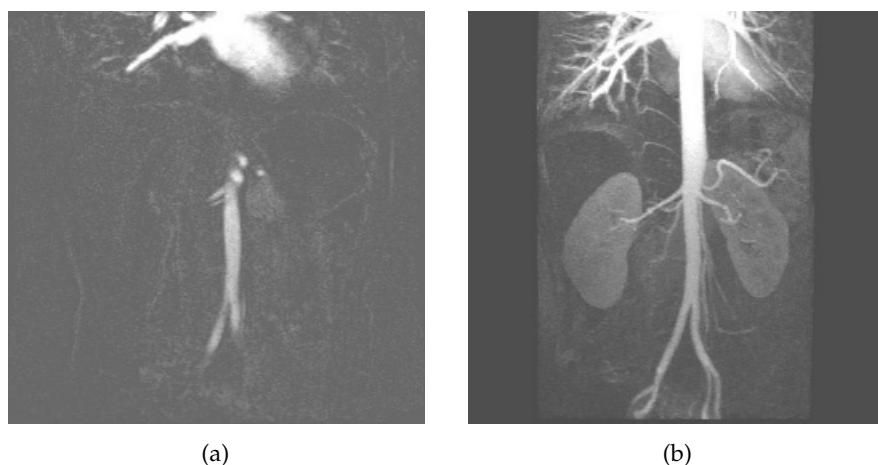


**FIGURE 11-6** MR angiography of aorta and renal arteries following bolus administration of gadolinium-chelate contrast agent. Measurement parameters are: pulse sequence, 3D refocused gradient echo, postexcitation;  $TR$ , 3 ms;  $TE$ , 1.1 ms; excitation angle,  $20^\circ$ ; acquisition matrix:  $N_{PE}$ , 128;  $N_{RO}$ , 256;  $FOV$ , 350 mm  $PE \times 400$  mm  $RO$ ;  $N_{SA}$ , 1; effective slice thickness, 2.0 mm. (a) Source image, one from data set. Image was obtained following subtraction of enhanced scan from unenhanced scan. (b) Coronal postprocessed image of (a).

tional gradient pulses that induce a phase shift in blood moving with a particular direction and flow velocity. The moving protons are rephased at the echo time  $TE$  and the resultant image is subtracted from the reference image to produce images of only the moving protons. The blood-signal amplitude will depend on its velocity, with maximum signal obtained from flowing blood at an operator-specified velocity known as the  $venc$  or velocity encoding value. Additional scans may be performed to sensitize flow in other directions or at other velocities. The resultant difference images may be combined to produce images sensitive to flow in any direction at the chosen velocity (Figure 11-8).

Phase contrast MRA has several advantages over time-of-flight techniques. Being a subtraction rather than a saturation technique, it has better background suppression than time-of-flight methods. Through their directional sensitization, phase contrast methods enable flow in each primary direction to be separately assessed. In addition, quantitation of the flow veloc-



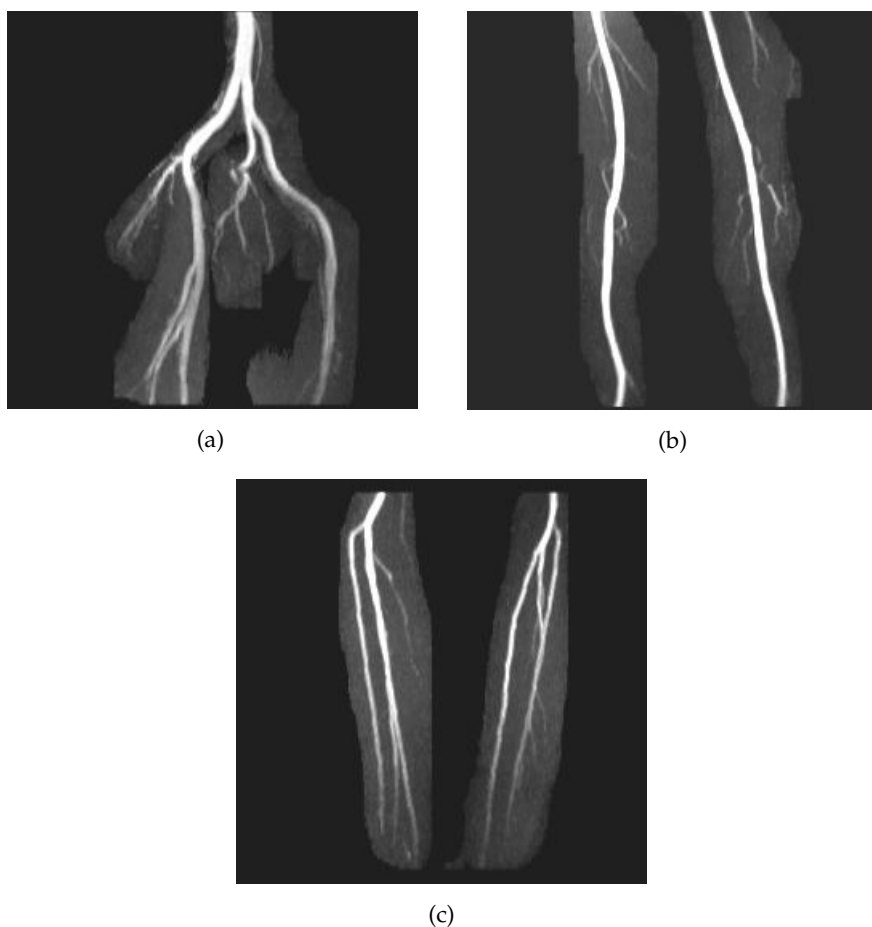
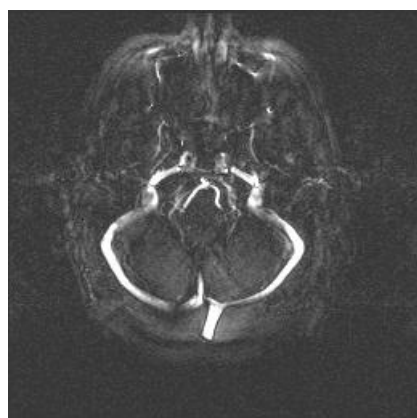
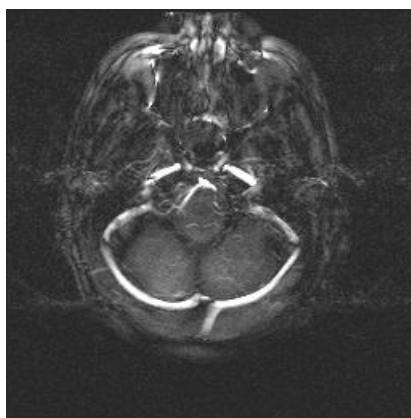


**FIGURE 11-7** Peripheral MRA, postprocessed images. Images were acquired at three different scan table positions. Measurement parameters: 2D spoiled gradient echo;  $TR$ , 300 ms;  $TE$ , 3.6 ms; excitation angle,  $50^\circ$ ; acquisition matrix:  $N_{PE}$ , 144;  $N_{RO}$ , 256;  $FOV$ , 191 mm  $PE \times 340$  mm  $RO$ ;  $N_{SA}$ , 1; slice thickness, 4.0 mm; pulse triggered. (Images courtesy of H. Cecil Charles, Duke University.)

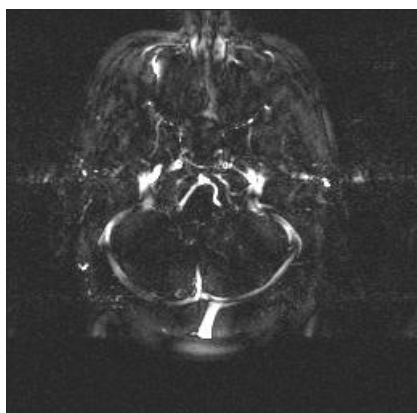
ity in each direction is possible. However, phase contrast methods suffer from two problems. One is a significantly longer scan time. Four separate acquisitions are required to measure flow in all three directions. The scan time is four times longer than for a time-of-flight method with similar acquisition parameters. In addition, prior knowledge of the maximum veloci-



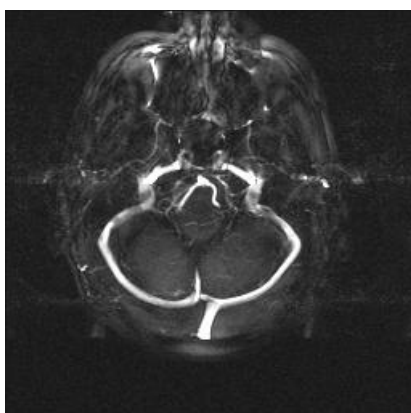
(a)



(b)

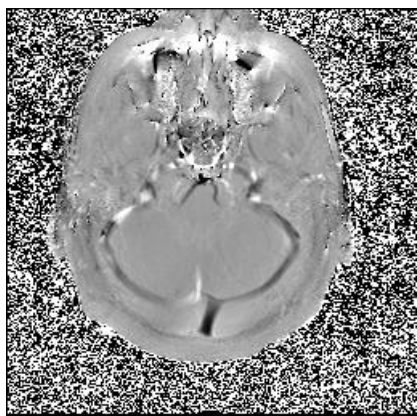


(c)

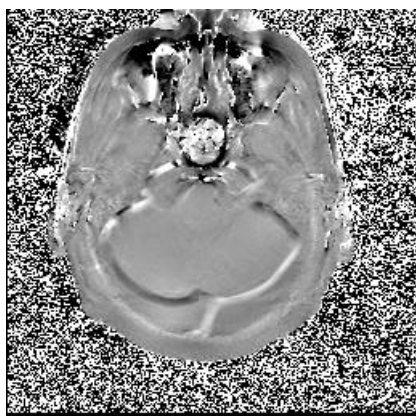


(d)

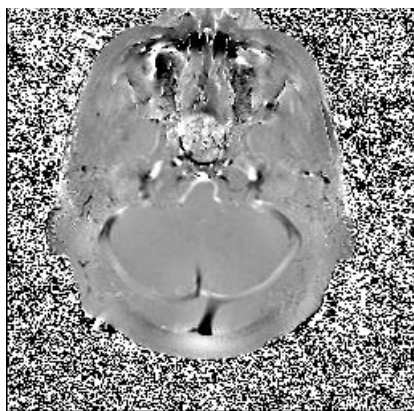
**FIGURE 11-8** Phase contrast MRA. Venc, 30 cm/s in all directions. Other measurement parameters: 2D spoiled gradient echo;  $TR$ , 211 ms;  $TE$ , 8.4 ms; excitation angle,  $15^\circ$ ; acquisition matrix:  $N_{PE}$ , 192;  $N_{RO}$ , 256;  $FOV$ , 240 mm  $PE \times 240$  mm  $RO$ ;  $N_{SA}$ , 1; slice thickness, 40.0 mm. (a) Flow image, flow direction A-P. (b) Flow image, flow direction R-L. (c) Flow image, flow direction S-I. (d) Magnitude sum of images (a)–(c). (e) Phase image, flow direction A-P. (f) Phase image, flow direction R-L. (g) Phase image, flow direction S-I.



(e)



(f)



(g)

FIGURE 11-8 *Continued.*

ty is necessary to ensure that the proper venc is used. The maximum signal is achieved for blood flowing at the chosen venc. Flow velocities exceeding this velocity are misregistered in the image and appear as slower flow, a situation known as flow aliasing. This artifact is analogous to the high-frequency aliasing problem observed in phase encoding (see Chapter 9). Blood signal is reduced at these higher velocities until a complete loss of flow signal occurs at flow velocities that are even multiples of the venc. At

the other extreme, a *venc* too large will minimize contrast between velocity changes within a vessel. Proper choice of the *venc* allows adequate visualization of all flow with good sensitivity to velocity variations within a vessel. This choice can be facilitated by the use of velocity measurements measured using Doppler ultrasound techniques or by scanning the volume using 2D techniques with multiple *vencs* to see which one provides the best results.

### 11.3 MAXIMUM INTENSITY PROJECTION

Regardless of the choice of acquisition technique, examination of the individual images from an MRA scan can provide details regarding flow variations within a vessel. However, a vessel is seldom located within a single slice but usually extends through several slices at an arbitrary angle, making the vessel tortuosity and spatial relationship with neighboring vessels difficult to assess, particularly if the vessels are oriented perpendicular to the imaging volume. Bright-blood MRA images may be analyzed using a postprocessing technique known as maximum intensity projection (MIP) to better visualize the three-dimensional vessel topography.

The MIP process generates images from the entire set of MRA images. A view direction is chosen and the entire set of images is projected along that direction onto a perpendicular plane using a “ray tracing” approach. The pixel of maximum intensity is chosen as the pixel for the MIP image, regardless of the input slice in which the pixel is located (Figure 11-9). Because the bright-blood MRA technique accentuates blood signal over stationary tissue signals, the MIP process preferentially selects blood vessels whenever possible, which enables the entire vessel to be examined no matter where it is located within the imaging volume. Multiple images may be obtained from the same data set through change of the view direction (rotation of the projection angle). Vessels that are superimposed in one projection may be clearly resolved in another one. It is also possible to perform the MIP process on a subset of the data, a so-called “targeted” approach. This is useful for isolating the left and right carotid arteries, for elimination of suborbital or subcutaneous fat in cerebral MRA studies, or for tailored reconstruction of the renal arteries. Care must be taken in the

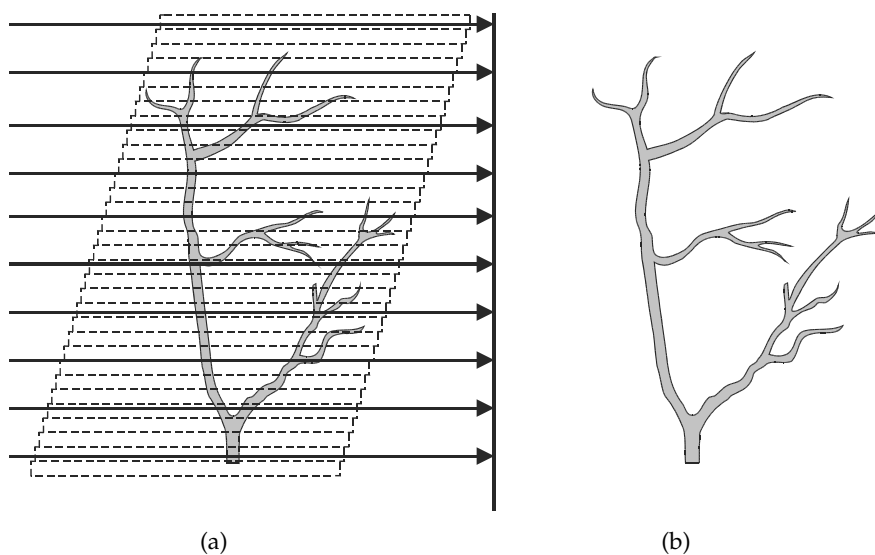


**FIGURE 11-9** Maximum intensity projection (MIP). The MR images are acquired so that moving blood has pixels of maximal intensity. The MIP process maps the pixels of maximum intensity into a single projection or view regardless of which slice the pixel was located in. Changing the direction of projection provides a different perspective of the vessels.

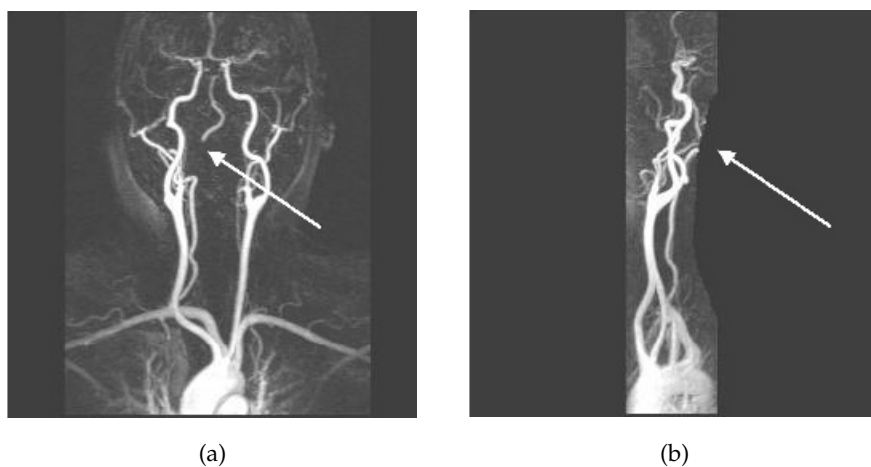


**FIGURE 11-10** Maximum intensity projections of MRA exam, coronal (a) and sagittal (b) projections. Note: absence of vessel in (a) indicated by arrow is due to its exclusion in MIP, as indicated by arrow in (b).

definition of the targeted area so that the vessel of interest does not leave the area. The MIP process causes the vessel to be cut off at the edge of the defined region, simulating a vessel obstruction (Figure 11-10). Careful examination of the source images and/or MIP images in multiple orientations is necessary to ensure the inclusion of the entire vessel within the reconstructed area.

## ADVANCED IMAGING APPLICATIONS

---

Initially, MR imaging was restricted to visualizing hydrogen nuclei using basic spin echo techniques. As hardware and software have evolved, newer and faster imaging techniques have been developed. The advent of subsecond imaging techniques has provided the ability to measure metabolic processes within tissues with significantly faster temporal resolution than was previously possible. Also, imaging of nuclei other than hydrogen has become more feasible. Four such applications are described in this chapter: diffusion, perfusion, functional imaging, and imaging of hyperpolarized noble gases.

### 12.1 DIFFUSION

As mentioned in Chapter 1, all matter is made of atoms that bond to form molecules. These molecules continually move due to interactions with their surroundings. Two types of movement are found in tissues. One is coherent bulk flow, which occurs for blood or cerebrospinal fluid. This movement arises from a difference in pressure between two locations, produced by contractions of the heart. Direct visualization of blood flow within the vascular network is accomplished using MR angiographic techniques, as described in Chapter 11.

Another manifestation of this continuous movement of molecules is a relatively small displacement of the molecule in space, known as translational motion. Although many processes in nature can cause translational

motion, one of the most important ones in biological systems is diffusion. Diffusion of molecules occurs due to a concentration difference between two environments, such as on either side of a cell membrane. Diffusion is thermodynamic in origin and is a nonequilibrium process responsible for the random transport of gases and nutrients from the extracellular space into the cell interior. The transit occurs from a region of high concentration to low concentration, analogous to heat flow between hot and cold regions. In pure solutions, diffusion is characterized by a constant known as the diffusion coefficient  $D$ , measured in units of  $\text{mm}^2\text{s}^{-1}$ , which describes the amount of material transported across the membrane.

Studies of diffusion have been performed using MR for many years. The standard method uses a symmetric pair of gradient pulses to increase the amount of spin dephasing observed in a spin echo (Figure 12-1). Known as the Stejskal–Tanner method (Stejskal and Tanner, 1963), spins that move during the gradient pulses experience unequal effects from the gradient pulses and do not rephase at the echo time  $TE$ . This causes a loss in signal amplitude from those spins:

$$S(TE) \propto \exp(-TE/T_2) * \exp(-b * D) \quad (12-1)$$

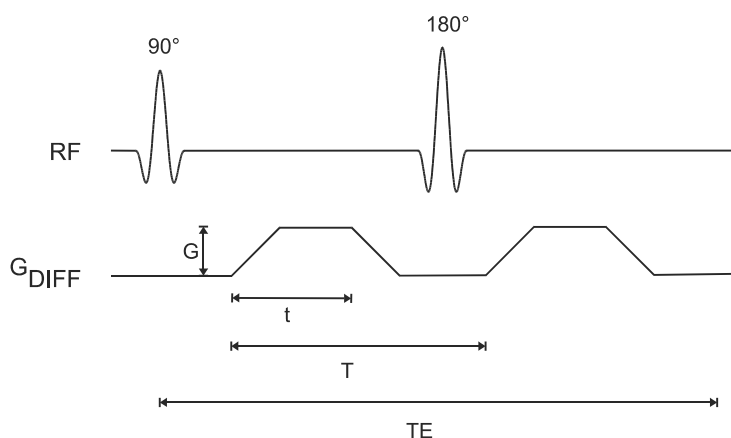


FIGURE 12-1 Spin echo pulse sequence showing diffusion gradients, known as the Stejskal–Tanner approach.  $G$  is the amplitude for each of the gradient pulses,  $t$  is the duration of the gradient pulse during which the diffusion weighting occurs, and  $T$  is the time between the two pulses.



where  $T$ ,  $t$ , and  $G$  are defined in Figure 12-1 and

$$b = \gamma^2 G^2 t^2 (T - t/3) \quad (12-2)$$

The signal sensitivity to motion for the technique is determined by the  $b$  value. Larger  $b$  values can be obtained through larger gradient amplitudes, longer duration gradient pulses, or longer times between the gradient pulses. MRI applications of this technique are referred to as diffusion-weighted imaging. Tissues with small  $D$  values undergo little motion and sustain little signal loss when imaged. Tissues with large  $D$  values move significantly during the gradient pulses and produce a significantly attenuated signal.

In biological systems, measurements of diffusion in tissue are complicated by several factors:

1. Perfusional blood flow. Normal perfusion of tissue by blood flow can be assessed through MR techniques as described below. However, blood flow through randomly oriented microscopic blood vessels within a tissue voxel results in a loss of signal, known as intravoxel incoherent motion, that is indistinguishable from diffusion. For this reason, measurements of diffusion in tissues in vivo measure a quantity known as the apparent diffusion coefficient ( $ADC$ ).
2.  $T_2$  effects. MRI measurements of diffusion are made using echo-based techniques with relatively long  $TE$  times (70 ms or longer), allowing significant  $T_2$  weighting in the images. Based on Equation 12-1, any measured signal losses from changes in the  $T_2$  relaxation times for a tissue are indistinguishable from changes in the  $ADC$ .
3. Directional dependence. In pure solutions, diffusion is isotropic in nature, meaning that  $D$  is equal in all directions. In tissue, diffusion is anisotropic in nature, meaning that the  $ADC$  may have different values in different directions. A more accurate description for diffusion represents the  $ADC$  as a tensor quantity, expressed as a matrix with nondiagonal terms. In addition, the principal axes for the tensor (for which the matrix is diagonal) will generally not coincide with the gradient axes or with obvious patient anatomy; in other words, the sensitive directions for diffusion may not be readily apparent.

To address  $T_2$  effects, an  $ADC$  map may be calculated (Figure 12-2). This is an extrapolated image, with pixel values corresponding to the  $ADC$  values for the tissue. Two or more images are acquired with different  $b$  values, and the  $ADC$  value for a pixel is calculated based on Equation 12-1 (substituting  $ADC$  for  $D$ ). The range of  $b$  values is usually between 0 and 1000 or higher, with increased accuracy achieved by using more  $b$  values. Low  $ADC$  values are characteristic of regions with restricted diffusion, whereas regions where the spins are relatively free to move have high  $ADC$  values.

Two approaches are currently used to address the directional dependence of diffusion. The first approach is to acquire a trace image. This is effectively an average of the diffusion in three directions. The trace image has the advantage that it is independent of the particular axes used for the measurement as long as they are orthogonal (perpendicular); that is, the

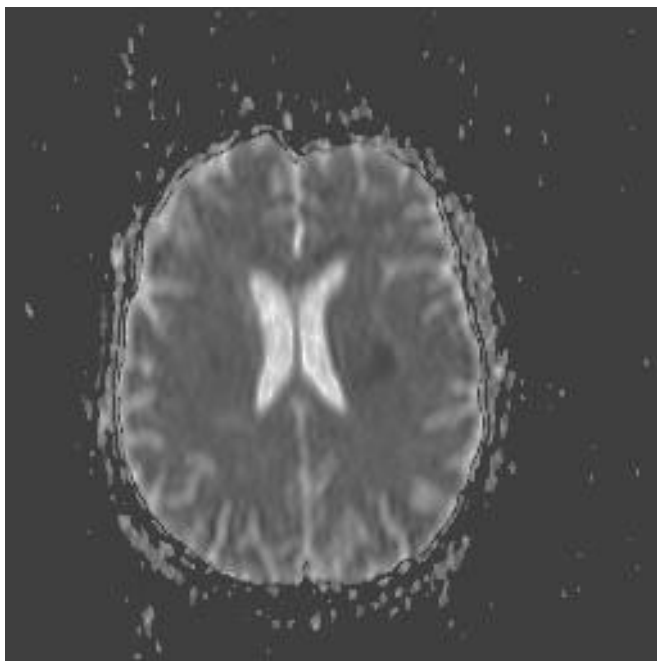


**FIGURE 12-2**  $ADC$  map, calculated from images in Figure 12-3. Low pixel amplitudes indicate restricted water movement. High pixel amplitudes indicate free water movement.

resulting trace image is the same whether the three primary gradient axes ( $G_x$ ,  $G_y$ ,  $G_z$ ) are used or the principal axes of the tensor. The other approach for analyzing the directional dependence is to measure the complete diffusion tensor and calculate its principal components. The nondiagonal terms can be measured directly if the two gradient pulses in Figure 12-1 have different directions ( $G_x$ – $G_y$ ,  $G_y$ – $G_z$ , etc.). A matrix diagonalization of the results will identify the principal directions and the *ADC* in each direction.

One of the most important applications of diffusion-weighted imaging is in the evaluation of cerebral ischemia and stroke. Normal cells maintain a concentration gradient of sodium ions extracellular and potassium ions intracellular, and are surrounded by and contain water. The enzymatic process responsible for the maintenance of this gradient is known as active transport or the sodium–potassium–ATP pump. The energy for this process is provided by adenosine triphosphate (ATP) and requires oxygen as one of the reactants for its production. The oxygen for this process is carried to the tissue from the lungs, coordinated to hemoglobin found in erythrocytes. Following the onset of ischemia and the loss of oxygen by the tissue, the *ADC* of the affected tissue water has been observed to decrease, leading to a decrease in signal dephasing and an increase in signal amplitude (Figure 12-3). Although the reason for this decrease in *ADC* is unclear, it is presumably due to a change in the membrane permeability to the sodium and potassium ions and an accompanying increase in intracellular water content. This *ADC* decrease is reversible upon restoration of blood flow, provided it occurs before complete cell membrane breakdown.

## 12.2 PERFUSION

Although angiographic techniques visualize the vascular network within a patient, they do not have sufficient spatial resolution to visualize blood flow through a tissue in bulk. However, it is possible in many instances to observe changes in tissue signal due to the blood flow through it, a process known as perfusion. Proper tissue perfusion is critical to ensure an adequate supply of nutrients to the constituent cells as well as removal of metabolic byproducts. It also aids in maintenance of a stable tissue temperature.

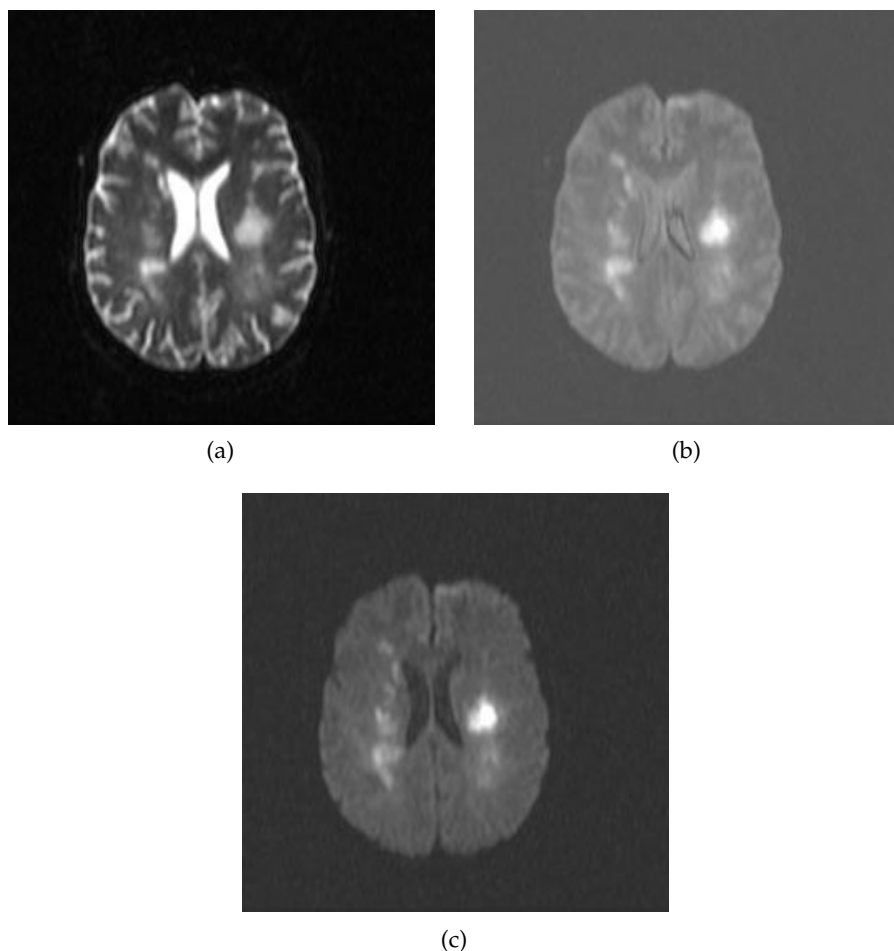


**FIGURE 12-3** Diffusion-weighted EPI sequence. (a)  $b = 0 \text{ s mm}^{-1}$ . (b)  $b = 500 \text{ s mm}^{-1}$ . (c)  $b = 1000 \text{ s mm}^{-1}$ . Normal tissue has moderate diffusion of water, whereas tissue under stress, such as that at risk for a stroke, has restricted motion of tissue water and shows increased signal on image with significant diffusion sensitivity (c).

Abnormalities in perfusion can lead to an increased temperature sensitivity and a loss of tissue viability through hypoxia.

Three approaches are used for MR perfusion studies, two of which are analogous to radioisotope tracer studies and use similar methods for analysis of the flow dynamics. One approach acquires a series of rapid (less than

20 seconds per image)  $T1$ -weighted imaging studies following the bolus administration of a gadolinium-chelated contrast agent. These images are typically acquired using spoiled gradient echo,  $T1$ -weighted magnetization-prepared or echo planar techniques. An increase in tissue signal occurs as the contrast agent infuses the extravascular spaces of the tissue. Perfusion defects are visualized as a lack of signal increase for the affected region of tissue. The other approach is useful if the contrast agent remains in the blood vessels, such as in cerebral tissue with an intact blood-brain barrier. In this case, the paramagnetic nature of the contrast agent increases the local tissue susceptibility, causing increased  $T2^*$  dephasing of nearby tissues. Serial  $T2^*$ -weighted gradient echo or echo planar sequences are acquired, and the well-perfused tissue exhibits a reduction of signal relative to the precontrast images or the poorly perfused tissues.

The third approach does not use contrast media to highlight the flowing spins. Instead, two sets of images are acquired using an EPI pulse sequence. One set is acquired following a region-selective inversion pulse that inverts or "tags" the spins outside the slice of interest, whereas the other set of images serves as a reference. A variable delay time between the tagging pulse and the data collection allows control of the tag position based on the flow velocity. Two flow imaging methods that differ in the nature of the reference image have been developed using this tagging approach. One method is known as EPISTAR (Edelman and Chen, 1998). The reference image is acquired following application of either an inversion pulse on the opposite side of the imaged slice, or a pair of inversion pulses at the same position as the tagging inversion pulse. The other approach is known as FAIR (Kim, 1995). This method acquires the reference image following a non-slice-selective inversion pulse. In both methods, the resulting difference image has signals primarily from the moving spins.

Two areas in which perfusion studies have shown promise are the examination of abnormalities of blood flow within tissue and the detection of tumors. Blood flow anomalies in the myocardium following infarction have been studied for many years using radionuclide agents. First-pass MR perfusion studies have shown good correlation with these studies and have enabled visualization of different phases of perfusion (Wilke et al, 1999). In these examinations, the measurement parameters are chosen so that the

blood signal is minimal prior to contrast agent administration. Reduced uptake of the contrast agent in poorly perfused tissue causes a delay in signal enhancement. Liver studies following administration of gadolinium-chelated contrast agents have also demonstrated differences in tissue perfusion. Images acquired immediately following contrast administration show capillary phase perfusion, whereas images acquired 45 seconds postadministration show substantial portal phase perfusion (Figure 12-4). The normal spleen usually shows a serpiginous enhancement pattern immediately fol-

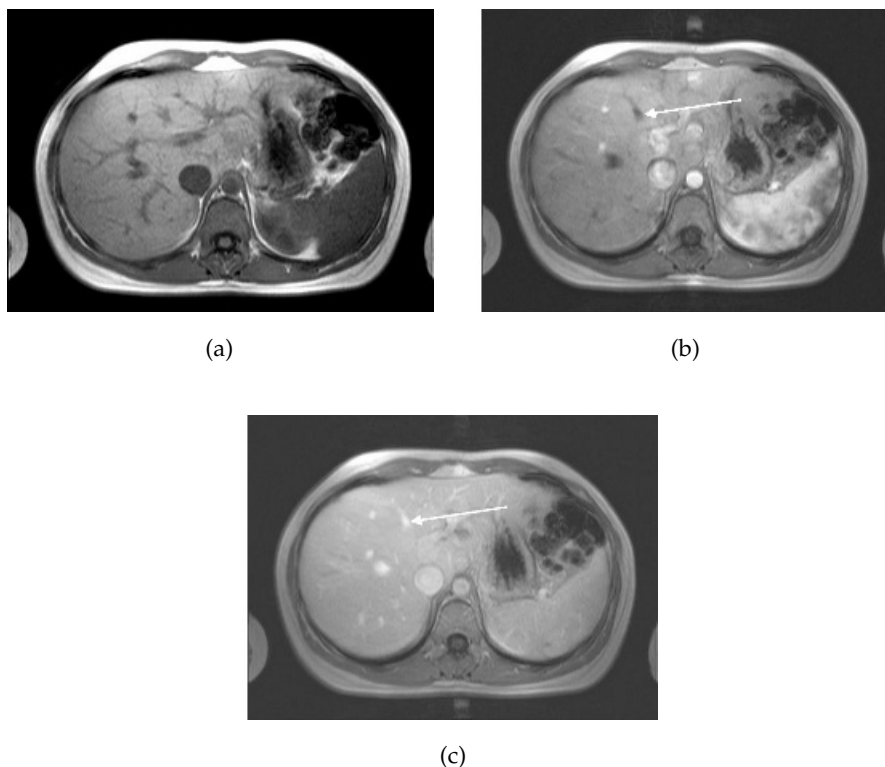


**FIGURE 12-4** T1-weighted spoiled gradient echo imaging of liver following administration of gadolinium-chelate contrast agent. (a) Image acquired prior to contrast administration. (b) Image acquired immediately following administration. Contrast agent is in the hepatic arterial phase, as evidenced by the nonopacified hepatic vein (arrow). (c) Image acquired 45 seconds following administration. Contrast agent is now in the capillary phase, as evidenced by its presence in the hepatic vein (arrow).

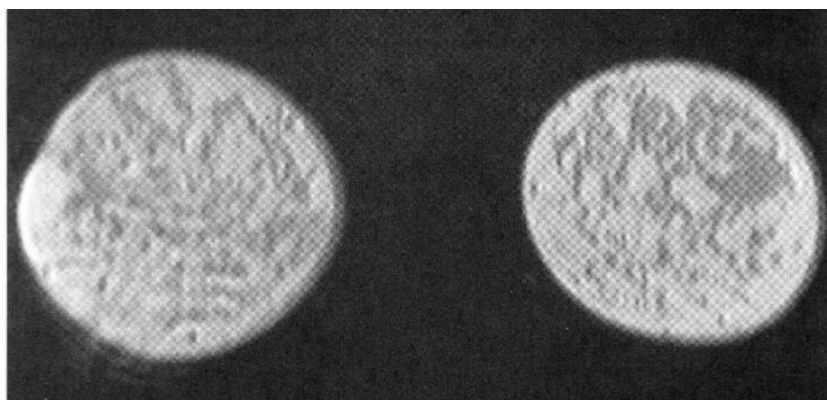
lowing contrast administration, with a more uniform signal intensity observed on images acquired 45 seconds or later.

The other studies in which differential perfusion has been used are in the detection of certain tumors. Pituitary adenomas have demonstrated a perfusional difference in microadenomas and macroadenomas following contrast administration (Finelli and Kaufman, 1993). Also, malignant breast tumors have demonstrated a significantly faster uptake of contrast media than benign tumors in some studies (Kvistad et al., 2000). Rapid scanning is necessary because both classes of tumors have similar signal amplitudes 3 minutes following contrast administration. Use of a 3D volume scan enables a bilateral breast study with good spatial and temporal resolution (Figure 12-5).

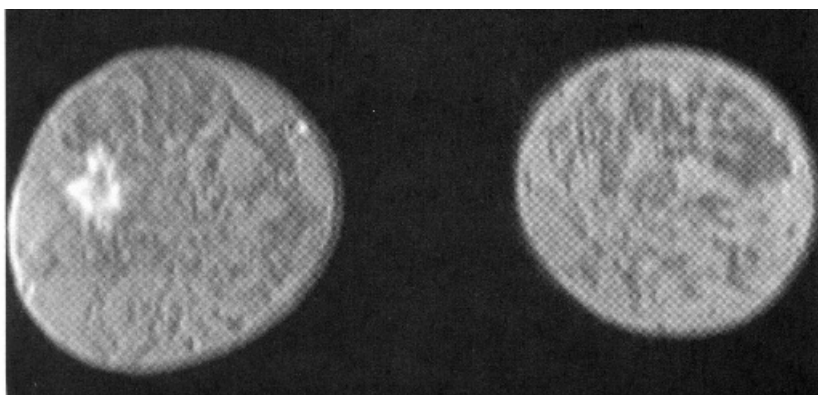
### 12.3 FUNCTIONAL BRAIN IMAGING

An active area of research in which perfusion techniques are used is in the study of brain activity in response to an external stimulus. The basic approach is very similar to that mentioned earlier for bolus contrast agent studies of brain tissue, namely using  $T2^*$ -weighted gradient echo or echo planar images. However, instead of administering an exogenous agent to reduce the  $T2^*$  relaxation time, the local tissue susceptibility is shortened by the presence of endogenous paramagnetic species present in blood. As mentioned earlier in the description of diffusion-weighted imaging for the evaluation of stroke, oxygen is delivered to cells bonded to hemoglobin. Oxygenated hemoglobin is diamagnetic, with a very small magnetic moment, whereas deoxygenated hemoglobin has a significant paramagnetic moment. Significant concentrations of deoxygenated hemoglobin shorten the  $T2^*$  relaxation time of the tissue and result in a decrease in signal compared to tissue with oxygenated hemoglobin.

Brain activation studies are based on the assumption that stimulated tissue undergoes an increase in blood flow with an increased delivery of oxygenated hemoglobin. The amount of deoxygenated hemoglobin decreases within the tissue, reducing the concentration of paramagnetic molecules. This condition reduces the amount of susceptibility dephasing induced and thereby increases the  $T2^*$  for the stimulated tissue relative to the



(a)

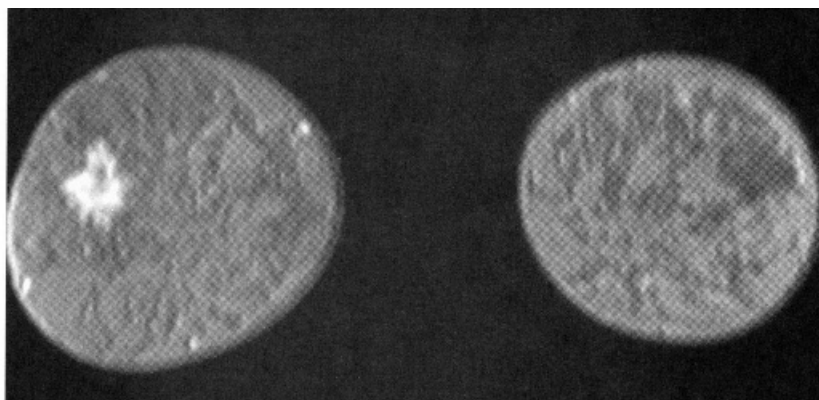


(b)

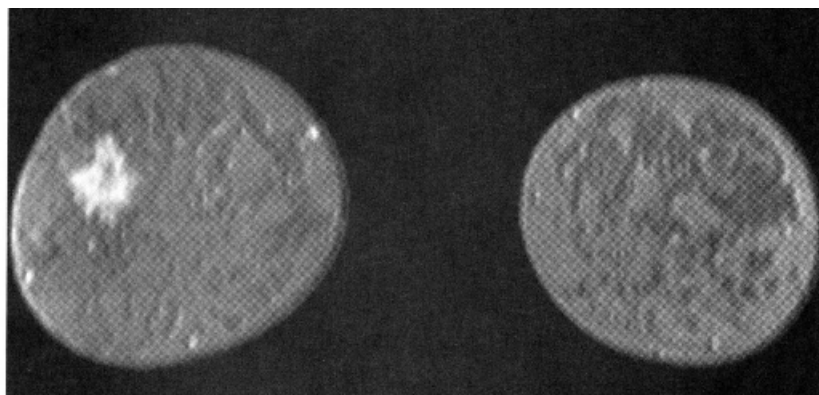
**FIGURE 12-5** 3D-volume  $T_1$ -spoiled gradient echo imaging of breast following administration of gadolinium-chelate contrast agent. (a) Precontrast image, lacking evidence of lesion. (b–d) Serial images acquired every 48 seconds following contrast agent administration. Note increased signal from lesion in later images.

unstimulated tissue. As a result, the stimulated tissue appears higher in signal on  $T_2^*$ -weighted images. This phenomenon is known as the blood-oxygenation-level-dependent effect or BOLD effect (DeYoe et al., 1994). The typical approach is to perform a large series of measurements in the presence and absence of the stimulus and subtract the images, leaving pixels presumably from the activated region of tissue.





(c)



(d)

FIGURE 12-5C,D (Continued)

Several aspects must be considered when performing brain activation studies. Correction for patient movement between measurements must be performed. Also, conversion to a standardized coordinate system is necessary if image comparison between patients (compensating for brain size, shape, and positional differences) and with other measurement techniques (CT, PET) is to be performed. The experimental paradigm or stimulus execution scheme is a critical aspect. Performance of the paradigm by the patient during the examination is of fundamental importance to ensure that the measured activation is a result of the executed paradigm. One approach used to

confirm this correlation is to perform the measurements as several sets of paired scans (stimulus present, stimulus absent). The correlation coefficient of the voxel intensity and the time variation of the stimulus is also calculated to ensure that the observed variation is in response to the stimulus. A threshold of significance, known as the  $z$  score, below which the signal difference is assumed not to be relevant, must also be defined for the particular study. Finally, the pixel intensity from the stimulated image typically exceeds that from the unstimulated image by less than 5%. This necessitates the repetition of the measurement many times (1000 or more) to ensure that the observed signal variation from the voxel is real and not artifactual in origin. High magnetic field strengths (1.5 T or greater) are necessary to increase the change in  $T2^*$  between activated and nonactivated tissue. The development of 3 T scanners have allowed more reliable and reproducible results to be obtained through an overall increase in the S/N ratio.

BOLD-type functional MRI studies have been used for studying many areas of the brain, including the visual, auditory, motor, and frontal cortices. Their results have compared favorably with those obtained using positron emission tomography (PET). Simple stimuli such as flashing lights or finger tapping have been used successfully. More complex stimuli such as cognitive processes (word or picture association) are currently being evaluated.

## 12.4 ULTRA-HIGH FIELD IMAGING

This section discusses concepts that are more fully explained in Chapter 14.

The development of MR scanners with  $B_0$  significantly greater than 1.5 T presents a number of challenges. Although clinical images have been demonstrated at field strengths of 8.0 T, commercial available scanners are limited to 4.0 T or less. As of this writing, though, the various governmental regulatory bodies have approved routine clinical scanning at field strengths up to 2.0 T. Scanning at field strengths up to 4.0 T are approved for research purposes, subject to approval by local institutional review boards. The challenges of so-called ultra-high magnetic field scanners can be divided into two categories: those exclusive of patient tissue and those due to changes in the tissue response to the increased magnetic field.

As might be expected, many of the areas of concern with conventional field strength magnets are also valid with ultra-high field systems, and in some cases they are of greater concern. For example, current ultra-high field magnets are superconducting solenoidal magnets and use liquid helium as the cryogen, as do most conventional imaging magnets. The higher field strengths require greater amounts of magnet wire windings, increasing the overall size and weight of the magnet, and greater amounts of electrical current to generate the magnetic field. The larger  $B_0$  will also exert larger forces of attraction than conventional magnets of the same physical size. This will increase the audible noise of the scanner during measurements. The fringe magnetic field will also extend outside the magnet housing to a greater extent, increasing the influence of the environment on the magnet homogeneity. Shimming of the magnet is also more problematic, in that the absolute inhomogeneity (measured in Hz or  $\mu\text{T}$  over a particular distance or volume) increases with increased  $B_0$ , whereas the relative homogeneity (measured in ppm) might remain constant. Ferromagnetic objects must be kept at greater distances to prevent uncontrollable attraction into the bore. Safe distances for patients with metal implants or for electronic equipment will extend farther from the magnet isocenter. Proper site planning and preparation is critical for safe and successful magnet installations.

As with scanning at conventional  $B_0$ , there are issues with RF power at ultra-high field strengths. As stated in Equation 1-1, the resonant frequency  $\omega_0$  is proportional to  $B_0$ . There are increased problems with RF penetration into patients at higher frequencies, a phenomenon known as the skin effect. This can cause inhomogeneous excitation of a slice, producing shading in images. In addition, increased power from the transmitter is necessary to produce the rf pulses. As mentioned in Chapter 14, the power from a pulse is used in the calculation of the specific absorption rate (SAR) for a scan. The power produced by a pulse is proportional to the square of its frequency, so that increasing  $B_0$  by a factor of 2 increases the pulse power by a factor of 4. This means that whole-body scanning at ultra-high  $B_0$  will require different examination protocols in order not to exceed current SAR guidelines.

There are also tissue response differences to ultra-high  $B_0$ . The net magnetization  $M$  is directly proportional to  $B_0$ , so that the potential exists to ob-

tain increased signals. This is particularly beneficial for MR examinations of nuclei other than hydrogen. The absolute chemical shift difference between fat and water hydrogen atoms (measured in Hz) increases linearly with  $B_0$ , whereas it remains constant when measured in relative units (ppm). Increased receiver bandwidths will be required in order to reduce chemical shift artifacts to acceptable levels. On a practical basis, the S/N ratio will increase proportionally to  $B_0$ . This can be exploited in two ways. Smaller voxels can be scanned, allowing improved spatial resolution. For example,  $1024 \times 1024$  image matrices with excellent image quality can be obtained with acceptable scan times using echo-train spin echo sequences. Alternately, MR scans with equivalent S/N ratios can be acquired with fewer signal averages. This can result in shorter scans, allowing better time resolution in dynamic examinations.

There are additional tissue response issues that can have a significant effect on clinical scanning. As mentioned in Chapter 3, the  $T1$  relaxation times increase significantly with increasing  $B_0$ , whereas the  $T2$  relaxation times are relatively constant. This means that significant  $T1$  saturation can occur in scans at ultra-high  $B_0$  using measurement parameters that produce minimal saturation in conventional scanners. As a result, longer  $TR$  times are necessary to achieve equivalent tissue contrast. This aspect, together with the increased SAR, has limited use of traditional spin echo for acquiring  $T1$  images of the brain or spine. Instead, use of gradient echo is being explored to provide acceptable image quality. There are also increased magnetic susceptibility differences at ultra-high  $B_0$ . This can produce more severe artifacts in areas where these differences are significant, but can be exploited when performing perfusion or functional MR examinations.

## 12.5 NOBLE GAS IMAGING

As discussed in Chapter 1, the most common nucleus observed in MRI is  $^1\text{H}$ , due to its high natural abundance and its large nuclear magnetic moment. In spite of these advantages, the net magnetization produced in patients by the  $^1\text{H}$  atoms in water or fat through the Zeeman interaction at normal imaging magnetic fields is very small and induces a weak signal.

Other attempts at measuring MR signals from endogenous nuclei such as  $^{23}\text{Na}$  have succeeded, but their low sensitivity has limited their practical implementation.

Successful MRI studies of lung air spaces using hyperpolarized  $^3\text{He}$  and  $^{129}\text{Xe}$  gases have been reported (MacFall et al., 1996; Mugler et al., 1997). Visualizing lung air spaces using normal  $^1\text{H}$  imaging is difficult due to the low concentration of water in air, large magnetic susceptibility differences due to the paramagnetic nature of molecular oxygen, and artifacts from respiratory or cardiac motion. Although the latter two problems can be minimized using rapid scan techniques with short  $TE$  times, the low signal amplitude produced by water vapor cannot. Helium and xenon are noble gases that are relatively unreactive and dissolve into tissues readily. They can rapidly permeate into the lung spaces. They are also well tolerated by most patients, with the most common side effect being a mild sedative effect produced by xenon.

The source of the MRI signal from noble gases is spin polarization between the parallel and antiparallel orientations just as for any MR measurement, but it is generated in a different manner. Rather than use the natural spin polarization produced by the MRI magnet, these gases are polarized outside the patient through the use of a laser and rubidium atoms. The rubidium atoms are excited by the laser and transfer the energy to the particular gas (He or Xe). This results in a net magnetization 10,000–100,000 times that produced by the MRI magnet. This hyperpolarized gas is then inhaled by the patient through a ventilator bag. Gradient echo imaging techniques are used to produce images until the net magnetization is completely lost through  $T2^*$  relaxation (approximately one minute following inhalation) (Figure 12-6).

There are several technical difficulties in performing noble gas imaging. First, the  $^3\text{He}$  and  $^{129}\text{Xe}$  active isotopes are not the predominant isotopes for these nuclei (see Table 1-1). For this reason, they are relatively expensive and recovery of the gas following patient studies is performed to reduce the expense. Second, the resonant frequencies for these nuclei are very different from  $^1\text{H}$  so that different transmitter and receiver coils are used than those used in standard MRI studies. Third, noble gas imaging is a single-pass study. Because of the method used to produce the net magnetization, there



**FIGURE 12-6**  $^3\text{He}$  image of normal lung acquired following inhalation of hyperpolarized helium gas. Note significant signals in trachea and upper lobes of lungs and lack of signals from other tissues in the body. Measurement parameters: pulse sequence, 2-D refocused gradient echo, postexcitation;  $TR$ , 25 ms;  $TE$ , 10 ms; acquisition matrix:  $N_{PE}$ , 128;  $N_{RO}$ , 256;  $FOV$ , 350 mm  $PE \times 350$  mm  $RO$ . (Image courtesy of James R. MacFall, Duke University.)

is no possibility of a repeat measurement following inhalation. Finally, only gradient echo techniques are possible. Spin echoes require  $180^\circ$  refocusing pulses and the recovery of net magnetization through  $T_1$  relaxation prior to subsequent excitation pulses. There is no natural regeneration of the net magnetization of hyperpolarized noble gases once it is dephased.

# MAGNETIC RESONANCE SPECTROSCOPY

---

Although MRI is the most common application of the MR phenomenon used in the medical community, it is a relatively recent development. The original application of magnetic resonance is MR spectroscopy (MRS), a technique that allows examination of individual molecules or portions of molecules within a sample. The development of whole-body scanners has allowed MRS to be used to study the biochemistry of disease processes within a patient without the need for invasive procedures such as biopsies. Many of the principles of MRS are the same as those of MRI, although their focus is somewhat different. While theoretically possible on any MRI system, most MRS studies are performed using magnets of 1.5 T or higher, due to the low intrinsic sensitivity of the technique. Hydrogen spectroscopic studies can be performed on standard imaging systems with no additional hardware required. This chapter summarizes some of the basic concepts of hydrogen MRS. For more complete discussions of the field, see Salibi and Brown, 1998 and Mukherji, 1998.

## 13.1 ADDITIONAL CONCEPTS

### 13.1.1 CHEMICAL SHIFT

A description of the basic principles of MRS begins at the same place as that of a description of the principles of MRI. The basic concepts of net magnetization produced by a collection of spins in a magnetic field, signal produc-

tion following absorption of rf energy, and  $T_1$  and  $T_2$  relaxation as described in Chapters 1 through 3 are identical for MRS and MRI. However, there are two important differences between MRS and MRI. First, MRS signals are normally detected in the absence of a gradient. All molecules are detected in the presence of the same base magnetic field. The chemical shift described in Chapter 2 is the only source of magnetic field variation present during signal detection. Rather than being the source of artifactual signals as it is in MRI, the chemical shift is the means by which molecular species are identified in MRS studies. Second, unlike MRI, relaxation effects are avoided as much as possible in MRS studies. The molecules under observation are relatively small in size and have relatively long  $T_1$  and  $T_2$  values. Long  $TR$  (typically ~1500 ms) are used in order to minimize  $T_1$  saturation effects.  $T_2$  dephasing effects are dominated by main field inhomogeneities and are more properly described by  $T_2^*$ .

As mentioned in Chapter 2, chemical shift values are measured to a reference frequency. The traditional reference frequency used for  $^1\text{H}$  is that of tetramethylsilane (TMS). This is impractical to use in biological systems due to its toxicity and the difficulty in achieving uniform tissue distribution. In its place, an endogenous secondary reference is normally used. This is the methyl  $^1\text{H}$  signal of *N*-acetyl aspartate, which has a chemical shift of 2.0 ppm relative to TMS. This allows standard tables of chemical shifts to be used and for in vivo spectral displays to match with traditional displays (Figure 13-1).

### 13.1.2 SPIN COUPLING

In addition to the chemical shift, there is another molecular interaction that modifies the environment of a proton. Protons located on the same molecule interact with each other and each has its local magnetic field affected. The most common instance of this in biological systems is facilitated by the bonding electrons in the molecule and is known as spin coupling or  $J$  coupling. Spin coupling differs from the chemical shift in two very important ways: it is independent of magnetic field strength (chemical shifts increase with  $B_0$  when measured in Hz) and there is always another spin involved in the coupling.



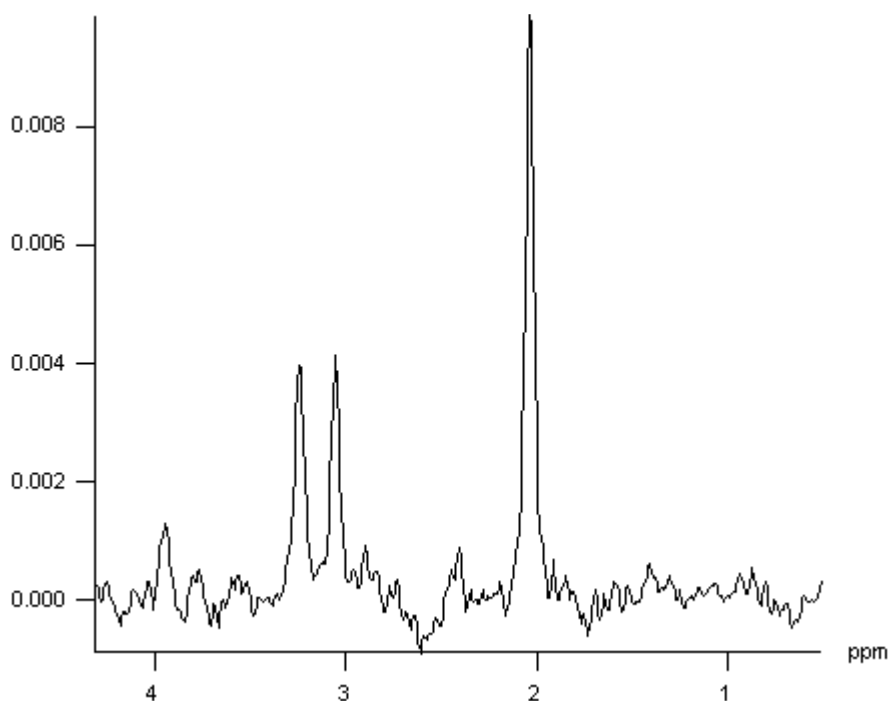


FIGURE 13-1 Typical  $^1\text{H}$  spectrum from normal brain. Measurement parameters: pulse sequence, PRESS; TR, 1500 ms; TE, 270 ms;  $N_{SA}$ , 256; voxel size,  $20 \times 20 \times 20$  mm $^3$ .

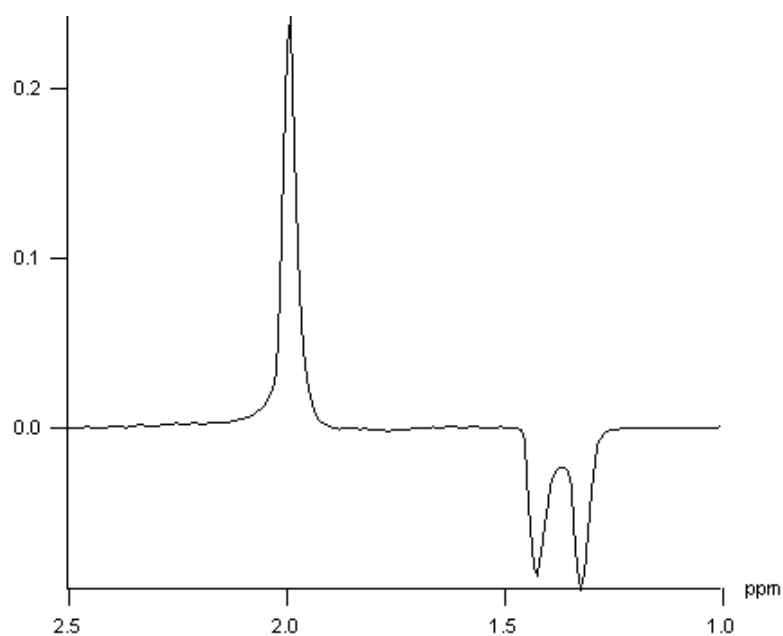
Spin coupling involves a pairing interaction between spins on the same molecule that causes the MR signal of each member to be divided. The number of resultant signals and their relative amplitudes depend on the number of spins of each type. For hydrogen MRS studies in biological systems, the molecule in which spin coupling is most easily viewed is lactate,  $\text{CH}_3\text{CHOHCOO}^-$ . Attached to the middle carbon of the molecule is a methyl group and a hydrogen atom. The hydrogen atom can be oriented parallel or antiparallel to  $B_0$ . The methyl group will sense slightly different molecular magnetic fields in each case. On average, there will be an equal number of possibilities for the hydrogen atom in each orientation, so the signal detected for the methyl group is split into two peaks separated by approximately 7 Hz, centered about the chemical shift for the methyl group. The 7 Hz value is referred to as the coupling constant  $J$  for this particular

coupling. In a similar fashion, the methyl protons can be arranged in one of four configurations: all three parallel to  $B_0$ , all three antiparallel to  $B_0$ , two parallel and one antiparallel to  $B_0$ , or one parallel and two antiparallel to  $B_0$ . The last two configurations occur three times more frequently than the first two, so that the hydrogen atom will be divided into four peaks with relative amplitudes 1:3:3:1, each separated by 7 Hz. Because of its low amplitude and its nearness to the water resonant frequency, this resonance is normally not visualized in in vivo MRS studies.

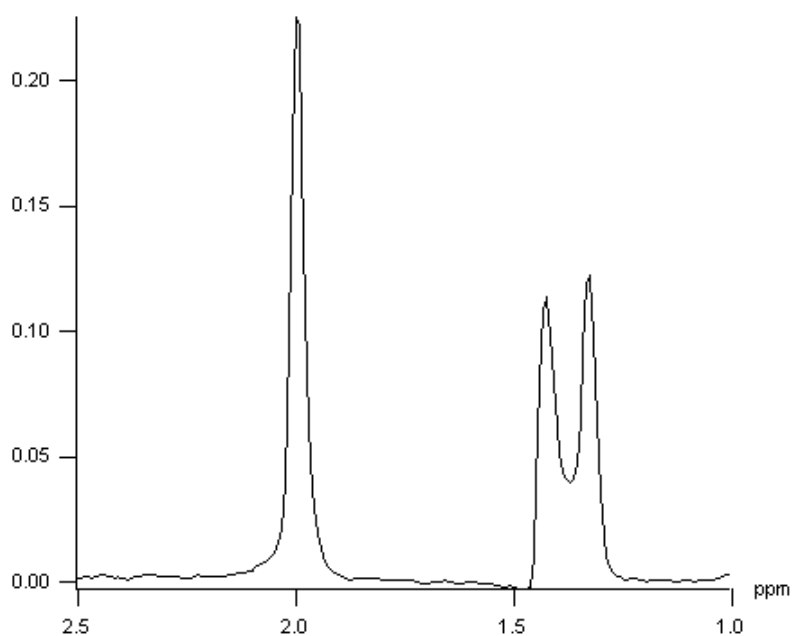
An important feature of spin coupling is that it is not reversed by the application of a  $180^\circ$  refocusing rf pulse. As discussed below, one method of spatial localization uses  $180^\circ$  refocusing rf pulses to produce a spin echo. The lactate signal is modulated in amplitude, based on the elapsed time between the rf pulses, which means that the lactate protons may or may not be in phase with the other protons at the echo time  $TE$ . This condition is analogous to the phase modulation seen in gradient echo MRI studies for fat and water. The rate of this modulation is proportional to  $1/J$ . For the 7 Hz coupling, it corresponds to a phase modulation period of approximately 270 ms. Use of a  $TE$  of 270 ms ensures that the lactate resonances are in phase with the other noncoupled resonances, whereas use of a  $TE$  of 135 ms has the lactate signals  $180^\circ$  out of phase compared to the other resonances (Figure 13-2).

### 13.1.3 WATER SUPPRESSION

Clinical MRI techniques visualize the water and fat within the desired slice. The high concentration of water and fat within the tissue makes this feasible. In MRS, the metabolites under observation are as much as 10,000 times less concentrated than water, which makes their detection in the presence of tissue water difficult. In order to accomplish this, suppression of the water is necessary. The most common approach uses a frequency-selective rf pulse or pulses known as a chemical shift selective (CHESS) pulse. It is centered at the water resonant frequency to saturate the water protons. This technique is analogous to the fat saturation pulse described in Chapter 8. Water suppression factors of 100 or more are possible from a single pulse, making it an easy and effective way for reducing the signal contamination from water.



(a)



(b)

FIGURE 13-2 PRESS  $^1\text{H}$  spectra of lactate (doublet) and acetate (singlet). Choice of  $TE$  affects the relative polarity of the lactate peak compared to acetate, due to modulation of spin-coupled  $^1\text{H}$  atoms. (a)  $TE = 135$  ms. (b)  $TE = 270$  ms.

## 13.2 LOCALIZATION TECHNIQUES

Current techniques used for spatial localization of the MRS signals were derived from similar techniques used in MRI. Slice selective excitation pulses in conjunction with gradient pulses are used to localize the rf energy to the desired volume of tissue, in the same manner as described in Chapter 4. However, unlike MRI, in which the voxel size is typically  $1 \times 1 \times 5 \text{ mm}^3$  or less, MRS voxel sizes are usually  $15 \times 15 \times 15 \text{ mm}^3$  or larger. Therefore, MRS studies are limited to the examination of relatively large regions of tissue. The two general categories of localization techniques are based on the number of separate voxels from which spectra are obtained in each measurement.

### 13.2.1 SINGLE VOXEL TECHNIQUES

Single voxel techniques (also called single voxel spectroscopy or SVS) acquire spectra from a single small volume of tissue. The most common approaches excite only the desired tissue volume through the intersection of three slice-selective rf excitation pulses. Two schemes of rf pulses are used. The first approach, known as point resolved spectroscopy (PRESS), uses a  $90^\circ$  and two  $180^\circ$  rf pulses in a fashion similar to a standard multiecho sequence (Figure 13-3). Each rf pulse is applied using a different physical gradient as the slice selection gradient. Only protons located at the intersection of all three pulses produce the spin echo at the desired TE. The other approach, known as stimulated echo acquisition method (STEAM), uses three  $90^\circ$  rf pulses, each with a different slice selection gradient (Figure 13-4). The resulting stimulated echo (see Section 9.2.5) is produced by protons located at the intersection of the pulses.

There are several differences between PRESS and STEAM. The major difference is in the nature of the echo signal. In PRESS, the entire net magnetization from the voxel is refocused to produce the echo signal, whereas in STEAM, a maximum of one-half of the entire net magnetization generates the stimulated echo. As a result, PRESS has a S/N ratio significantly larger than for STEAM for equivalent scan parameters. Another difference is that PRESS uses  $180^\circ$  rf pulses, whereas STEAM uses only  $90^\circ$  rf pulses.

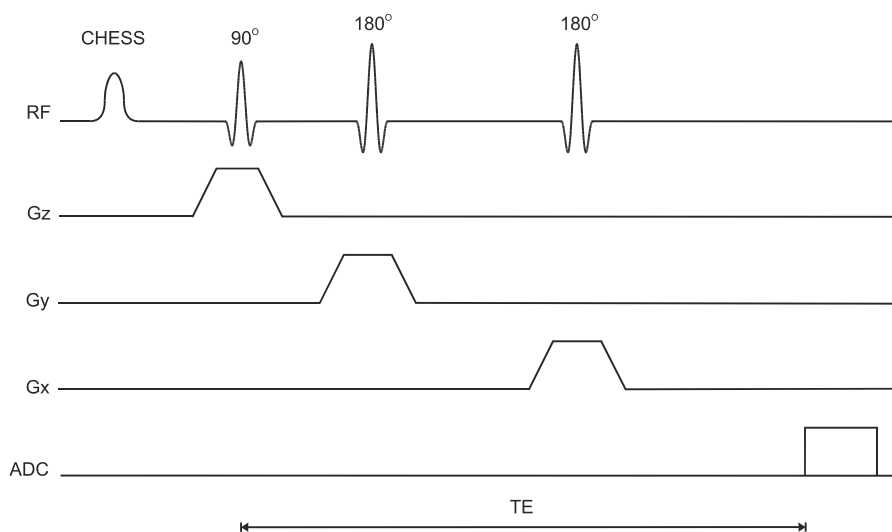


FIGURE 13-3 PRESS pulse sequence timing diagram. The CHESS rf pulse is used for suppression of water.

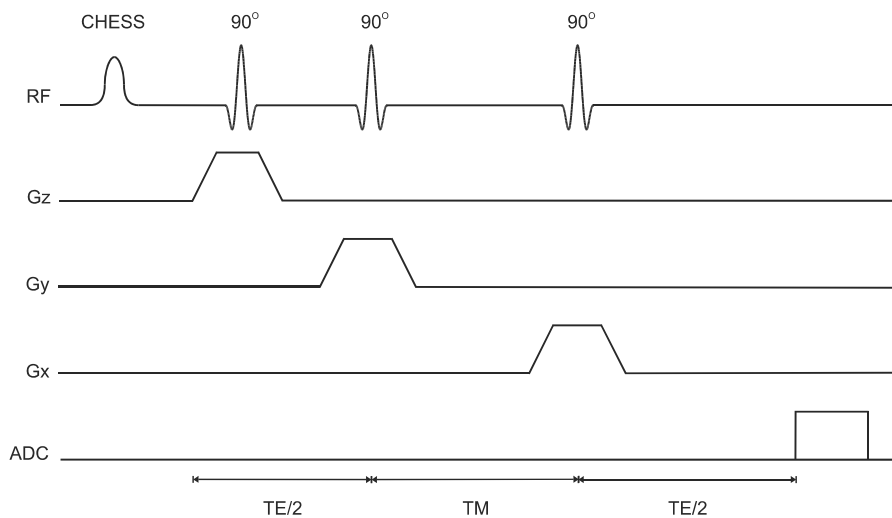


FIGURE 13-4 STEAM pulse sequence timing diagram. The CHESS rf pulse is used for suppression of water.

The voxel dimensions with PRESS may be limited by the high transmitter power for the  $180^\circ$  rf pulses. STEAM spectra are also unaffected by  $J$  coupling of spins, whereas PRESS spectra show a modulation of the signal from any coupled spins, such as lactate methyl protons. Finally, STEAM allows for shorter  $TE$  values, reducing signal losses from  $T_2$  relaxation and allowing observation of metabolites with short  $T_2^*$ .

### 13.2.2 MULTIPLE VOXEL TECHNIQUES

Multiple voxel techniques are those from which multiple spectra are obtained during a single measurement. The most common of these methods is known as chemical shift imaging (CSI). CSI techniques are analogous to standard imaging techniques in that phase-encoding gradient tables are used for spatial localization. They are subdivided into 1D, 2D, and 3D versions, depending on the number of gradient tables used for spatial localization. The most common of these approaches is 2D-CSI, in which two gradient tables are used. Volume-selective rf excitation pulses are used, either with a PRESS or STEAM rf pulse train. The most common scheme has the three excitation pulses in mutually perpendicular directions and is termed volume-selective CSI (Figure 13-5). This scheme enables the volume of excitation to be tailored so that areas producing contaminating signal can be avoided. For example, brain studies using volume-selective CSI can minimize the signal from the skull and subcutaneous fat.

Volume-selective CSI techniques have the advantage over SVS techniques in that spectra from several volumes of tissue can be measured simultaneously, which is advantageous if the disease under observation is diffuse or covers a large area of anatomy. However, the measurement times for CSI techniques are generally relatively long, and the entire data collection must be completed in order to obtain all the localization phase-encoding steps. With SVS techniques, the measurement times are long due to multiple acquisitions necessary to produce an adequate S/N ratio, but the number of acquisitions can be adjusted depending on the voxel size. In addition, the multiple voxels must be individually postprocessed, making analysis of CSI data more operator intensive.

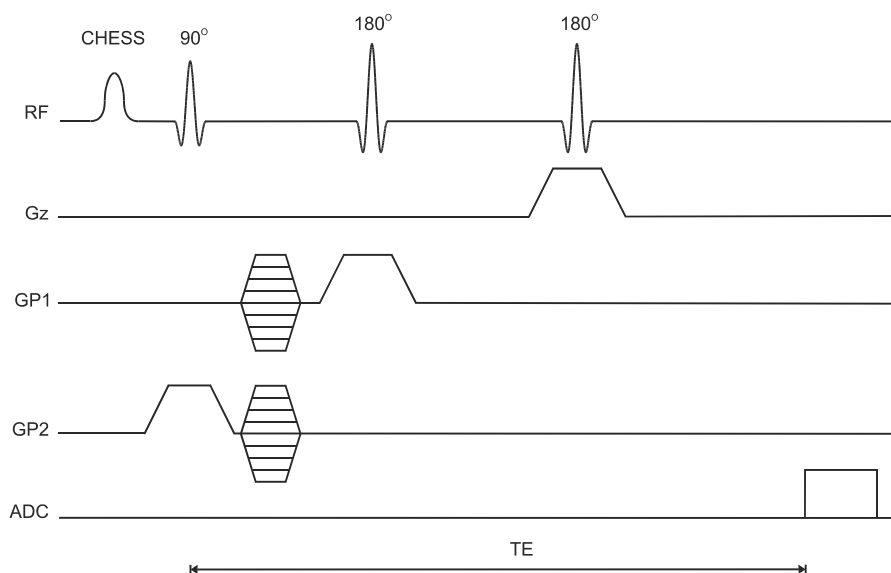


FIGURE 13-5 Volume selective 2D-CSI pulse sequence timing diagram, using PRESS excitation method. The CHES rf pulse is used for suppression of water.

### 13.3 SPECTRAL ANALYSIS AND POSTPROCESSING

The MRS signal from a voxel contains information regarding the identity, molecular environment, and concentration of the metabolite producing the signal. This information is provided by the resonant frequency, the linewidth (full width at half maximum height), and the integrated peak area, respectively. Although this information could be extracted from the time domain form of the signal, it is more convenient to analyze the frequency domain form, obtained following a Fourier transformation. This analysis is aided by various data processing techniques applied both prior to and following the Fourier transformation (Figure 13-6). Many of these techniques are often used in MRI. Filtering of the echo signal is performed to reduce noise that can be induced during the very long sampling times for the echo (typically 1000 ms). This is the same type of filter used in MRI to reduce truncation artifacts. Zero filling consists of adding data points of zero amplitude to the end of the detected time domain signal. This data is typi-

cally background noise in the measurement. Following Fourier transformation, the frequency resolution of the resulting spectrum is increased through interpolation of the measured data points. This approach, termed sinc interpolation in MRI, provides a smoother appearance to the final spectrum. The final processing that is applied to the time domain signal is a correction for distortion from residual eddy currents. Eddy currents are produced as a result of the time-varying nature of the gradient pulses and result in fluctuating magnetic fields that distort the MR signal. The measurement hardware performs some type of eddy current compensation to correct for this, as described in Chapter 14. Although sufficient for MRI studies, this compensation is often insufficient to produce distortion-free MR spectra. Acquisition of a second signal, usually a water-unsuppressed signal from the same voxel, is used to provide a reference for residual field variations due to eddy currents. Alternately, if the eddy currents are not too severe, a small amount of water signal may be retained and can be used as the reference signal.

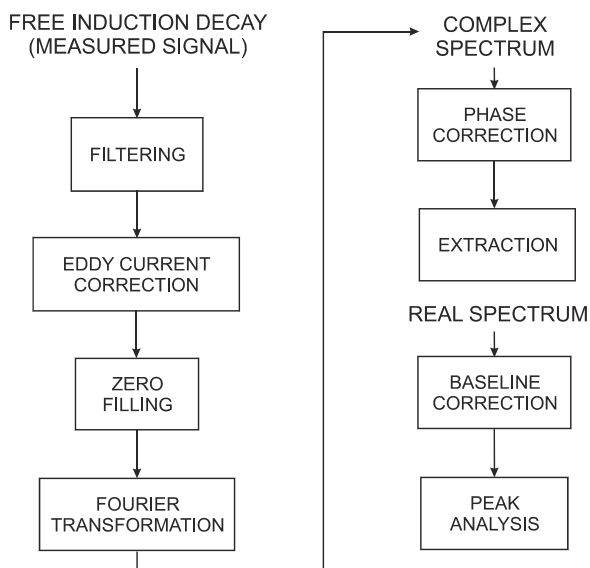


FIGURE 13-6 Typical spectroscopy postprocessing steps.



Following Fourier transformation, the resulting complex frequency domain signal is not a single-mode signal, but is usually a mixture of both the in-phase (dispersion) and out-of-phase (absorption) signals relative to the transmitter (Figure 13-7). In MRI studies, rather than separating these two signals, they are combined to form the magnitude image. For MRS studies, the pure absorption mode is preferred, due to its simpler spectra and to enable semiquantitative spectral analysis. A process known as phase correction is used to separate the two modes and extract the absorption portion. A mathematical manipulation combines the two components of the complex signal together in such a way as to isolate the absorption mode to the real portion and the dispersion mode to the imaginary portion. If the real spectrum is not flat due to hardware imperfections or incomplete water sup-

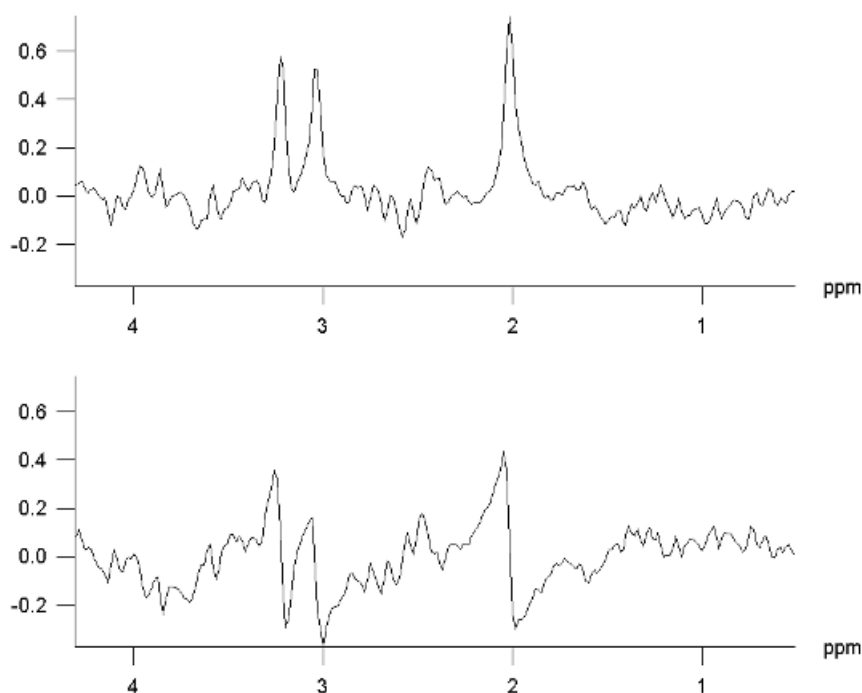
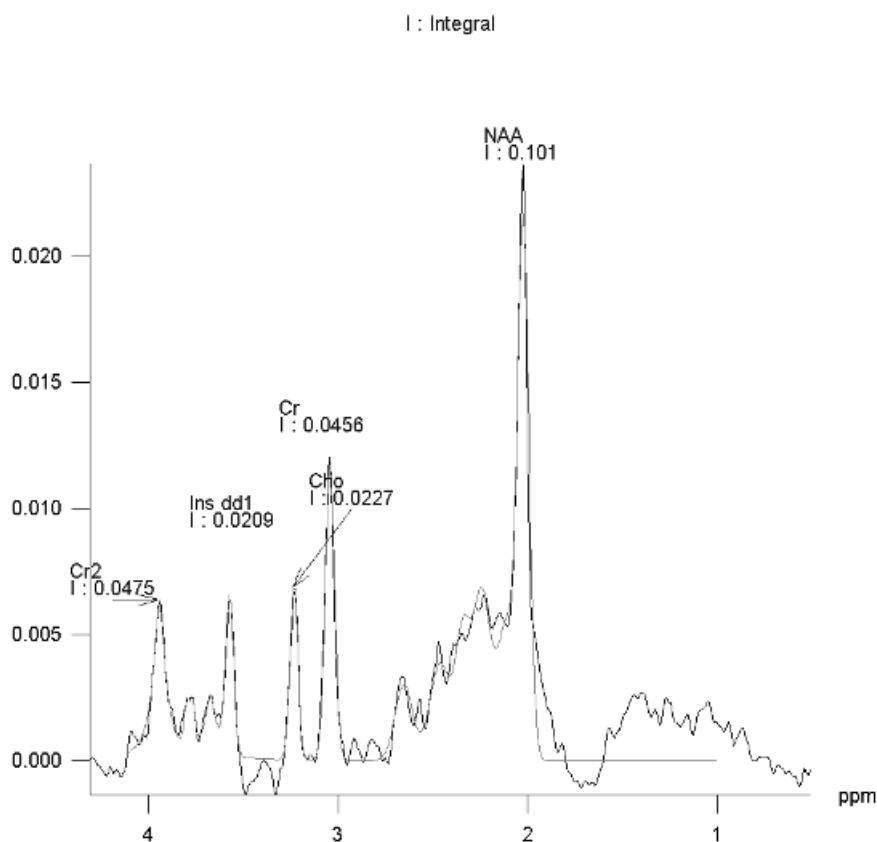


FIGURE 13-7 Phase-corrected complex spectrum resulting from Fourier transformation of FID signal. (a) Real portion of spectrum, also known as the absorption spectrum. (b) Imaginary portion of spectrum, also known as the dispersion spectrum.

pression, it may also be necessary to perform a baseline correction. Finally, the resonant frequency, linewidth, and integrated area for each peak in the spectrum can be measured. Although a visual examination of the spectrum can provide an approximation of these parameters, the most accurate method for analysis involves fitting of the peaks to theoretical curves of the appropriate lineshape. Whereas the frequencies and linewidths can be compared directly from one spectrum to another, peak areas are influenced by various hardware-related variables that are difficult to quantify. Instead, ra-



(a)

FIGURE 13-8  $^1\text{H}$  PRESS spectra acquired at 1.5 T (a) and 3.0 T (b). Note overall improvement in SNR and spatial resolution in (b). (Spectra courtesy of H. Cecil Charles, Duke University.)

tios of peak areas are used in evaluating the relative concentrations of the metabolites. Absolute concentrations for metabolites can be determined if a simultaneous measurement of a reference compound is performed, in which the concentration of the reference is known by other means.

One example of a clinical application of MRS is in the evaluation of temporal lobe epilepsy. Normal brain spectra obtained with long  $TE$  (135 and 270 ms) show three major peaks: *N*-acetyl aspartate (NAA) at 2.0 ppm, creatine/phosphocreatine (Cr) at 3.0 ppm, and choline (Cho) at 3.2 ppm relative to water at 4.7 ppm. The relative area ratios in adults are typically 1.4–1.5

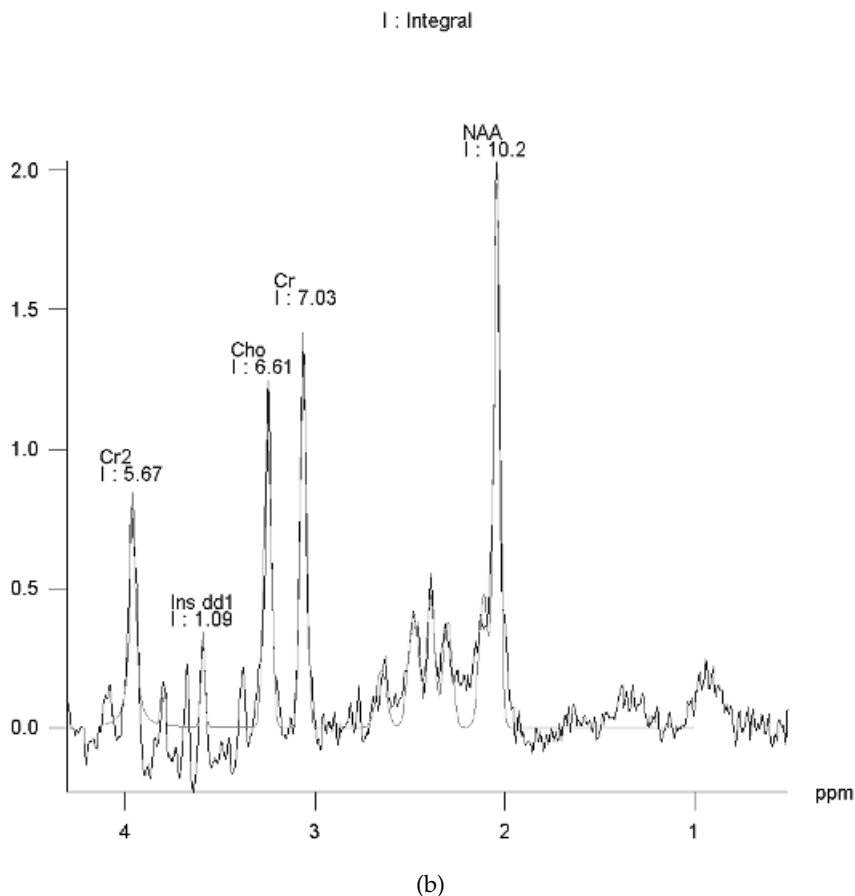


FIGURE 13-8 (Continued)

for NAA/Cr and 0.8 for Cho/Cr. Patients with temporal lobe epilepsy have been found to have reduced levels of NAA and increased levels of Cho and Cr in the diseased lobe (Achten, 1997). Acquisition of spectra from both temporal lobes enables a clear identification of the affected region. Use of MRS in evaluating brain tumors is somewhat more problematic. Spectra from both primary and metastatic tumors can have increased levels of Cho, decreased levels of NAA, and the signals from lactate at 1.3 ppm and lipids at 1.2 ppm. Tissue biopsy or use of other techniques should be used to confirm the presence or absence of tumor tissue.

### 13.4 ULTRAHIGH FIELD SPECTROSCOPY

MRS examinations also benefit from use of ultrahigh  $B_0$ . As mentioned in Chapter 1, the net magnetization  $M$  is directly proportional to  $B_0$ , so that the potential exists to obtain increased signal. This is particularly beneficial for MRS examinations of  $^{31}\text{P}$  and  $^{13}\text{C}$ , in which the sensitivity is significantly less than that of  $^1\text{H}$ . The increased chemical shift difference enables better spectral resolution between metabolites with similar resonant frequencies. The spectral linewidths generally appear narrower, due to the increased frequency range. On a practical basis, the increased S/N ratio can be exploited in two ways. Smaller voxels can be scanned, allowing improved spatial resolution. For example, MR spectra can be acquired with equivalent S/N ratio with fewer signal averages. This can result in shorter scan times, allowing better time resolution in kinetic examinations. Alternately, resolution of gray and white matter into separate voxels can be performed using 2D-CSI (Figure 13-8).

There are two areas in which ultrahigh  $B_0$  can cause problems. Signals from fat will significantly increase compared to that measured at conventional  $B_0$ . Suborbital fat or fat from bone marrow in the skull can potentially cause contamination in brain examinations. Outer volume saturation or narrow-band inversion of the lipid signal may be necessary to obtain good quality spectra. The second area of concern is due to the increased chemical shift differences between metabolite signals. When using volume-selective excitation, there will be a misregistration of the metabolites being excited by the frequency-selective rf pulse. This is analogous to the chemical shift arti-

fact observed in MRI. In particular, this is problematic with 2D-CSI, in which the excitation volume is localized in all three directions by frequency-selective rf pulses. Voxels near the edges of the excitation volume will exhibit intensity variations due to nonuniform metabolite excitation. Although this problem is observed at conventional  $B_0$ , it is worsened at ultrahigh  $B_0$  due to the increased chemical shift between the metabolite resonances. Care must be taken in positioning the excitation volume as a result.

## **INSTRUMENTATION**

---

A very important aspect of the production of MRI images is the instrumentation used in the measurement. Many MR systems are commercially available, each possessing different features and capabilities that are often difficult to evaluate and compare objectively. Many of these features are based on the operating software provided by the manufacturer, but certain hardware components are common to all systems. The following sections describe the basic subsystems of an MRI scanner and technical aspects to consider when comparing systems. The major components are the computer and image processing systems, a magnet system, a gradient system, a radiofrequency system, and a data acquisition system (Figure 14-1).

### **14.1 COMPUTER SYSTEMS**

Currently, every MRI system has a minimum of two computers. The main or host computer controls the user interface software. This software enables the operator to control all functions of the scanner either directly or indirectly. Scan parameters may be selected or modified, patient images may be displayed or recorded on film or other media, and postprocessing operations such as region-of-interest measurements or magnification can be performed. Several peripheral devices are typically attached to the main computer. One or more hard disks are used to store the patient images immediately following reconstruction. This disk or disks are used for short-term storage; currently available disk drives are able to store upwards of 100,000–150,000 images, depending on the image size. A device for long-

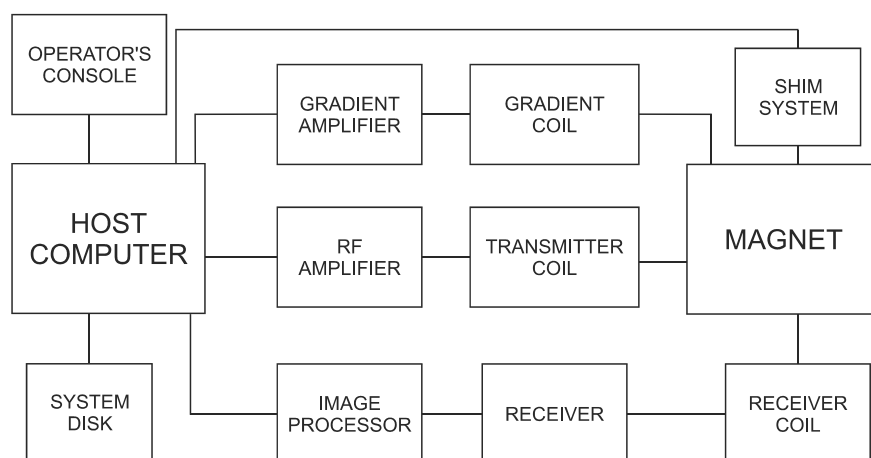


FIGURE 14-1 Block diagram of an MRI system.

term archival storage, either a laser optical disk or CD-ROM, is usually included. A hard-copy camera may be connected via a network or attached to the main computer if filming is controlled by the operating software.

The second computer system is a dedicated image processor used for performing the Fourier transformations or other processing of the detected data. This processor is controlled by software provided by the manufacturer. The raw data is stored from the receiver into memory in the image processor itself or onto a separate hard disk. The image processors currently used with MRI scanners are capable of performing the Fourier transformation for a  $256 \times 256$  matrix in less than 50 milliseconds. Additional image processors may be present that perform computationally intensive postprocessing.

One or more consoles may be attached to the main computer or may have direct access to the reconstructed images. The main console is the primary device for operator input. Each console has a keyboard and one or more monitors for displaying images and text information. A computer mouse is often used for more interactive control. Additional consoles may be directly attached to the same main computer, allowing convenient viewing or postprocessing of the images. Alternately, other viewing stations may be completely detached from the primary computer system and access

the image data through a network connection. They may be used as a common viewing station for analysis of images acquired using additional imaging modalities such as computed tomography, ultrasound, or traditional X-ray. In addition, there may be an archive server known as a PACS (picture archiving and communications system) unit. This system is used as a centralized digital repository for images. PACS systems allow multiple users to access the images and patient data easily and can provide long-term archiving of the images in a central location.

MRI systems are often incorporated into a facility's computer network. This allows images to be transferred directly from the MRI host computer to another computer in a remote location rather than using a removable medium (e.g., film or CD-ROM). The interconnections between the two computers are normally one of two types. An Ethernet connection is a physical cable. This is typically used for connecting computers within a building or small group of buildings; for example, between two scanners or between the scanner and a viewing station. Alternately, the connection may be through a dial-up or cable modem, using standard or high-speed telecommunication. This is used for long-distance transmission of images and data. In many facilities, both types of connections are used.

Most computer networks use a communications protocol known as TCP/IP (Transmission Control Protocol/Internet Protocol) for the actual data transfer between the computers. Each computer on the network will have a unique identification number assigned to it by the network administrator, known as the IP address. This is a series of four numbers, each less than 255 (written as, e.g., 121.232.22.21), that act as an address for the computer on the network. There will also be one computer on the network known as a router, which facilitates the data transfer. Data transfer is initiated from one computer (e.g., the MRI host computer) with the IP address of the destination computer (e.g., the viewing station). The data is initially sent to the router, which will direct the data to the destination computer based on the IP address. Both the initiating and destination computers must have each other's IP address in order to transfer data in both directions.

The use of TCP/IP provides a means for transferring data between computers, but there must be a common format for writing the data if it is to be interpreted correctly. This is of particular importance if the two comput-



ers use software from different manufacturers, as each manufacturer will use its own proprietary format for data storage. One format that is becoming the industry standard for facilitating image and medical data transfer is known as DICOM, which stands for Digital Imaging and Communications in Medicine. It is the result of a joint committee of the American College of Radiology and the National Electrical Manufacturers Association (ACR-NEMA). The DICOM standard provides a framework allowing equipment (scanners, digital cameras, viewing stations) from different manufacturers to accept and interpret data accurately. Images written using this standard have the basic measurement information stored so that any vendor can read and properly display the images with the correct anatomic labeling and basic measurement parameters. Manufacturers who subscribe to the DICOM standard have available a DICOM Conformance Statement, which provides details on their implementation. Programmers writing software that use DICOM-formatted images should consult the conformance statement for the particular manufacturer to ensure proper interpretation of the image header variables.

Although a discussion of the complete DICOM standard is beyond the scope of the current discussion, two aspects of it are likely to be encountered with current MRI systems. The first is the format in which images are stored. Images stored in the DICOM format are written with the measurement parameters and other information organized in a fashion as specified in the DICOM Conformance Statement. This allows image display and analysis programs to be written without knowledge of the manufacturer's proprietary methods. Programs for reading DICOM-format images are available from several companies, with some programs available at no cost and others available for a fee.

The second aspect of DICOM that is frequently encountered is in the nature of the data transfer between computers. The DICOM standard has features that control the communication relationship between systems. This is critical to ensure confidentiality of patient information. Two levels of connectivity are commonly used. The first is known as the DICOM Store Service Class (commonly known as Send/Receive). This allows one computer system (e.g., the scanner) to send images to another system or to receive images from another system. This is normally used to connect scanners of dif-

ferent modalities (i.e., MR to CT). The other level of connectivity is known as the DICOM Query Service Class (commonly known as Query/Retrieve). This allows a remote computer to query the image database on a scanner and retrieve the images without operator intervention required. This is the normal connectivity between two scanners of the same modality or between a scanner and an archive server. This connectivity is controlled by the application entity title (AET) and both computers must have matching AETs in order for the transfer to be successful. The connectivity relationships are assigned by the network administrator during system installation or configuration based on the preferences and policies of the facility.

## **14.2 MAGNET SYSTEM**

The magnet is the basic component of an MRI scanner. Magnets are available in a variety of field strengths, shapes, and materials. All magnet field strengths are measured in units of tesla or gauss (1 tesla = 10,000 gauss). Magnets are usually categorized as low-, medium-, or high-field systems. Low-field magnets have main field strengths less than 0.5 T. Medium-field systems have main magnetic fields between 0.5 and 1.0 T, high-field systems have fields between 1.0 T and 1.5 T, and ultra-high-field systems have fields of 3.0 T or greater.

Magnets are also characterized by the metal used in their composition. Permanent magnets are manufactured from metal that remains magnetic for extremely long periods of time (years). They can be solenoidal (tube shaped) or have a more open design. Permanent magnets have minimum maintenance costs because the field is always present. However, care must be taken to keep ferrous material away from the magnet. Such material will be attracted forcefully into the magnet and the magnetic field cannot be eliminated to allow its extraction. Permanent magnets also have their mass concentrated over a small area. Additional structural support of the scanner room may be necessary in some cases.

The other types of magnets are electromagnets in which the flow of electrical current through wire coils produces the magnetic field. Traditional electromagnets are made of copper wire wound in loops of various shapes. A power supply provides a current source. The magnetic field is

present as long as current flows through the magnet windings. Copper-wire-based electromagnets are low-field systems and may also be of solenoidal or open-type design. The most common type of magnets are solenoidal superconducting electromagnets using niobium–titanium alloy wire immersed in liquid helium. This alloy has no resistance to the flow of electrical current below a temperature of 20° K. The magnet cryostat, which contains the liquid helium, may be a double dewar design with a liquid nitrogen container surrounding the helium container, or a helium-only design with a refrigeration system to reduce the helium boiloff to a minimum. Refrigeration systems used with current magnets allow helium replenishment rates of one or two times per year.

The primary consideration in magnet quality is the homogeneity or uniformity of the magnetic field. One factor affecting magnet homogeneity is the magnet design. Large-bore solenoidal magnets generally have the best homogeneity over the largest volume. Short-bore magnets tend to have smaller regions of good homogeneity due to the reduced number of magnet windings used. Open-design magnets will also have reduced regions of good homogeneity. Magnetic field homogeneity is usually expressed in units of ppm relative to the main field over a certain distance. Magnetic field values are measured at various locations inside the magnet and used to calculate the field variation using Equation 2-4, replacing the frequencies with the measured magnetic field values. High homogeneity means the magnetic field changes very little over the specified region or volume. The protons in this region resonate at the same frequency in a coherent manner and thus induce the maximum possible signal. Great effort is taken during magnet manufacturing and installation to ensure the best homogeneity possible. However, manufacturing imperfections or site problems (e.g., nearby steel posts, asymmetrical metal arrangements) may produce significant field distortions. To analyze and compensate for this, the distortions are characterized by the mathematical shape of the field corrections required as a function of distance away from the magnet center. This classification is referred to as the order of the field or shim correction used. First-order or linear corrections in each direction are achieved using the imaging gradient coils described in Section 14.3. Second- or higher-order corrections are non-linear in nature and many MRI systems use a coil known as a shim coil to

correct for them. The design of the shim coil may be passive in that it holds pieces of metal (shim plates) or small magnets that correct the field distortions, or active in that there are loops of wire through which current passes to correct the field distortions. In some systems, both types of shim correction may be used. Passive shimming is generally performed at the time of magnet installation as a one-time event. Active shimming (also called electrical shimming) is usually performed on a regular basis during system maintenance. Field homogeneity is an important factor to consider when evaluating an MRI system, as inadequate homogeneity can cause problems with fat saturation or even general imaging.

Certain precautions should be exercised around all magnets, regardless of field strength. The examination room in which the magnet is located should have restricted access. Any metal near the magnet should be non-magnetic. Metal items such as stethoscopes or pens may be attracted to the magnet, possibly causing injury. Breathing gases used for sedated patients should be either built into the wall or supplied from nonferrous tanks. Electrical equipment must be protected or shielded from the magnetic field in order to function properly. Patients with surgical implants or metal fragments in their bodies as a result of trauma or occupation (e.g., sheet metal workers) should be scanned only if there is no risk to the patient should the implant or fragment move during the procedure. Patients with magnetic pacemakers or ferromagnetic intracranial aneurysm clips should not be scanned under any circumstances due to the risk of patient injury. The magnetic properties of various medical implants have been extensively described by Shellock and coworkers (Shellock, 2001).

It is also important to realize that the magnetic field of all magnets extends in all directions away from the center of the field. The amount of fringe magnetic field (the portion outside the magnet housing) is a very important consideration in siting an MRI system. The fringe field is greatest near the magnet in the *z* direction and decreases with increasing distance away from the magnet. The fringe field is also larger for higher-field magnets. A low-field magnet has a very small fringe field, making it possible to use standard patient monitoring equipment. High-field systems are often manufactured with magnetic shielding of some variety to reduce the fringe field. This shielding may surround the magnet (passive shielding), be gen-

erated by a second set of superconducting magnet windings surrounding the main field (active shielding), or be built into the wall (room shielding). Two distances are of concern regarding the fringe field. The 0.5 mT (5 G) distance is considered the minimum safe distance for persons with pacemakers. This distance prevents interference of the pacemaker operation by the magnetic field. The 0.1 mT (1 G) distance, the nominal distance for other equipment that uses video monitors, prevents distortion of the image on the monitor by the magnetic field. The actual distances are installation and equipment specific. Contact the manufacturer regarding individual situations.

### 14.3 GRADIENT SYSTEM

As mentioned in Chapter 4, small linear distortions to  $B_0$  known as gradient fields or gradients are used to localize the tissue signals. Three gradients are used, one each in the x, y, and z directions, to produce the orthogonal field variations required for imaging. They are each generated by the flow of electrical current through separate loops of wire mounted into a single form known as the gradient coil. Variations in gradient amplitude are produced by changes in the amount or direction of the current flow through the coil.

One of the major criteria for evaluation of an MRI scanner is the capabilities of the gradient system. There are four aspects that are important in assessing gradient system performance: maximum gradient strength, rise time or slew rate, duty cycle, and techniques for eddy current compensation. Gradient strength is measured in units of mT m<sup>-1</sup> or G cm<sup>-1</sup> (1 G cm<sup>-1</sup> = 10 mT m<sup>-1</sup>), with typical maximum gradient strengths for current state-of-the-art MRI systems being 30–40 mT m<sup>-1</sup> (3.0–4.0 G cm<sup>-1</sup>). These maximum gradient strengths allow thinner slices or smaller FOV to be obtained without changing other measurement parameters. Another quantity often used to describe maximum gradient amplitudes is the effective gradient amplitude  $G_{eff}$ . This is the vector sum of all three gradients when applied during the scan:

$$G_{eff} = (G_x^2 + G_y^2 + G_z^2)^{1/2}$$

Care must be made to distinguish between the effective gradient and the actual gradient being applied. For example, for slice selection, orthogonal slices will only use one gradient axis, whereas only double oblique slices will require all three axes.

The response of a gradient coil to the flow of current is not instantaneous. Gradient pulses require a finite time known as the rise time to achieve their final value. This rise time is nominally 0.2–0.5 ms, which defines a rate of change or slew rate for a gradient pulse. If the desired gradient pulse amplitude is  $20 \text{ mT m}^{-1}$  with a 0.5 ms rise time, the slew rate is  $40 \text{ mT m}^{-1} \text{ ms}^{-1}$  or  $40 \text{ T m}^{-1} \text{ s}^{-1}$ . Gradient rise times and/or slew rates are often used to evaluate the performance of the gradient amplifier or power supply producing the current. High-performance amplifiers allow shorter rise times (faster slew rates), enabling shorter gradient pulse durations and/or interpulse delays within a pulse sequence. As a result, the minimum *TE* may be reduced for a given technique while maintaining a small *FOV*.

The duty cycle of the gradient amplifier is another important measure of gradient performance. The duty cycle determines how fast the amplifier can respond to the demands of a pulse sequence. Duty cycles of 100% at the maximum gradient amplitude are typical for state-of-the-art gradient amplifiers for normal imaging sequences. Large duty cycles allow high-amplitude gradient pulses to be used with very short interpulse delays. Low duty cycles mean that the *TE* times will be longer for the scan to allow the gradient amplifiers to return to a standard operating state.

Another complication of gradient pulses is eddy currents. Eddy currents are electric fields produced in a conductive medium by a time-varying magnetic field. In MRI systems, eddy currents are typically induced by the ramping gradient pulse in the body coil located inside the gradient coil and the cryoshield (the innermost portion of the magnet cryostat) outside the coil. These currents generate a magnetic field that opposes and distorts the original gradient pulse. In addition, once the gradient plateau is reached and the ramp is stopped, the eddy currents begin to decrease. The net result is that the distorting field will change with time as the eddy currents decay. Therefore, the magnetic field homogeneity and the corresponding frequencies change with time as well. Correction of these eddy-current-induced distortions is known as eddy-current compensation. Two

approaches are commonly used for compensation. One method predistorts the gradient pulse so that the field variation inside the magnet is the desired one. This predistortion may be done via hardware or software. A second approach uses a second set of coil windings surrounding the main gradient coil. This approach is called an actively shielded gradient coil, analogous to the actively shielded magnet described previously. The current flow through the shield coil reduces the eddy currents induced structures outside the coil. Typical state-of-the-art scanners use both methods of eddy current compensation.

## 14.4 RADIO FREQUENCY SYSTEM

The radio frequency (rf) transmitter system is responsible for generating and broadcasting the rf pulses used to excite the protons. The rf transmitter contains four main components: a frequency synthesizer, the digital envelope of rf frequencies, a high-power amplifier, and a coil or antenna. As discussed in Chapter 5, each rf pulse has both a frequency and a phase defined for it. These features are determined by the combination of frequency and phase from the frequency synthesizer and the rf envelope defining the pulse shape.

The frequency synthesizer produces the center or carrier frequency for the rf pulse. It also provides the master clock for the measurement hardware during the scan. The frequency synthesizer also controls the relative phase of the rf pulse. Many pulse sequences alternate the phase of the excitation pulse for each measurement by  $180^\circ$  to help reduce stimulated echo artifacts caused by pulse imperfections. Spin echo sequences also typically have the refocusing rf pulses shifted in phase  $90^\circ$  relative to the excitation pulse (known as the Carr–Purcell–Meiboom–Gill or CPMG technique). This phase variation may be done through modulation of the rf envelope or the carrier frequency. More sophisticated synthesizers allow phase changes of  $1\text{--}2^\circ$  increments. This finer control also allows for coherence spoiling through incremental phase change of the transmitter, a process known as rf spoiling (Chapter 9).

The rf envelope is stored as a discrete envelope or function containing a range or bandwidth of frequencies. It is mixed with the carrier frequen-

cy prior to amplification to produce an amplitude- or phase-modulated pulse centered at the desired frequency. For some scanners, the final frequency is produced exclusively by the frequency synthesizer, whereas for other scanners, the rf envelope is modulated to incorporate a frequency offset into the pulse. In either case, the final frequency is determined based on Equation 4-2 and generated as a phase coherent signal by the synthesizer.

The rf power amplifier is responsible for producing sufficient power from the frequency synthesizer signal to excite the protons. The amplifier may be solid state or a tube type. Typical rf amplifiers for MR scanners are rated at 2–30 kW of output power. The actual amount of power required from the amplifier to rotate the protons from equilibrium depends on the field strength, coil transmission efficiency, transmitter pulse duration, and desired excitation angle.

The final component of the rf system is the transmitter coil. All MR measurements require a transmitter coil or antenna to broadcast the rf pulses. Although transmitter coils can be any size and shape, the one requirement that must be met is that they generate an effective  $B_1$  field perpendicular to  $B_0$ . Another feature of most transmitter coils is that they can produce uniform rf excitation over a desired area; that is, a volume can be defined within the coil in which all protons experience the same amount of rf energy. Solenoidal MR systems use either a saddle or bird cage coil design, which produces uniform rf excitation even though the coil opening is parallel to  $B_0$ . These coils are often adjusted or tuned to the patient to achieve the maximum efficiency in rf transmission. Two types of coil polarity are used: linear polarized (LP) and circularly polarized (CP), also called quadrature. In an LP system, a single coil system is present and the rf pulse is broadcast as a plane wave. A plane wave broadcast at a frequency  $\omega_{TR}$  has two circularly rotating components, rotating in opposite directions at the same frequency  $\omega_{TR}$ . For MR, only the component rotating in the same direction as the protons (in phase) induces resonance absorption. The other component (out of phase) is absorbed by the patient as heat. In a CP transmitter system, two coils are present, one rotated  $90^\circ$  from the other. Phase-shifted rf pulses are broadcast through each coil. The out-of-phase components cancel each other while the in-phase components add coherently. The



patient absorbs only the energy from the in-phase components from each coil. A 40% improvement in efficiency from the transmitter system is achieved for a CP system relative to an equivalent LP system for the same proton rotation.

Although MR is considered a relatively safe imaging technique, the absorbed rf power generates heat inside the patient. Manufacturers are required by the governing regulatory organizations [Food and Drug Administration (FDA), International Electrotechnical Commission (IEC), etc.] to monitor the rf power absorbed by the patient so that excessive patient heating does not occur in both the excited tissue volume (localized) and the entire patient. To accomplish this, the specific absorption rate of energy dissipation or SAR is monitored. The SAR is measured in watts of energy per kilogram of patient body weight (W/kg). MRI systems are designed to operate at or below the SAR guidelines, which are set to limit the patient heating to approximately 1°C or less. For low-field scanners, the SAR seldom limits the measurement protocols. For high-field scanners, the SAR limits have a significant effect on the number of slices or saturation pulses that can be applied to the patient within a scan.

## 14.5 DATA ACQUISITION SYSTEM

The data acquisition system is responsible for measuring the signals from the protons and digitizing them for later postprocessing. All MRI systems use a coil to detect the induced voltage from the protons following an rf pulse. The coil is tuned to the particular frequency of the returning signal. This coil may be the same one used to broadcast the rf pulse, or it may be a dedicated receiver coil. The exact shape and size of the coil are manufacturer specific, but its effective field must be perpendicular to  $B_0$ . The sensitivity of the coil depends on its size, with smaller coils being more sensitive than larger coils. Also, the amount of tissue within the sensitive volume of the coil, known as the filling factor, affects the sensitivity. For large-volume studies such as body or head imaging, the transmitter coil often serves as the receiver coil. For smaller-volume studies, receive-only surface coils are usually used. These coils are small, usually ring-shaped,

have high sensitivity but limited penetration, and are used to examine anatomy near the surface of the patient's body. Phased-array coils use two or more smaller surface coils to cover a larger area. The small coils are configured so that there is minimal interference between them. This arrangement provides the sensitivity of the small coil but with the anatomical coverage of the larger coil.

The signals produced by the protons are usually  $\text{nV}$ – $\mu\text{V}$  in amplitude and  $\text{MHz}$  in frequency. In order to process them, amplification is required, which is usually performed in several stages. The initial amplification is performed using a low-noise, high-gain preamplifier located inside the magnet room or built into the coil itself. This signal is further amplified, then demodulated to a lower frequency. Further digital amplification will be performed by the receiver module. Two types of receivers are used in MRI systems. Analog receivers amplify then demodulate the measured signal relative to the input frequency from the frequency synthesizer to produce a quadrature signal (real and imaginary) with frequencies between  $1000$ – $250,000$   $\text{Hz}$  (audio frequency). The signals will be filtered with band-pass filters, then digitized using analog-to-digital converters (ADCs). The ADCs digitize each analog signal at a rate determined by the sampling time and number of data points specified by the user. Typical ADCs can digitize a  $10$   $\text{V}$  signal into 16 bits of information at a rate of  $0.5$ – $1000$   $\mu\text{s}$  per data point. Digital receivers demodulate the signal to an intermediate frequency, and then digitize it using an ADC. The final signal amplification, application of a bandpass filter, demodulation to an audio range, and quadrature formulation are done on the digital signal. Digital receivers allow for better signal fidelity of the final signal compared to analog receivers. The digitized data is stored on a hard disk or in computer memory for later Fourier transformation. Phased-array coils typically have a separate preamplifier and ADC for each coil in the array.

Although not formally part of the data acquisition system hardware, an important component of an MRI scanner is rf shielding of the scan room. The weak MR signals must be detected in the presence of background rf signals from local radio and television stations. To filter this extraneous noise, MRI scanners are normally enclosed in a copper or stainless steel shield known as a Faraday shield. Maintaining the integrity of

this Faraday shield is very important to minimize noise contamination of the final images.

## 14.6 SUMMARY OF SYSTEM COMPONENTS

Following is a list of system features or characteristics to consider in comparing MRI systems according to subsystem. Individual software features offered by a manufacturer are not included.

### Computer Systems

- Main computer processor speed, MHz
- Capacity of short-term storage disk, GBytes
- Type of archive device and capacity, MBytes
- Number and speed of image processors, s image<sup>-1</sup>
- Number of consoles and method of interconnection
- Network capability
- Filming capabilities
- Level and nature of DICOM compliance

### Magnet System

- Field strength, T
- Field homogeneity, ppm [measured over a specified diameter of a spherical volume (dsv)]
- 0.5 mT (5.0 G) distance from isocenter (in all directions), ft
- Cryogen capacity and evaporation rate, l He day<sup>-1</sup>

### Gradient System

- Maximum gradient amplitude per axis, mT m<sup>-1</sup> (or G cm<sup>-1</sup>)
- Duty cycle, percent
- Maximum slew rate, T m<sup>-1</sup> s<sup>-1</sup>
- Method(s) of eddy current correction

### Radiofrequency System

- Rf spoiling capabilities (phase behavior)
- Maximum output power, kW
- Type of transmitter coils (CP, LP)
- Operating frequency range (if multinuclear imaging or spectroscopy is planned)

### Data Acquisition System

Number and type of receiver channels

Digitization speed of ADCs, min  $\mu\text{sec}/\text{point}$

Dynamic range of receiver system (maximum number of available digital bits)

Raw data storage capacity, MBytes

Types of receiver coils (CP, LP, phased array)

Nature and quality of rf shielding

## CONTRAST AGENTS

---

One of the strengths of MRI is the significant amount of intrinsic contrast between tissues that it produces. This contrast is based upon differences in signal intensity between adjacent pixels in the image. It is a result primarily of differences in the  $T_1$  and/or  $T_2$  relaxation times of the tissues under observation accentuated by the chosen  $TR$  and  $TE$ . Pathologic tissue may or may not have significant differences in  $T_1$  or  $T_2$  from the surrounding normal tissue. For this reason, there may be little signal difference between normal and pathologic tissue in spite of the inherent high contrast in the images. This signal difference can be increased through the administration of a contrast agent.

Contrast agents for MRI have several advantages over those used for computed tomography (CT). CT agents are direct agents in that they contain an atom (iodine, barium) that attenuates or scatters the incident X-ray beam differently from the surrounding tissue. This scattering permits direct visualization of the agent itself regardless of its location. Most MRI contrast agents are indirect agents in that they are never visualized directly in the image, but affect the relaxation times of the water protons in the nearby tissue. The concentration and dosage for MRI agents are also significantly lower than for CT agents, which in part explains the lower occurrence of adverse reactions to MRI agents. They are normally excreted through the renal system within three to four days, though the excretion rate varies substantially from agent to agent. Contrast agents are usually categorized as  $T_1$  or  $T_2$  agents based on their primary effect of shortening the  $T_1$  or  $T_2$  relaxation times, respectively. However, these agents also shorten the other relaxation time to a lesser degree. The amount of reduction depends on the concentra-

tion of the agent: when concentrated,  $T_1$  agents shorten  $T_2$  or  $T_2^*$  times and when dilute,  $T_2$  agents reduce  $T_1$  times. Contrast agents may also be grouped into intravenous and oral agents depending on the route of administration. The following is a brief discussion of MR contrast agents with emphasis on those in current clinical use.

## **15.1 INTRAVENOUS AGENTS**

### **15.1.1 $T_1$ RELAXATION AGENTS**

Most intravenous contrast agents currently in clinical use are  $T_1$  relaxation agents. A variety of formulations are available, all of which consist of one or more paramagnetic metal ions that contain one or more unpaired electrons. The metal ions are either bound into a chelate complex or contained within a macromolecule. The relaxation efficiency per molecule depends on several factors, including the nature of the metal ion and the size of the metal–chelate complex. The primary mode of operation for  $T_1$  contrast agents is as a relaxation sink for the water protons. As mentioned in Chapter 3,  $T_1$  relaxation depends upon the “lattice” receiving the energy that the protons have absorbed from the rf excitation pulse. This energy transfer occurs most efficiently when the protons are in the innermost layer of atoms surrounding the metal ion, known as the coordination sphere. Because the chelate molecules are relatively large and have many bonds to the metal ion, there is limited free space in the coordination sphere. This prevents the protons on large molecules such as fat from getting sufficiently close to the metal ion for efficient energy transfer. The tissue water is able to diffuse into the coordination sphere of the metal ion and give up its energy, then exchange with the bulk tissue water, enabling additional water molecules to enter the coordination sphere. This diffusion/exchange happens very rapidly ( $\sim 10^6$  times per second) so that the bulk tissue water is relaxed when the subsequent excitation pulse is applied (Figure 15-1). The result is that the tissue water near the contrast agent has a larger net magnetization  $M$  than water in the neighboring tissue and will contribute more signal in a  $T_1$ -weighted image (Figure 15-2). In addition, the rapid exchange process enables many water molecules to be affected by a single chelate complex,

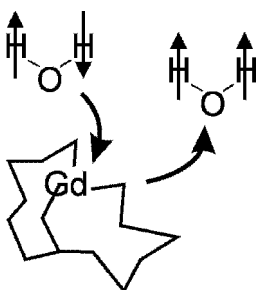
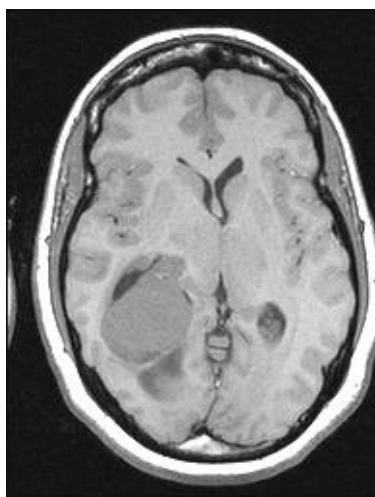
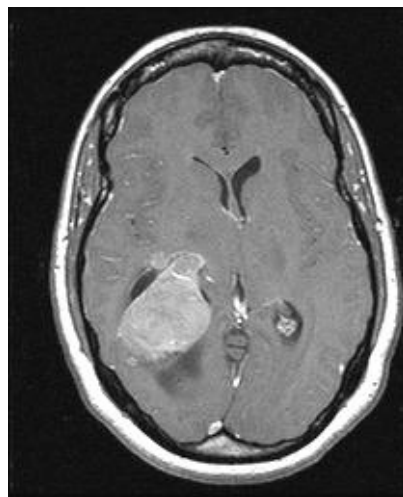


FIGURE 15-1 Exchange of water molecules in the coordination sphere of a gadolinium–chelate contrast agent. The chelate molecule causes steric hindrance (crowding) around the gadolinium atom, restricting its access. An excited water molecule is small enough to reach the inner sphere and transfer its energy to the gadolinium ion. It then leaves the complex unexcited as another molecule replaces it.



(a)



(b)

FIGURE 15-2 T1-weighted spin-echo images before and after administration of gadolinium–chelate contrast agent. (a) No contrast agent present. (b) Contrast agent present. Signal increase due to presence of agent.

which allows low concentrations of contrast agent to be used in clinical studies. MR contrast agents were originally developed for use in neuroimaging to differentiate between normal and neoplastic tissues, but their usage has extended to other examinations including routine and angiographic imaging in the abdomen and thorax (Figure 15-3).

Intravenous *T1* contrast agents are available in both ionic and nonionic formulations. The most common agents use gadolinium as the metal ion and either diethylenetriaminepentaacetate [(DTPA); ionic; Magnevist; Schering AG, Berlin, Germany], diethylenetriaminepentaacetate bismethylamide [(DTPA-BMA); nonionic; Omniscan; Nycomed Amersham, New York, NY], or 10-(2-hydroxypropyl)-1,4,7,10-tetraazacyclododecane-1,4,7-triacetate [(HP-DO3A); nonionic; Prohance; Bracco Diagnostic, Princeton, NJ] as the chelate molecule. The agents currently licensed for use in the United States are nonspecific extracellular agents in that the agents diffuse rapidly from the vascular space into the interstitial space of the tissue (see Figure 12-4). The major elimination pathway of these agents is through glomerular filtration and renal excretion. The half-life is typically in the order of 90 minutes with virtually complete elimination of these agents within 24 hours. The safety profile for these agents is excellent, with few reported

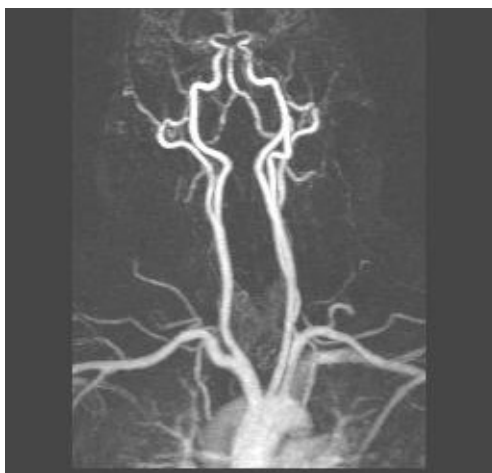


**FIGURE 15-3** MRA of aortic arch and carotid arteries acquired following administration of gadolinium–chelate contrast agent.



side effects and rare cases of major side effects. These agents are therefore frequently employed in patients with a known history of allergies to iodinated contrast agents. In addition, these agents are considered to be extremely safe for administration to patients with compromised renal function, due to both their intrinsic safety and the relatively small volume of the agent administered for most studies (typically 10 to 20 ml). On the other hand, the adverse effect of iodinated contrast agents in patients with renal failure is a well-known problem. Therefore, patients with renal failure or elevated levels of serum creatinine are more likely to tolerate an MRI examination with administration of a gadolinium-chelated contrast agent rather than a CT examination using iodinated contrast media.

Other formulations of gadolinium-chelated contrast agents have both hydrophilic and hydrophobic properties. Two examples of these use benzoxypropionic tetraacetate (BOPTA) and ethoxybenzyl diethylenetriamine-pentaacetate (EOB-DTPA) as the ligand. The presence of a hydrophobic ligand enables hepatocyte uptake of these agents and elimination by the biliary system, rather than strictly through renal excretion. Approximately 10% of Gd-BOPTA (Multihance; Bracco Diagnostic, Princeton, NJ) is eliminated by the hepatobiliary system and 90% by renal excretion, whereas 50% of Gd-EOB-DTPA (Eovist; Schering AG, Berlin, Germany) is eliminated by the hepatobiliary system and 50% by renal excretion. The dual pathways of elimination for these agents enable postcontrast imaging emphasizing both tissue perfusion (immediately following administration), and hepatocellular uptake and bile duct elimination (subsequent times). These agents are currently not licensed for clinical use in the United States; however, the combined effect of their ease of use, safety, and dual-phase behavior suggest that they have great potential as liver contrast agents.

Another metal ion that has been formulated into a T1 contrast agent for liver imaging is manganese. Manganese ion chelated to *N,N'*-dipyridoxal ethylenediamine-*N,N'*-diacetate 5,5' bis (phosphate) (DPDP) (Mangofodipir; Teslascan; Nycomed Amersham, New York, NY) is a T1-weighted contrast agent that is hepatocyte-selective but is also absorbed by other organs and tissues including pancreas and adrenal and renal cortex. Approximately 70% of the agent is eliminated by the hepatobiliary system and 30% by the urinary system. Mangofodipir is administered via a slow intra-

venous injection over 1 to 2 minutes. This agent has a long imaging window with maximal hepatic parenchymal enhancement lasting from 15 minutes to 4 hours. The major clinical indication for the use of Mangofodipir is in the determination of the extent of liver metastases in patients under consideration for surgical resection. Mangofodipir may also be used to characterize whether liver lesions contain hepatocytes and to improve delineation of pancreatic tumors (Figure 15-4). Adverse reactions are relatively uncommon with this agent.

Other  $T_1$  contrast agents have been developed using gadolinium ions chelated to macromolecules or polymers. These agents remain within the bloodstream rather than diffuse into the tissue. Their use as MR angiographic agents and as agents to assess the integrity of capillary basement membrane is currently under investigation.

### 15.1.2 $T_2$ RELAXATION AGENTS

The other class of intravenous contrast agents are  $T_2$  relaxation agents. They are typically macromolecules containing several iron atoms that collectively form a superparamagnetic center. The large magnetic susceptibility of the macromolecule distorts the local magnetic field in the vicinity of the agent, causing the nearby water protons to dephase more rapidly than the surrounding tissue. This condition results in significant signal loss in  $T_2$ -weighted spin-echo or gradient-echo images. The most common  $T_2$  contrast agents are based on superparamagnetic iron oxide (SPIO) particulate molecules, also known as ferumoxides. These agents are selectively absorbed by the reticuloendothelial cells located in the liver, spleen, and bone marrow. Normal tissue in these organ systems take up the agent and generate low signal in  $T_2$ - or  $T_2^*$ -weighted images. Lesions that do not contain reticuloendothelial cells in appreciable numbers do not take up the agent and remain unaffected and therefore contribute relatively high signal (Figure 15-5).

Currently, the only  $T_2$  contrast agent licensed for clinical use in the United States is Feridex (magnetite-dextran; Schering AG, Berlin, Germany). It is usually administered as a slow drip infusion over 30 minutes. A further delay of 30 minutes prior to imaging allows for maximal uptake of



(a)



(b)

**FIGURE 15-4** T1-weighted spoiled gradient echo images of liver following administration of Mn-DPDP contrast agent. Increased biliary excretion of  $Mn^{+2}$  ion is demonstrated by the increased signal level (arrows). (a) Fat suppression pulse is applied. (b) No fat suppression is used.



FIGURE 15-5  $T_2$ -weighted single-shot echo-train spin-echo image of liver following administration of superparamagnetic iron oxide contrast agent. The  $T_2$  relaxation times of the normal tissue are reduced by the iron oxide, whereas the metastatic lesion (arrow) shows less agent uptake.

the agent by reticuloendothelial cells. Contrast enhancement can be observed from 30 minutes to 4 hours following infusion. Feridex has a good safety profile, but has a potential side effect of acute back pain developing during infusion, occurring in less than 3% of patients. This side effect is usually self-limiting and disappears when the infusion is stopped or slowed. The most important clinical indication for Feridex is in the determination of the extent of liver metastases in patients under consideration for surgical resection. This agent can also distinguish between tumors of hepatic origin that contain reticuloendothelial cells and tumors that do not. Resovist (magnetite/maghemite-carboxydextran; Schering AG, Berlin, Germany) is another formulation of a ferumoxide agent that can be administered in a small dose by bolus injection. The advantage of this agent is ease of administration and the lack of back pain as a side effect. It is an ultrasmall particulate iron oxide (USPIO) that also increases  $T_1$  contrast in dynamic-gradient echo scanning immediately following administration, enabling one agent to af-

fect both  $T_1$ - and  $T_2$ -weighted scans. Resovist is currently under consideration for approval by the U.S. FDA.

SPIO agents formulated to a smaller particle size than used for liver imaging are under investigation as contrast agents for the examination of lymph nodes. Normal or hyperplastic lymph nodes take up the agent and lose signal in  $T_2$ -weighted images, whereas malignant lymph nodes do not take up the agent and therefore have relatively high signal levels. Iron oxide particles have also been used to label monoclonal antibodies targeted to specific tissues receptor sites. Asialoglycan protein receptor contrast agents are one example that is under development.

## 15.2 ORAL AGENTS

Oral MRI contrast agents are typically nonspecific in nature. They are most often used in abdominal and pelvic studies to provide reliable differentiation of bowel from adjacent structures and to provide better delineation of bowel wall processes. Oral agents may be categorized as positive or negative agents. Positive agents increase the overall signal intensity within the image, generally by shortening the  $T_1$  or  $T_2$  relaxation times of tissue water. These agents are generally solutions of paramagnetic metal ions or metal-chelate complexes. Many of these agents are present in naturally occurring products (manganese in green tea and blueberry juice) or in over-the-counter medications (ferric ammonium citrate; Geritol; Beecham, Bristol, TN). Other agents have been specifically formulated for use with MRI such as Lumenhance (manganese chloride; Bracco Diagnostic, Princeton, NJ) and Magnevist Enteral (gadolinium-DTPA; Schering AG, Berlin, Germany) as  $T_1$  relaxation agents and OMR (ferric ammonium citrate; Oncomembrane, Seattle, WA) as a  $T_2$  relaxation agent. Positive agents can provide excellent delineation of the bowel, but the increased signal level may induce greater artifacts as a result of respiratory motion or peristalsis.

The other type of oral contrast agent is a negative agent. Negative agents eliminate tissue signals from the area of interest. Two approaches are used for negative agents. One method reduces the  $T_2$  relaxation times using suspensions of ferumoxide particles. The particles may be suspended in aqueous solution (Ferumoxsil; Advanced Magnetix, Cambridge, MA) or

adsorbed onto a polymer. The other approach uses an agent that contains no protons, and therefore produces no visible MR signals. The most common agent of this type is Perflubron (perfluorooctylbromide, PFOB; Alliance Pharmaceutical, San Diego, CA). Barium sulfate, clay, and air have also been used for intraluminal studies. One significant problem with many negative contrast agents, particularly the iron-based agents, is that they increase the local magnetic susceptibility, which may induce significant dephasing artifacts at high field strengths.

## CLINICAL APPLICATIONS

---

In selecting pulse sequences and measurement parameters for a specific application, MRI allows the user tremendous flexibility to produce variations in contrast between normal and diseased tissue. This flexibility is available when imaging both stationary tissue as well as flowing blood. For example, the use of both bright-blood and dark-blood MRA techniques described in Chapter 11 permits more accurate assessment of vascular patency and intravascular mass lesions. A typical patient examination acquires sets of images with multiple types of contrast (proton density,  $T_1$ ,  $T_2$ ) and multiple slice orientations (transverse, sagittal, coronal, oblique), providing the clinician with more complete information on the nature of the tissue under observation and increasing the likelihood of lesion detection. It is important that the MR examinations be tailored to the organ or organs under investigation, the type of disease process, and the individual patient. The MR physician may choose to provide detailed measurement parameters for each examination, or have a predetermined regimen of scans that are to be performed by a technologist. Establishing fixed measurement protocols ensure the efficient operation of the MR scanner and that reliable, reproducible imaging examinations are performed.

## 16.1 GENERAL PRINCIPLES OF CLINICAL MR IMAGING

The fundamental principles of diagnostic MRI of the body are:

1. Accurate and reproducible image quality
2. Good visualization of disease processes
3. Comprehensive imaging information for the area under observation

Because ideal achievement of all three goals may not be practical, the proper choice of pulse sequences and/or measurement parameters can provide adequate results within a clinically acceptable scan time. In particular, the ability to visualize disease relative to normal tissue can be dramatically affected by the measurement protocol. One common approach to enhance the contrast between abnormal and background tissue is to make the signal of one of the tissues significantly different from the other one. For example, variation of the signal from fat through the use of fat-unsuppressed and fat-suppressed techniques aids in the detection of lymph nodes. On *T1*-weighted images, lymph nodes have low signal levels and therefore are conspicuous on a background of high-signal fat, whereas on *T2*-weighted images, lymph nodes are relatively bright and their conspicuity is improved by decreasing the signal of background fat using fat-suppression techniques. Following administration of a gadolinium-chelated contrast agent, lymph nodes have significantly shorter *T1* values and produce high signal levels on *T1*-weighted images. The use of fat suppression is helpful to reduce the competing high signal levels of fat. The combined use of gadolinium-chelated contrast agents and fat suppression to increase the signal level of diseased tissue and to decrease signals from background fat, respectively, is widely used in various organ systems including the orbits, bony skeleton, soft tissue of the extremities, and the breast.

An additional consideration is in the choice of pulse sequence, in that there may be differences in signal levels from flowing tissue or dramatic differences in image quality. For example, fat-suppressed spoiled gradient echo may be preferable to fat-suppressed spin echo when concomitant evaluation of patency of vessels is desired, as in imaging vascular grafts for pa-



tency or infection, or for imaging extremities to assess soft tissue infection or vascular thrombosis. This is because spoiled gradient echo images acquired within 2 minutes following administration of gadolinium-chelated contrast media display patent vessels with high signal intensity and occluded vessels with low signal intensity, whereas spin-echo images may have a signal void from both patent and thrombosed vessels. Flowing tissue is commonly seen as a signal void on spin-echo images due to the dephasing of moving spins during the gradient pulses, whereas blood clots produce low signal levels due to the presence of fibrinous clots and increased  $T2^*$  effects from blood breakdown products.

It is important when defining protocols for MRI studies to obtain a sufficient variety of sequences to provide comprehensive information, while at the same time not to be too redundant and generate excessively long exams. For example, our approach for imaging of the abdomen has been to employ a variety of short duration  $T1$ - and  $T2$ -weighted sequences with the majority of them performed in the transverse plane, but also obtain at least one set of images in a plane orthogonal to the transverse plane. The particular choice of planes for a measurement is dictated by the area of anatomy under observation.

## 16.2 EXAMINATION DESIGN CONSIDERATIONS

The initial studies of MRI used primarily transverse  $T1$ - and  $T2$ -weighted spin echo techniques. As the modality has matured, it has become clear that imaging strategies must be modified beyond this elementary approach. There are several reasons for this:

*Imaging of organs in the plane of the best anatomical display.* Imaging of the spine or the female pelvis requires the use of both sagittal and transverse images to best demonstrate the anatomical structures. Similarly, the evaluation of large masses in the region of the upper poles of the kidneys is facilitated by sagittal as well as transverse images. On the other hand, coronal images are useful for visualization of the left lobe of the liver.

*Compensation for the most severe artifacts generated by various organ systems.*

Abdominal imaging is severely compromised by artifacts from respiratory motion. Imaging protocols that employ breath-hold spoiled gradient echo sequences (e.g., FLASH, spoiled GRASS) as described in Chapter 10 can produce images with substantial  $T_1$ -weighting while minimizing respiratory artifacts. Cardiac gating is essential when imaging the thorax in order to minimize phase artifacts from cardiac motion.

*Increased spatial resolution and/or signal-to-noise ratio.* Imaging of small anatomical regions such as extremities (e.g., ankles, wrists, knees) or the breast require specialized surface coils to maximize both the signal-to-noise ratio and spatial resolution.

*The use of contrast agents.* Imaging of nonorgan-deforming focal lesions in the liver, spleen, and pancreas using intravenous gadolinium-chelated complexes requires rapid, breath-hold imaging techniques to capture the capillary phase of lesion enhancement. This approach necessitates the use of spoiled gradient echo techniques (e.g., FLASH or spoiled GRASS) with temporal resolution of less than 20 seconds. In many instances, the visualization of contrast enhancement in  $T_1$ -weighted images may be improved through the use of fat suppression to remove the competing high signal from fat.

## **16.3 PROTOCOL CONSIDERATIONS FOR ANATOMICAL REGIONS**

The following considerations and recommendations are offered for imaging various organs systems. They are intended to indicate general guidelines for use in developing imaging examinations. Exact sequence protocols are not provided because different manufacturers offer different imaging capabilities and functions.

### **16.3.1 BRAIN**

A number of innovations have been developed for brain examinations. These include diffusion-weighted imaging (visualizing acute stroke),

ETSE, fat suppression, MRA (vascular disease), FLAIR (white matter inflammation), contrast agent enhancement using gadolinium-chelated complexes (neoplasm), and magnetization-transfer suppression (in conjunction with contrast administration for background water suppression). Despite advancements, the standard for MR examinations of the brain remains sagittal *T1*-weighted spin echo and transverse *T1*- and *T2*-weighted conventional spin echo. Thin-slice (3 mm) coronal images provide excellent visualization of the pituitary gland and sella tursica. Replacement of *T2*-weighted conventional spin echo with ETSE is often done with little loss in diagnostic content. Routine use of a *T1* contrast agent in the investigation of neoplastic disease is recommended. Many centers use MRA techniques regularly in the investigation of cerebrovascular disease (Figures 16-1, 16-2, 16-3).

### 16.3.2 NECK

The use of a surface coil for neck imaging is essential due to the small volume of tissue. High-resolution *T1*- and *T2*-weighted spin-echo sequences are useful for visualizing soft tissue. The use of gadolinium-chelated con-

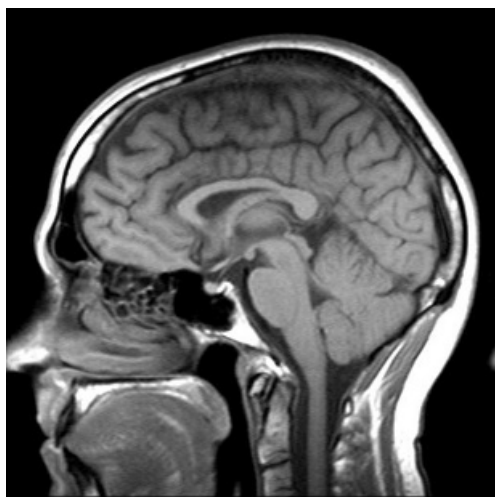


FIGURE 16-1 Sagittal spin-echo *T1*-weighted head image. *TR*, 500 ms; *TE*, 7.7 ms.

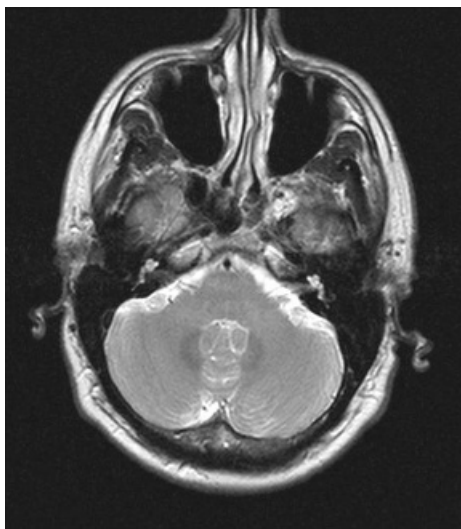


FIGURE 16-2 Transverse echo-train spin echo  $T_2$ -weighted head image.  $TR$ , 4000 ms; effective  $TE$ , 100 ms; echo-train length 5.

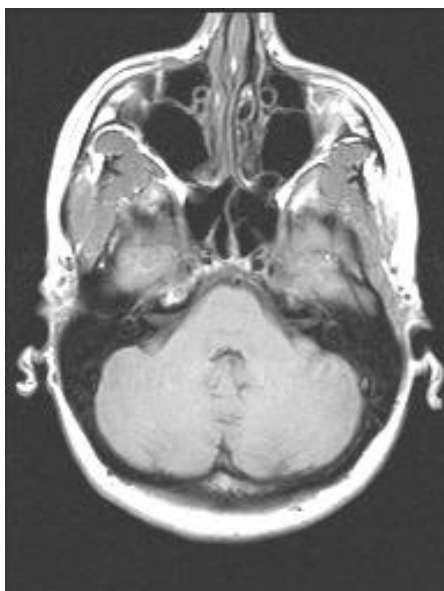


FIGURE 16-3 Transverse spin echo  $T_1$ -weighted head image,  $TR$ , 532 ms;  $TE$ , 12 ms.

trast agents may be helpful for tumor and lymph node detection, and for thyroid and parathyroid studies. The addition of fat suppression to post-contrast studies is helpful to delineate tissue. Uniform fat suppression may be difficult to achieve due to magnetic field distortions from the large magnetic susceptibility differences between the neck and the upper thorax.

### 16.3.3 SPINE

A combination of *T1*- and *T2*-weighted images is important. Both sagittal and transverse images are valuable for examining the spinal cord and structural deformations such as disk herniations (Figures 16-4, 16-5, 16-6). Transverse images allow excellent visualization of nerve roots and possible disk fragments. Use of spatial presaturation pulses is recommended to reduce artifacts from jaw motion in cervical studies or abdominal motion in lumbar studies. Administration of gadolinium-chelated contrast media and fat sup-



**FIGURE 16-4** Sagittal echo-train spin echo *T1*-weighted lumbar spine image. *TR*, 646 ms; effective *TE*, 15 ms; echo-train length, 3. Anterior spatial presaturation pulse is used to suppress peristalsis and respiration artifacts.



FIGURE 16-5 Sagittal echo-train spin echo T2-weighted lumbar spine image. *TR*, 4600 ms; effective *TE*, 137 ms; echo-train length, 23. Anterior spatial presaturation pulse is used to suppress peristalsis and respiration artifacts.

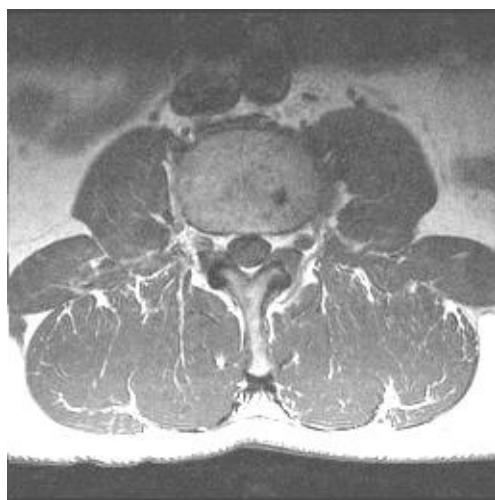


FIGURE 16-6 Transverse spin echo T1-weighted lumbar spine image. *TR*, 736 ms; *TE*, 15 ms.

pression are recommended in circumstances in which bony metastases are suspected.

### 16.3.4 MUSCULOSKELETAL

A combination of  $T1$ - and  $T2$ -weighted images is routinely used in musculoskeletal imaging. Images should be acquired in at least two orthogonal planes to ensure proper anatomical visualization (Figures 16-7, 16-8, 16-9). STIR images are frequently valuable for detection of tumors, inflammation, or avascular necrosis and may replace  $T2$ -weighted images in some settings.  $T2^*$ -weighted images are often used for visualizing fluid and bony detail. Use of gadolinium-chelated contrast agents is important for the evaluation of inflammatory and neoplastic disease, often in combination with fat suppression. When imaging small anatomical regions away from the magnet isocenter, field homogeneity may limit the usefulness of fat suppression.



FIGURE 16-7 Sagittal echo-train spin echo proton density-weighted knee image.  $TR$ , 3500 ms; effective  $TE$ , 17 ms; echo-train length, 5.



FIGURE 16-8 Coronal echo-train spin echo  $T_2$ -weighted knee image.  $TR$ , 3500 ms; effective  $TE$ , 102 ms; echo-train length, 5.



FIGURE 16-9 Sagittal echo-train inversion recovery knee image.  $TR$ , 6000 ms; effective  $TE$ , 30 ms.;  $TI$ , 140 ms.



### **16.3.5 THORAX**

Cardiac triggering is essential to minimize motion artifacts from the heart. Transverse *T1*-weighted spin-echo images provide good anatomical evaluation of the mediastinum and chest wall. *T2*-weighted transverse images are helpful, particularly in the evaluation of the chest wall or mediastinal involvement with cancer. *T1*-weighted images acquired following administration of gadolinium-chelated contrast media provide similar and complementary information. Fat suppression is a useful adjunct when gadolinium-chelated contrast agents are employed. The lowered signal from fat improves the visualization of abnormal tissue enhancement, which is helpful for delineating the presence of chest wall invasion by malignant or infectious processes. Lesions in the lung apex and occasionally in the lung base require additional coronal or sagittal views. Breath-hold imaging following administration of gadolinium-chelated contrast media improves visualization of small peripheral lung lesions; metastases can be reliably seen at a diameter of 5 mm using this approach. A 3D gradient echo sequence is preferred for imaging lung parenchyma because the technique minimizes phase artifacts from cardiac motion. For most examinations, imaging between 2 and 5 minutes following contrast administration provides a good balance between contrast enhancement of lung masses and diminished enhancement of the blood pool.

### **16.3.6 BREAST**

Optimal breast MR examination requires a dedicated breast coil to maximize spatial resolution. *T1*-weighted images acquired following administration of gadolinium-chelated contrast media are important for detection of lesions. Thin-section 3D-volume acquisition, rapid imaging, image subtraction, and application of techniques to reduce fat signals (fat saturation, water excitation, or STIR) should be considered when designing scanning protocols. Serial dynamic imaging following gadolinium-chelated contrast media administration provides useful information on lesion characterization (see Figure 12-5). Many carcinomas exhibit intense enhancement rapidly, whereas most benign disease processes enhance in a delayed, less in-

tense fashion. Further information regarding lesion morphology may be provided using high-resolution T2-weighted ETSE sequences.

### **16.3.7 HEART AND GREAT VESSELS**

Transverse cardiac-triggered T1-weighted spin echo or segmented gradient echo sequences are essential in the evaluation of cardiac anatomy. When possible, breath-hold scanning or use of navigator echoes is preferred to minimize artifacts from respiratory motion. High spatial resolution is frequently needed, particularly in assessing congenital heart disease; therefore, a slice thickness of less than 5 mm is recommended. Coronal and sagittal cardiac-triggered T1-weighted images may provide additional information in many instances. They are essential in the evaluation of congenital heart disease because they provide anatomical information regarding vessels, airways, and cardiac chambers. The left anterior oblique sagittal plane is an important view for the evaluation of the thoracic aorta.

Signals from flowing blood within the cardiac chambers is often heterogeneous as a result of changes in flow direction and velocity. For T1-weighted sequences, it is helpful to minimize the blood signals, both to reduce flow artifacts and to delineate vessels using dark-blood techniques. Application of superior and inferior presaturation pulses or gradient dephasing may be required. Flow compensation should be avoided because it results in an increase in signals from flowing blood. Alternately, techniques that result in high signal levels from flowing blood (bright-blood techniques) are often helpful for the evaluation of chamber dynamics. Multiphasic techniques (cine MR) are particularly useful in the evaluation of wall motion and thickening, valvular disease, and shunts. Useful image orientations include sagittal plane for evaluating the pulmonary valve, coronal and left ventricular long axis for the aortic valve, and transverse plane for the tricuspid and mitral valves, and for assessing atrial and ventricular septal defects (Figure 16-10). Single-shot echo-train spin echo techniques can minimize cardiac motion artifacts and are useful as bright- or dark-blood techniques (Figure 16-11). For the evaluation of the aorta and

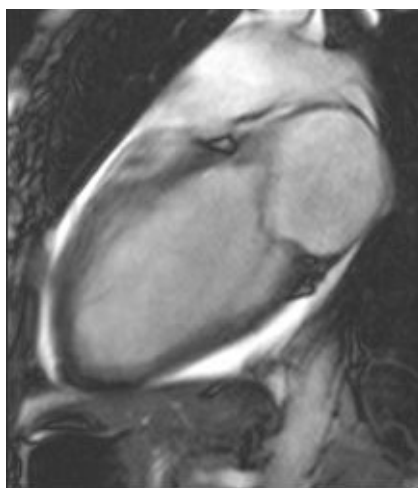


**FIGURE 16-10** Oblique sagittal gradient echo heart bright-blood image. *TR*, 35 ms, *TE*; 1.4 ms.

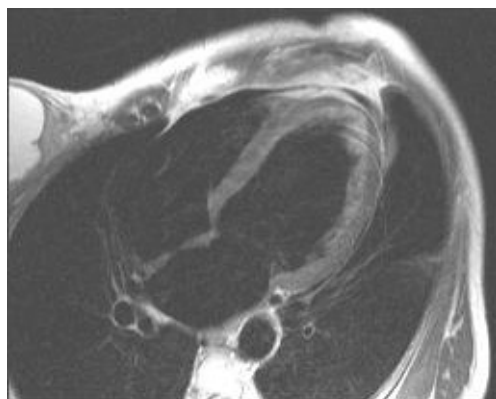


**FIGURE 16-11** Oblique transverse echo-train spin echo dark-blood image. *TR*, 1587 ms; effective *TE*, 67 ms.

major branches, a widely used technique is MR angiography employing a dynamic 3D gradient echo sequence following gadolinium-chelated contrast media administration.

### 16.3.8 LIVER

Both  $T1$ - and  $T2$ -weighted transverse images are important for evaluating the liver. Combining breath-hold and non-breath-hold sequences is often useful since some patients can suspend respiration but cannot breathe regularly, whereas other patients breathe regularly but cannot hold their breath well. Most current protocols combine breath-hold  $T1$ - and  $T2$ -weighted sequences with breathing-independent  $T2$ -weighted sequences. A spoiled gradient echo sequence is most often used for  $T1$ -weighted imaging; however,  $T1$ -weighted spin echo with respiratory compensation may be considered for some patients. For  $T2$ -weighted images, breathing-averaged ETSE with fat suppression is a useful technique. Compared to standard  $T2$ -weighted spin echo techniques, the imaging time is significantly reduced. The addition of fat suppression diminishes respiratory ghosts, removes chemical shift artifacts, and diminishes the signal level of a fatty infiltrated liver, which permits good visualization of the liver capsular surface and facilitates lesion detection. In many cases,  $T2$ -weighted single-shot ETSE techniques acquired with and without fat suppression may be sufficient (Figures 16-12, 16-13, 16-14).

The use of intravenous contrast agents significantly improves lesion detection over nonenhanced imaging techniques. Currently available contrast agents include gadolinium-chelated complexes and Mn-DPDP for  $T1$  enhancement, and ferumoxides for  $T2$  enhancement. When using gadolinium-chelated contrast agents, it is important to image early after contrast (~30 seconds) to maximize the specific enhancement features of various focal hepatic lesions (Figure 16-15). Spoiled gradient echo techniques are extremely useful to accomplish this goal. In addition, serial sequence repetition with additional acquisitions at approximately 1 and 5 minutes may be routinely useful to visualize the temporal behavior of contrast uptake. Although traditional spoiled gradient echo imaging uses 2D techniques, 3D gradient echo techniques together with fat suppression are continuously improving

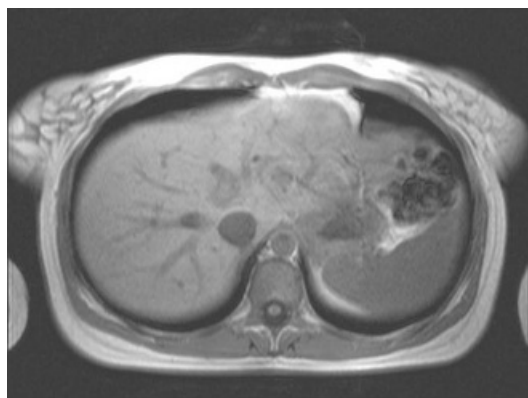


FIGURE 16-12 Transverse T1-weighted spoiled gradient echo liver image. *TR*, 142 ms; *TE*, 4 ms; excitation angle, 70°.

in image quality and are the method of choice in many facilities for dynamic contrast examinations (Figure 16-16).

Mn-DPDP has a longer imaging window (30 minutes–4 hours), so it lacks dynamic contrast enhancement ability. Because of this, it is not essential that the patient be able to suspend respiration because dynamic imaging is not performed. High-resolution (512 matrix) spoiled gradient echo is a



FIGURE 16-13 Transverse echo-train inversion recovery liver image. *TR*, 5000 ms, effective *TE*, 81 ms; *TI*, 170 ms; echo-train length, 31.

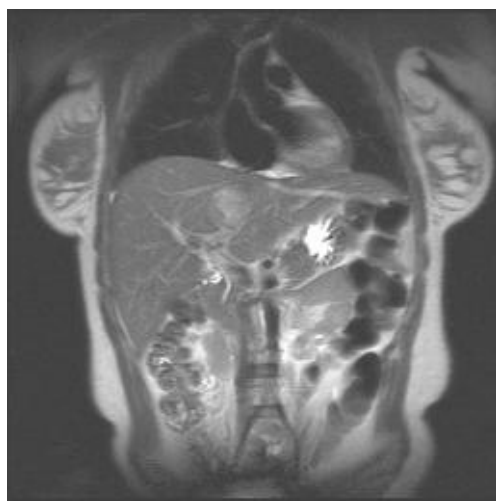
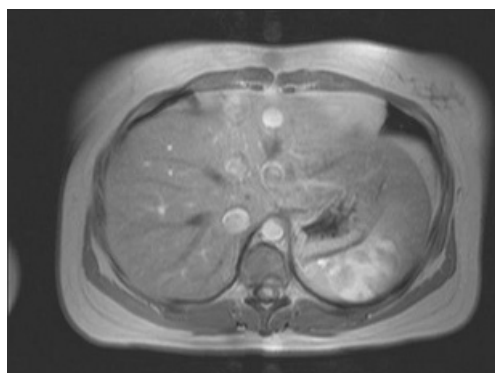


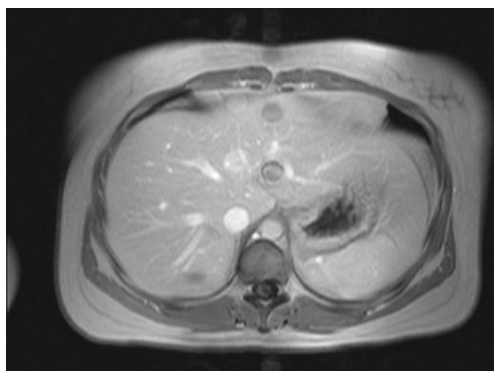
FIGURE 16-14 Coronal single shot echo-train  $T_2$ -weighted image of liver and kidneys. Effective  $TE$ , 90 ms.

useful sequence in combination with Mn-DPDP in that it permits detection of smaller focal lesions in conjunction with the  $T_1$ -shortening effect of the agent. Fat suppression is another useful modification to employ with Mn-DPDP, the fat suppression serves to maximize the conspicuity of contrast enhancement (Figure 16-17). This may be particularly beneficial for imaging the pancreas.

Like Mn-DPDP, Feridex also has a long imaging window of 30 minutes–4 hours and does not require the patient be able to suspend respiration. When using a ferumoxide agent, an important consideration for the choice of sequence is the dosage of iron administered. In Europe, a dosage of iron is used that is one and one-half times that of the dose used in North America. This higher dosage permits a greater choice of sequences that may be effective, including gradient echo sequences that are fundamentally  $T_1$ -weighted. Because of this, care must be exercised in extrapolating information from European studies to American studies, particularly in regard to sequence use. Sequences that are useful in conjunction with ferumoxide agents include fat-suppressed ETSE, single-shot ETSE, echo-train STIR, and gradient echo sequences with a relatively long  $TE$  and relatively low flip angle (e.g.,  $TR = 150$  ms,  $TE = 9$  ms, flip angle =  $45^\circ$ ). Examining for fatty infil-



(a)



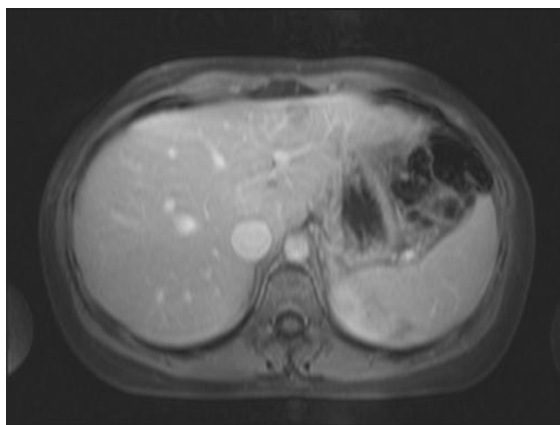
(b)

**FIGURE 16-15** Transverse  $T_1$ -weighted spoiled gradient echo liver images acquired following gadolinium–chelate contrast agent injection.  $TR$ , 170 ms;  $TE$ , 4 ms; excitation angle,  $70^\circ$ . (a) Immediately following administration; (b) 45 s following administration.

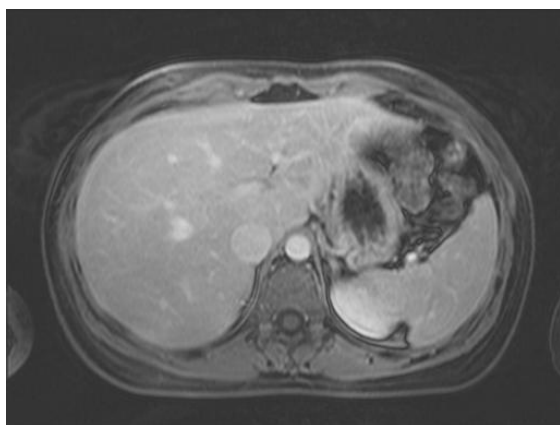
tration requires out-of-phase gradient echo images prior to contrast administration.

### 16.3.9 ABDOMINAL ORGANS

$T_1$ -weighted, breath-hold spoiled gradient echo and  $T_1$ -weighted, fat-suppressed spin echo are both useful for controlling respiratory artifacts in the



(a)



(b)

**FIGURE 16-16** Transverse *T1*-weighted spoiled gradient echo liver images with fat suppression. (a) 2D gradient echo, *TR*, 242 ms; *TE*, 4.8 ms; excitation angle, 70°; (b) 3D gradient echo; *TR*, 4.8 ms; *TE*, 2.3 ms; excitation angle, 10°.

abdomen. As with the liver, combining breath-hold with breathing-independent sequences is advantageous. Single-shot ETSE *T2*-weighted sequences are particularly effective at demonstrating the bowel and for distinguishing the bowel from other entities. Transverse fat-suppressed and conventional spoiled gradient echo images are useful in combination both





**FIGURE 16-17** Coronal magnetization prepared T1-weighted liver image. Effective  $TE$ , 30 ms. Image is acquired following administration of Mn-DPDP.

prior to and following administration of intravenous gadolinium-chelated contrast agents. Following contrast administration, the unsuppressed technique is useful to visualize capillary phase enhancement, whereas the subsequent acquisition of the fat-suppressed technique provides interstitial phase information. For the kidneys and pancreas, dynamic acquisition of fat-suppressed 3D gradient echo images enables excellent organ visualization. Imaging of the adrenal glands require noncontrast out-of-phase gradient echo images.

### **16.3.10 PELVIS**

Transverse images are routinely used for pelvic examination, whereas sagittal images provide a useful adjunct. T1-weighted images are frequently best performed as conventional spin echo or spoiled gradient echo, whereas T2-weighted images may be acquired as breathing-averaged ETSE or single-shot ETSE. Thin slices (5 mm thickness) in the sagittal plane are necessary to

optimally visualize the uterus and ovaries in the female and the seminal vesicles in the male (Figures 16-18, 16-19, 16-20). Detailed imaging of the pelvis also requires high in-plane spatial resolution ( $512 \times 512$  matrices, ETSE, small FOV). Gadolinium-chelated contrast administration is important in the evaluation of uterine and adnexal masses. Fat suppression is an important adjunct to contrast administration when ovarian cancer is clinically suspected.



FIGURE 16-18 Coronal spin echo T1-weighted pelvis image. TR, 437 ms; TE, 14 ms.

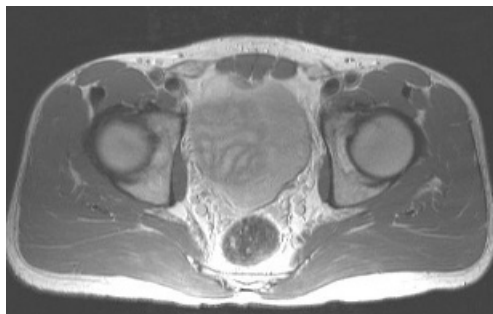


FIGURE 16-19 Transverse echo-train spin echo proton density-weighted pelvis image. TR, 4530 ms; effective TE, 27 ms; echo-train length 7.

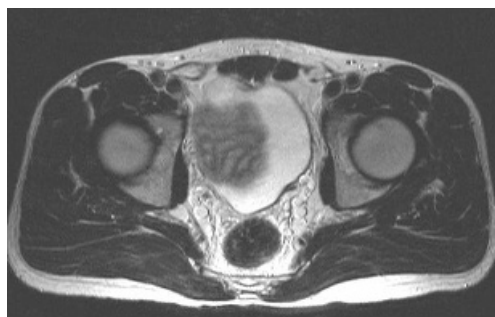


FIGURE 16-20 Transverse echo-train spin echo  $T_2$ -weighted pelvis image.  $TR$ , 4530 ms; effective  $TE$ , 137 ms; echo-train length 7.

## 16.4 RECOMMENDATIONS FOR SPECIFIC SEQUENCES AND CLINICAL SITUATIONS

### 16.4.1 $T_1$ -WEIGHTED TECHNIQUES

**Single-Echo Spin Echo.** For routine  $T_1$ -weighted imaging, a moderate  $TR$  is recommended (400–700 ms at 1.0 and 1.5 T) with a short  $TE$  (20 ms or less). This combination allows acquisition of a sufficient number of slices yet provides acceptable contrast between most tissues. The slice thickness and in-plane spatial resolution can be tailored to the particular anatomical region under examination.

**Spoiled Gradient Echo.** Imaging parameters include a relatively long  $TR$  (~140 ms), the shortest in-phase echo time (4.5 ms at 1.5 T, 6.67 ms at 1.0 T), one-signal average, and an excitation angle of 70–90°. These parameters maximize the number of slices, S/N ratio, and  $T_1$ -weighting, yet minimize artifacts and the measurement time. Spoiled gradient echo sequences are ideal for  $T_1$ -weighted imaging of the abdomen, for imaging in multiple planes, and for imaging following administration of intravenous gadolinium-chelated contrast media. When thin sections and high spatial resolution are desired and respiratory artifacts are not a problem,  $T_1$ -weighted spin echo may be preferred.

**Out-of-Phase Gradient Echo.** Imaging parameters should include the shortest possible  $TE$ , preferably shorter than the in-phase  $TE$  (2.25 ms at 1.5

T, 3.3 ms at 1.0 T), though this may be impractical at 3.0 T. This technique allows easy detection of fat and water in similar proportions within a tissue volume through signal cancellation. For clinical use, the most important applications for this technique are the examination for fatty infiltration of the liver and for benign adenoma. In both cases, the observation of signal drop observed in out-of-phase images compared to in-phase images permits the diagnosis of fatty infiltration. For adrenal glands, this technique is virtually pathognomonic for benign disease in which the signal loss is uniform.

**Fat Saturation.** This technique is ideal when an expanded range of soft tissue signal intensities and decreased phase artifacts from moving tissues containing fat is desired. Improved demonstration of tissue with a high protein content (e.g., normal pancreas) or detection of subacute blood are important uses for *T1*-weighted fat saturation techniques. When used following administration of gadolinium-chelated contrast media, the removal of the high signal intensity of fat results in easier discrimination of diseased tissue (e.g., diseased bowel or peritoneum, breast cancer, musculoskeletal neoplasms or inflammation). Fat-suppressed spin echo or spoiled gradient echo imaging is also useful in assessing the fat composition in certain masses such as adrenal myelolipoma, colonic lipoma, or ovarian dermoid cyst. Unlike out-of-phase gradient echo techniques, in which the maximal signal loss occurs in tissues in which the fat and water are of equal proportions, fat suppression is most effective when the fat content in the tissue approaches 100%.

**STIR.** Musculoskeletal imaging benefits from the use of STIR imaging because of the relatively high signal level from diseased tissue. Images resemble those obtained using fat-suppressed, *T2*-weighted spin echo techniques. STIR is not as sensitive to magnetic field homogeneity as fat saturation and therefore is well suited for imaging small anatomical regions, regions away from the magnet isocenter, or regions where there are large differences in magnetic susceptibility, such as the cervical spine. STIR sequences acquired using *TI* times for fat and for silicon suppression are useful for the investigation of breast implant rupture. Because long *TR* times are necessary, most implementations of STIR incorporate an echo train in order to dramatically

shorten acquisition time. Performed as a breath-hold scan, this technique has achieved clinical utility in liver imaging.

### 16.4.2 T2-WEIGHTED TECHNIQUES

**Standard Multiecho Spin Echo.** Standard multiecho spin echo techniques are used when subtle differences in  $T_2$  between normal and diseased tissue are expected. A long  $TR$  (greater than 2000 ms at 1.0 and 1.5 T) is used to minimize  $T_1$  saturation of most tissues, though CSF and other fluids are significantly suppressed in signal due to saturation. A short  $TE$  (less than 20 ms) is used to produce proton-density weighted images, whereas a long  $TE$  (80 ms or greater) generates  $T_2$ -weighted images. Flow compensation is normally used on the long  $TE$  image in brain and spine imaging to minimize flow artifacts from bright CSF.

**Echo-Train Spin Echo.** ETSE techniques are useful when high spatial resolution or decreased imaging time is desired for  $T_2$ -weighted images (e.g., brain, spine, or pelvic imaging). These sequences are best used when  $T_2$  differences between normal and diseased tissues are significant since they result in an averaging of  $T_2$  information. Use of very long  $TR$  (greater than 3500 ms) allows coverage of anatomical regions and reduces the amount of signal loss from CSF saturation. Caution should be employed when using ETSE techniques for imaging the liver, particularly in the investigation for hepatocellular carcinoma, because the  $T_2$  difference between tumor and background liver may be slight. This is normally not a problem if this technique is used in conjunction with spoiled gradient echo immediately following administration of gadolinium-chelated contrast media, as the latter technique is the preferred method.

**Fat Saturation.** Fat-suppressed  $T_2$ -weighted spin echo is useful for liver or musculoskeletal imaging. It results in a decreased phase artifact from respiratory motion of the abdominal wall, and provides expanded dynamic range of tissue signal intensities and increased conspicuity of focal lesions. It is an excellent technique for imaging capsular-based disease (e.g., hepatosplenic candidiasis or metastases spread through peritoneal seeding)

since chemical-shift artifacts are absent. Fat saturation can also be applied to echo-train and single shot echo-train sequences. It is essential to use fat saturation when performing  $T_2$ -weighted ETSE sequences of the liver to attenuate the signals from fat in the setting of fatty liver, because the high signal level of fatty liver on nonsuppressed ETSE sequences can mask the presence of liver lesions. The use of fat suppression on  $T_2$ -weighted sequences also facilitates the detection of lymph nodes, which appear relatively bright against a background of low fat signals.

### 16.4.3 SEDATED OR AGITATED PATIENTS

Optimal MR imaging results require cooperation from patients to minimize motion artifacts. For brain, spine, or musculoskeletal imaging, pads or restraints may be used to restrict patient movement. For abdominal imaging, patients who are unable to hold their breath because of sedation or decreased consciousness cannot be imaged with breath-hold imaging. Spin echo sequences may produce images of good quality in sedated patients, but poor image quality may result in agitated patients. Use of reordered phase encoding or navigator echoes may prove advantageous. For dynamic scanning following administration of gadolinium-chelated contrast media, images can be obtained using slice-selective  $180^\circ$  inversion pulse-prepared snapshot gradient echo sequences (e.g., slice-selective TurboFLASH, IR-prepared GRASS) followed by either regular or fat-suppressed  $T_1$ -weighted spin echo techniques.

Patients who are unable to hold their breath or who are slightly agitated require imaging using rapid techniques that are motion insensitive. These include snapshot inversion pulse-prepared gradient echo sequences for  $T_1$ -weighted images and snapshot ETSE for  $T_2$ -weighted images. These techniques are less sensitive to respiratory motion and acceptable image quality may be obtained. Imaging studies of sedated patients can produce results of good quality when combining breathing-averaged spin echo or navigator echo-based techniques with single-shot approaches.

## REFERENCES AND SUGGESTED READINGS

---

- Achten, Eric, Paul Boon, Tom Van De Kerckhove, Jacques Caemaert, Jacques De Reuek, and Marc Kunnen. 1997. Value of Single-Voxel Proton MR Spectroscopy in Temporal Lobe Epilepsy. *AJNR: American Journal of Neuroradiology* **18**, 1131–1139.
- Chien, Daisy, and Robert R. Edelman. 1991. Ultrafast Imaging Using Gradient Echoes. *Magnetic Resonance Quarterly* **7**, 31–56.
- Debatin, Jörg F., and Graeme C. McKinnon, eds. 1998. *Ultrafast MRI: Techniques and Applications*. Springer-Verlag, Heidelberg.
- DeYoe, Edgar A., Peter Bandettini, Jay Neitz, David Miller, and Paula Winans. 1994. Functional Magnetic Resonance Imaging (fMRI) of the Human Brain. *Journal of Neuroscience Methods* **54**, 171–187.
- Edelman, Robert R., Piotr Wielopolski, and Franz Schmitt. 1994. Echo-Planar MR Imaging. *Radiology* **192**, 600–612.
- Edelman, Robert R., and Qun Chen. 1998. EPSTAR MRI: Multislice Mapping of Cerebral Blood Flow. *Magnetic Resonance in Medicine* **40**, 800–805.
- Ehman, Richard L., ed. 1995. *Glossary of MR Terms*, 4th ed. American College of Radiology, Reston, Virginia.
- Finelli, Daniel A., and Benjamin Kaufman. 1993. Varied Microcirculation of Pituitary Adenomas at Rapid, Dynamic Contrast-Enhanced MR Imaging. *Radiology* **189**, 205–210.
- Govindaraju, Varanavasi, Karl Young, and Andrew A. Maudsley. 2000. Proton NMR Chemical Shifts and Coupling Constants for Brain Metabolites. *NMR in Biomedicine* **13**, 129–153.
- Guyton, Arthur C., and John D. Hall. 1996. *Textbook of Medical Physiology*, 9th ed. W. B. Saunders, Philadelphia.
- Haacke, E. Mark, Robert W. Brown, Michael R. Thompson, and Ramesh Venkatesan.

1999. *Magnetic Resonance Imaging: Physical Principles and Sequence Design*. Wiley-Liss, New York.
- Henkelman, R. Mark, and Michael J. Bronskill. 1987. Artifacts in Magnetic Resonance Imaging. *Reviews of Magnetic Resonance in Medicine* **2**, 1–126.
- Hetherington, H. P., J. W. Pan, W.-J. Chu, G. F. Mason, and B. R. Newcomer. 1997. Biological and Clinical MRS at Ultra-High Field. *NMR in Biomedicine*, **10**, 360–371.
- Kim, Seong-Gi. Quantification of Relative Cerebral Blood Flow Change by Flow-Sensitive Alternating Inversion Recovery (FAIR) Technique: Application to Functional Mapping. 1995. *Magnetic Resonance in Medicine* **34**, 293–301.
- Kvistad, Kjell A., Jana Rydland, Jari Vainio, et al. 2000. Breast Lesions: Evaluation with Dynamic Contrast-Enhanced T1-Weighted MR Imaging and with T2\*-Weighted First-Pass Perfusion MR Imaging. *Radiology* **216**, 545–553.
- Le Bihan, Denis, ed. 1995. *Diffusion and Perfusion Magnetic Resonance Imaging: Applications to Functional MRI*. Raven Press, New York.
- MacFall, James R., H. Cecil Charles, Robert D. Black, et al. 1996. Human Lung Air Spaces: Potential for MR Imaging with Hyperpolarized He-3. *Radiology* **200**, 553–558.
- Marks, Michael P., Alex de Crespigny, Daniel Lentz, Dieter R. Enzmann, Gregory W. Albers, and Michael E. Moseley. 1996. Acute and Chronic Stroke: Navigated Spin-Echo Diffusion-Weighted MR Imaging. *Radiology* **199**, 403–408.
- Mezrich, Reuben 1995. A Perspective on K-Space. *Radiology* **195**, 297–315; *Radiology* **199**, 874–875.
- Mills, Ian, ed. 1989. *Quantities, Units, and Symbols in Physical Chemistry*. International Union of Pure and Applied Chemistry, Physical Chemistry Division. Blackwell, Oxford, UK.
- Mugler, John P., III, and James R. Brookeman. 1988. The Optimum Data Sampling Period for Maximum Signal-to-Noise Ratio in MR Imaging. *Reviews in Magnetic Resonance Imaging* **3**, 1–51.
- Mugler, John P., III, Bastiaan Driehuys, James R. Brookeman, et al. 1997. MR Imaging and Spectroscopy Using Hyperpolarized  $^{129}\text{Xe}$  Gas: Preliminary Human Results. *Magnetic Resonance in Medicine* **37**, 809–815.
- Mukherji, Suresh K., ed. 1998. *Clinical Applications of MR Spectroscopy*. Wiley-Liss, New York.
- Neil, Jeffrey J. 1997. Measurement of Water Motion (Apparent Diffusion) in Biological Systems. *Concepts in Magnetic Resonance* **9**, 385–401.
- Nitz, W. R. 1999. MR Imaging: Acronyms and Clinical Applications. *European Radiology* **9**, 979–997.
- Nitz, W. R. 2002. Fast and Ultrafast Non-echo-planar MR Imaging Techniques. *European Radiology* **12**, 2855–2882.
- Oosterwijk, Herman. 2000. DICOM Basics. Cap Gemini Ernst & Young.



- Parker, Dennis L., and Grant Guilberg. 1990. Signal-to-Noise Efficiency in Magnetic Resonance Imaging. *Medical Physics* **17**, 250–257.
- Pipe, James G., and Thomas L. Chenevert. 1991. A Progressive Gradient Moment Nulling Design Technique. *Magnetic Resonance in Medicine* **19**, 175–179.
- Prüssmann, Klass P., Markus Weiger, Scheidegger, Markus B., and Peter Bösigger. 1999. SENSE: Sensitivity Encoding for Fast MRI. *Magnetic Resonance in Medicine* **42**, 952–962.
- Salibi, Nouha, and Mark A. Brown. 1998. *Clinical MR Spectroscopy: First Principles*. Wiley-Liss, New York.
- Sandstede, Jörn J. W., Claudia Lipke, Meinrad Beer, et al. 2000. Analysis of First-Pass and Delayed Contrast-Enhancement Patterns of Dysfunctional Myocardium on MR Imaging: Use in the Prediction of Myocardial Viability. *AJR* **174**, 1737–1740.
- Semelka, Richard C. 2001. *Abdominal–Pelvic MRI*. Wiley-Liss, New York.
- Shaw, Derek. 1984. *Fourier Transform N.M.R. Spectroscopy*, 2nd edition. Elsevier, Amsterdam, Netherlands.
- Shellock, Frank G. 2001. *Pocket Guide to MR Procedures and Metallic Objects: Update 2001*. Lippincott Williams & Wilkins, Philadelphia.
- Slichter, Charles P. 1996. *Principles of Magnetic Resonance*, 3rd edition. Springer-Verlag, Heidelberg.
- Sodickson, Daniel K., and Warren J. Manning. 1997. Simultaneous Acquisition of Spatial Harmonics (SMASH): Fast Imaging with Radiofrequency Arrays. *Magnetic Resonance in Medicine* **38**, 591–603.
- Stejskal, E. O., and J. E. Tanner. 1965. Spin Diffusion Measurements: Spin Echoes in the Presence of a Time-Dependent Field Gradient. *Journal of Chemical Physics* **42**, 288–292.
- Tannús, Alberto, and Michael Garwood. 1997. Adiabatic Pulses. *NMR in Biomedicine* **10**, 423–434.
- Wolff, Steven D., and Robert S. Balaban. 1994. Magnetization Transfer Imaging: Practical Aspects and Clinical Applications. *Radiology* **192**, 593–599.
- Wilke, Norbert M., Michael Jerosh-Herold, Andrey Zenovich, and Arthur Stillman. 1999. Magnetic Resonance First-pass Myocardial Perfusion Imaging: Clinical Validation and Future Applications. *Journal of Magnetic Resonance Imaging* **10**, 676–685.
- Young, Ian R. 2000. Notes on Current Safety Issues in MRI. *NMR in Biomedicine* **13**, 109–115.

# INDEX

---

- Abdominal images:
  - artifacts, effect on, 226
  - characteristics of, generally, 72, 104
  - contrast agents, 216, 221, 239–241
  - gating method, 148
  - motion artifacts, 115–117, 141–144, 148
  - patient sedation, 246
  - T1 -weighted, 243
- Abdominal MRA, 156
- Absorption:
  - energy, 8
  - magnetic resonance spectroscopy (MRS), 191
  - radiofrequency(rf), 12–13, 97
  - resonance, 1, 207
  - specific rate (SAR), 135, 177
- Acceleration, 150
- Acquisition matrix, 39, 41, 44, 99, 118, 160
- Acquisition parameters:
  - magnetic resonance angiography (MRA), 156
  - modification, motion artifacts, 142–143
  - phase contrast MRA, 159
  - standard 2D/3D, 102
- Actively shielded gradient coil, 206
- Active shielding, 204
- Active shimming, 203
- Active transport, 169
- Acute stroke, 226
- ADC values, diffusion studies, 167–169
- Adenosine triphosphate (ATP), 169
- Adrenal myelolipoma, 244
- Advanced imaging applications:
  - diffusion, 165–169
  - functional brain imaging, 173–176
  - noble gas imaging, 178–180
  - perfusion, 169–173
  - ultra-high field imaging, 176–178
- Agitated patients, diagnostic procedures, 246
- Aliasing:
  - artifacts, 62, 99, 118–119
  - phase contrast MRA, 161
- Alternating current (AC), 136, 139
- American College of Radiology and the National Electrical Manufacturers Association (ACR-NEMA), 200
- Amplifier system, 205, 207
- Amplitude, *see specific types of amplitudes*
  - calibration, 135
  - chemical-shift artifacts, 121
  - coherence artifacts, 126, 128
  - defined, 15
  - frequency-selective excitation, 50
  - fixed gradient pulses, 43
  - gradient ( $G_{eff}$ ), 33–34, 43, 204
  - magnetic field distortions, 133
  - motion artifacts and, 114
  - phase encoding, 40–41, 43
  - slice selection and, 35
  - truncation artifacts, 124
- Analog receivers, 53–54, 209
- Analog signal, 50
- Analog-to-digital converter (ADC), 69, 73, 126, 136, 209

- Aneurysm clips, 133, 203  
 Anisotropic voxels, 42  
 Ankles, examination techniques, 226  
 Aorta, examination techniques, 115, 158, 234  
 Apodization filters, types of, 124  
 Application entity title (AET), 201  
 Arterial flow, 152. *See also* Great vessels  
 Artifact-free images/imaging, 56, 61  
 Artifacts:  
   aliasing, 118–119  
   chemical-shift, 119–121  
   coherence, 125–129  
   external, overview, 129–139  
   magnetic field distortions, 130–134  
   magnetic-susceptibility difference, 129–131  
   measurement hardware, 134–135  
   motion, 113–117, 134, 141–150, 229, 233  
   noise, 135–139  
   phase cancellation, 122–123  
   sequence/protocol-related, overview, 117–129  
   truncation, 123–125  
 Asialoglycan protein receptor contrast agents, 221  
 Aspect ratio, 42  
 Atom(s):  
   atomic number, 1–2  
   atomic weight, 1–2  
   principles and properties of, 1  
 Attenuation, 96  
 Axis of precession, 5  
 Axis of rotation, 2–3, 5  
  
 Background noise, 43, 93–94, 135  
 Bandwidth, significance of, 35–36, 39–40, 49, 50–51, 123, 136  
 Bar magnet, 3  
 Benzoxypionic tetraacetate (BOPTA), 217  
 Biological systems applications, 2–3, 167  
 Black-blood MRA, 152  
 Bladder imaging, 129  
 Blipped phase encoding, 81  
 Blood, *see* Blood flow  
   abdominal imaging, 104  
   saturation, time-of-flight MRA, 153–154  
 Blood clots, 225  
 Blood flow:  
   functional brain imaging, 173  
   gradient echo sequences, 77  
   motion artifacts, 115–116, 142  
   perfusion studies, 169–172  
 Blooming artifact, 131  
  
 BOLD (blood-oxygenation-level-dependent) effect, 174  
 Boltzmann distribution, 6  
 Boltzmann's constant, 6  
 Bone marrow studies, 194, 218  
 Bony skeleton, 224. *See also* Musculoskeletal systems  
 Bowel imaging, 117, 129, 143. *See also* Abdominal imaging  
 Brain activation studies, 173–175  
 Brain imaging:  
   characteristics of, generally, 72, 116  
   clinical protocols, 226–227  
   functional, 173–176  
   multiecho spin echo techniques, 245  
   patient sedation, 246  
   ultrahigh field spectroscopy, 194  
 Breast examination:  
   characteristics of, generally, 173  
   diagnostic principles, 224, 233–234  
   examination design, 226  
 Breath-hold imaging techniques, 226, 234, 236, 245–246  
 Breath-hold spoiled gradient echo sequences, 226, 239  
 Bright-blood, generally:  
   image, 235  
   MRA technique, 151–152, 162, 223  
 Bulk magnetic susceptibility, 8  
  
<sup>13</sup>C, 194  
 Calibration, measurement hardware, 134–135  
 Cancer/carcinoma, detection of:  
   breast, 233  
   hepatocellular, 245  
   ovarian, 242  
 Capillary phase, 172  
 Cardiac cycle, 146–147  
 Cardiac motion artifacts, 141, 143, 146, 179  
 Cardiac triggering, 233–234  
 Carotid arteries, 162  
 Carrier frequency, 206–207  
 Carr-Purcell-Meiboom-Gill (CPMG) technique, 206  
 Cartesian coordinate system, 5  
 Caudal images, 37  
 CD-ROM, 198–199  
 Center frequency, 35, 44  
 Centric ordering, 59–60, 88, 91  
 Cerebral MRA studies, 162  
 Cerebrospinal fluid (CSF), 21, 77, 86–87, 116, 150, 165, 245

- Cerebrovascular disease, 227
- Cervical spine studies, 229, 244
- Chelate complex, 214
- Chemical shielding, 17
- Chemical-shift artifacts (CSA), 100, 119–121, 194–195, 246
- Chemical shift difference, 19
- Chemical shift imaging (CSI), 188
- CHES rf pulse, 187
- Chest wall examinations, 233
- Choline (Cho), 193–194
- Cine heart imaging, 146–148
- Cine MR, 234
- Circularly polarized (CP) transmitter system, 207–208
- Clinical applications, protocols:
  - abdominal organ imaging, 239–241
  - brain examinations, 226–227
  - breast examination, 224, 233–234
  - great vessel examination, 234–236
  - heart imaging, 234–236
  - liver imaging, 236–239
  - musculoskeletal system imaging, 231–232
  - neck imaging, 227, 229
  - pelvic examination, 225, 241–243
  - spine imaging, 229–231
  - thoracic imaging, 233
  - T1-weighted techniques, 224–230, 243–245
  - T2-weighted techniques, 224–230, 245–246
- Clinical imaging, generally:
  - agitated patients, 246
  - benefits of, 223
  - diagnostic principles, 224–225
  - examination design, 225–226
  - protocols, *see* Clinical protocols
  - sedated patients, 246
- Clinical MRI, 33
- Clinical scanning, 176–178. *See also* Clinical imaging
- Coherence:
  - artifacts, 125–129
  - relaxation and, 26–27, 29–30
  - transverse, 77
- Coherent bulk flow, 165
- Coherent noise, 136
- Coil geometry, 64
- Colonic lipoma, 244
- Compensation, eddy-current, 205–206
- Composite pulses, 110–112
- Computed tomography, 199, 213
- Computer disks, 197, 209
- Computer systems, 197–201, 210
- Congenital heart disease, 234
- Consoles, in computer system, 198–199
- Constant-amplitude gradient pulses, 69
- Constant frequency, 136
- Constant rate, 2
- Constant velocity, 150
- Continuous phase-encoding gradient pulse, 80
- Contrast, and measurement parameters, 93
- Contrast agents:
  - brain examination, 227
  - characteristics of, generally, 87, 109, 151, 156, 158, 171–172
  - examination design, 226
  - functions of, 213–214
  - intravenous, 214–221, 226, 243
  - oral, 221–222
- Contrast-to-noise ratio, 43, 93, 100
- Coordinate systems, 9, 175
- Coordination sphere, 214–215
- Copper-wired-based electromagnets, 202
- Coronal images, 37, 115–116, 163, 225, 227, 232, 234, 238, 241–242
- Cortex, functional brain imaging, 176
- Cortical bone tissue, 129
- Cranial images, 37
- Creatine levels, 217
- Creatine/phosphocreatine (Cr/PCr), 193–194
- Crosstalk, 97–98
- Cysts, 244
- Dark-blood MRA techniques, 223
- Dark-blood techniques, 234–235
- Data acquisition system:
  - coils, 208–209
  - importance of, 128
  - rf shielding, 209–210
  - signals, 209
  - summary of, 211
- Data collection:
  - extrinsic measurement parameters, 94
  - loop, phase encoding, 40–41
  - magnetization-prepared (MP) sequences, 88–89, 91
  - motion artifacts, 141, 144
  - noise, 136
  - perfusion studies, 171
  - rectilinear, 58
  - rf pulses, 88
  - sequence looping, 43
  - time-of-flight MRA, 154
  - timing signal, relationship with, 144
  - traditional, 58–59

- Data collection (*continued*)
  - truncation artifacts, 123
- Data sampling, 34
- Data transfer, 199–200
- $\Delta\phi$ , 43
- $\Delta\omega$ , 35
- Demodulation, 209
- Density,  $k$  space, 58
- Deoxygenated hemoglobin, 173
- Dephasing process, 27, 29–30, 37–38, 94, 104–105, 107, 129, 133, 149
- DICOM (Digital Imaging and Communications in Medicine):
  - Conformance Statement, 200
  - defined, 200
  - Query Service Class, 201
  - Store Service Class, 200–201
- Diethylenetriaminepentaacetate (DTPA), 216
- Diethylenetriaminepentaacetate bismethylamide (DTPA-BMA), 216
- Diffusion, 165–169
- Diffusion-weighted imaging, 167, 169, 226
- Digital amplification, 209
- Digital receivers, 53–54, 209
- Directional dependence, in diffusion studies, 167–168
- Discrete values, 2
- Disk herniation, 229
- Display matrix, 54–55
- Doppler ultrasound techniques, 162
- Double phase-encoding, 46
- Dummy pulses, 25
- Duration, frequency-selective pulses, 50–51
- Duty cycle, gradient system, 204–205
- Dynamic-gradient echo scanning, 220
- Dynamic imaging/scanning, 237, 246
- Echo planar imaging (EPI):
  - characteristics of, 80–82
  - chemical-shift artifacts, 121
  - diffusion-weighted, 170
  - intrinsic measurement parameters, 94, 96
  - motion artifacts, 143
  - perfusion studies, 171
- Echo sampling, 123, 125
- Echo signal, 44, 56
- Echo time ( $TE$ ), 69, 75–76, 94–95, 100, 122–123, 126, 129, 133, 150, 158, 179
- Echo-train inversion recovery sequence, 83–84, 94, 232
- Echo train length, 96
- Echo-train sequences, generally, 114, 230
- Echo-train spin echo (ETSE) techniques:
  - brain examination, 227–228
  - cardiac studies, 147, 235
  - characteristics of, 47, 70–72, 82
  - chemical-shift artifacts (CSA), 121
  - dark-blood image, 235
  - fat-suppressed, 238
  - heart examination, 235
  - intrinsic measurement parameters, 94
  - inversion recovery sequence, 83–84, 96
  - magnetic field distortions, 132–133
  - magnetization sequences, 88
  - measurement parameters, 96
  - motion artifacts, 117
  - pelvic examination, 242–243
  - spine imaging, 229
  - $T_2$ -weighted technique, 245
  - ultra-high field scanning, 178
- Echo-train STIR, 238
- Echo-train  $T_2$ -weighted techniques, knee image, 232
- Eddy current:
  - defined, 190
  - compensation, 205–206
  - gradient system, 204–206
- Electrical current, standard, 136, 139
- Electrical shimming, 203
- Electrocardiograms (ECG), 97, 143, 146, 148
- Electrode placement, ECG, 146
- Electromagnets, 201–202
- Electronic equipment, 177
- Electrons, properties of, 1
- Energy absorption, 8, 12, 21, 26
- Energy difference ( $\Delta E$ ), 7, 12
- Energy frequency ( $\omega_0$ ), 11–13, 25–26, 41
- Energy levels, 7–8
- Energy transfer, 21–23, 25, 179, 214
- EPISTAR, 171
- Equilibrium, 13, 25–26
- Ernst angle, 97
- Erythrocytes, diffusion studies, 169
- Ethernet connection, 199
- Ethoxybenzyl
  - diethylenetriaminepentaacetate (EOB-DTPA), 217
- Excitation, generally:
  - angle, 97, 153, 160, 240
  - frequency-selective, 49–53
  - order, 97–98
  - profiles, 52
  - pulse, 11, 29, 94, 125–126, 154
- Experimental paradigm, functional brain imaging, 175–176
- Exponential decay process, 28–29

- External artifacts:
  - characteristics of, 129–130
  - magnetic field distortions, 130–134
  - measurement hardware, 134–135
  - noise, 135–139
- External interference artifacts, 136, 138
- Extremities imaging, 224–226
- Eye movement, 142
- FAIR, 171
- Faraday shield, 139, 209–210
- Fast flow velocity, 154
- Fast spin echo sequences:
  - coherence artifacts, 126
  - phase cancellation artifacts, 122
- Fat:
  - characteristics of, 17, 19, 21
  - chemical-shift artifacts (CSA), 120–121
  - magnetization, 87–88
  - phase cancellation artifacts, 122
  - saturation techniques, 53, 105–107, 132–134, 244–246
  - suppression techniques, 121, 124, 219, 223–224, 226–227, 229, 231, 233, 238, 242
  - truncation artifacts, 124
  - ultrahigh field spectroscopy, 194–195
- Female patients:
  - breast examinations, 173, 224, 226, 233–234
  - ovarian cancer, 242
  - ovarian cysts, 244
  - pelvic imaging, 225
- Feridex, 218, 220, 238
- Fermi filters, 124
- Ferric ammonium citrate, 221
- Ferromagnetic intracranial aneurysm clips, 203
- Ferromagnetic objects, 177
- Ferumoxide particles, 218, 221–222
- Ferumoxsil, 221
- Fibrinous clots, 225
- FID (free induction decay):
  - characteristics of, 13–15, 26, 29, 77
  - coherence artifacts, 125–126, 128
  - magnetic resonance spectroscopy (MRS), spectral analysis, 191
- Field gradients, 33
- Field homogeneity, 112, 133–134, 177, 202, 205, 231
- Field imaging, ultra-high, 176–178
- Field of view (FOV):
  - aliasing, 118–119
  - flow compensation, 150
  - $k$  space, 56, 62
  - magnetic field distortions, 134
  - magnetic resonance angiography (MRA), 157
  - measurement parameters, 99
  - motion artifacts, 117, 143
  - phase encoding ( $FOV_{PE}$ ), 41, 118
  - phase contrast MRA, 160
  - readout process ( $FOV_{RO}$ ), 38–40, 118
- Field strength, 203
- Filling factor, 208
- Filtering, 124–125, 139, 189
- First-order corrections, 202
- First-order motion, 150
- Fixed amplitude gradient pulses, 43
- Fixed coordinate system, 9
- FLAIR, 227
- FLASH, 226
- Flip angle, 24, 50, 97, 110, 238
- Flow, *see* Blood flow; Flow velocity
  - compensation, 148–150, 157–158
  - dynamics, perfusion studies, 170–171
- Flow velocity:
  - heart and great vessel examination, 234
  - magnetic resonance angiography (MRA), 153
  - phase contrast MRA, 158–159, 161–162
- Food and Drug Administration (FDA), 208, 221
- Fourier transformation, 15, 47, 53, 58–59, 62, 118, 123, 189–191, 198, 209
- Free induction decay, *see* FID (free induction decay)
- Frequency/frequencies, generally:
  - defined, 15
  - encoding, 34, 37–40
  - oversampling, 118–119
  - plotting guidelines, 14
  - range, 50
  - resolution, 39–40
  - synthesizer, 206
- Frequency-selective excitation, 34
- Frequency-selective pulses, 50, 103
- Frequency-selective saturation, 106–107
- Fringe field, 203–204
- Gadolinium, 216
- Gadolinium-chelate contrast agent, 158, 171–172, 174, 215, 217, 224, 227, 229, 233, 236, 239, 242–243, 245–246
- Gadolinium-DTPA (Gd-DTPA), 87–88, 221
- Gain, measurement hardware and, 135
- Gap-free raw data, 58

- Gating methods, 147–148, 226
- Gauss, 201
- Gaussian filters, 124
- Gaussian pulses, 52–53
- Gauss per centimeter, 34
- Gd-EOB-DTPA, 217
- Ghost images, 117
- Ghosting, 142, 148
- Ghost vessels, 115
- $G_{PE}$ , 148
- Gradient(s), generally:
- calibration of, 134–135
  - instrumentation, 204–206
  - pulses, 34, 38
  - spoiling, 128
  - system, 204–206, 210
  - tables, 69, 73
- Gradient echo sequences:
- acronyms, 74
  - cardiac studies, 147
  - characteristics of, generally, 25, 47, 73–74
  - chemical-shift artifacts (CSA), 121
  - first-order compensation, 150
  - intrinsic measurement parameters, 94
  - liver examination, 238
  - magnetic field distortions, 132–133
  - magnetic resonance angiography (MRA), 152–153
  - magnetization-prepared (MP), 89–91
  - magnetization-transfer suppression, 109
  - noble gas imaging, 179–180
  - refocused, 76–80, 157–158
  - spoiled, 75–77, 79
  - steady-state, 76–77
  - ultra-high field scanning, 178
- Gradient motion rephasing (GMR), 148–149
- GRASS, 246
- Gray matter, 21, 155
- Great vessels:
- aorta, 115, 158, 234
  - arterial flow, 152
  - blood flow, *see* Blood; Blood flow
  - carotid arteries, 162
  - examination design, 234–236
  - hepatic vein, 172
  - inferior vena cava (IVC), 104, 115–116
  - renal arteries, 158, 162
  - sinus vein, 142
- $G_{RO}$ , 37–38, 40, 58, 114, 118
- Gross patient motion, 45
- $G_{SS}$ , 35–36, 40, 97
- Gyromagnetic ratio, 6
- $^1\text{H}$ , 2–3, 178–179, 192, 194
- Half-integral value, 2
- Hanning filters, 124
- Hard pulses, 50
- Hardware, measurement, 134–135
- Head imaging, 208. *See also* Brain imaging
- $^3\text{He}$ , 179
- Heart imaging/heart studies, 97, 141, 143, 146–147, 179, 223, 234–236
- Heart rate, pulse triggering and, 145
- Hemodynamics, cardiac, 146
- Hemoglobin, 173
- Hepatic vein, 172
- Hepatocellular carcinoma, 245
- Hepatosplenic candidiasis, 245
- Hermitian symmetry, 62
- Higher-order corrections, 202
- High-field magnets, 101, 203
- High-field scanners, 208
- High-frequency aliasing, 118
- High homogeneity, 202
- Homogeneity, *see* Field homogeneity; Inhomogeneity
- Hyberbolic secant, 53
- Hydrocarbon chain, 19
- Hydrogen, 2, 4, 17, 165, 178
- 10-(2-hydroxypropyl)-1,4,7,10-tetraazacyclododecane-1,4,7-triacetate (HP-DO3A), 216
- Hyperpolarized noble gases, 179–180
- Hypoxia, 170
- I*, 2
- Image data, 54–55
- Image matrix (*a*), 99
- Image processors, 198
- Image quality, 178
- Image reconstruction process, 84–85
- Imaging gradients, 27
- Imaging volume, 105–106, 154, 162
- Implants, effect of:
- metal, 131–133, 177, 203
  - pacemakers, 203
  - surgical, 132, 203
- Inferior vena cava (IVC), 104, 115–116
- Inflammatory disease, 231
- Inhomogeneity, 27, 31, 74, 177
- In-phase echo time, 243
- In phase image, 122
- In-phase *TE*, 243–244
- Institutional review boards, functions of, 176
- Instrumentation:
- computer systems, 197–201, 209

- data acquisition system, 208–211
- gradient system, 204–206, 209
- magnet system, 201–204, 209
- radio frequency system, 206–208, 210
- system components summary, 210–211
- Integral value, 2
- Intensity, significance of:
  - image, 57, 63
  - magnetic field distortions, 133
  - maximum projection, MRA, 162–164
  - measurement parameters, 100
  - motion artifacts, 114, 149
  - pixels, 34
  - voxels, 176
- Interference banding artifact, 79
- Interleaved acquisition ordering, 114–115
- Interleaved ordering, 98
- International Electrotechnical Commission (IEC), 208
- Intraluminal studies, 222
- Intravenous contrast agents:
  - examination design, 226
  - T1 relaxation, 213–218
  - T1-weighted techniques, 243
  - T2 relaxation, 213, 218–221
- Intrinsic frequency, 25
- Intrinsic spin, 2
- Inversion pulses, 53
- Inversion recovery (IR):
  - acronyms, 83
  - echo-train sequence, 83–84, 87
  - image reconstruction, 84–85
  - intrinsic measurement parameters, 94
  - looping modes, multislice imaging, 84–85
  - phase-sensitive, 86
  - recovery curves, 86
  - signal intensity, standard, 100–101
  - STIR techniques, 87–88
- Inversion time (TI), 94–95
- Iodinated contrast agents, 217
- IP address, 199
- Iron, 25, 29, 238
- IR-prepared GRASS, 246
- Irradiation, 11, 97
- Isotopes, 1–2
- k* space:
  - defined, 56
  - magnetization-prepared (MP) sequences, 89
  - raw data and, 55–62
  - reduced, 62–64
  - sampling, 58–59
  - spin echo sequences, 70
  - trajectory, 59
- Kernel time, 96, 103, 145, 147
- Kidney images:
  - clinical protocols, 129, 226, 232, 241
  - examination design, 225
  - renal arteries, 158, 162
  - renal failure, 217
- Laminar flow, 153
- Large-bore solenoidal magnets, 202
- Large-volume studies, 208
- Larmor equation, 5–6, 11, 34, 56
- Laser, 179
- Laser optical disk, 198
- Lead wires, high-resistance, 146
- Lesions, identification of:
  - liver, 236
  - lung, 233
  - vascular, 223
- Linear corrections, 202
- Linear polarized (LP) transmitter system, 207–208
- Linear trajectory, 59
- Line gradient amplitudes, 46
- Lines-in-partitions, 46
- Liver images/imaging:
  - characteristics of, generally, 172, 217–221, 236–239
  - contrast agents, 226
  - examination design, 225–226
  - fat saturation techniques, 246
  - STIR, 245
  - T1-weighted techniques, 236, 238–241, 244
- Logical gradients, 34
- Longitudinal magnetization, 105
- Longitudinal relaxation time, 21
- Low-field magnets, 201, 203
- Low-field scanners, 208
- Lumbar spine imaging, 104, 116, 229–230
- Lumenhance, 221
- Lung imaging:
  - clinical protocols, 233
  - magnetic-susceptibility difference artifact, 129, 179
- Lymph nodes imaging:
  - clinical protocols, 224, 229, 246
  - fat saturation techniques, 246
- Macroadenomas, 173
- Macromolecules, 107, 214, 218
- Macroscopic picture, 4, 7, 23, 26



- Magnet, generally:  
  homogeneity, 80  
  location of, 33  
  manufacturing, 27, 202  
  system, 201–204, 210
- Magnetic field ( $B_0$ ):  
  homogeneity, *see* Field homogeneity  
  implications of, 1, 3–7, 11, 13, 17, 26–28, 31, 203–204  
  distortions, 130–134  
  ultra-high field scanners, 176–178
- Magnetic moment, 3
- Magnetic resonance angiography (MRA):  
  black-blood, 152  
  bright-blood method, 151–152, 162  
  defined, 151  
  gradient echo sequences, 152–153  
  maximum intensity projection (MIP), 162–164  
  phase contrast, 151, 157–162  
  problems with, generally, 153  
  time-of-flight techniques, 151, 153–157
- Magnetic resonance spectroscopy (MRS):  
  basis for, 19  
  chemical shift, 181–182  
  defined, 181  
  localization techniques, 186–189  
  postprocessing, 189–194  
  readout process, 37  
  spectral analysis, 189–194  
  spin coupling, 182–184  
  ultra-high field spectroscopy, 194–195  
  water suppression, 184
- Magnetic susceptibility, 8, 74, 80
- Magnetic-susceptibility difference:  
  artifacts, 129–131  
  neck examination, 229
- Magnetization-preparation pulses, 82
- Magnetization-prepared (MP) sequences:  
  gradient echo, 94  
  inversion recovery (IR), 82–88  
  longitudinal magnetization, 88  
  spin-echo-based, 88  
  timing diagrams, 89–90
- Magnetization-transfer (MT), generally:  
  pulse, 108–110, 154–155  
  suppression, 53, 107–110, 227
- Magnevist Enteral, 221
- Magnitude, 15
- Main field inhomogeneity, 27
- Manganese, 25
- Manganese chloride, 221
- Manganese *N,N'*-dipyridoxal ethylenediamine-*N,N'*-diacetate 5,5' bis (phosphate) (Mn-DPDP), 217, 219, 237–238
- Mangofodipir, 217–218
- Maximum gradient strength, 204
- Maximum intensity projection (MIP), 162–164
- Measurement parameters:  
  extrinsic, 94, 97–102  
  flow compensation, 149–150  
  intrinsic, 93–97, 100–101  
  overview of, 93–94  
  perfusion studies, 171–172  
  selection factors, 334
- Medium-field magnets, defined, 201
- Megahertz (MHz), 6, 25, 209
- Metabolite excitation, ultra-high field spectroscopy, 194–195
- Metal-chelate complexes, 221
- Metal ions, 25, 214, 216
- Microadenomas, 173
- Microscopic picture, 4, 7, 23, 26
- Millitesla, 34
- Miscalibration, 135–136
- Misregistration artifacts, 116–117, 121
- Mitral valves, 234
- Modems, 199
- Modulation, frequency-selective excitation, 50
- Monoclonal antibodies, 221
- Motion artifacts:  
  acquisition parameter modification, 142–143  
  cardiac triggering, 233  
  characteristics of, 113–117, 134  
  flow compensation, 148–150  
  reduction techniques, 141–150, 229  
  triggering/gating, 144–148
- Motional artifact suppression technique (MAST), 148–149
- Moving spins, 225
- Multiecho spin sequences, 70, 245
- Multiple subloops, 114–115
- Multislice imaging, inversion recovery, 84
- Multislice looping, 44–46
- Multislice loop structure, 70
- Multislice scanning, 44–45
- Musculoskeletal system imaging:  
  clinical protocols, 231–232, 244  
  patient sedation, 246
- $^{23}\text{Na}$ , 179
- N*-acetyl aspartate (NAA), 193–194
- Navigator echo, 144

- Navigator echo-based techniques, 246  
Neck imaging, 227, 229  
Negative agents, 221–222  
Neoplastic disease, 231  
Net magnetization ( $M_0$ ), production of:  
  energy absorption, 12  
  nuclear spin, 1–4  
  overview, 11  
  spin orientation, 6–8  
  spin vectors, 4, 6  
Neutrons, properties of, 1  
90° pulse, 13, 24, 26–27, 29–30, 91  
Noble gas imaging, 178–180  
Noise, 63, 135–139. *See also* Background noise; Signal-to-noise (S/N) ratio  
Nonalternating (DC) current, 139  
Non-breath-hold sequences, 236  
Nonferrous tanks, 203  
Nonlinear gradient pulses, 135  
Nonrectilinear sampling, 58–59  
Nonselective pulses, 50  
Nonuniform respiration, 148  
 $N_{\text{SUBLOOP}}$ , 44–45  
Nuclear spin, 1–4  
Nucleus, properties of, 2  
Null time, 86  
Nyquist frequency ( $\omega_{\text{NQ}}$ ), 14, 38–40, 99  
Nyquist limit, 118–119  
  
Occlusions, 151  
Off-resonance protons, 106, 111  
OMR, 221  
180° pulse, generally, 29–31, 37, 73, 83, 86, 91, 122  
Open-design magnets, 202  
Oral contrast agents, 221–222  
Orbits, 224  
Ordering methods, 56  
Order of the field correction, 202  
Oscillation, 123  
Out-of-phase, generally:  
  gradient echo, 239, 243–244  
  TE, 122–123  
Ovarian cancer, 242  
Ovarian dermoid cysts, 244  
Oversampling, 118–119  
Oxygen, 17, 169, 173, 179  
  
 $^{31}\text{P}$ , 194  
Pacemakers, 203  
PACS (picture archiving and communications system), 199  
Pancreas imaging, 217, 226, 241  
Parallel acquisition, 64  
Paramagnetic metal ions, 214, 221  
Paramagnetic molecules, 173  
Parathyroid studies, 229  
Partial Fourier imaging, 62  
Partitions ( $N_{\text{PART}}$ ), 46–47, 98  
Passive shielding, 203  
Passive shimming, 203  
Patient(s), generally:  
  agitated, 246  
  body weight, 208  
  gross motion, 45  
  monitoring devices, 138–139  
  positioning, 34. *See also* specific types of imaging  
  sedated, 246  
Pelvic studies:  
  clinical protocols, 241–243  
  contrast agents, 221  
  female patients, 225  
Perflubron, 222  
Perfluorooctylbromide (PFOB), 222  
Perfusion, 169–173  
Perfusional blood flow, 167  
Periodic table, 1  
Peripheral MRA, 159  
Peristalsis, 117  
Peritoneal seeding, 246  
Permanent magnets, 201  
Phantom, 57, 63  
Phase accumulation, 149  
Phase angle, 15  
Phase cancellation artifacts, 122–123  
Phase contrast MRA, 151, 157–162  
Phased-array coils, 64, 209  
Phase encoding:  
  characteristics of, 34, 40–43, 45  
  chemical-shift artifacts (CSA), 121  
  echo planar imaging (EPI), 80  
  gating methods, 148  
  k space, 56  
  loop, 47  
  measurement parameters, 99  
  motion artifacts, 141–142  
  phase contrast MRA, 161  
  raw data, 54–55  
Phase encoding gradient ( $G_{\text{PE}}$ ):  
  characteristics of, 40–42, 54, 114  
  k space, 58–60, 62  
Phase modulation, 129  
Physical gradients, 33–34  
Pituitary gland, 227  
Pixels, significance of, 34, 39–41, 120–121, 151, 162–163

- Plateau, 59
- Point resolved spectroscopy (PRESS), 186–188, 192
- Polarization, 129, 179
- Positron emission tomography (PET), 176
- Postexcitation pulse signals, 77–79
- Potassium ions, 169
- ppm, 177–178
- Precession, 5
- Precessional cycle, 26
- Preexcitation imaging sequence, 78
- Preparatory phase-encoding pulse, 80
- Preparatory pulses, 25
- Presaturation, 103–105
- Presaturation pulse, 126, 152
- Primary tumors, 194
- Protocol-related artifacts:
- aliasing, 118–119
  - characteristics of, generally, 117–118
  - chemical-shift artifacts (CSA), 119–121
  - coherence artifacts, 125–129
  - magnetic-susceptibility difference artifacts, 129–131
  - phase cancellation artifacts, 122–123
  - truncation artifacts, 123–125
- Proton(s):
- chemical-shift artifacts, 120
  - coherence artifacts, 126
  - composite pulses, 111
  - density, 24
  - dephasing, 27, 29–30, 37–38, 73–74, 94, 129, 133–134, 149
  - frequency-selective excitation, 50–52
  - magnetic field distortions, 134
  - magnetization-transfer suppression, 107–108
  - motion artifacts, 114, 134
  - phase encoding process, 40–43
  - relaxation times, 21–23
  - signal frequency and, 1, 3–4, 6, 8–9, 11, 13–15, 17
- Proton-proton energy transfer, 26
- Pulmonary valve, 234
- Pulsatility, 150
- Pulse, *see specific types of pulses*
- amplitude, 50
  - angle, 24
  - defined, 11
- profile, 51–52
- sequences, *see* Pulse sequences
  - triggering, 144–147
- Pulsed excitation, 49
- Pulsed rf energy, 22
- Pulse sequences:
- comparison of, 68–69
  - defined, 67
  - echo planar imaging sequences, 80–82
  - gradient echo sequences, 73–80
  - parameter limits, 67
  - magnetization-prepared sequences, 82–91
  - spin echo sequences, 69–73
- Quadrature, 14, 17, 207
- Quantum mechanics, applications of, 3
- Radiofrequency (rf) energy, 11–12, 23, 49
- Radio frequency system:
- frequency synthesizer, 206–207
  - manufacturing regulations, 208
  - power amplifier, 207
  - resonance absorption, 207–208
  - summary of, 210
  - transmitter coil, 207
  - transmitter system, 206
- Radioisotopes, 170
- Ramped sampling, 59
- Rapid scanning:
- perfusion studies, 173
  - techniques, 179
- RARE (rapid acquisition with relaxation enhancement), 70
- Raw data:
- image data matrices, 53–55
  - matrix, 55–56, 62
  - $K$  space, 55–62
- Readout:
- aliasing, 118
  - chemical-shift artifacts (CSA), 120–121
  - defined, 34
  - implications of, 37–40
  - $k$  space, 56
  - measurement parameters, 99
  - motion artifacts, 114
  - raw data, 54–55
- Receive-only coils, 208
- Receiver(s), generally:
- bandwidth ( $BW_{REC}$ ), 99–100
  - calibration, 134, 136
  - coherence artifacts, 129
  - noise, 136
  - noble gas imaging, 179
- Rectangular pulses, 50
- Rectilinear data collection, 58
- Reference image, 157, 171
- Refocused gradient echo sequences, 76–80, 157
- Refocusing pulses, 69–70, 128, 133, 180, 206
- Relaxation, *see*  $T_1$  relaxation;  $T_2/T_2^*$

- relaxation
  - defined, 15, 21
  - impact of, 1
  - inversion recovery (IR), 84–85
  - measurement parameters, 94–96, 102
  - spin echo sequences, 70–71
  - spin-lattice, 94
- Renal arteries, 158, 162
- Renal failure, 217
- Repetition time (*TR*), 69, 76, 83, 94–96, 100, 104–105, 143
- Rephasing, 149
- Resonance absorption, 1, 207
- Resonant frequency:
  - implications of, generally, 12, 17, 25, 29, 49, 120
  - magnetic field distortions, 134
  - phase cancellation artifacts, 123
  - spectral analysis, 189
  - ultrahigh field spectroscopy, 194
- Resovist, 220–221
- Respiratory artifacts, 143, 239, 243
- Respiratory compensation, 148
- Respiratory gating, 148
- Respiratory motion, 147–148, 226, 234
- Respiratory motion artifacts, 117, 179
- Restraint use, 246
- Reticuloendothelial cells, 218, 220
- rf calibration, 135
- rf profiles, 52
- rf pulse:
  - center frequencies, 44
  - classification of, 50
  - frequency-selective, 34–35
  - implications of, 12–14, 34
  - power deposition, 105–106, 135
  - refocusing, 206
  - relaxation times and, 21–25, 29
  - slice-selective, 44
  - TONE, 156–157
  - types of, generally, 103
- rf spoiling, 75, 128–129
- rf transmitter, 69
- RF power, 177
- Ring, 123
- Rise time, gradient system, 204–205
- Rotating frame of reference, 7–8, 13, 19, 28, 30
- Rotations, 27
- R-R interval, 145–146
- Rubidium atoms, 179
- R wave, 148
- benefits of, 225, 234
- brain examination, 227
- defined, 37
- heart examination, 235
- knees, 232
- pelvic examination, 241–242
- sinus vein, 142
- spine examination, 229–230
- Sample-induced inhomogeneity, 27
- Saturated hydrocarbon chain, 19
- Saturation:
  - defined, 22
  - fat, *see* Fat saturation
  - frequency-selective pulses, 53
  - phase contrast MRA, 158
- Scanner room, 138–139
- Scan time:
  - measurement parameter, 93, 98
  - parallel acquisitions, 64
  - phase contrast MRA, 159
  - pulse triggering, 144–145
  - spin echo sequences, 72
- Snapshot ETSE, 72
- Secondary echoes, 128
- Second-order corrections, 202
- Second-order motion, 150
- Sedation, 246
- Segmented data collection, 59–60
- Segmented EPI sequences, 80, 82
- Sella tursica, 227
- Semiquantitative spectral analysis, 191
- SENSE (sensitivity encoding), 65
- Sequence artifacts, types of:
  - aliasing, 118–119
  - characteristics of, generally, 117–118
  - chemical-shift artifacts (CSA), 119–121
  - coherence artifacts, 125–129
  - magnetic-susceptibility difference artifacts, 129–131
  - phase cancellation artifacts, 122–123
  - truncation artifacts, 123–125
- Sequence looping, 43–47, 114–115
- Sequence modifications:
  - composite pulses, 110–112
  - fat saturation, 105–107
  - magnetization-transfer suppression, 107–110
  - spatial presaturation, 103–105
- Sequential filling, 59
- Sequential slice technique, 44
- Sequential stepping, 61
- Shim correction, 202–203
- Short-bore magnets, 202
- Short duration pulses, 52

- Shunts, 234
- Signal averages ( $N_{SA'}$ ), 44–45, 99, 102
- Signal-difference-to-noise ratio, 100
- Signal loss, 30, 129
- Signal-to-noise (S/N) ratio, 63–64, 99–100, 102, 176, 178, 186, 188, 192, 194, 226, 243
- Sinc function, 51–53
- Sinc interpolation, 190
- Sine waves, 51
- Single-shot EPI sequences, 80
- Single-shot echo-train spin echo (ETSE) sequences:
- characteristics of, generally, 234
  - contrast agents, 220
  - liver examination, 236, 238
  - motion artifacts, 143
  - pelvic examination, 241
- Single spin echo, standard signal, 100–101
- Single voxel spectroscopy (SVS), 186–187
- Skin effect, 177
- Slew rate, gradient system, 204–205
- Slide gap, 97
- Slice loop:
- coherence artifacts, 129
  - fat saturation process, 106–107
  - multiple, *see* Multislice loop
  - subloops, 114–115, 152
  - 3D images, 61
- Slice position, 115
- Slice selection, 34–37, 121
- Slice-selective excitation pulses, 50–51
- Slice-selective TurboFLASH, 246
- Slice thickness ( $TH$ ), 97, 153–154, 243
- Smaller-volume studies, 208
- Small vessel detection, 154
- SMASH (simultaneous acquisition of spatial harmonics), 64
- Sodium ions, 169
- Sodium-potassium-ATP pump, 169
- Soft pulses, 50
- Soft tissue, 129, 224–225, 227, 244
- Solenoidal MR systems, 207
- Solenoidal superconducting electromagnets, 202
- Spatial localization, 27, 135
- Spatial presaturation, 103–105, 229–230
- Spatial relationship, MRA scan, 162
- Spatial resolution, 39–41, 43, 62–63, 93, 99, 226, 234, 245
- Specific absorption rate (SAR), 135, 177–178, 208
- Spikes, 136–137
- Spin dephasing, 166
- Spin down energy levels, 12, 23
- Spin echo imaging, *see* Spin echo sequences
- cardiac studies, 146
  - characteristics of, generally, 25–31
  - diagnostic principles, 225
  - fat saturation, 244
- Spin echo pulse sequences, diffusion studies, 166–167
- Spin echo sequences:
- brain examination, 227
  - characteristics of, 25–31, 69–73
  - chemical-shift artifacts, 121
  - coherence artifacts, 128
  - fat-suppressed, 239
  - flow compensation, 150
  - magnetization-transfer suppression, 109
  - motion artifacts, 115
  - phase cancellation artifacts, 122
- Spin-echo spin echo techniques, T1-weighting, 243
- Spine imaging:
- characteristics of, 72, 104, 116, 120
  - clinical protocols, 229–231
  - motion artifacts, 141
  - multiecho spin echo techniques, 245
  - patient sedation, 246
- Spin-lattice relaxation time, 21, 25, 94
- Spin polarization, 129, 179
- Spin-spin relaxation time, 25–30
- Spin up energy levels, 11–12, 23
- Spin vectors, 4, 6
- Spiral sampling, 59
- Spleen imaging, 172–173, 218, 226
- Spoiled gradient echo EPI sequences, 82
- Spoiled gradient echo imaging:
- abdominal organs examination, 240
  - characteristics of, 75–77, 79
  - clinical applications, 245
  - contrast agents, 219, 226
  - diagnostic principles, 225
  - functional brain imaging, 174
  - liver examination, 236–237, 239–240
  - magnetic field distortions, 132
  - magnetic-susceptibility difference artifacts, 129–130
  - perfusion studies, 171–172
  - phase contrast MRA, 159–160
  - signal intensity, standard, 100–101
  - T1-weighting techniques, 243
- Spoiled GRASS, 226
- Spontaneous energy transfer, 21
- State-of-the-art scanners, 204–206

- Stationary coordinate system, 9
- Stationary frame of reference, 13
- Statistical mechanics, 4
- Steady-state, generally:
  - characteristics of, 24–25
  - gradient echo sequences, 76–77
  - magnetization, 104, 108
- Stejskal-Tanner method, 166
- Stenoses, 151, 153
- Stethoscopes, 203
- Stimulated echo acquisition method (STEAM), 186–188
- Stimulus execution scheme, 175–176
- STIR imaging, 87–88, 105, 231, 233, 244–245
- Subloops, 114–115, 152
- Subsecond imaging techniques, 165
- Superparamagnetic iron oxide (SPIO)
  - particulate molecules, 218, 220–221
- Surface coils, 226
- Tantalum, 132
- Targeted MRA, 162, 164
- Taylor series expansion, 150
- TCP/IP (Transmission Control Protocol/Internet Protocol), 199–200
- Template pulse sequence, 93
- Temporal lobe epilepsy, 193–194
- Tensor quantity, diffusion studies, 167, 169
- Tesla (T), 6, 201
- Thermodynamics, 166
- Thin-section 3D-volume acquisition, breast examination, 233
- Third-order motion, 150
- Thorax imaging:
  - contrast agents, 216
  - examination design, 226, 233
  - neck examination, 229
- Three-dimensional (3D) imaging:
  - characteristics of, generally, 44
  - gradient echo images, 233, 236, 240–241
  - imaging acquisition, standard, 102
  - looping structures, 61
  - MR angiography, 109
  - volume acquisition, 46–47, 152
  - volume scanning, 59, 61, 173
- 3T scanners, 176
- Through-plane flow, 153–154
- Thyroid studies, 229
- Tilted optimized nonuniform excitation (TONE) rf pulses, 156–157
- Time-of-flight MRA, 151, 153–157
- Time-varying signals, 136
- Timing diagrams:
  - echo-train inversion recovery sequence, 84
  - pulse sequences, 68–69, 73
  - 3D-MP sequence, 89
  - 2D-MP sequence, 90
- Tissue movement, 165
- Titanium, 132
- T1 relaxation:
  - characteristics of, generally, 21–25, 34
  - coherence artifacts, 126
  - contrast agents, 213–218
  - magnetic resonance angiography (MRA), 152–154, 156
  - magnetization-prepared sequences, 82–87, 90
  - magnetization-transfer suppression, 109–110
  - as measurement parameter, 94, 97–98
  - noble gas imaging, 178–180
  - perfusion studies, 171
  - pulse triggering and, 145
  - saturation and, 24–25
  - spatial presaturation, 105–106
- TONE rf pulse, 156–157
- T1-weighted techniques:
  - abdominal organs examination, 239
  - brain examination, 227–228
  - breast examination, 233
  - characteristics of, generally, 148, 214–215
  - clinical protocols, 224–225, 243–245
  - examination design, 226
  - liver examination, 236, 238–241, 244
  - musculoskeletal system examination, 231
  - pelvic examination, 242
  - spin echo, 246
  - spine imaging, 229
- Trace image, 168–169
- Traditional looping, 45
- Translational motion, 165–166
- Transmitter(s):
  - calibration of, 134
  - coil, 52, 207–208
  - composite pulses, 110
  - duration, 50
  - frequency  $\omega_{TR}$ , 13–14
  - measurement hardware and, 134
  - noble gas imaging, 179
  - noise, 136
  - phase modulation, 129
  - system components, 206
- Transverse coherence, 126, 128–129

- Transverse images:
  - benefits of, 225
  - brain examination, 227
  - characteristics of, 37, 235, 237, 243
  - heart, 234
  - neck examination, 228
  - pelvic examination, 242
- Transverse magnetization:
  - characteristics of, generally, 26–27, 37, 75, 77–79, 97, 104–105
  - coherence artifacts, 126, 128
  - time-of-flight MRA, 154
- Transverse relaxation time, 25–26
- Tricuspid valves, 234
- Truncation, 51
- Truncation artifacts, 123–125
- $T2/T2^*$  relaxation:
  - characteristics of, generally, 25, 34, 37
  - coherence artifacts, 126
  - contrast agents, 213, 218–221
  - diffusion studies, 167–168
  - functional brain imaging, 173–174, 176
  - gradient echo sequences, 77, 90
  - magnetic field distortions, 133
  - magnetic resonance angiography (MRA), 152
  - magnetization-prepared sequences, 90–91
  - magnetization-transfer suppression, 107–108
  - measurement parameters, 94, 96
  - perfusion studies, 171
  - spin echoes, 25–31
- $T2$ -weighted techniques:
  - brain examination, 227–228
  - breast examination, 234
  - characteristics of, generally, 220–221
  - clinical protocols, 224–225, 245–246
  - liver examination, 236
  - musculoskeletal system examination, 231, 244
  - spine imaging, 229
- Tumor detection:
  - brain, temporal lobe epilepsy, 193–194
  - echo-train spin echo techniques, 245
  - pancreatic, 218
  - perfusion studies, 173
- Turbo factor, 96
- Two-dimensional (2D) imaging:
  - characteristics of, generally, 41, 44
  - CSI, 192–195
  - Fourier transformation, 54–55
  - gradient echo imaging, 240
  - imaging acquisition, standard, 102
  - multislice imaging, 44–45
  - sequential slice, 152
  - volume scanning, 61
- Ultrafast ETSE, 72
- Ultra-high field imaging, 176–178
- Ultra-high-field magnets, defined, 201
- Ultrasmall particulate iron oxide (USPIO), 220–221
- Ultrasound, 199
- Unsaturated hydrocarbon chain, 19
- User-interface software, 93, 197
- Valvular disease, 234
- Vascular disease, 227
- Vascular grafts, 224–225
- Vascular system, 151
- Vector rotation, 13
- Vectors, functions of, 4–5
- Velocity:
  - encoding value, 158
  - significance of, 2
- Venc, phase contrast MRA, 158, 160–162
- Venetian blinds, 117
- Venous flow, 152
- Vibrations, 27
- Voltage, 13
- Volume-selective chemical shift imaging, 188–189
- Voxels:
  - characteristics of, 34, 41, 99, 106, 119, 122–123, 176
  - multiple MRS techniques, 188–189
  - single MRS techniques, 186–188
  - ultrahigh field spectroscopy, 195
- Water:
  - characteristics of, generally, 17, 19, 21, 26
  - chemical-shift artifacts (CSA), 120–121
  - composite pulses, 111
  - excitation, 111–112
  - magnetic field distortions, 134
  - magnetization, 87–88
  - magnetization-transfer suppression, 107–108
  - phase cancellation artifacts, 122
  - saturation process, 107
  - suppression techniques, 227
  - $T1$  relaxation agents, 214–215

- 
- Water vapor, 179  
White matter, 155  
White matter inflammation, 227  
Wrists, 226  
 $^{129}\text{Xe}$ , 179  
X-ray angiography, 154, 157  
X-rays, 199  
Zeeman interaction, 6–7, 178  
Zero filling, 189  
z score, 176